Single walled carbon nanotube photovoltaics

Thesis submitted to the
School of Chemical and Physical Sciences
Faculty of Science and Engineering
The Flinders University of South Australia
in fulfilment of the requirements for the degree of
Doctor of Philosophy
July 2013

Daniel D. Tune

Supervisor: Prof. Joseph G. Shapter
Co-supervisors: Assoc. Prof. Jamie S. Quinton & Prof. Amanda V. Ellis

Boldface is used for vectors and hat notation for unit vectors. Numbering begins with the title page for compatibility with electronic document conventions.

For my beloved family

Preface

Energy has been a challenge for us since the dawn of time and we continue to invent even more clever ways of capturing and harnessing it. However, only recently have we become so numerous, and the waste from our industrial scale energy generation so great, that getting our energy in the wrong ways now poses a real, existential threat to us all. Fortunately, there is more than one form of energy and many technologies are available to us to capture, store and use it without generating much waste. Unfortunately, the ability of many economies, including Australia's, to respond effectively to our changing energy needs is constrained by the preponderance of established infrastructure investment and the watering down or outright capture of government and regulatory bodies. In short, we already have the technological solutions we need to solve our current energy challenges, but due to the pervasive influence of those who continue to profit from fossil fuels at everyone else's expense, renewable technologies are at a disadvantage. The large-scale deployment of green energy quickly becomes the most profitable investment on any mid to long term scale when tax payer handouts to the fossil fuel industry are taken out of the equation. That is, the energy problem is no longer a scientific or engineering one, but one of public policy in our choice of industrial subsidies.

Thus, the need is great for disruptive new technologies or advances in current systems or processes that, through performance or cost improvements, render untenable any attempts to thwart or delay further our requirement for technologies that enable a sustainable energy future. It is the sincere hope of the Author that the use of single walled carbon nanotubes in photovoltaics will become such a technology.

Table of Contents

Abstract

The environmental and climatic drivers for massively increased use of photovoltaics for energy generation can hardly be understated. Due to the high cost of energy from the current generation of silicon-based photovoltaics relative to that from highly subsidised fossil fuels, there is great interest in finding alternative materials and device architectures for light harvesting applications. Single walled carbon nanotubes are an allotrope of carbon with some unique electrical and optical properties which make them promising as various elements of photovoltaic systems. Exploring and developing methods of harnessing their properties is thus desirable and much work has already been done in this emerging field. Before the work presented in this thesis began in 2009, carbon nanotubes had been employed in various roles in different types of solar cells including as transparent electrodes, as additives to improve charge dissociation and transport in organic bulk heterojunctions and the titania of dye sensitised solar cells, and as contributing or scaffolding elements of donor-acceptor type photoelectrochemical systems with porphyrins, quantum dots and more.

Throughout this thesis, the results of new experimental and theoretical investigations into some further applications of single walled carbon nanotubes in photovoltaics will be presented, with particular focus on carbon nanotube-silicon solar cells.

Declaration

I certify that this thesis does not incorporate without acknowledgment any material previously submitted for a degree or diploma in any university; and that to the best of my knowledge and belief it does not contain any material previously published or written by another person except where due reference is made in the text.

Acknowledgements

In acknowledging the input of others in the production of this work I must start with the most important of all - my wife Melissa. Without her almost sole-parenting our girls for the last six months, and much more over the years, I could never have done any of this and indeed, without her inspiration, I wouldn't have even tried. I would also like to sincerely thank my supervisor Joe Shapter for his steadfast guidance and ever helpful advice throughout the PhD process and for his untiring support, and my co-supervisors Jamie Quinton and Amanda Ellis for all their input over the years. My doctoral studies were made easier by having friends and colleagues in the same field, in particular Benjamin Flavel, with whom I have also shared many a collaboration, and Katherine Moore, as well as Adam Blanch and Chris Gibson, Mark Bissett, Cameron Shearer and Ashley Slattery, not to mention the understanding and backing of old mates. I could not have become the first Doctoral student in my family without the solid and continuing foundation of love and support from my parents, Karen and Richard, and my inspirational sister, Luanne. I wish to extend my thanks also to Ralph Krupke for hosting my research stay at Karlsruhe Institute of Technology and for ongoing collaborations, The Flinders University of South Australia for providing a supportive environment in which I could pursue and develop my research, as well as for my undergraduate degree, the Australian Microscopy and Microanalysis Research Facility for many of the instruments I have relied upon and the Australian Nanotechnology Network for so many helpful conferences and workshops. Lastly, for good measure, I will thank my wife again.

Contextual statement

Each chapter in this thesis is either a complete published work, or a complete published work with additional data, analysis and discussion expanding upon that which can be found in the literature. The work in this thesis follows the Author's interest in exploring the use of single walled carbon nanotubes in photovoltaics, partly with a view to determining solar cell architectures which exploit the ability of single walled carbon nanotubes to absorb sunlight energy. Chapter 1 introduces the issues, states the case for using carbon nanotubes in solar cell applications and reviews some of the important background theory and literature, focussing particularly on carbon nanotube-silicon solar cells which form the bulk of this thesis. Chapter 2 reports the fabrication and characterisation of dye sensitised solar cells in which the titanium dioxide working electrode is replaced with nanotubes. Chapter 3 comprises a device structure analysis of carbon nanotube-silicon solar cells whilst Chapter 4 delves into the role that the nanotubes play in them. Chapter 5 compares devices with either semiconducting or metallic nanotubes and investigates the effect of nanotube film metallicity on solar cell output. In Chapter 6, the conductive polymer, polyaniline, is used in conjunction with the nanotubes with a synergistic effect on performance. Lastly, the modelling presented in Chapter 7 explores the use of single walled carbon nanotubes as the primary light absorbing elements of tandem solar cells and highlights the great potential of them for this purpose. All chapters have been edited for consistency however there may still remain some minor repetition and formatting differences.

Publications

The following is a list of the original publications arising from the Author's Doctor of Philosophy studies where this thesis incorporates all except publications 3 and 5.

[1] **Tune, D.D.,** Flavel, B.S., Quinton, J.S., Ellis, A.V., and Shapter, J.G., *Single walled carbon nanotube network electrodes for dye solar cells.* Solar Energy Materials and Solar Cells, 2010. 94(10): p. 1665-1672. DOI: 10.1016/j.solmat.2010.05.026

[2] **Tune, D.D.,** Gibson, C.T., Quinton, J.S., Ellis, A.V., and Shapter, J.G. *Single walled carbon nanotube array as working electrode for dye solar cells*. in *ICONN2010: International Conference on Nanoscience and Nanotechnology*. 2010. Sydney, Australia. DOI: 10.1109/iconn.2010.6045232

[3] Vogt, A.P., Gibson, C.T., **Tune, D.D.,** Bissett, M.A., Voelcker, N.H., Shapter, J.G., and Ellis, A.V., *High-order graphene oxide nanoarchitectures.* Nanoscale, 2011. 3(8), pp.3076-3079. DOI: 10.1039/c1nr10406c

[4] **Tune, D.D.,** Flavel, B.S., Krupke, R., and Shapter, J.G., *Carbon nanotube-silicon solar cells.* Advanced Energy Materials, 2012. 2(9): p. 1043-1055. DOI: 10.1002/aenm.201200249

[5] Larsen, L.J., **Tune, D.D.,** Kemppinen, P., Winzenberg, K.N., Watkins, S.E., and Shapter, J.G., *Increased performance of single walled carbon nanotube photovoltaic cells through the addition of dibenzo[b,def]chrysene derivative.* Journal of Photochemistry and Photobiology A: Chemistry, 2012. 235(0): p. 72-76. DOI: 10.1016/j.jphotochem.2012.03.001

[6] **Tune, D.D.,** Flavel, B.S., Hennrich, F., Krupke, R., and Shapter, J.G. *The role of nanotubes in carbon nanotube-silicon heterojunction solar cells*. in *ICONN2012: International Conference on Nanoscience and Nanotechnology*. 2012. Perth, Western Australia.

[7] **Tune, D.D.** and Shapter, J.G. *Comparison by chirality of the sunlight absorption efficiency of carbon nanotube solar cells*. in *IWCN12: 3rd ISESCO International Workshop and Conference on Nanotechnology*. 2012. Bangi, Malaysia.

[8] **Tune, D.D.,** Flavel, B.S., Quinton, J.S., Ellis, A.V., and Shapter, J.G., *Single walled carbon nanotube/polyaniline/n-silicon heterojunction solar cells: fabrication, characterisation and performance measurements.* ChemSusChem, 2013. 6(2): p. 320-327. DOI: 10.1002/cssc.201200600

[9] **Tune, D.D.,** Hennrich, F., Dehm, S., Klein, M.F.G., Colsmann, A., Shapter, J.G., Lemmer, U., Kappes, M., Krupke, R., and Flavel, B.S., *The role of nanotubes in carbon nanotube-silicon solar cells.* Advanced Energy Materials, 2013. 3(8): p. 1091-1097. DOI: 10.1002/aenm.201200949

[10] **Tune, D.D.** and Shapter, J.G., *The potential sunlight harvesting efficiency of single walled carbon nanotube solar cells.* Energy & Environmental Science, 2013. 6(9): p. 2572-2577. DOI: 10.1039/c3ee41731

[11] **Tune, D.D.** and Shapter, J.G., *The potential sunlight harvesting efficiency of single walled carbon nanotube solar cells.* in *NT13: The Fourteenth International Conference on the Science and Application of Nanotubes.* 2013. Helsinki, Finland.

[12] **Tune, D.D.,** and Shapter, J.G., *Single walled carbon nanotube front electrodes for silicon heterojunction solar cells.* In preparation, 2013.

[13] **Tune, D.D.,** Blanch, A.J., Flavel, B.S., Krupke, and Shapter, J.G., *The effect of nanotube film metallicity on single walled carbon nanotube-silicon heterojunction solar cells.* In preparation, 2013.

Chapter 1
Introduction

1.1 The energy challenge

Over the last two centuries the human population of the world has increased from about 1 billion people in 1800 to 7 billion in 2011 with projections of a peak around 9 billion in 2050.[1] With this increase in population has come a very large increase in energy consumption (**Figure 1.1**).[2] For early humans (before the control of fire) the only energy source was that gained from the daily consumption of food (~ 9000 kJ per day, equivalent to 2.5 kWh or approximately 900 kWh annually).[3] With the control of fire came a doubling of energy consumption via combustion of biomass (wood). The domestication of animals afforded further increases in energy consumption since a portion of the energy consumed through animals' food intake was harnessed to the will of their human masters for agricultural work and transportation. The control of water again doubled energy consumption through the use of waterwheels and mills and then dams and the directing of water into power channels, and for transportation via rivers and canals. Energy for transportation was also gleaned from the wind via sails and wind power was further exploited with windmills.

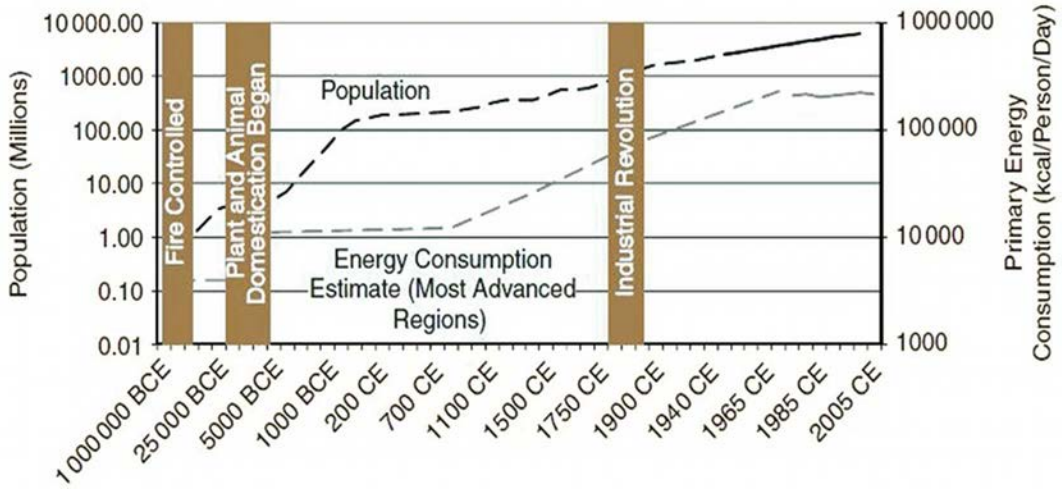

Figure 1.1 Trends in world population and energy consumption.[2]

The burning of coal beginning around 1000 CE allowed mankind to access the vast storage of solar energy trapped within this material and began a rapid increase in world per capita energy consumption. In harnessing coal, the atmospheric steam engine, invented by Savery in 1698 and refined by Watt around 1770, was

superseded around 1800 by Trevithick's pressure steam engine and thus began what we now refer to as the Industrial Revolution.[3] It was these inventions and that of their eventual replacement, the internal combustion engine, that set in motion the processes of large scale industrial and transportational emission of CO_2 which have seen world energy use reach 13 TWh annually and have culminated in the current 'climate crisis'.

Energy production is still heavily reliant upon the use of fossil fuels such as coal, oil and natural gas. Unfortunately, whilst these sources successfully supply current demand their use is not possible without the release of CO_2 - the primary greenhouse gas contributing to global climatic change.[4] Fossil fuels are non-renewable sources of energy, with exhaustion of world supplies predicted by the middle of the 21st century.[5] These resources are invaluable to the global polymer, chemical and pharmaceutical industries and whilst energy can be easily gained from other sources it would be exceedingly costly and difficult, if not practically impossible, to produce many industrial scale polymers, chemicals and medicines by other means. Despite suggestions that the immense pressure placed on fossil fuels can be eased through process improvements that ensure their efficient use, increases in absolute world population and the increases in world per capita energy consumption which accompany development of the non-Western world will vastly outpace any reductions due to efficiency.

There is a very strong correlation between per capita electricity use and the United Nations' Human Development Index (HDI) which encompasses three key indicators: life expectancy, educational achievement and adjusted gross domestic product (GDP) (**Figure 1.2**).[6] To attempt to deny energy use and associated development to the undeveloped world is not possible (and would be unethical) thus alternative forms of energy generation are required.

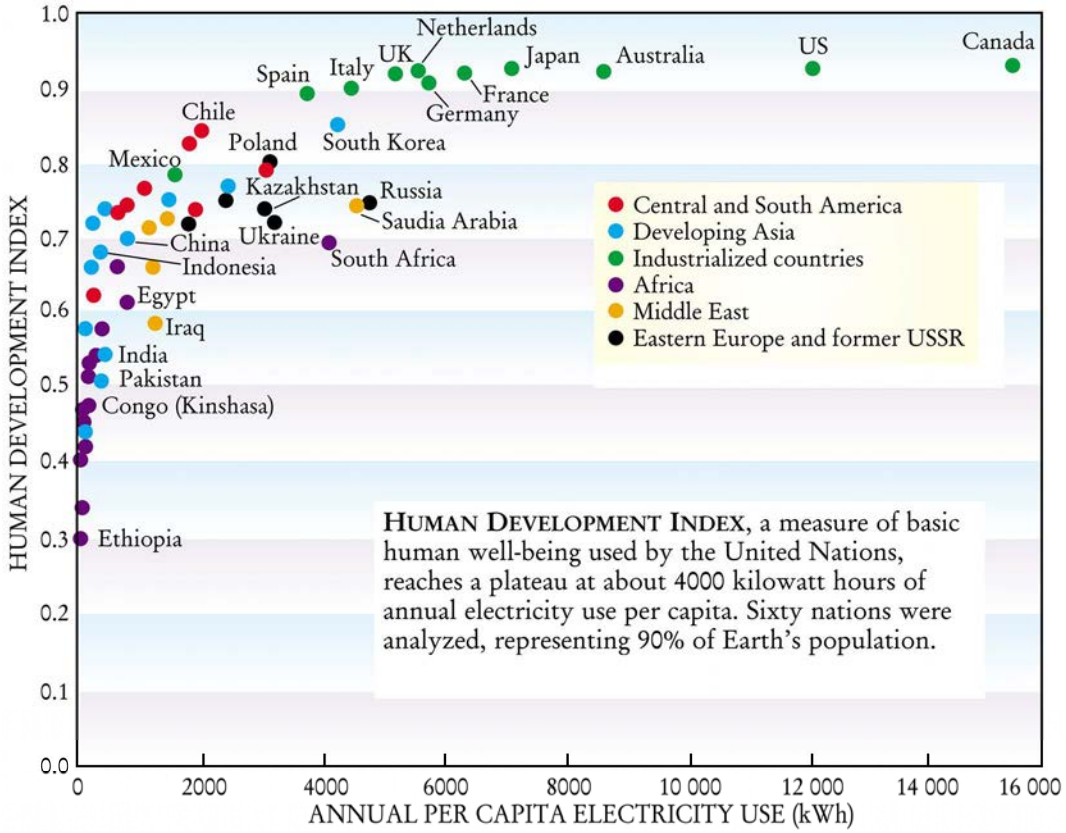

Figure 1.2 The relationship between Human Development Index and per capita electricity use.[6]

It has been proposed that fossil fuels continue to be used but rather than emitting the resultant CO_2 into the atmosphere it is instead liquefied and injected into the Earth's crust at very high pressure - a process termed carbon capture and storage (CCS).[7] Perhaps unsurprisingly, the concept has gained some traction in coal producing countries with a wealth of funding opportunities available from established industry bodies. However there are clearly some serious issues with the concept including the expected high cost, the unknown consequences of containment failure and, of course, the issue of the energy required to liquefy, transport and sequester the gas. Additionally, the development of knowledge and infrastructure needed to implement this technology on the kind of massive scales required to reduce atmospheric CO_2 emissions to desired targets would require many years. A more prudent approach would be to mitigate the production of CO_2 entirely.

Expansion of the use of nuclear fission has been proposed as an alternative to the use of traditional fossil fuels. However the prohibitive cost of nuclear power plant installation, eventual decommissioning, and fuel mining and refining, as well as the highly technical expertise required, local community issues and global security concerns have so far limited its more widespread use. Additionally, there are the potentially catastrophic ecological consequences of unforeseen nuclear disasters, such as the recent incident near Fukushima, and the incalculable cost of the safe storage of large volumes of highly radioactive waste for thousands of years.[8-9] There have been recent advances in fission technology with the promise of future fourth generation reactors that produce only low-level nuclear waste.[10] However, in light of the ready availability of other energy solutions which are more cost effective and vastly safer, the further large scale implementation of nuclear fission as an energy source seems unnecessary.

Clearly alternative forms of energy generation are required that are renewable, cost effective, non-polluting and produce no net increase in CO_2. Barring the widespread implementation of as-yet-unrealised nuclear fusion, which could provide emission-free energy for many years to come, the only sensible solution is to employ other renewable energy technologies from sources such as geothermal, hydro, wave, wind, tidal and solar. Each and all of which, by themselves, have the theoretical capacity to meet current world demand. Hydropower is a good example, accounting for ~ 15 - 16 % of all world energy generation (3x all other renewables combined),[11] but many prime locations are already exploited and future projects to develop other locations face issues of environmental and social impact. The combustion of biomass can be very helpful in gaining extra energy from what would otherwise be agricultural waste but the growth of biomass for the explicit purpose of generating energy generally requires land for which the highest priority use must be food production. On- and off-shore wind farms are being installed in huge numbers as farmers, companies and investors take the opportunity of an early entrance to a new market using a simple, proven technology to exploit a very reliable resource. Tidal and wave power will likely see similar investment in the near future as the

technologies mature. However all of these resources are small relative to global demand and are limited to strict geographic locations where the resource is both abundant and consistent. In these locations they may come to supplement or even supplant other forms of energy production but are evidently unsuitable as worldwide energy sources.

1.2 Solar energy

Only solar energy is present across (almost) the entire world and harnessing it appears to be the only really worldwide technological solution to the current energy challenge. The Sun's heat can be simply and easily captured by solar thermal technologies and then released overnight to provide so-called base load power. The simplest of these are the rooftop arrays of black tubing which heat a small reservoir to supply round the clock domestic hot water needs. But even though the most complex large scale solar thermal farms comprise little more than mirrors, tubing and a medium such as molten salts in which to store the energy, they are often hindered by the need to convert that thermal energy into electricity using a steam turbine and the requirements of a steady water supply.

Solar photovoltaics (PV), otherwise known as solar cells, are a well-established technology that functions by converting solar radiation directly into electrical energy which can then be used immediately or stored/transported for later use. Large scale solar PV farms can be erected on land which is otherwise useless (e.g. ex-industrial, high altitude, arid, deserts), do not need any additional resources (fuel, water) and require little ongoing maintenance. Small scale and domestic solar cells can be integrated into new and existing buildings, windows and rooftops making them invisible to the population. Such building integrated photovoltaics (BIPVs) provide additional benefits including less demand for air cooling and since energy is produced at the point of consumption the efficiency of the local energy grid can be significantly improved through reduced transportation and transformer losses.

Despite the first deliberate fabrication of a photovoltaic device by Fritts in 1883[12] it was not until 1954, when Chapin and co-workers at Bell Labs developed a 6 % efficient silicon pn junction solar cell,[13] that the photovoltaic industry was born. Initially photovoltaics were only used in specialist applications where conventional power sources were unavailable or undesirable such as satellites and high-end electronic devices. In 1985, with the development of the first ~20 % efficient solar cells such as by Green and co-workers,[14] the field of photovoltaics established itself as a serious energy resource capable of supplying domestic demand.

To date many different semiconducting materials have been used in the fabrication of pn junction based PV including mono-, poly- and multi-crystalline silicon,[15] CdTe,[16] CIS[17] and GaAs.[18] Owing to many years of research in the field, these technologies typically provide relatively high conversion efficiencies. For example, Guter et al.[19] recently demonstrated a metamorphic GaInP/GaInAs/Ge triple junction with 41.1 % efficiency (454x concentrated sunlight) and King et al.[18] using a similar architecture have reported 40.7 % efficiency (240x concentrated). However, despite promising conversion efficiencies these cells suffer from the critical drawbacks of high production cost and restricted supply and/or high toxicity of input materials.[20] In the case of silicon, although it is non-toxic, readily available and inexpensive, highly purified crystalline silicon with specific electronic doping is required for photovoltaic devices. The manufacture of silicon solar cells thus involves repeated high temperature heating and extended processing which costs a lot of energy and is the largest contributing factor to the final device price. Add to this the balance of system (BOS) costs including such things as power inverters, frames, installation and, in the case of large scale PV power plants, land. However in the case of say, coal, it's a lot easier; you dig it up, transport it somewhere, then burn it and capture the heat to do work. Coupled with typically significant institutionalised taxpayer subsidies of local coal industries, the result is that energy from coal costs less than that from current silicon PV technology.

Excluding government policy initiatives, there are three main ways in which the cost of energy from PV can be reduced;

- By reducing the BOS costs, of which the inverter is generally the greatest
- By reducing the cost of PV materials/technologies
- By increasing the power conversion efficiency (PCE) of PV

The BOS costs account for around 50 % of the total installed cost of a PV module.[21] Improvements in inverter lifetime would reduce the need for replacement over the life of a PV module whilst new and improved inverter technology could potentially reduce cost directly hence continued research into inverters is essential. PV based on single- or poly-crystalline silicon has already seen several decades of technological optimisation and, although difficult to say for certain, it is unlikely that there will be very large reductions in the cost of silicon PV through technological advances alone. A doubling of efficiency in commercial devices from ~ 15 - 30 % would halve the cost of PV energy but due to fundamental efficiency limits imposed on silicon PV, large increases in the efficiency of commercial modules are difficult to achieve. Even if achievable, such efficiency increases often involve exponential increases in costs which make such modules commercially uncompetitive. Alternative PV materials and technologies are therefore desirable.

The last few decades have seen the growth of several new PV technologies, however all alternatives so far suffer from at least one drawback in regards to replacing silicon. For example, despite widespread research efforts the PCE of dye sensitised solar cells (DSCs) appears to have plateaued at around 12 % with no significant improvement in close to a decade.[22] Add to this the material requirements of indium and ruthenium (both in limited supply on Earth) and although it is a very low cost technology it can provide only a small share of future renewable energy. Organic photovoltaics (OPVs) based on bulk heterojunctions such as the paradigmatic poly(3-hexylthiophene)/[6,6]-phenyl-C_{61}-butyric acid methyl ester (P3HT/PCBM) mix have great potential as ultra-cheap thin film technologies and are seeing steadily increasing PCEs, but are hampered by issues of long term stability and performance degradation.[23]

So in order to overcome the production costs associated with silicon solar cells and the toxicity and/or scarcity issues of other solid state semiconductors there is currently great interest in finding alternative semiconductor materials and/or alternative ways of fabricating the current generation of solar cells. One material with great potential in these areas is carbon, in the form of carbon nanotubes. Carbon is certainly not in limited supply and this material could be made very, very cheap with economies of scale in production.

1.3 Carbon nanotubes

Since first reports of carbon nanotubes by Iijima,[24] and of single walled carbon nanotubes by Iijima and Ichihashi[25] and Bethune et al.[26] in the early 1990s the explosion of research into carbon nanotubes has continued to expand exponentially largely due to their excellent and often unique electrical[27-28] and optical[29-30] properties. Carbon nanotubes are an allotrope of carbon having the form of hollow cylinders composed of rolled-up sheets of graphene. Carbon nanotubes can be single walled (SWCNTs), double walled (DWCNTs) or multi walled (MWCNTs) where DWCNTs and MWCNTs are composed of two or multiple concentric graphene cylinders, respectively.

The orientation of hexagons in the sidewall lattice with respect to the longitudinal axis defines an intrinsic geometric property called chirality and a SWCNT can be completely described, except for its length, by $\mathbf{C_h}$, known as the chiral or roll-up vector.[31-33] The chiral vector is defined by $\mathbf{C_h} = n\mathbf{a_1} + m\mathbf{a_2}$[34-35] where the integers (n,m) are the number of steps along the *zig-zag* carbon bonds and $\mathbf{a_1}$, $\mathbf{a_2}$ are the graphene lattice basis vectors in real space. As can be seen in **Figure 1.3** the chiral vector makes an angle, θ, defined by $\theta = \tan^{-1}\left[\sqrt{3}m/(m+2n)\right]$ and known as the chiral angle, with the *zig-zag* or $\mathbf{a_1}$ direction.[32] The chiral angle determines the amount of 'twist' in the nanotube and two limiting cases exist where the chiral angle is at 0° and 30°.[31] These limiting cases are known as *zig-zag* (0°) and *armchair* (30°) based on the geometry of the carbon bonds around the circumference of the nanotube.[36-37] All other conformations in which the C–C bonds lie at angles $0° < \theta < 30°$ are known as *chiral* (**Figure 1.4**).[32]

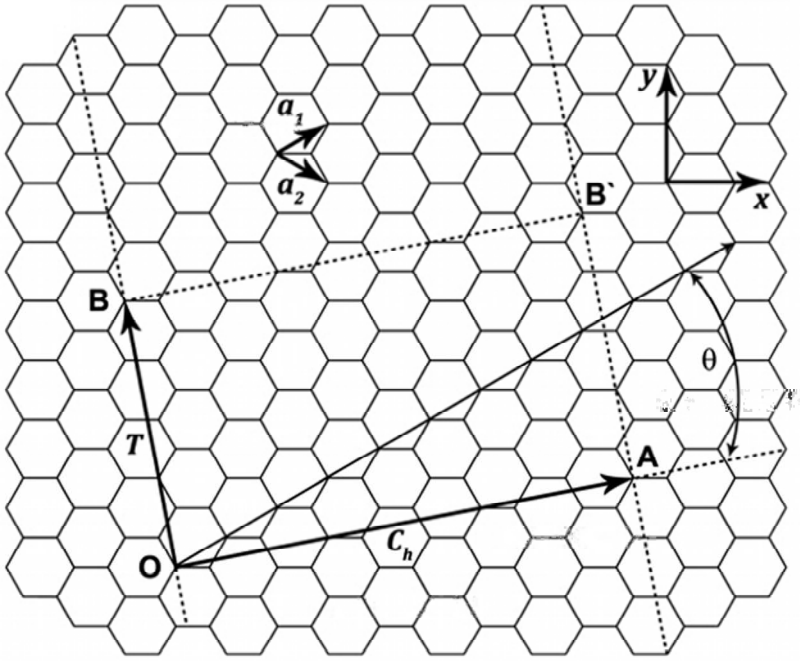

Figure 1.3 (a) Unrolled graphene sheet showing the geometry of the (4,2) nanotube. OA and OB define the chiral and translational vectors $\mathbf{C_h}$ and $\mathbf{T}$, respectively, and the rectangle OAB'B defines the unit cell; O, A, B and B' are reference atoms, $\mathbf{a_1}$, $\mathbf{a_2}$ are the graphene lattice real basis vectors and θ is the chiral angle (image adapted from [38]).

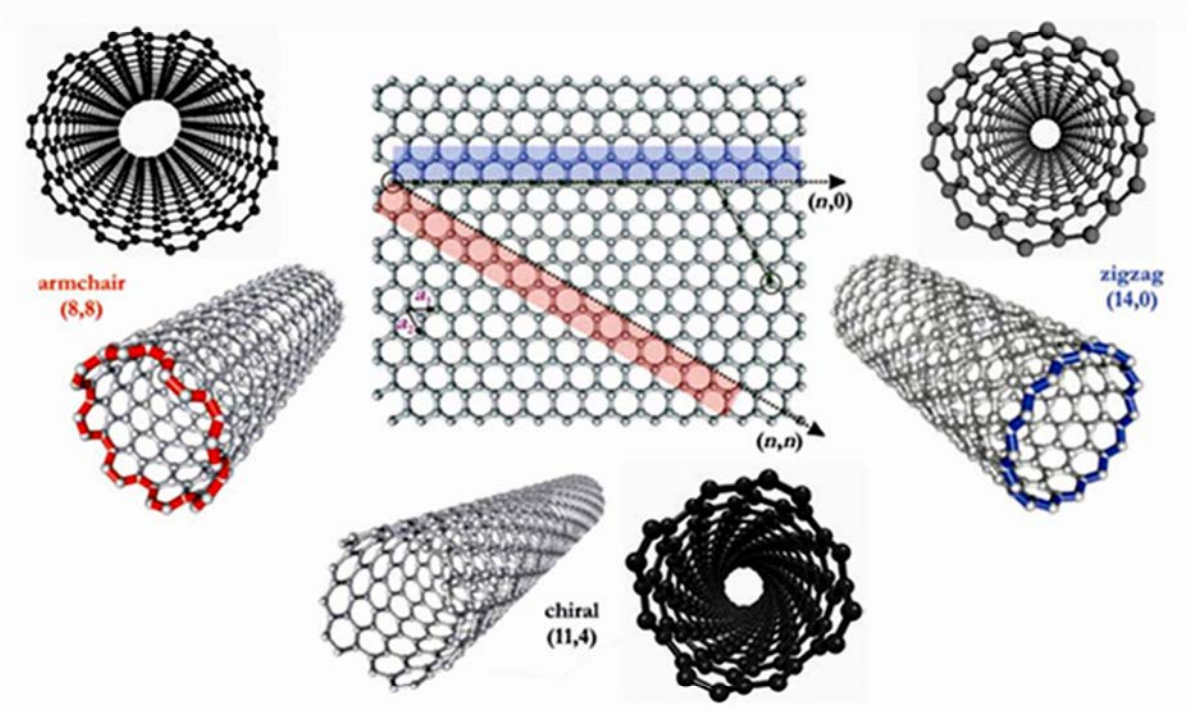

Figure 1.4 Schematics of the three categories of SWCNT.[39]

The graphene primitive cell is described in terms of the unit cell vectors (**Figure 1.5**(a));

$$\mathbf{a_1} = \frac{a}{2}\left(\sqrt{3}x + y\right) \text{ and } \mathbf{a_2} = \frac{a}{2}\left(\sqrt{3}x - y\right) \qquad \textbf{Equation 1.1}$$

where a is the lattice constant equal to $\sqrt{3}a_{cc}$ and a_{cc} is the C-C interatomic bond distance of 1.4 Å. The reciprocal lattice unit vectors are;

$$\mathbf{b_1} = \frac{2\pi}{a}\left(\frac{1}{\sqrt{3}}\hat{x} + \hat{y}\right) \text{ and } \mathbf{b_2} = \frac{2\pi}{a}\left(\frac{1}{\sqrt{3}}\hat{x} - \hat{y}\right) \qquad \textbf{Equation 1.2}$$

The SWCNT diameter can be expressed in terms of the (n,m) indices as;

$$d_t = \frac{C_h}{\pi} = \frac{\sqrt{3}}{\pi} a_{cc}(m^2 + mn + n^2)^{\frac{1}{2}} \qquad \textbf{Equation 1.3}$$

The energy dispersion relation for the p_z electrons in graphene (of which the SWCNTs are a subset in $\mathbf{k}$) can be determined by applying the tight binding model approximation (**Figure 1.5**(b)), which considers only interactions with the three nearest neighbours;

$$E(k_x, k_y) = \pm V_{pp\pi}\left[1 + 4\cos\left(\frac{\sqrt{3}K_x}{2}a\right)\cos\left(\frac{K_y}{2}a\right) + 4\cos^2\left(\frac{K_y}{2}a\right)\right]^{1/2} \qquad \textbf{Equation 1.4}$$

where $V_{pp\pi}$ is the C-C nearest neighbour potential overlap integral and K_x and K_y are the x and y components of the wave vector $\mathbf{K}$ found using the relation;[40-42]

$$(K_x, K_y) = \left(\mathbf{k}\frac{\mathbf{K_2}}{|\mathbf{K_2}|} + q\mathbf{K_1}\right) \text{ for } \left(-\frac{\pi}{|T|} < k < \frac{\pi}{|T|}\right) \text{ and } q = 1 \,..\, N \qquad \textbf{Equation 1.5}$$

where $\mathbf{k}$ is the wave vector along the tube axis, N is the number of hexagons in a unit cell and $|T|$ is the magnitude of the translational vector.[43] $\mathbf{K_1}$ and $\mathbf{K_2}$ are the allowed reciprocal lattice wave vectors along the tube axis and circumference, given by;

$$\mathbf{K_1} = \frac{(2n + m)\mathbf{b_1} + (2m + n)\mathbf{b_2}}{N d_R} \text{ and } \mathbf{K_2} = \frac{m\mathbf{b_1} - n\mathbf{b_2}}{N} \qquad \textbf{Equation 1.6}$$

where d_R is the largest common divisor of (2n+m) and (2m+n). Using the allowed $\mathbf{K}$ vectors, the energy band diagram in momentum ($\mathbf{k}$) space can be plotted (**Figure 1.6**) giving the one dimensional (1D) density of states (DOS).

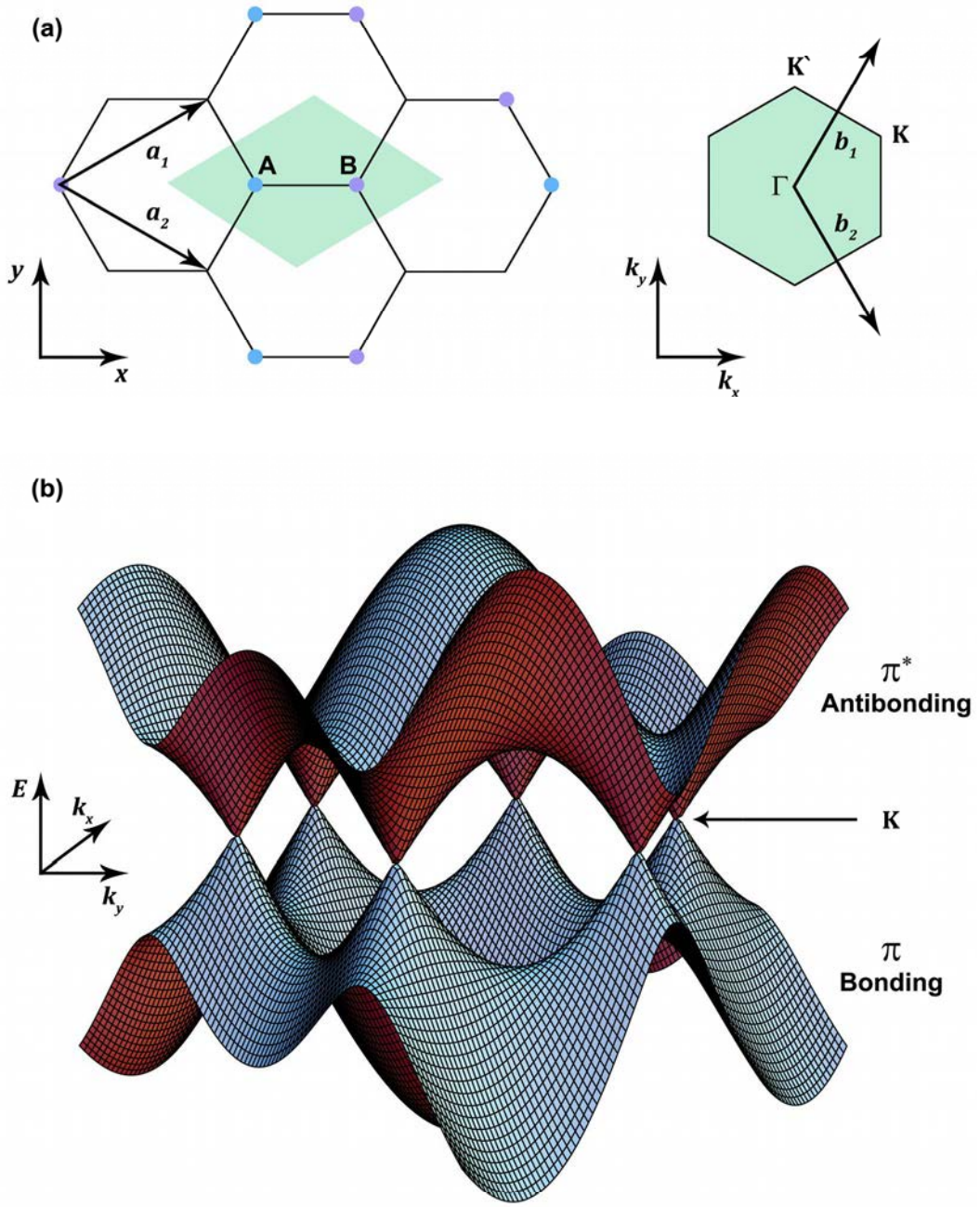

Figure 1.5 (a) The unit cell (shaded area) defined by the basis vectors $\mathbf{a}_1$ and $\mathbf{a}_2$ and containing sites A and B where carbon atoms are located, and the Brillouin zone (shaded hexagon) of a graphene or 2D graphite layer. The reciprocal lattice vectors $\mathbf{b}_1$ and $\mathbf{b}_2$ and the high symmetry points, Γ, K are indicated, (b) A plot of the energy dispersion relation, $\mathbf{E}(k_x,k_y)$, for the p_z electrons of the (4,2) nanotube.[40-42, 44]

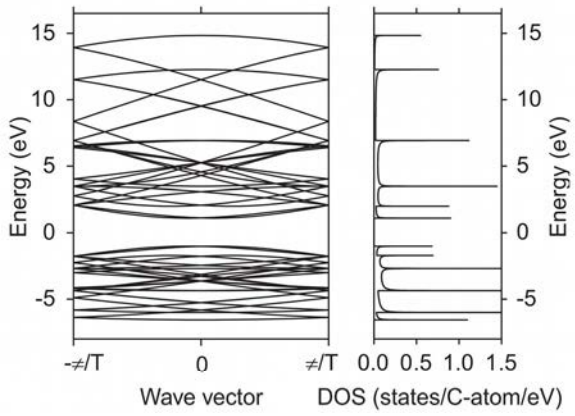

Figure 1.6 Plot of the energy bands in **k**-space for the (4,2) nanotube.[43]

The (n, m) integers completely describe nanotube chirality and thus specify the electronic band structure. It is the chirality that has significant implications for the optical, mechanical and electronic properties of carbon nanotubes.[36] In particular by slightly changing the chiral angle it is possible to switch between metallic, low band gap and high band gap semiconducting carbon nanotubes.[31, 36] When n - m = 3p (p is an integer) the SWCNT is metallic (m-SWCNT), when n - m ≠ 3p the SWCNT is semiconducting[38] (s-SWCNT) with band gap energy, E_g, dependant on the SWCNT diameter, d_t, the C-C nearest neighbour potential overlap integral, $V_{pp\pi}$, and the C-C bond distance, a_{cc}, such that;

$$E_g = \frac{2V_{pp\pi}a_{cc}}{d_t} \qquad \textbf{Equation 1.7}$$

Thus armchair SWCNTs are the only intrinsically metallic type (no bandgap) although approximately one third of all zigzag SWCNTs are also termed 'metallic' at room temperature since the energy gap is smaller than the thermal energy, ~ $k_B T$, allowing thermal excitation of carriers into the conduction band. This use of the term metallic can lead to some confusion if it is assumed to have the same meaning as is the case for bulk metals. For example, whereas the colour of nanoparticulate metals is a result of plasmon resonance, the colour of m-SWCNTs arises from their excitonic properties.[46] All chiral SWCNTs and the remaining two thirds of zigzag SWCNTs are therefore semiconducting with band gaps defined by Equation 1.7. This leads to the observation that approximately 60 % of all SWCNT chiralities are semiconducting with the remaining 40 % metallic.[47]

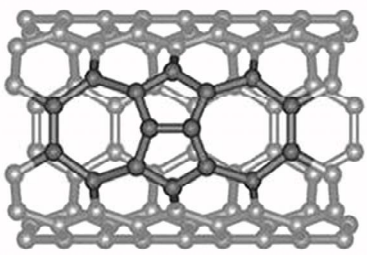

Figure 1.7 A Stone-Wales defect.[48]

As with graphene the carbon-carbon bonding is sp^2 hybridised so the sidewalls of a perfect SWCNT are also chemically quite inert.[49] Some of the C-C bonds experience curvature-induced misalignment of π-orbitals resulting in strain on the lattice and causing an increase in reactivity over (uncurved) graphene. The π-orbital misalignment is diameter dependent hence smaller diameter tubes are more reactive than larger ones.[50] Stone-Wales defects (**Figure 1.7**) are another source of strain. These consist of a pair each of pentagons and heptagons and involve some tetrahedral sp^3 hybridisation.

The strain on the lattice resulting from this non-planar geometry means that Stone-Wales defects are a site of greater reactivity. Since the end caps are also composed of pentagons and heptagons they are similarly more reactive than the sidewalls as evidenced by the finding that oxidation is energetically more favourable at the end caps than on the sidewalls.[51] As can be clearly seen in **Figure 1.6**, SWCNTs are a direct band gap material (there is no momentum change required to go from the maxima of the HOMO to the minima of the LUMO, unlike in silicon where a phonon is required for each transition from the valence band maximum to the conduction band minimum, in addition to the photon). SWCNTs are so small they exhibit quasi-one dimensional properties and the 1D confinement of electrons into allowed **k**-states gives rise to Van Hove singularities (VHSs) in the electronic density of states (**Figure 1.8**(a) and (b)).

In bulk semiconducting materials the energy gap between the valence and conduction bands defines the absorption onset wavelength of the optical spectra. If SWCNTs are considered similarly, in the manner of single particle excitations, then the discrete electronic transitions in the DOS should produce characteristic peaks in

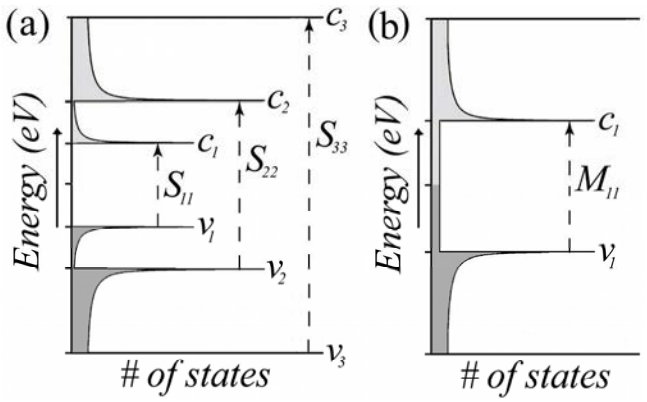

Figure 1.8 Schematic of the electronic density of states (DOS) of (a) semiconducting and (b) metallic zigzag SWCNTs showing valence and conduction bands, v_i and c_i, and optically active electronic transitions, S_{ii} and M_{ii}.

the UV-Vis-NIR absorption spectra of SWCNTs at wavelengths corresponding to the transition energies of the respective SWCNTs. However it is now known that the optical absorption spectra of SWCNTs are entirely excitonic in nature and thus many-body effects must be considered for an accurate description of the optical properties of SWCNTs.[52] This means that the actual light energy required to produce a "$v_i - c_i$" transition is (Ec_i - Ev_i) + binding energy (eh) - self energy (ee), and leads to the experimental finding that E_{22}/E_{11} tends to a value of 1.8 with decreasing tube diameter, rather than the value of 2 as would be expected from density functional theory calculations alone.[53]

Shockley and Queisser used detailed balance calculations to derive a fundamental limit to the PCE of a single junction solar cell.[54] One outcome is that a criteria for obtaining the highest efficiency devices is correct matching of the semiconductor's optical band gap to the solar spectrum.[21] The optimal band gap of ~ 1.1 eV is easily obtained with ~ 12 - 15 different s-SWCNT chiralities having a fundamental optical gap between 1.0 - 1.2 eV.[55] However calculations for the optimal band gap criterion are based on the assumption of one photon producing one exciton and apply to bulk semiconductors in which there is a smooth continuum of states above and below the gap. SWCNTs have been shown to exhibit multiple exciton generation (MEG) from a single photon.[56-57] In this process, a photon having energy equal to *n* multiples of the band gap is absorbed and produces *n* excitons.

However, a complete solar cell device exploiting this property, and thus allowing violation of the SQ limit, is yet to be realised. Chapter 7 uses numerical simulations of the UV-Vis-NIR absorption spectra of SWCNTs, with their discrete DOS features, to determine the optimal species for harvesting sunlight. S-SWCNTs have a Fermi level in the middle of the band gap but when exposed to air they develop p-type characteristics due to the electron withdrawing nature of adsorbed oxygen molecules. Even in ultra-high vacuum this adsorbed oxygen is very difficult to remove and has likely skewed the results of much research carried out to date.[58] In addition, SWCNTs can be chemically doped p-type by electron withdrawing species such as strong oxidisers or oxidising acids,[59-60] or n-type by electron donating species such as alkali metals,[61] hydrazine, [60, 62] nitrogen-rich polymers[63] and nitrogen-rich aromatic compounds.[64] Substitutional doping has also been demonstrated with boron (p-type)[65] and nitrogen (n-type).[66-67] This raises the exciting prospect of all-SWCNT photovoltaics based on pn or p-i-n homo- or heterojunctions, although such architectures have not yet been reported for other than single tube devices.

SWCNTs were initially touted as the quintessential nanostructure and expectations of them were high. However the successful application of SWCNTs into new and improved devices has been limited by the polychirality of as-produced and purified SWCNTs. Electrical, optical and physical properties of SWCNTs are highly dependent on chirality but although there are many reports of the sorting and characterisation of SWCNTs in the literature these have often been in very small quantities unsuitable for further device fabrication. The performance of thin film and other solar cell devices does not scale up well from very small research cells due to the domination of edge effects thus appreciable quantities of sorted SWCNTs are required for the fabrication of devices large enough to provide meaningful, scalable performance data. The sorting of SWCNTs into populations of individual chirality in such quantities has until recently been unattainable. Today a number of methods for sorting of SWCNTs are available such as dielectrophoresis,[68-69] density-gradient ultracentrifugation (DGU),[69-70] selective polymer wrapping[71-72] or gel

chromatography (GC).[73-76] The choice of method depends on the targeted application and the subsequent need for sorting tubes by metallicity, diameter and/or chiral angle. For solar cells one would ideally like to use quantities of s-SWCNTs of a single chirality to have uniform electrical and optical properties. Selective polymer wrapping, DGU and GC can deliver single-chirality fractions for small-diameter SWCNTs (< 1.1 nm). However depending on the diameter and chirality distribution of the raw material the yield in obtaining a specific (n,m) fraction can be rather low. The strategy must therefore be to sort out (n,m)-tubes from raw material that already has a very narrow diameter distribution.

Currently the literature contains many cases of research using SWCNTs in solar cell devices. For example, SWCNTs have been integrated into a variety of OPVs.[77-83] However in these systems the SWCNTs are not so much responsible for exciton generation upon absorption of light but rather, by introducing SWCNTs into these polymeric systems, exciton dissociation or electron transport is enhanced within the material. There has been much work in recent years incorporating SWCNTs into photoelectrochemical cells (PECs) either on their own[84-86] or as elements in donor-acceptor hybrids in conjunction with fullerenes,[87-89] fullerenes/P3HT,[90] fullerenes/porphyrin,[91] porphyrins,[92-97] pyrenes,[98-99] polythiophenes[100-102] and other photoactive polymers,[103] phthalocyanines,[97, 104] PAMAM dendrons,[105] quantum dots,[106-107] chrysenes[108] and more. There is also a plethora of fundamental work looking at photoinduced charge transfer processes between SWCNTs and other species and it must be noted that the line between OPVs and PECs is blurred since photoelectrochemistry is also a method of characterising new OPV systems. Similarly, the implementation of SWCNTs in DSCs has included replacement for the platinum catalyst counter electrode,[109-111] improvement of the electrical properties of the titania[112-113] or replacement of the titania scaffold.[82, 114-115] Further information on the use of SWCNTs in these types of light harvesting devices and structures is provided by Imahori,[116] Sgobba,[117] Chitta,[118] Guldi,[119-121] and D'Souza.[122-123]

1.4 Carbon nanotube-silicon solar cells

If carbon nanotubes are to offer a viable alternative to silicon it is necessary to understand how photogeneration, transport and dissociation of excitons and charge carriers operates in large carbon nanotube ensembles. One of the many paths to this

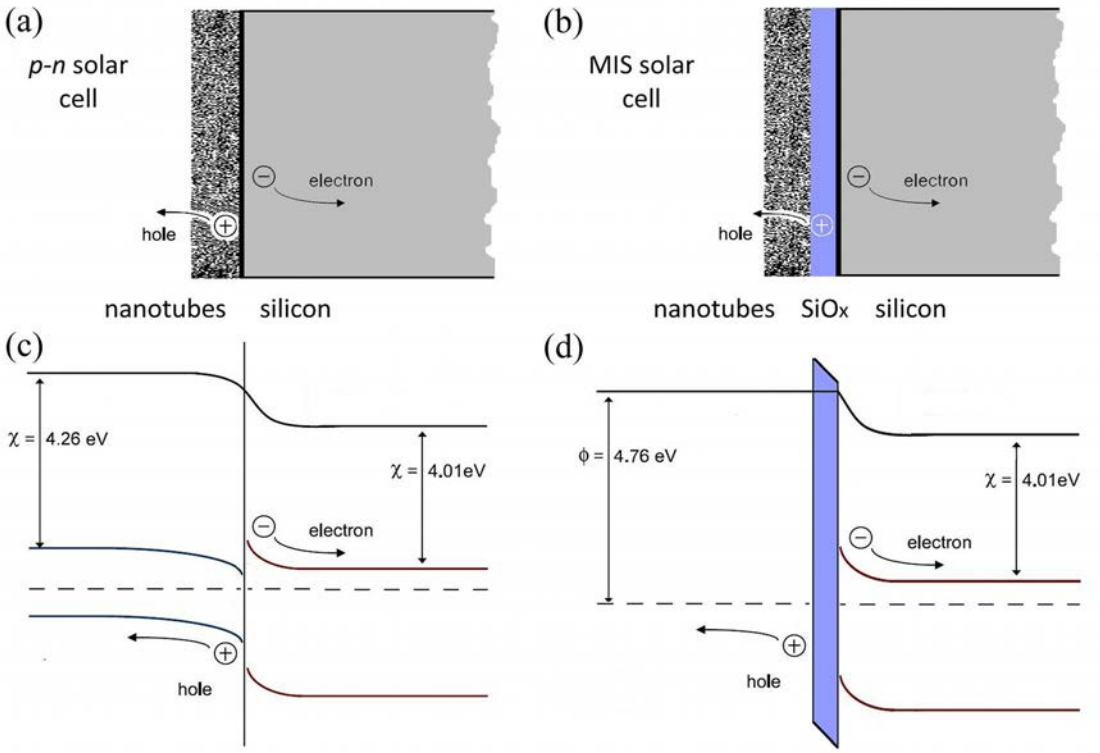

Figure 1.9 Device schematics and energy diagrams for pn ((a) and (c)) and MIS ((b) and (d)) solar cells. The examples assume an electron affinity, work function and band gap for s-SWCNTs of 4.26 eV, 4.76 eV and 0.7 eV, respectively, a work function for m-nanotubes of 4.76 eV, and an electron affinity and band gap for silicon of 4.01 eV and 1.12 eV, respectively. The nanotube Fermi level is assumed to be ~ 0.1 eV below the middle of the bandgap due to oxygen adsorption and a dopant concentration of ~ 10^{15} cm^{-3} is assumed in silicon yielding a Fermi level ~ 0.25 eV below the conduction band edge (image adapted from [124]).

goal is to combine them with a well understood, model semiconductor material such as, ironically, silicon. Carbon nanotube-silicon heterojunction solar cells are a recent photovoltaic system which has been purported to utilise carbon nanotubes directly for photocurrent generation. A typical device has an architecture similar to that of a single junction monocrystalline n-type silicon solar cell with the exception that the p-type emitter is replaced by a thin film of carbon nanotubes. The exact mechanism of operation of such cells is not well established however the operation mechanisms

mentioned in the literature fall into two categories. In the first, the mechanism is that of a pn heterojunction solar cell (**Figure 1.9**(a) and **Figure 1.9**(c)), with the nanotubes acting as the p-type emitter material. Photons are absorbed mainly in the n-type silicon base with resulting excitons diffusing to the space-charge region where they are separated into free charge carriers under the action of the built in potential formed by Fermi level equilibration at the junction. Photons can also be absorbed in the p-type nanotube layer but since the nanotube films typically have 85+ % transmittance this is not expected to be the dominant charge generation process.

In the second, the mechanism is that of a Schottky junction solar cell, or the structurally related metal insulator semiconductor (MIS)[125-126] solar cell (**Figure 1.9**(b) and **Figure 1.9**(d)). A Schottky junction is formed between a metal and a semiconductor[127] and can be employed as a solar cell device.[128] In this configuration the nanotubes act as the metal, a thin SiO_x passivation layer on the silicon surface serves as the insulator (for MIS) and the n-type silicon is the semiconductor base. Photons absorbed in the base region produce excitons which diffuse to an inversion or depletion layer created in the silicon adjacent to the Si/SiO_x or Si/metal junction. Charges are separated by the built in potential formed between the metal or SiO_x (which has a Fermi level pinned to that of the adjacent metal) and the silicon. Once the charges are separated, tunnelling is the mechanism of minority carrier transport through the thin insulating oxide layer of the MIS solar cell.

In fact, unlike in a bulk silicon pn homojunction there are a great multitude of tiny nanotube-silicon heterojunctions, which are then further complicated by the presence of a distribution of chiralities. To date most carbon nanotube-silicon solar cells have employed inhomogeneous mixtures of m-SWCNTs and s-SWCNTs and hence a combination of operation mechanisms is possible. It is tempting to presume that a device constructed with only s-SWCNTs would behave as a pn junction solar cell whilst one with only m-SWCNT would behave as a Schottky or MIS solar cell depending on the presence of an intermediate insulating layer.

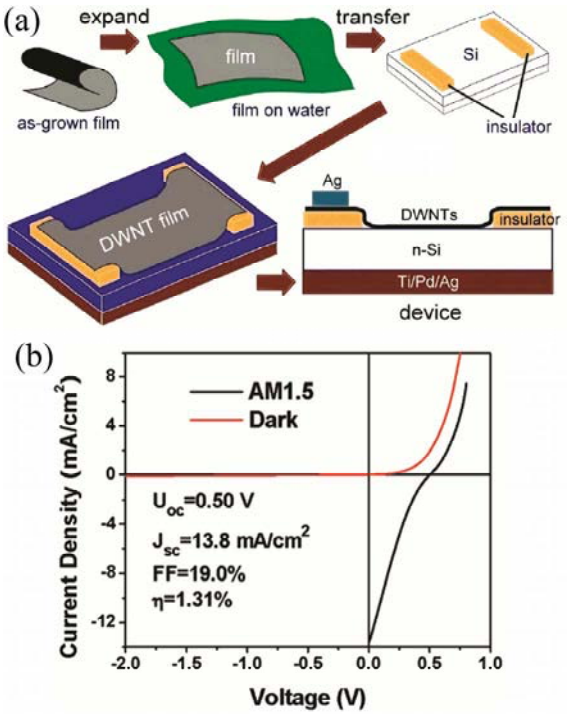

Figure 1.10 (a) Schematic showing the fabrication process for DWCNT-silicon solar cell device and (b) JV data (image adapted from [129]).

Although not an exhaustive list, the work detailed in the following covers some important and intriguing findings in the development of the field and is summarised in **Appendix 1**. The reporting of carbon nanotube-silicon solar cells began in 2007 with Wei et al.[129] who demonstrated a 1.3 % efficient device. In the design of Wei et al. DWCNTs were deposited on n-type silicon substrates via H_2O expansion and subsequent aqueous film transfer of an as-grown chemical vapour deposition (CVD) film as shown in **Figure 1.10**(a). Wei et al.[129] also demonstrated the importance of appropriate electrical contact to the bottom of the n-type silicon substrate, an obvious contributing factor to series resistance. By depositing a Ti/Pd/Ag layer, which has good adhesion to, and forms good ohmic contacts with, silicon, the measured short circuit current density (J_{SC}) was enhanced by a factor of 10 compared with the use of silver paint as contact. However, overall PCE was low due to a poor fill factor (FF) of 0.19 as can be seen in **Figure 1.10**(b). Benham et al.[130] probed the fundamental properties of nanotube-silicon junctions showing that tunnelling is the dominant mechanism of charge transport at room temperature whilst, at temperatures above ~ 240 K, thermionic emission dominates.

Jia et al.[131] reported a significant step forward from their 2007 work upon demonstrating a 7.4 % efficient DWCNT-silicon device. The DWCNT film was prepared and deposited as in the earlier work. Although the authors fail to explicitly state it, the higher efficiency relative to the earlier work can be attributed to a lowered series resistance. This was obtained in part by replacing the relatively thick isinglass (mica) front window with a thin SiO_x window etched using photolithography. Reducing front window thickness has the effect of reducing bending/stretching of the nanotube film over the step that exists between the front window and the silicon active area. The lower series resistance gave a gain in J_{SC} from 13.8 mA cm^{-2} to 26 mA cm^{-2} and an increase in FF from 0.29 to 0.53 compared to the earlier work.

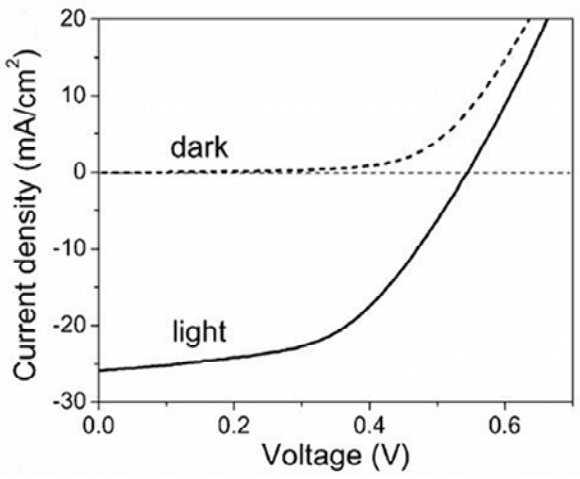

Figure 1.11 J-V characteristics of the DWCNT/Si solar cell with a PCE of 7.4 %.[131]

Subsequently other groups have used alternative methods to deposit thin films of SWCNTs onto n-type silicon. Li et al.[132] reported a SWCNT-silicon solar cell employing a SWCNT film spray coated using an airbrushing technique from a dimethylformamide (DMF) suspension (**Figure 1.11**). Final devices were found to afford an efficiency of 1.3 %. Li et al. investigated SWCNT film post-treatment methods in order to increase device efficiency. Hall Effect measurements showed that post-treatment of the SWCNT film with thionyl chloride ($SOCl_2$) leads to increases in carrier density and effective mobility from 3.1 x 10^{15} to 4.6 x 10^{17} cm^{-2} and 0.23 to 1.02 cm^2 V^{-1} s^{-1}, respectively. Quoting the authors, "The major conduction mechanism of the SWCNT coating network shifted from variable range

hopping toward tunnelling after the $SOCl_2$ treatment. The $SOCl_2$ treatment of SWCNT films also leads to a slight increase in the open-circuit voltage and a significant increase in the short-circuit current through readjusting the Fermi level and enhancing the carrier density and mobility." Li et al. subsequently published a paper reporting a trebling of efficiency for similarly constructed, $SOCl_2$ post-treated devices[133] and further characterised the performance of devices fabricated by transferring of an as-grown 'spiderweb' onto silicon.[134] The effect of $SOCl_2$ on SWCNTs has been relatively well-studied and it has been shown to be a very good p-type dopant for SWCNTs that increases conductivity in part by shifting the SWCNT Fermi level into the valance band.[60] However, as will be seen in Chapters 3, 5 and 6, $SOCl_2$ treatment bleaches the S_{11} transition in s-SWCNTs and it is unclear if this affects the mechanism of action of SWCNT-silicon devices. It may well be that some devices function as pn junctions before post treatment but then switch to (in this case much better performing) Schottky junction devices after the post treatment dramatically increases the metallicity of the SWCNTs.

Jia et al.[135] reported a SWCNT deposition method employing vacuum filtration onto mixed cellulose ester (MCE) films with subsequent removal of the MCE by dissolving in acetone. The MCE deposition method was used for SWCNTs and MWCNTs but aqueous film transfer of a self-assembled film (as per their prior work)[129, 131] was used for DWCNTs. This renders the comparison of these three films' performance in carbon nanotube-silicon solar cells less certain than would be the case if MCE deposition was also used for DWCNTs. The report analyses the effect on performance of varying the area density of nanotubes. It was found that SWCNT films outperform MWCNTs only when the density is low, which is interpreted as indicating that optical transmittance is the most important variable in comparing SWCNTs and MWCNTs. The authors also correlate a figure of merit (FM) for transparent, conductive films with the PCE of carbon nanotube-silicon solar cells such that FM = T_{550} (%) / R_{sheet} (Ω sq^{-1}) where T_{550} is the optical transmittance for λ = 550 nm and R_{sheet} is the sheet resistance. It was found that the FM is proportional to PCE such that increasing film transparency or decreasing

sheet resistance yields higher device efficiency. Optical transparency is increased for thinner films whereas the sheet resistance is decreased for thicker films. Thus at some point there must be a trade-off between these two variables with the optimal thickness likely constrained by the optimisation of other cell parameters. It is also interesting to note that $T \sim e^{-\alpha d}$, where α is the attenuation coefficient and d is the film thickness, and $R \sim 1/d$. Thus, the FM is apparently dominated by the exponential dependence of T on d and only for very thin films does R_{sheet} dominate. Even though the nanotube films are indeed very thin, this dependence of the PCE on the FM would seem to suggest that the role of the nanotubes is more that of a transparent, conducting film rather than as photoactive material. The effect of nanotube film thickness has also been investigated by Castrucci et al.[136] who similarly found that the density of the nanotube film (number of nanotube-silicon junctions) is a vital parameter in optimising performance.

Ong et al.[137] reported that for their devices, "comparison of the photocurrent with the near infrared (NIR) absorption spectra clearly indicates an excellent matching of the S_{11} band (corresponding to the first interband transition for SWCNTs with (7,6) and (8,6) chirality) with the photocurrent band located at ~ 1150 nm." Thus, "the SWCNT film contributes to the photoconversion process not only as a charge separator/transporter/collector but also as a light absorber. This is an important fact, distinguishing between a heterojunction solar cell with two active light absorbing components and a Schottky cell, where the metal component is not capable of absorbing photons". However the data in **Figure 1.12**(b) shows a small shoulder on the low energy side of the silicon photoresponse that is ~ 50 nm lower in wavelength than the relevant peak in the SWCNT absorption spectrum. It is unclear why the photocurrent due to silicon drops off so sharply as the photon energy is increased - a much flatter response is expected in the range of 500 – 900 nm for crystalline silicon solar cells. Le Borgne et al.[137] observe a similar, but smaller, drop in the high energy region of the photocurrent spectrum however, comparison with a silicon only cell shows a small improvement in the UV response that is said to correspond with

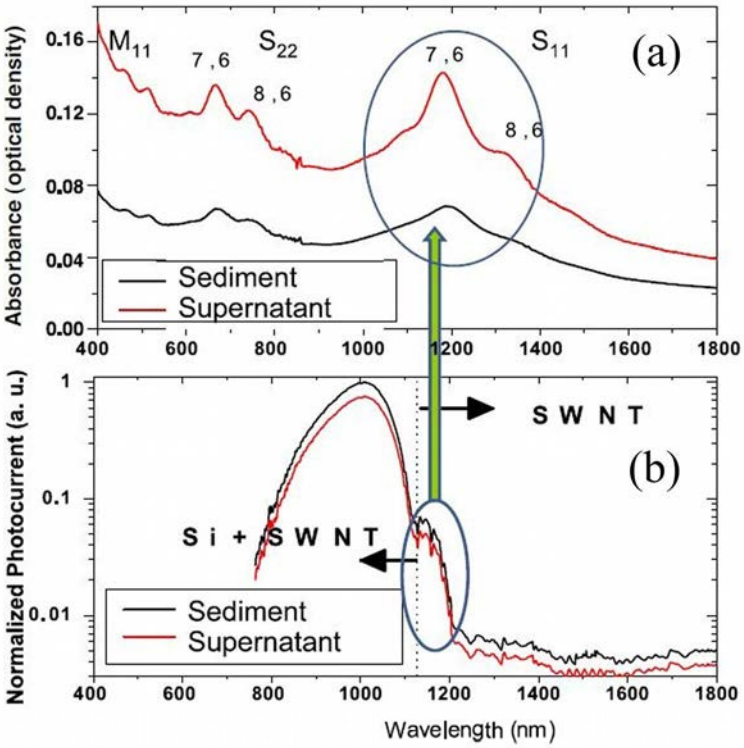

Figure 1.12 (a) UV-Vis-NIR spectra of SWCNT films on glass, (b) photocurrent spectra showing current peak corresponding to SWCNT's S_{11} transition.[137]

the π-π^* transitions of the SWCNTs. SWCNT films are known to produce photocurrents when deposited on semiconductor substrates (independent of any substrate photocurrent)[139-140] so, if there is a contribution from the SWCNTs in **Figure 1.12**(b) then this seems to imply that the underlying mechanism of the SWCNT-silicon architecture is that of a pn junction not a Schottky junction. A rigorous study of the capacitance of SWCNT-silicon junctions would likely shed more light on the issue.

In related work, Tsolov et al.[141] reported the mid-IR response of a silicon-carbon nanotube photodiode fabricated by CVD growth using an anodized aluminium oxide (AAO) template method (**Figure 1.13**(a)). Whilst the use of a template is demonstrated as a facile method for producing aligned nanotube arrays on silicon it is claimed that the broad photocurrent response observed to span ~ 1.5 – 10 μm is due to the absorption of photons and generation of excitons by the nanotubes themselves. However this feature in the photocurrent spectrum could be due to free

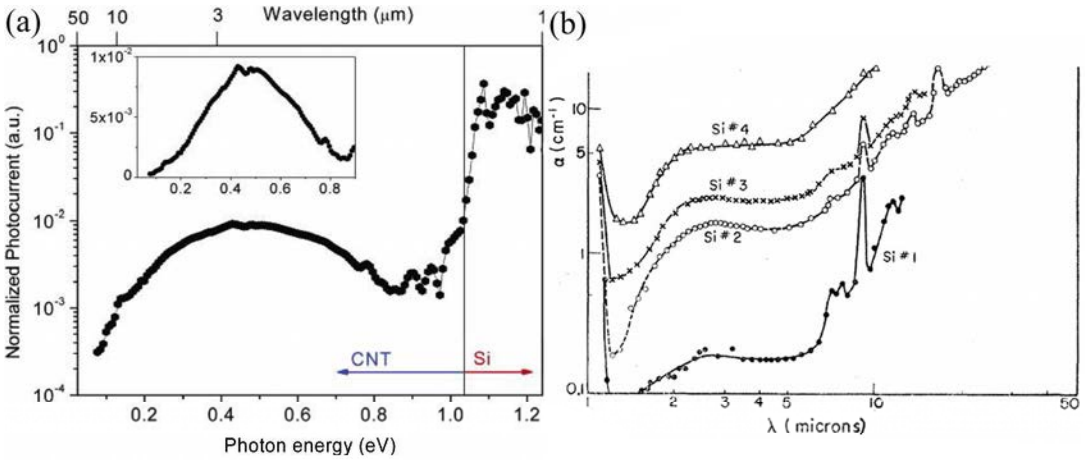

Figure 1.13 (a) Mid-IR photocurrent response of AAO-templated aligned nanotube array on silicon[141] (b) IR absorption spectra of n-type silicon doped with: #1 arsenic (N_d = $1.4x10^{16}$ cm^{-3}), #2 antimony (N_d = $8.0x10^{16}$ cm^{-3}), #3 antimony (N_d = $1.7x10^{17}$ cm^{-3}), #4 phosphorous (N_d = $3.2x10^{17}$ cm^{-3}) (image adapted from [142]).

carrier absorption in the silicon as reported by Spitzer[142] (**Figure 1.13**(b)) and Schroder.[143]

Comparison of **Figure 1.13**(a) and **Figure 1.13**(b) reveals the presence of three features at ~ 0.75 eV, 0.9 eV and 0.95 eV in (a) which are not represented in (b). These features are too far from the absorption band edge of silicon (1.12 eV) to be due to the silicon and might originate from the nanotubes. However MWCNTs such as those used have not been shown to exhibit such well-defined absorption characteristics. On the contrary MWCNTs are renowned for having rather broad featureless absorption spectra due to the complex mixing of states resulting from interactions between chirally dissimilar walls. It is also worth noting that a similar feature is observed on the low energy side of the silicon absorption as in the later work of Ong.[137] The data of neither Tsolov nor Ong conclusively proves whether the nanotubes are contributing to the photocurrent of these devices. This question could likely be answered by an experiment similar to Ong's whereby cells are fabricated with larger diameter nanotubes where the energy of the first excitonic transition << absorption onset of silicon (e.g. 1400 nm) and the spectral response of such devices is measured. In this case any contribution from the nanotubes should be easily resolved. The outcomes of that experiment are detailed in Chapter 4.

Wadhwa et al.[144] report a novel method of improving SWCNT-silicon solar cells through electronic junction control of a SWCNT-silicon device by the use of a gate potential applied to the junction via the ionic liquid electrolyte 1-ethyl-3-methylimidazolium bis(trifluoromethylsulfonyl)imide (EMI-BTI) (**Figure 1.14**). The device exhibited a PCE of 8.5 % which was dynamically and reversibly adjusted to between 4 % and 11 % by electronic gating. The mechanism of action of the electronic junction control is explained by considering the gate-induced modulation of the SWCNT Fermi level and the gate-modulated enhancement or suppression of the interface dipole at the junction. Of course this argument would apply to both Schottky and pn junction solar cells.

Jia et al.[145] achieved a much higher PCE of 13.8 % by in situ doping of the SWCNT film with 0.5 M HNO_3 (**Figure 1.15**) although, as shown in the later work of Jung,[146] this may have been partly due to lensing by the acid droplet. The untreated device exhibited a PCE of 6.2 % and the improvement was due to an increase in J_{SC} from 27 mA cm^{-2} to 36 mA cm^{-2} coupled with an increase in the FF from 0.47 to 0.72. Even after drying of the acid solution the cell maintained a higher efficiency than the original. Nitric acid doping of SWCNT films has been shown to both decrease the tube-tube resistance and shift the Fermi level down towards the valance band (p-doping)[147] and these findings are used to explain to the observed increases in efficiency. Whilst decreasing the series resistance is necessary for a large FF, the observation of a slight decrease in open circuit voltage (V_{OC}) is incongruent with p-doping. An increase in J_{SC} with nitric acid treatment is explained by considering the nanoscale structure of the junction, which is composed of many tiny junctions and leads to some SWCNTs having no contact at all with the underlying silicon. It is proposed that the HNO_3 can play the part of an electrolyte, effectively bridging these 'unconnected' SWCNTs to the silicon and allowing for the rapid shuttling of charge back and forth between tube and substrate. These Si-acid-SWCNT units in the pores of the film form tiny photoelectrochemical cells where the silicon is the anode and the SWCNTs are the cathode. This proposal is verified

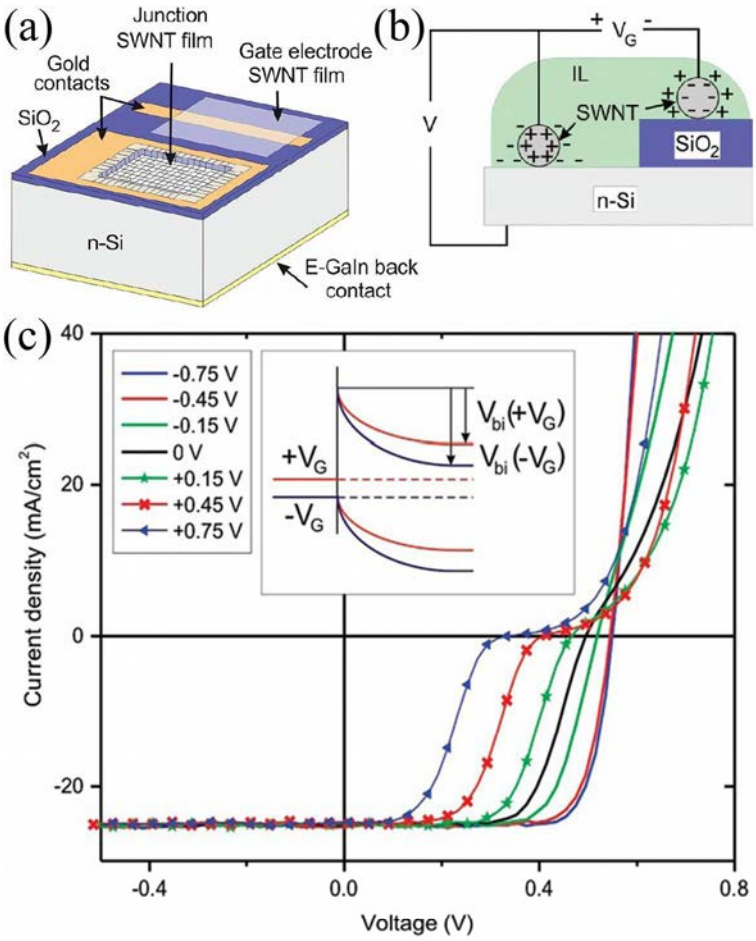

Figure 1.14 (a) Schematic of electrically-gated SWCNT-silicon solar cell (b) schematic of charge distribution during gated operation (c) J-V characteristics of the device with varying gate voltage. **Inset** shows the change in built in potential, V_{bi}, due to more or less silicon band bending with gate voltage (image adapted from [144]).

by showing that a similar (wet state) device in which the SWCNTs and the silicon are separated by a distance of 300nm also produces an appreciable photocurrent. Further support is given to the hypothesis by replacing the HNO_3 with an aqueous solution of NaCl. In this case a similar increase in the current density is also observed but, since the NaCl does not have the ability to reduce the series resistance or dope the SWCNTs, there is no corresponding increase in FF. Again though, there is the caveat regarding droplet lensing.

In another work by Jia et al.,[124] encapsulation of the active area by the insulating polymer polydimethylsiloxane (PDMS) is shown to increase efficiency whilst providing greatly improved device stability. Additionally, it is shown that the

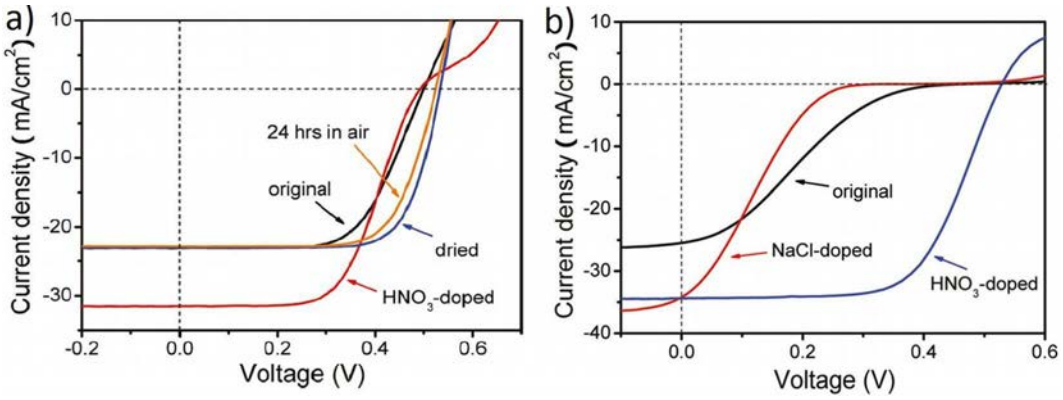

Figure 1.15 (a) J-V characteristics of the device before, during and after the HNO3 doping (b) J-V characteristics of the device comparing the effect of NaCl and HNO_3 showing that the increases in efficiency are due to more than electrolyte effects alone.[145]

formation of a thin SiO_x layer inbetween the SWCNTs and the underlying silicon leads to gains in V_{OC}. A schematic of the encapsulated device and fabrication steps is shown in **Figure 1.16**(a). The gains in V_{OC} shown in **Figure 1.16**(c) are provided via the formation of the thin insulating oxide layer and can be understood by considering the effect the oxide has upon majority carrier transport across the junction. Majority carriers can surpass the potential barrier at the junction by thermionic emission but this process is suppressed in the presence of the oxide (while the minority carrier current across the junction via tunnelling would be largely unaffected). This reduces recombination between majority and minority carriers and hence the increased V_{OC}. Evidence for this is given by the reduction in dark current density at -1 V from 1.2×10^{-3} mA cm^{-2} to 6.2×10^{-4} mA cm^{-2} after HNO_3 oxidation (**Figure 1.16**(d)). Additionally, minority carrier lifetime is increased from 14 µs to 19 µs after oxide formation whilst the bulk lifetime remains constant indicating that this is a surface effect. Presumably the increase in lifetime is due to the passivation of surface trap states and reduction in the frequency of recombination events. PDMS encapsulation is shown to improve the stability of the devices (**Figure 1.16**(c)) although a slight reduction in performance observed in the 20 day period which is attributed to the growth of an oxide layer that becomes too thick for tunnelling. PDMS encapsulation increases cell efficiency by reducing the reflectance from ~ 35 - 40 % for silicon and silicon-SWCNT to ~ 10 % for the encapsulated device (**Figure 1.16**(d)).

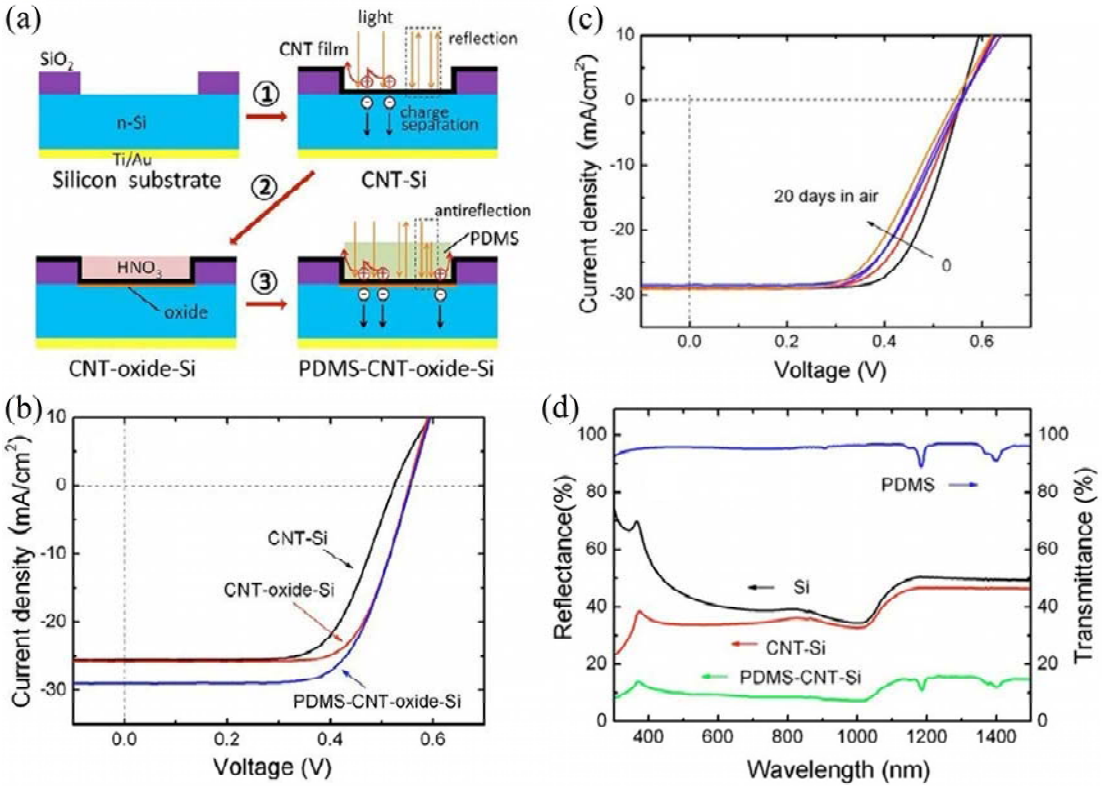

Figure 1.16 (a) Schematic of device fabrication (b) J-V characteristics of the SWCNT-silicon cells before and after oxide formation and after encapsulation with PDMS (c) change in J-V characteristics of the PDMS encapsulated device over 20 days in air (d) reflectance data for the cells (image adapted from [124]).

It is suggested that the SWCNT-oxide-Si resembles a traditional MIS structure and an energy band diagram is proposed, but this conflicts with the earlier work by Ong[137] where the SWCNTs appear to display a photocurrent response. An analysis of the photocurrent spectra would perhaps shed light on this but such measurements can be problematic. This is due to two factors; a) the SWCNT film has very high transmittance and is thus expected to produce only a small fraction of the total photocurrent and b) if the SWCNT chirality is such that the position of the S_{11} transition overlaps the absorption ranges of the silicon such a small contribution may be difficult to elucidate. Nevertheless, if the SWCNTs have been shown to produce a photocurrent when in the SWCNT-silicon architecture then this is incompatible with the proposed MIS mechanism.

Wadhwa et al.[148] extend previously reported work by engineering a grid pattern in the SWCNT layer through oxygen plasma etching. A modest improvement in PCE

from ~ 11 % to ~ 12% is observed via this strategy. In this work the junction electrostatics are modelled showing that the mere presence of the ionic liquid EMI-BTI induces a depletion layer in the silicon without any applied gate voltage. This finding is commensurate with the observation of a prompt improvement in performance immediately upon introduction of the electrolyte. Although an electrolyte is used in the cell the authors are careful to distinguish between this architecture and that of a photoelectrochemical liquid junction cell (e.g. Grätzel cell)[149] in which the electrolyte plays the part of a redox shuffle between photoanode (silicon) and cathode (the SWCNTs). This mechanism is precluded by the deliberately chosen large electrochemical window of the EMI-BTI electrolyte (-2.6 to 2.0 V vs. Fc/Fc^+). Thus the necessary depletion layer in the silicon is set up by the accumulation of negative ions at the surface. The cell is similar to the grating MIS cells reported by Godfrey and Green[150] and the mechanism of action of the grating is reasonably assumed to be as in those devices whereby there is photogeneration of excitons in the silicon which then travel along the surface until reaching a junction where the grid lines are. It is suggested that the increase in performance is due to the blocking of majority carrier current by the strong surface dipole setup by the accumulation of negative ions repelling electrons. This may also be relevant for the nitric acid doped work of Jia et al. whereby some of the performance gains in those works could be due in part to a similar build-up of NO_3^- ions at the junction providing majority carrier blocking in addition to that of the oxide layer. Chen, et al.[151] have continued this work, modelling the effect of the ionic liquid on inversion layer properties and furthermore demonstrating significant improvements in device performance by the introduction of a highly doped back contact region. Such back contacts are shown to function as hole blocking layers, improving carrier separation and lowering surface recombination thus providing gains in both J_{SC} and FF.

It is clear that carbon nanotube films function, at least, as transparent conducting front electrodes. Carbon nanotube films have been used similarly in amorphous silicon solar cells,[152-153] heterojunction solar cells of quantum dots and silicon,[154-155]

on silicon nanowires with[156] and without[157-158] photoactive polymers, as well as enhancing the performance of 'standard' pn junction silicon solar cells.[159] Photovoltaic output from SWCNT-silicon cells can be improved by the addition of graphene 'patches' to the nanotube film[160] and by flowing gasses over the surface of the nanotube film,[160] an effect that has been used to fabricate gas sensors.

A recent development is the use of highly aligned SWCNT films.[146, 162] Devices made with such films show good performance, likely due to the greatly improved electrical characteristics of aligned SWCNT films. Measurements by Jung et al.[146] appear to preclude the MS/MIS operating mechanisms. For example, the activation energy of devices correlates with the bandgap of silicon and is much larger than in conventional MS Schottky cells. A very long carrier lifetime is measured, also inconsistent with the MS Schottky model, and the presence of an oxide is shown to be detrimental to performance, which is counter to the apparent MIS mechanism observed by Jia et al.[124] In work by Shi et al.[163] the use of a TiO_2 antireflection layer has been reported to yield SWCNT-silicon solar cells with a PCE of 15 % which puts them into the same region of efficiency as many commercial solar panels.

1.5 Other carbon nanotube solar cells

Svrcek et al.[164] introduced a new branch in the SWCNT-silicon solar cell field by combining s-SWCNTs with silicon nanocrystals (Si-ncs) in a bulk heterojunction (BHJ) device (**Figure 1.17**(a)). This architecture differs from the (planar) silicon case in that both the SWCNTs and the silicon are of nanoscale dimension, with the Si-ncs having a diameter of ~ 3 nm. Another important difference is that, in contrast to SWCNT-(planar) silicon devices which only generate power when the silicon is n-type, these BHJ devices only display a strong photocurrent when the Si-ncs are p-type (in n-type devices J_{SC} is ~ 2 orders of magnitude smaller). The SWCNTs were enriched in semiconducting chiralities by interaction with the p-type polymer poly(9,9-di-n-octyl-fluorenyl-2,7-diyl) (PFO) followed by ultra-centrifugation. Comparison of the absorption spectra of PFO-wrapped SWCNTs in

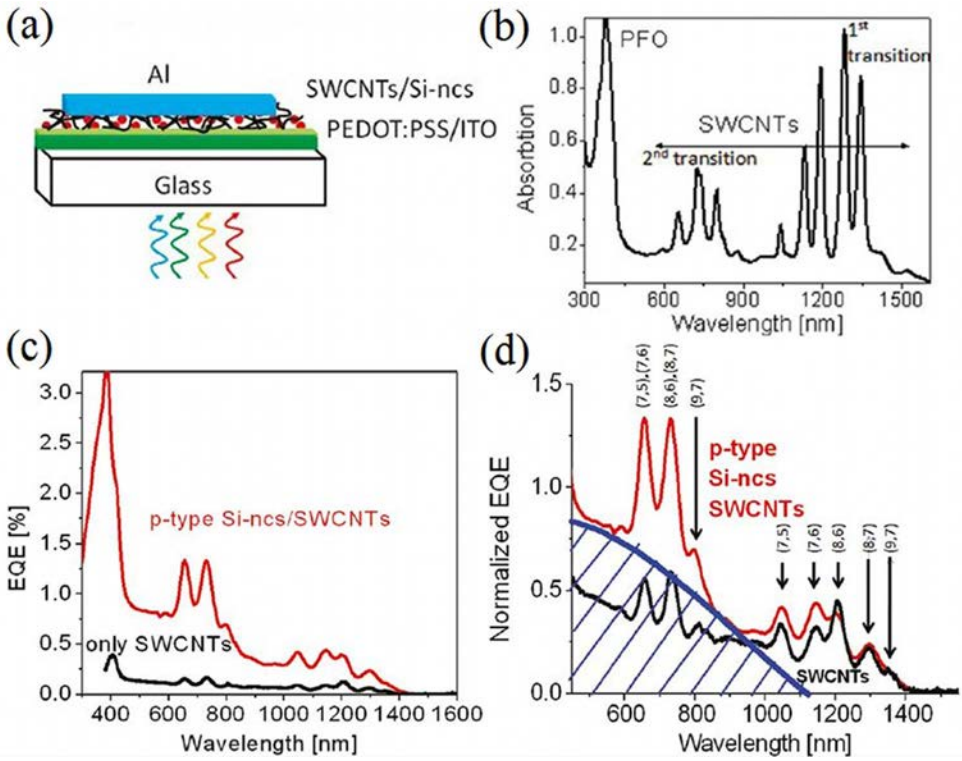

Figure 1.17 (a) Device schematic (b) optical absorption spectrum of the PFO-wrapped SWCNTs (c) spectrally resolved short circuit external quantum efficiency (EQE) of devices ith (red) and without (black) Si-ncs (d) normalised EQE showing peak assignments to first and second excitonic transitions in semiconducting SWCNTs, the blue line indicates overlap with the silicon absorption (image adapted from [164]).

Figure 1.17(b) with the EQE data in **Figure 1.17**(c) shows unambiguously that the wrapped SWCNTs contribute to the observed photocurrent, although contributions from both the Si-ncs and the PFO are also observable. In **Figure 1.17**(d) discrete photocurrent peaks are assigned to the individual SWCNT chiralities present and show that the introduction of Si-ncs preferentially enhances the photocurrent due to smaller diameter, larger band gap SWCNTs. The proposed mechanism of charge transfer from Si-ncs to SWCNTs is supported by the observation of photoluminescence quenching (by a factor of > 2) in Si-ncs upon addition of SWCNTs.

In different but related work, Bindl et al.[165-166] combined semiconducting SWCNTs with C_{60} in devices that build on their prior SWCNT photophysics work.[167] This differs from other work involving SWCNTs and fullerenes in that it is the SWCNTs that do the primary work of absorbing light energy rather than the fullerenes or

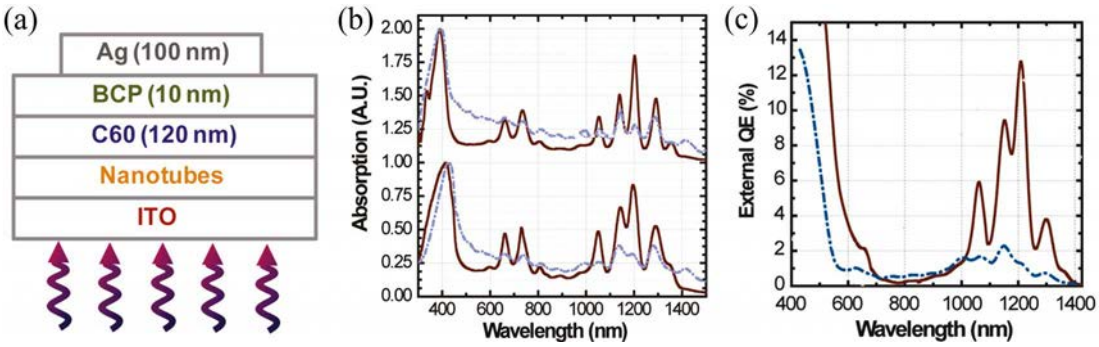

Figure 1.18 (a) Device schematic (b) absorption spectra of mixed (blue dash) and semiconducting-enriched (solid red) SWCNT solutions (top) and films (bottom) (c) EQE of devices fabricated with mixed (blue dash) and semiconducting-enriched (solid red) SWCNTs (image adapted from [165]).

other species complexed to them. As in the later work of Svrcek et al.[164] both the SWCNTs and semiconductor are of nanoscale dimension and the thermal deposition method employed for the C_{60} produces a conformal covering on the SWCNT layer (**Figure 1.18**(a)). Importantly, the devices incorporated an exciton blocking layer of bathocuproine (BCP) between the C_{60} and the silver cathode. Comparison of the data in **Figure 1.18**(b) and **Figure 1.18**(c) shows a clear correlation between the S_{11} absorption bands and the EQE of the devices, providing strong evidence of light harvesting by the SWCNTs. The excitation of the smaller diameter SWCNTs produces better device performance and there is a cut-off for the SWCNT diameter above which excitation of these SWCNTs yields significantly reduced performance. This is related to the band offset at the SWCNT-C_{60} junction resulting in a positive driving force ΔE for C_{60} junctions with the smaller diameter, larger gap SWCNTs and this effect has also been demonstrated elsewhere.[97, 168] It is shown that semiconducting-enriched SWCNTs clearly outperform mixtures of semiconducting and m-SWCNTs (**Figure 1.18**(d)). Efficiency was found to be limited by the relatively short diffusion length which was estimated to be ~ 3 nm. In more recent work, Bindl et al. and others have improved understanding of the role of the SWCNTs in these devices,[169] particular in the role of chiral purity,[170-171] and raised internal quantum efficiencies (IQE) to ~ 85 %.[172] The short diffusion length in the SWCNT film may be due to the insulating effect of the PFO wrapping agent inhibiting tube-tube transfer. If so the devices may be improved by removing the PFO prior to deposition of the SWCNTs, if possible. Tung et al. described a similar

device but free of the wrapping agent,[173] but these were constructed with a mixture of C_{60}, SWCNTs and reduced graphene oxide (rGO) and used PEDOT:PSS on the indium tin oxide (ITO) anode rather than BCP on the cathode. The fact that the SWCNTs' discrete absorption ranges produce correspondingly discrete features in the spectrally resolved EQE is an inherent disadvantage in solar cell devices where it is desirable for the photoactive layer to absorb across the useful spectrum of solar radiation. However, a multijunction device comprising an appropriately engineered stack of SWCNT chiralities can be envisioned whereby the individual absorption ranges of the component layers could be tailored such that the complete device exhibits a net absorption covering the desired spectral range. This issue is explored in detail in Chapter 7.

1.6 Summary

Various properties of carbon nanotubes make them promising candidates for incorporation into a range of future photovoltaic device architectures. From early reports of ~ 1 % power conversion efficiency the field of nanotube-silicon heterojunction solar cells has rapidly seen performance gains up to 11.5 %[162] for dry-state devices (15 % with an antireflection layer).[163] However the mechanism of action is still unclear, with findings such as the figure of merit established by Jia et al.[135] suggesting Schottky/MIS whilst the photocurrent spectra of Ong et al.[137] and the extensive heterojunction characterisation of Jung et al.[146] suggest pn characteristics. The polychirality of SWCNTs employed in many of the devices reported so far certainly confounds this issue. Chapter 4 shows whether or not SWCNTs can be found to contribute to photocurrent generation in SWCNT-silicon solar cells and in Chapter 5, significant differences will be discovered between devices employing purely metallic or semiconducting SWCNTs. Post treatment of SWCNT films with strong oxidisers and oxidising acids has been shown to markedly improve device performance through reduction in film resistivity and adjustment of the SWCNT Fermi level. The use of ionic liquid electrolytes to provide electronic junction control has been demonstrated to be an effective method of significantly

improving the performance of SWCNT-silicon heterojunction solar cells although it is unlikely this could see practical application in commercial devices. More generally, considering the simulations presented in Chapter 7, the recent reports of solar cells that successfully exploit SWCNTs directly as light harvesting elements are very promising.

As shown in the literature, carbon nanotube films function well as transparent, conducting electrode material and as such could offer performance gains through improved charge transport and reduced optical shading. Chapters 2 and 3 will use SWCNT films produced using different fabrication methods and in very different types of photovoltaics. Compared to several decades of very extensive research into silicon technology, the use of SWCNTs is a small and relatively new area of research and there is still much to be understood. Considering the apparent ease with which good performance has been achieved in a short time it is likely that significant potential exists in this field.

1.7 References

[1] *International population database*. 2011, US Census Bureau, Population Division.

[2] Lewis, N.S., *Materials Research Bulletin,* **2007**. 32: p. 808-820.

[3] Smil, V., *Essays in world history*. 1994: Westview Press.

[4] McKinney, M.L. and Schoch, R.M., *Environmental science, systems and solutions*, ed. G.T. Miller. 2003: Brooks / Cole Publishing Company, Pacific Grove, USA.

[5] *The critical decade: A report from the climate commission*, Commonwealth of Australia Department of Climate and Energy. 2011.

[6] Benka, S.G., *Physics Today,* **2002**. 55(4): p. 38-39.

[7] Haszeldine, R.S., *Science,* **2009**. 325(5948): p. 1647-1652.

[8] Keeney, R.L. and Winterfeldt, D.v., *Risk Analysis,* **1994**. 14: p. 107-130.

[9] Bodvarsson, G.S., Boyle, W., Patterson, R., and Williams, D., *Journal of Contaminant Hydrology,* **1999**. 38: p. 3-24.

[10] *The generation IV international forum*. http://www.gen-4.org/ (16/3/13)

[11] *Renewables 2012 global status report*, REN21: Renewable Energy Policy Network for the 21st Century. 2012.

[12] Fritts, C., *Proceedings of the American Association for the Advancement of Science,* **1883**. 33(97).

[13] Chapin, D.M., Fuller, C.S., and Pearson, G.L., *Journal of Applied Physics,* **1954**. 25(5): p. 676-677.

[14] Green, M.A., *Journal of Applied Physics,* **1985**. 58(11): p. 4402-4408.

[15] Bermann, R.B., *Applied Physics A,* **1999**. 69: p. 187-194.

[16] Kraft, C., Brömel, A., Schönherr, S., Hädrich, M., Reislöhner, U., Schley, P., Gobsch, G., Goldhahn, R., Wesch, W., and Metzner, H., *Thin Solid Films,* **2011**. 519(21): p. 7153-7155.

[17] Hibberd, C.J., Ernits, K., Kaelin, M., Müller, U., and Tiwari, A.N., *Progress in Photovoltaics: Research and Applications,* **2008**. 16: p. 585-593.

[18] King, R.R., Law, D.C., Edmondson, K.M., Fetzer, C.M., Kinsey, G.S., Yoon, H., Sherif, R.A., and Karam, N.H., *Applied Physics Letters,* **2007**. 18: p. 183516-183516-3.

[19] Guter, W., Schöne, J., Philipps, S.P., Steiner, M., Siefer, G., Wekkeli, A., Welser, E., Oliva, E., Bett, A.W., and Dimroth, F., *Applied Physics Letters,* **2009**. 94: p. 223504.

[20] Fthenakis, V., *Renewable and sustainable energy reviews,* **2009**. 13: p. 2746-2750.

[21] Luque, A. and Hegedus, S., eds. *Handbook of photovoltaic science and engineering*. 2nd ed. 2010, Wiley.

[22] Grätzel, M., *Journal of Photochemistry and Photobiology C: Photochemistry Reviews,* **2003**. 4(2): p. 145-153.

[23] Jørgensen, M., Norrman, K., and Krebs, F.C., *Solar Energy Materials and Solar Cells,* **2008**. 92(7): p. 686-714.

[24] Iijima, S., *Nature,* **1991**. 354(6348): p. 56-58.

[25] Iijima, S. and Ichihashi, T., *Nature,* **1993**. 363(6430): p. 603-605.

[26] Bethune, D.S., Kiang, C.H., Vries, M.S.d., Gorman, G., Savoy, R., Vazquez, J., and Beyers, R., *Nature,* **1993**. 363: p. 605-607.

[27] Mintmire, J.W. and White, C.T., *Carbon,* **1995**. 33(7): p. 893-902.

[28] Ouyang, Y., Yoon, Y., and Guo, J., *Journal of Computer-Aided Materials Design,* **2007**. 14(1): p. 73-78.

[29] Wu, Z., Chen, Z., Du, X., Logan, J.M., Sippel, J., Nikolou, M., Kamaras, K., Reynolds, J.R., Tanner, D.B., Hebard, A.F., and Rinzler, A.G., *Science,* **2004**. 305(5688): p. 1273-1276.

[30] Ugawa, A., Hwang, J., Gommans, H.H., Tashiro, H., Rinzler, A.G., and Tanner, D.B., *Current Applied Physics,* **2001**. 1(1): p. 45-49.

[31] Thostenson, E.T., Ren, Z., and Chou, T.-W., *Composites Science and Technology,* **2001**. 61: p. 1899-1912.

[32] Dresselhaus, M.S., Dresselhaus, G., and Jorio, A., *Annu. Rev. Mater. Res.,* **2004**. 34: p. 247-278.

[33] Odom, T.W., Huang, J.-L., Kim, P., and Lieber, C.M., *Journal of Physical Chemistry B,* **2000**. 104: p. 2794-2809.

[34] Odom, T.W., Huang, J.-L., Kim, P., and Lieber, C.M., *Nature,* **1998**. 391: p. 62-64.

[35] Dresselhaus, M.S., Dresselhaus, G., and Saito, R., *Carbon,* **1995**. 33(7): p. 883-891.

[36] Belin, T. and Epron, F., *Materials Science and Engineering B,* **2005**. 119: p. 105-118.

[37] Terrones, M., *Annu. Rev. Mater. Res.,* **2003**. 33: p. 419-501.

[38] Reich, S., Thomsen, C., and Maultzsch, J., *Carbon nanotubes: Basic concepts and physical properties*. 2004: Wiley-VCH Verlag GmbH & Co. KGaA, Weinheim.

[39] *Carbon nanotubes: Properties and applications*, ed. M.J. O'Connell. 2006: Taylor & Francis Group, LLC.

[40] Wallace, P.R., *Physical Review,* **1947**. 71(9): p. 622-634.

[41] Saito, R., Dresselhaus, G., and Dresselhaus, M.S., *Physical Review B,* **2000**. 61: p. 2981-2989.

[42] Ando, T., *Journal of the Physical Society of Japan,* **2005**. 74(3): p. 777-817.

[43] Saito, R., Dresselhaus, G., and Dresselhaus, M.S., eds. *Physical properties of carbon nanotubes*. 1998, Imperial College Press.

[44] Flavel, B.S., *Carbon nanotube based surface architectures on silicon for molecular electronics applications*, in *School of Chemical and Physical Sciences*. 2009, The Flinders University of South Autsralia: Adelaide, South Australia.

[45] Dresselhaus, M.S., Dresselhaus, G., Saito, R., and Jorio, A., *Physics Reports,* **2005**. 409(2): p. 47-99.

[46] Hároz, E.H., Lu, B.Y., Nikolaev, P., Arepalli, S., Hauge, R.H., and Kono, J., *Journal of the American Chemical Society,* **2011**. 10.1021/ja209333m.

[47] Ebbesen, T.W. and Ajayan, P.M., *Nature,* **1992**. 358(6383): p. 220-222.

[48] Andreas Hirsch, O.V., *Functionalization of carbon nanotubes*. 2005, Erlangen Germany: Institut fur Organische Chemie, Universitat Erlangen-Nurnberg, Henkestrasse.

[49] *Dekker encyclopedia of nanoscience and nanotechnology*, ed. J.A. Schwarz, C.I. Contescu, and K. Putyera. 2004, New York: Marcel Dekker.

[50] Chen, Z., Thiel, W., and Hirsch, A., *ChemPhysChem,* **2003**. 4(1): p. 93-97.

[51] Mawhinney, D.B., Naumenko, V., Kuznetsova, A., Yates, , J.T., L., J., , and and Smalley, R.E., *J. Am. Chem. Soc.,* **2000**. 122(10): p. 2383-2384.

[52] Spataru, C.D., Ismail-Beigi, S., Benedict, L.X., and Louie, S.G., *Physical Review Letters,* **2004**. 92(7): p. 077402.

[53] Bachilo, S.M., Strano, M.S., Kittrell, C., Hauge, R.H., Smalley, R.E., and Weisman, R.B., *Science,* **2002**. 298(5602): p. 2361-2366.

[54] Shockley, W. and Queisser, H.J., *Journal of Applied Physics,* **1961**. 32(3): p. 510-519.

[55] Weisman, R.B. and Bachilo, S.M., *Nano Letters,* **2003**. 3(9): p. 1235-1238.

[56] Wang, S., Khafizov, M., Tu, X., Zheng, M., and Krauss, T.D., *Nano Letters,* **2010**. 10(7): p. 2381-6.

[57] Gabor, N.M., Zhong, Z., Bosnick, K., Park, J., and McEuen, P.L., *Science,* **2009**. 325(5946): p. 1367-1371.

[58] Collins, P.G., Bradley, K., Ishigami, M., and Zettl, A., *Science,* **2000**. 287(5459): p. 1801-1804.

[59] Tantang, H., Ong, J.Y., Loh, C.L., Dong, X., Chen, P., Chen, Y., Hu, X., Tan, L.P., and Li, L.-J., *Carbon,* **2009**. 47(7): p. 1867-1870.

[60] Barnes, T.M., Blackburn, J.L., van de Lagemaat, J., Coutts, T.J., and Heben, M.J., *ACS Nano,* **2008**. 2(9): p. 1968-1976.

[61] Zhou, C., Kong, J., Yenilmez, E., and Dai, H., *Science,* **2000**. 290(5496): p. 1552-1555.

[62] Klinke, C., Chen, J., Afzali, A., and Avouris, P., *Nano Letters,* **2005**. 5(3): p. 555-558.

[63] Li, Z., Saini, V., Dervishi, E., Kunets, V.P., Zhang, J., Xu, Y., Biris, A.R., Salamo, G.J., and Biris, A.S., *Applied Physics Letters,* **2010**. 96(3): p. 033110-3.

[64] Biswas, C., Lee, S.Y., Ly, T.H., Ghosh, A., Dang, Q.N., and Lee, Y.H., *ACS Nano,* **2011**. 5(12): p. 9817-9823.

[65] Redlich, P., Loeffler, J., Ajayan, P.M., Bill, J., Aldinger, F., and Rühle, M., *Chemical Physics Letters,* **1996**. 260(3–4): p. 465-470.

[66] Ayala, P., Arenal, R., Rümmeli, M., Rubio, A., and Pichler, T., *Carbon,* **2010**. 48(3): p. 575-586.

[67] Pint, C.L., Sun, Z., Moghazy, S., Xu, Y.-Q., Tour, J.M., and Hauge, R.H., *ACS Nano,* **2011**. 5: p. 6925–6934.

[68] Krupke, R., Linden, S., Rapp, M., and Hennrich, F., *Advanced Materials,* **2006**. 18(11): p. 1468-1470.

[69] Arnold, K., Hennrich, F., Krupke, R., Lebedkin, S., and Kappes, M.M., *Physica Status Solidi (b),* **2006**. 243(13): p. 3073-3076.

[70] Hersam, M.C., *Nature Nanotechnology,* **2008**. 3: p. 387-394.

[71] Hwang, J.-Y., Nish, A., Doig, J., Douven, S., Chen, C.-W., Chen, L.-C., and Nicholas, R.J., *Journal of the American Chemical Society,* **2008**. 130(11): p. 3543-3553.

[72] Hennrich, F., Lebedkin, S., and Kappes, M.M., *Physica Status Solidi (b),* **2008**. 245(10): p. 1951-1953.

[73] Stürzl, N., Hennrich, F., Lebedkin, S., and Kappes, M.M., *The Journal of Physical Chemistry C,* **2009**. 113(33): p. 14628-14632.

[74] Moshammer, K., Hennrich, F., and Kappes, M.M., *Nano Research,* **2009**. 2: p. 599-606.

[75] Tu, X., Manohar, S., Jagota, A., and Zheng, M., *Nature,* **2009**. 460(7252): p. 250-253.

[76] Liu, H., Nishide, D., Tanaka, T., and Kataura, H., *Nature Communications,* **2011**. 2: p. 309.

[77] Landi, B.J., Raffaelle, R.P., Castro, S.L., and Bailey, S.G., *Progress in Photovoltaics: Research and Applications,* **2005**. 13: p. 165-172.

[78] Kymakis, E. and Amaratunga, G.A.J., *Applied Physics Letters,* **2002**. 80: p. 112.

[79] Kymakis, E., Alexandrou, I., and Amaratunga, G.A.J., *Journal of Applied Physics,* **2003**. 93(3): p. 1764-1768.

[80] Pasquier, A.D., Unalan, H.E., Kanwal, A., Miller, S., and Chhowalla, M., *Applied Physics Letters,* **2005**. 87: p. 203511.

[81] Sgobba, V. and Guldi, D.M., *Journal of Materials Chemistry,* **2008**. 18(2): p. 153-157.

[82] Kongkanand, A., Martinez Dominguez, R., and Kamat, P.V., *Nano Letters,* **2007**. 7(3): p. 676-680.

[83] Li, C., Chen, Y., Wang, Y., Iqbal, Z., Chhowalla, M., and Mitra, S., *Journal of Materials Chemistry,* **2007**. 17(23): p. 2406-2411.

[84] Wei, L., Tezuka, N., Umeyama, T., Imahori, H., and Chen, Y., *Nanoscale,* **2011**. 3(4): p. 1845-1849.

[85] Bissett, M.A. and Shapter, J.G., *The Journal of Physical Chemistry C,* **2010**. 114(14): p. 6778-6783.

[86] Barazzouk, S., Hotchandani, S., Vinodgopal, K., and Kamat, P.V., *The Journal of Physical Chemistry B,* **2004**. 108(44): p. 17015-17018.

[87] Umeyama, T., Tezuka, N., Fujita, M., Hayashi, S., Kadota, N., Matano, Y., and Imahori, H., *Chemistry – A European Journal,* **2008**. 14(16): p. 4875-4885.

[88] Umeyama, T., Tezuka, N., Seki, S., Matano, Y., Nishi, M., Hirao, K., Lehtivuori, H., Tkachenko, N.V., Lemmetyinen, H., Nakao, Y., Sakaki, S., and Imahori, H., *Advanced Materials,* **2010**. 22(15): p. 1767-1770.

[89] Tezuka, N., Umeyama, T., Seki, S., Matano, Y., Nishi, M., Hirao, K., and Imahori, H., *The Journal of Physical Chemistry C,* **2010**. 114(7): p. 3235-3247.

[90] Tezuka, N., Umeyama, T., Matano, Y., Shishido, T., Yoshida, K., Ogawa, T., Isoda, S., Stranius, K., Chukharev, V., Tkachenko, N.V., Lemmetyinen, H., and Imahori, H., *Energy & Environmental Science,* **2011**. 4(3): p. 741-750.

[91] D'Souza, F., Das, S.K., Sandanayaka, A.S.D., Subbaiyan, N.K., Gollapalli, D.R., Zandler, M.E., Wakahara, T., and Ito, O., *Physical Chemistry Chemical Physics,* **2012**. 14(8): p. 2940-2950.

[92] Umeyama, T., Tezuka, N., Kawashima, F., Seki, S., Matano, Y., Nakao, Y., Shishido, T., Nishi, M., Hirao, K., Lehtivuori, H., Tkachenko, N.V., Lemmetyinen, H., and Imahori, H., *Angewandte Chemie International Edition,* **2011**. 50(20): p. 4615-4619.

[93] Umeyama, T., Fujita, M., Tezuka, N., Kadota, N., Matano, Y., Yoshida, K., Isoda, S., and Imahori, H., *The Journal of Physical Chemistry C,* **2007**. 111(30): p. 11484-11493.

[94] Bissett, M.A. and Shapter, J.G., *Journal of The Electrochemical Society,* **2011**. 158(3): p. K53-K57.

[95] Hasobe, T., Fukuzumi, S., and Kamat, P.V., *The Journal of Physical Chemistry B,* **2006**. 110(50): p. 25477-25484.

[96] Rahman, G.M.A., Troeger, A., Sgobba, V., Guldi, D.M., Jux, N., Balbino, D., Tchoul, M.N., Ford, W.T., Mateo-Alonso, A., and Prato, M., *Chemistry – A European Journal,* **2008**. 14(29): p. 8837-8846.

[97] Sandanayaka, A.S., Subbaiyan, N.K., Das, S.K., Chitta, R., Maligaspe, E., Hasobe, T., Ito, O., and D'Souza, F., *ChemPhysChem,* **2011**. 12(12): p. 2266-73.

[98] Guldi, D.M., Rahman, G.M.A., Prato, M., Jux, N., Qin, S., and Ford, W., *Angewandte Chemie International Edition,* **2005**. 44(13): p. 2015-2018.

[99] Sgobba, V., Rahman, G.M.A., Guldi, D.M., Jux, N., Campidelli, S., and Prato, M., *Advanced Materials,* **2006**. 18(17): p. 2264-2269.

[100] Rahman, G.M.A., Guldi, D.M., Cagnoli, R., Mucci, A., Schenetti, L., Vaccari, L., and Prato, M., *Journal of the American Chemical Society,* **2005**. 127(28): p. 10051-10057.

[101] Sgobba, V., Troeger, A., Cagnoli, R., Mateo-Alonso, A., Prato, M., Parenti, F., Mucci, A., Schenetti, L., and Guldi, D.M., *Journal of Materials Chemistry,* **2009**. 19(25): p. 4319-4324.

[102] Giancane, G., Ruland, A., Sgobba, V., Manno, D., Serra, A., Farinola, G.M., Omar, O.H., Guldi, D.M., and Valli, L., *Advanced Functional Materials,* **2010**. 20(15): p. 2481-2488.

[103] Umeyama, T., Kadota, N., Tezuka, N., Matano, Y., and Imahori, H., *Chemical Physics Letters,* **2007**. 444(4–6): p. 263-267.

[104] Campidelli, S.p., Ballesteros, B., Filoramo, A., Díaz, D.D.a., de la Torre, G., Torres, T.s., Rahman, G.M.A., Ehli, C., Kiessling, D., Werner, F., Sgobba, V., Guldi, D.M., Cioffi, C., Prato, M., and Bourgoin, J.-P., *Journal of the American Chemical Society,* **2008**. 130(34): p. 11503-11509.

[105] Bissett, M.A., Koper, I., Quinton, J.S., and Shapter, J.G., *Physical Chemistry Chemical Physics,* **2011**. 13(13): p. 6059-6064.

[106] Guldi, D.M., Rahman, G.M.A., Sgobba, V., Kotov, N.A., Bonifazi, D., and Prato, M., *Journal of the American Chemical Society,* **2006**. 128(7): p. 2315-2323.

[107] Mountrichas, G., Sandanayaka, A.S.D., Economopoulos, S.P., Pispas, S., Ito, O., Hasobe, T., and Tagmatarchis, N., *Journal of Materials Chemistry,* **2009**. 19(47): p. 8990-8998.

[108] Larsen, L.J., Tune, D.D., Kemppinen, P., Winzenberg, K.N., Watkins, S.E., and Shapter, J.G., *Journal of Photochemistry and Photobiology A: Chemistry,* **2012**. 235(0): p. 72-76.

[109] Suzuki, K., Yamaguchi, M., Kumagai, M., and Yanagida, S., *Chemistry Letters,* **2003**. 32(1): p. 28-29.

[110] Murakami, T.N. and Gratzel, M., *Inorganica Chimica Acta,* **2008**. 361(3): p. 572-580.

[111] Zhu, H., Zeng, H., Subramanian, V., Masarapu, C., Hung, K.-H., and Wei, B., *Nanotechnology,* **2008**. 19(46): p. 465204.

[112] Lee, W., Lee, J., Lee, S.H., Chang, J., Yi, W., and Han, S.H., *J. Phys. Chem. C,* **2007**. 111(26): p. 9110-9115.

[113] Lee, T.Y., Alegaonkar, P.S., and Yoo, J.-B., *Thin Solid Films,* **2007**. 515(12): p. 5131-5135.

[114] Chen, T., Wang, S., Yang, Z., Feng, Q., Sun, X., Li, L., Wang, Z.-S., and Peng, H., *Angewandte Chemie International Edition,* **2011**. 50(8): p. 1815-1819.

[115] Brown, P., Takechi, K., and Kamat, P.V., *The Journal of Physical Chemistry C,* **2008**. 112(12): p. 4776-4782.

[116] Imahori, H. and Umeyama, T., *The Journal of Physical Chemistry C,* **2009**. 113(21): p. 9029-9039.

[117] Sgobba, V. and Guldi, D.M., *Chemical Society Reviews,* **2009**. 38(1): p. 165-184.

[118] Chitta, R. and D'Souza, F., *Journal of Materials Chemistry,* **2008**. 18(13): p. 1440-1471.

[119] Guldi, D.M., Rahman, G.M.A., Zerbetto, F., and Prato, M., *Accounts of Chemical Research,* **2005**. 38(11): p. 871-878.

[120] Guldi, D.M., *The Journal of Physical Chemistry B,* **2005**. 109(23): p. 11432-11441.

[121] Guldi, D.M., *Physical Chemistry Chemical Physics,* **2007**. 9(12): p. 1400-1420.

[122] D'Souza, F., Sandanayaka, A.S.D., and Ito, O., *The Journal of Physical Chemistry Letters,* **2010**. 1(17): p. 2586-2593.

[123] D'Souza, F. and Ito, O., *Chemical Society Reviews,* **2012**. 41(1): p. 86-96.

[124] Jia, Y., Li, P., Gui, X., Wei, J., Wang, K., Zhu, H., Wu, D., Zhang, L., Cao, A., and Xu, Y., *Applied Physics Letters,* **2011**. 98(13): p. 133115-3.

[125] Green, M.A., Godfrey, R.B., and Davies, L.W., *The Australian Physicist,* **1976**. 13(11): p. 177-179.

[126] Shewchun, J., Singh, R., and Green, M.A., *Journal of Applied Physics,* **1977**. 48(2): p. 765-770.

[127] Schottky, W., *Zeitschrift fuer Physik* **1939**. 113: p. 367-414.

[128] Anderson, W.A., Delahoy, A.E., and Milano, R.A., *Journal of Applied Physics,* **1974**. 45(9): p. 3913-3915.

[129] Wei, J., Jia, Y., Shu, Q., Gu, Z., Wang, K., Zhuang, D., Zhang, G., Wang, Z., Luo, J., Cao, A., and Wu, D., *Nano Letters,* **2007**. 7(8): p. 2317-2321.

[130] Behnam, A., Johnson, J.L., Choi, Y., Ertosun, M.G., Okyay, A.K., Kapur, P., Saraswat, K.C., and Ural, A., *Applied Physics Letters,* **2008**. 92(24).

[131] Jia, Y., Wei, J., Wang, K., Cao, A., Shu, Q., Gui, X., Zhu, Y., Zhuang, D., Zhang, G., Ma, B., Wang, L., Liu, W., Wang, Z., Luo, J., and Wu, D., *Advanced Materials,* **2008**. 20(23): p. 4594-4598.

[132] Li, Z., Kunets, V.P., Saini, V., Xu, Y., Dervishi, E., Salamo, G.J., Biris, A.R., and Biris, A.S., *Applied Physics Letters,* **2008**. 93(24): p. 243117-3.

[133] Li, Z., Kunets, V.P., Saini, V., Xu, Y., Dervishi, E., Salamo, G.J., Biris, A.R., and Biris, A.S., *ACS Nano,* **2009**. 3(6): p. 1407-1414.

[134] Li, Z., Jia, Y., Wei, J., Wang, K., Shu, Q., Gui, X., Zhu, H., Cao, A., and Wu, D., *Journal of Materials Chemistry,* **2010**. 20(34): p. 7236-7240.

[135] Jia, Y., Li, P., Wei, J., Cao, A., Wang, K., Li, C., Zhuang, D., Zhu, H., and Wu, D., *Materials Research Bulletin,* **2010**. 45(10): p. 1401-1405.

[136] Castrucci, P., Del Gobbo, S., Camilli, L., Scarselli, M., Casciardi, S., Tombolini, F., Convertino, A., Fortunato, G., and De Crescenzi, M., *Journal of Nanoscience and Nanotechnology,* **2011**. 11(10): p. 9202-9207.

[137] Ong, P.L., Euler, W.B., and Levitsky, I.A., *Nanotechnology,* **2010**. 21(10): p. 105203.

[138] Borgne, V.L., Castrucci, P., Gobbo, S.D., Scarselli, M., Crescenzi, M.D., Mohamedi, M., and Khakani, M.A.E., *Applied Physics Letters,* **2010**. 97(19): p. 193105.

[139] Castrucci, P., Scilletta, C., Del Gobbo, S., Scarselli, M., Camilli, L., Simeoni, M., Delley, B., Continenza, A., and De Crescenzi, M., *Nanotechnology,* **2011**. 22(11): p. 115701.

[140] El Khakani, M.A., Borgne, V.L., Aissa, B., Rosei, F., Scilletta, C., Speiser, E., Scarselli, M., Castrucci, P., and Crescenzi, M.D., *Applied Physics Letters,* **2009**. 95(8): p. 083114.

[141] Tzolov, M.B., Kuo, T.-F., Straus, D.A., Yin, A., and Xu, J., *The Journal of Physical Chemistry C,* **2007**. 111(15): p. 5800-5804.

[142] Spitzer, W. and Fan, H.Y., *Physical Review,* **1957**. 108(2): p. 268.

[143] Schroder, D.K., Thomas, R.N., and Swartz, J.C., *Solid-State Circuits, IEEE Journal of,* **1978**. 13(1): p. 180-187.

[144] Wadhwa, P., Liu, B., McCarthy, M.A., Wu, Z., and Rinzler, A.G., *Nano Letters,* **2010**. 10(12): p. 5001-5005.

[145] Jia, Y., Cao, A., Bai, X., Li, Z., Zhang, L., Guo, N., Wei, J., Wang, K., Zhu, H., Wu, D., and Ajayan, P.M., *Nano Letters,* **2011**. 11(5): p. 1901-1905.

[146] Jung, Y., Li, X., Rajan, N.K., Taylor, A.D., and Reed, M.A., *Nano Letters,* **2012**. 13(1): p. 95-99.

[147] Blackburn, J.L., Barnes, T.M., Beard, M.C., Kim, Y.-H., Tenent, R.C., McDonald, T.J., To, B., Coutts, T.J., and Heben, M.J., *ACS Nano,* **2008**. 2(6): p. 1266-1274.

[148] Wadhwa, P., Seol, G., Petterson, M.K., Guo, J., and Rinzler, A.G., *Nano Letters,* **2011**. 11(16): p. 2419-2423.

[149] O'Regan, B. and Gratzel, M., *Nature,* **1991**. 353(6346): p. 737-740.

[150] Godfrey, R.B. and Green, M.A., *Applied Physics Letters,* **1978**. 33(7): p. 637-639.

[151] Chen, W., Seol, G., Rinzler, A.G., and Guo, J., *Applied Physics Letters,* **2012**. 100(10): p. 103503.

[152] Del Gobbo, S., Castrucci, P., Scarselli, M., Camilli, L., De Crescenzi, M., Mariucci, L., Valletta, A., Minotti, A., and Fortunato, G., *Applied Physics Letters,* **2011**. 98(18): p. 183113-3.

[153] Schriver, M., Regan, W., Loster, M., and Zettl, A., *Solid State Communications,* **2010**. 150(13-14): p. 561-563.

[154] Li, X., Jia, Y., Wei, J., Zhu, H., Wang, K., Wu, D., and Cao, A., *ACS Nano,* **2010**. 4(4): p. 2142-2148.

[155] Li, P., Wang, S., Jia, Y., Li, Z., Ji, C., Zhang, L., Li, H., Shi, E., Bian, Z., Huang, C., Wei, J., Wang, K., Zhu, H., Wu, D., and Cao, A., *Nano Research,* **2011**. 4(10): p. 979-986.

[156] Golap, K. and et al., *Journal of Physics D: Applied Physics,* **2009**. 42(11): p. 115104.

[157] Shu, Q., Wei, J., Wang, K., Song, S., Guo, N., Jia, Y., Li, Z., Xu, Y., Cao, A., Zhu, H., and Wu, D., *Chemical Communications,* **2010**. 46(30): p. 5533-5535.

[158] Shu, Q., Wei, J., Wang, K., Zhu, H., Li, Z., Jia, Y., Gui, X., Guo, N., Li, X., Ma, C., and Wu, D., *Nano Letters,* **2009**. 9(12): p. 4338-4342.

[159] Zhang, Y.F., Y. F. Wang, N. Chen, Y. Y. Wang, Y. Z. Zhang, Z. H Zhou, and Wei, L.M., *Nano-Micro Lett.,* **2010**. 2: p. 22-25.

[160] Li, C., Li, Z., Zhu, H., Wang, K., Wei, J., Li, X., Sun, P., Zhang, H., and Wu, D., *The Journal of Physical Chemistry C,* **2010**. 114(33): p. 14008-14012.

[161] Fan, G., Fan, L., Li, Z., Bai, X., Mulligan, S., Jia, Y., Wang, K., Wei, J., Cao, A., Wu, D., Wei, B., and Zhu, H., *Journal of Materials Chemistry,* **2012**. 22(8): p. 3330-3334.

[162] Li, X., Jung, Y., Sakimoto, K., Goh, T.-H., Reed, M.A., and Taylor, A.D., *Energy & Environmental Science,* **2013**.

[163] Shi, E., Zhang, L., Li, Z., Li, P., Shang, Y., Jia, Y., Wei, J., Wang, K., Zhu, H., Wu, D., Zhang, S., and Cao, A., *Scientific reports,* **2012**. 2: p. 884.

[164] Švrček, V., Cook, S., Kazaoui, S., and Kondo, M., *The Journal of Physical Chemistry Letters,* **2011**. 2(14): p. 1646-1650.

[165] Bindl, D.J., Wu, M.-Y., Prehn, F.C., and Arnold, M.S., *Nano Letters,* **2011**. 11(2): p. 455-460.

[166] Bindl, D.J., Brewer, A.S., and Arnold, M.S., *Nano Research,* **2011**. 4.

[167] Bindl, D.J., Safron, N.S., and Arnold, M.S., *ACS nano,* **2010**. 4: p. 5657-5664.

[168] Sandanayaka, A.S.D., Maligaspe, E., Hasobe, T., Ito, O., and D'Souza, F., *Chemical Communications,* **2010**. 46(46): p. 8749-8751.

[169] Mehlenbacher, R.D., Wu, M.-Y., Grechko, M., Laaser, J.E., Arnold, M.S., and Zanni, M.T., *Nano Letters,* **2013**. 13(4): p. 1495-1501.

[170] Bindl, D.J., Shea, M.J., and Arnold, M.S., *Chemical Physics,* **2012**. 413: p. 29-34.

[171] Jain, R.M., Howden, R., Tvrdy, K., Shimizu, S., Hilmer, A.J., McNicholas, T.P., Gleason, K.K., and Strano, M.S., *Advanced Materials,* **2012**. 24(32): p. 4436-9.

[172] Bindl, D.J. and Arnold, M.S., *The Journal of Physical Chemistry C,* **2013**. 117(5): p. 2390-2395.

[173] Tung, V.C., Huang, J.-H., Kim, J., Smith, A.J., Chu, C.-W., and Huang, J., *Energy & Environmental Science,* **2012**. 5(7): p. 7810-7818.

Chapter 2
SWCNT working electrodes for dye sensitised solar cells

This chapter reports key findings from preliminary investigations of the photovoltaic properties of a new working electrode for dye sensitised solar cells. The electrode consisted of networks of covalently bound SWCNTs on ITO. Following covalent sensitisation of the SWCNT networks with a ruthenium dye an appreciable cathodic photocurrent was measured upon illumination with simulated sunlight. By building up sequential layers of SWCNTs cross-linked with ethylenediamine (EDA) to form a three dimensional dye sensitised SWCNT network, significant increases in photocurrent density were observed. Such electrodes may be promising for the future fabrication of low cost solar cells.

2.1 Introduction

SWCNTs have attracted interest across a diverse range of fields including microelectronics[1-3], medicine[4-7], energetic materials[8-9], polymers[10-12], energy storage[13-14] and more recently, light harvesting.[15-22] The electrical conductivity of SWCNTs, combined with their very large surface area to volume ratio, makes them a potential alternative scaffold material for photoactive sensitisers in photoelectrochemical DSCs based on the O'Regan/Grätzel architecture.[23] Replacement of the titania in these cells with SWCNTs is expected to increase the surface area per volume for dye attachment and perhaps provide an improved electrical pathway. The potential benefits of SWCNT based architectures for this application have been previously reported. For example, it has recently been shown that photoactive porphyrins coordinated to SWCNT arrays increase absorption of visible light and provide excellent electron transport.[16] Lee, Yoo and co-workers have used MWCNTs as a scaffold for covalently bound Ru(II) dye molecules and have additionally shown significant increases in the conversion efficiencies of TiO_2 solar cells by incorporating MWCNTs.[20-21] Lee, Han and co-workers have repeatedly shown increases in charge collection efficiencies of photoelectrochemical cells following incorporation of SWCNTs.[17, 19, 24] The increase has been shown to occur via suppression of electron-hole recombination and is largely independent of both the sensitiser used and the structure of the electrode surface.

It has been previously demonstrated that covalent attachment of SWCNTs to fluorine tin oxide (FTO) coated glass yields electrodes which produce photocurrent when incorporated into a photoelectrochemical cell.[25] However, the energy output of such a device is quite low due to the small amount of active material on the substrate. In this chapter, the amount of active material on the surface has been increased compared to previous reports via sequential addition of SWCNTs to form a random network. To achieve this, SWCNTs previously functionalised with carboxyl groups using a well-established technique[26] were covalently bound to

hydroxylated ITO coated glass by a simple condensation reaction. Subsequent addition of more SWCNTs was facilitated by an EDA linker, resulting in the formation of the three dimensional random network. Hybrid solar cell electrodes utilising dye sensitised SWCNTs were also fabricated in which networks of SWCNTs were used as a scaffold for ruthenium dye molecules which were covalently bound to the free end and side walls of the SWCNTs via EDA. Both the unsensitised and dye sensitised architectures were then used as the working electrode in solar cells.

2.2 Method

2.2.1 Preparation of functionalised SWCNT solutions

Arc-discharge SWCNTs (P2-SWCNT, Carbon Solutions Inc.) were refluxed for 24 hr in HNO_3 (3 M, 1 mg mL^{-1}) to dissolve any remaining catalyst and carbonaceous impurities and to increase the number of defect sites on the SWCNT sidewalls. The acid was then decanted and the SWCNTs were functionalised with carboxyl groups by ultrasonication at 50 W_{RMS} for 8 hr in a 3:1 v/v solution of 98 % H_2SO_4 and 70 % HNO_3 at a concentration of 1 mg mL^{-1}. The temperature was maintained at ~ 5 °C throughout the reaction. The acid/SWCNT mixture was then poured into 1 L of deionised (DI) water (pH 5.5, ~ 5 °C), filtered through 0.45 μm polycarbonate membrane filters (HTTP, MilliPore) and washed with DI water until the pH of the filtrate stabilised at 5.5. The filtered SWCNTs were dried in air at 80 °C for 24 hr then added at a concentration of 0.2 mg mL^{-1} to a solution of dimethylsulphoxide (DMSO) (99.9 %, Sigma-Aldrich) containing N,N′-dicyclohexylcarbodiimide (DCC) (0.2 mg mL^{-1}, 99 % Fluka Production GmbH) and 4-dimethylaminopyridine (DMAP) (0.05 mg mL^{-1}, Sigma-Aldrich). A suspension of SWCNTs was produced from this mixture by ultrasonication at 50 W_{RMS} for 1 hr under nitrogen and was then used immediately.

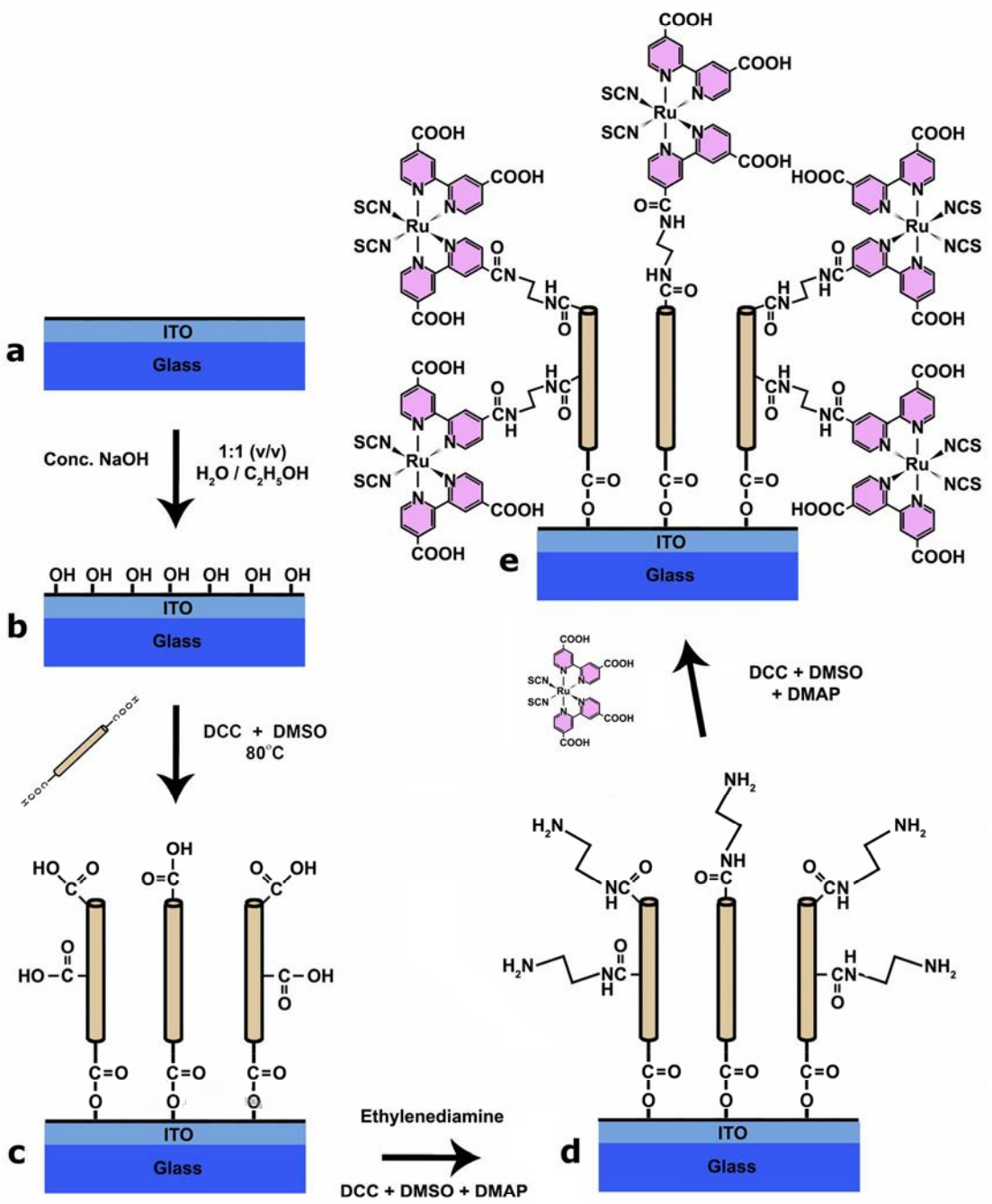

Figure 2.1 Reaction pathway beginning with (a) ITO coated glass which is (b) hydroxylated and then (c) SWCNTs are added. To these are attached (d) EDA linker molecules which facilitate (e) addition of the N3 dye sensitiser.

2.2.2 SWCNT attachment to ITO

The preparation of SWCNT on ITO is shown schematically in **Figure 2.1**(a-c). ITO coated glass slides (Sigma-Aldrich) with a sheet resistance of 8 - 12 Ω sq^{-1} and film thickness of 120 - 160 nm were cut into 2 cm × 1.5 cm samples. All samples were ultrasonically cleaned for a period of 10 min each in DI water, ethanol and acetone. The ITO surfaces were then hydroxylated by ultrasonication for 10 min in a solution of 1:1 v/v ethanol and DI water saturated with sodium hydroxide.[27] The hydroxylated ITO surfaces were rinsed with a copious amount of DI water and dried under a stream of nitrogen. The samples were then immersed in the freshly prepared functionalised SWCNT suspension and maintained at 80 °C under nitrogen for 1 hr to produce ITO-SWCNT samples. Upon removal the samples were rinsed with DMSO followed by acetone and dried under a stream of nitrogen. The ITO-SWCNT samples were immersed in EDA (Sigma-Aldrich) containing DCC (0.2 mg mL^{-1}) and DMAP (0.05 mg mL^{-1}) at 50 °C for 30 min to produce ITO-SWCNT-EDA samples (**Figure 2.1**(d)). After rinsing with DI water and drying under a stream of nitrogen the samples were returned to the SWCNT solution and maintained at 80 °C under nitrogen for 1 hr to produce ITO-SWCNT-EDA-SWCNT samples (i.e. 2 treatments of SWCNT hereafter referred to as ITO-2-SWCNT). Rinsing followed by re-immersion in the above EDA solution at 50 °C for 30 min produced ITO-SWCNT-EDA-SWCNT-EDA (i.e. 2 treatments of SWCNT terminating in EDA, hereafter referred to as ITO-2-EDA) and the process was repeated for subsequent treatments. EDA terminated samples were immersed for 24 hr at 50°C in a DMSO solution containing DCC (0.2 mg mL^{-1}), DMAP (0.05 mg mL^{-1}) and a ruthenium dye (0.2 mg mL^{-1}) to produce ITO-x-SWCNT-N3 (**Figure 2.1**(e) and **Figure 2.1**(f)). The ruthenium dye used was (*cis*-bis(4,4-dicarboxy-2,2-bipyridine) dithiocyanato ruthenium(II)) (Ru535, Solaronix SA) first reported by Nazeeruddin et al.[28] and otherwise known as 'N3' Upon removal the samples were rinsed with DMSO and acetone then dried with a stream of nitrogen.

2.2.3 Atomic Force Microscopy (AFM)

AFM images were taken in air with a multimode head and Nanoscope IV controller (Digital Instruments, Veeco) operating in tapping mode using commercially silicon cantilevers (FESP series, Veeco) with resonance frequencies between 70 and 85 kHz. Topographic (height) images were obtained at a scan rate of 0.5 $\mu m\ s^{-1}$ with the parameters set point, amplitude and feedback control optimised for each sample. Digital Instruments' Nanoscope software version 6.14. was used to analyse surface properties such as roughness and to background subtract all images to a 3rd order polynomial.

2.2.4 Scanning Electron Microscopy (SEM)

High resolution images of the SWCNT electrodes in this chapter were obtained with an SEM (MX2500, CamScan Electron Optics Ltd) within an hour of preparation. Prior to imaging all samples were coated with 5 nm platinum using a sputter coater (Emitech K575X, Quorum Technologies) equipped with an in-situ quartz crystal microbalance (QCM).

2.2.5 UV-Visible Spectroscopy

Spectra were obtained on a Varian Cary 50 with a resolution of 2 nm. In all experiments the spectrum of the quartz cuvette was used as the baseline although additional subtraction of solvent spectra was performed where indicated.

2.2.6 Fabrication of DSC

The counter electrode used was FTO coated glass and platinum (5 nm) was deposited on the counter electrode surface. A thermoset plastic gasket (Surlyn™ - Solaronix SA) was placed between each ITO sample (24× 18 mm^2) and a similarly sized FTO counter electrode (**Figure 2.2**). The resulting device was maintained at 100 °C for 10 min to set the gasket. The active area was 150 ± 10 mm^2 with a rectangular geometry (15 mm x 10 mm). The electrolyte used was a solution of

1-propyl 3-methylimidazolium iodide (0.8 M), iodine (0.1 M) and benzimidazole (0.3 M) in 3-methoxypropionitrile (MPN) (all from Sigma-Aldrich) and the cell was hermetically sealed with a Surlyn™ thermoset polymer gasket. Note that no reflective material was used to seal the fill hole in the counter electrode to prevent double passing of incident light.

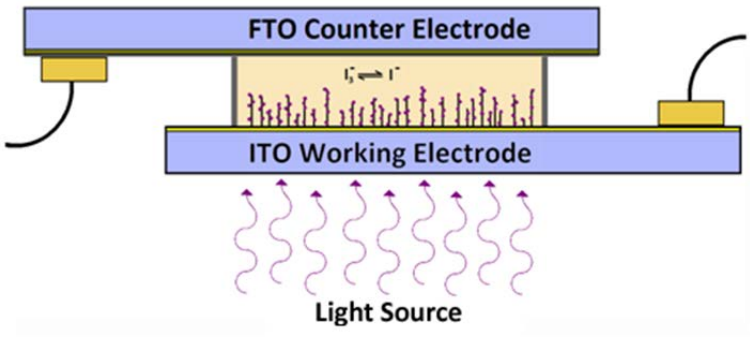

Figure 2.2 Schematic of a complete cell incorporating ITO-SWCNT-EDA-N3 (ITO-1-SWCNT-N3) as the working electrode.

2.2.7 Photovoltaic Performance Measurements

In this chapter, all cells tested were illuminated with a quartz arc lamp producing 25 mW cm^{-2} at the sample surface and all tests were conducted at 25 °C. Light was channelled to the cell through an optical fibre with 2 cm between fibre output and the cell which was aligned perpendicularly to the source. Light entered the cell through the ITO working electrode. Current-voltage data was collected on a Keithley 2400 Source Measure Unit (SMU) using a Digital Instruments LabView™ virtual instrument. The irradiance of the light source was measured using a NIST-calibrated photodiode (818-SL, Newport Corporation) with OD3 filter.

FF was calculated as $FF = \frac{J_{MP} \times V_{MP}}{J_{SC} \times V_{OC}}$ where MP denotes the maximum power point on the JV curve. PCE was calculated as $PCE = \frac{P_{MP}}{P_{in}} \times 100 = J_{MP} \times V_{MP}$ because the incident light intensity, P_{in} = 100 mW cm^{-2}.

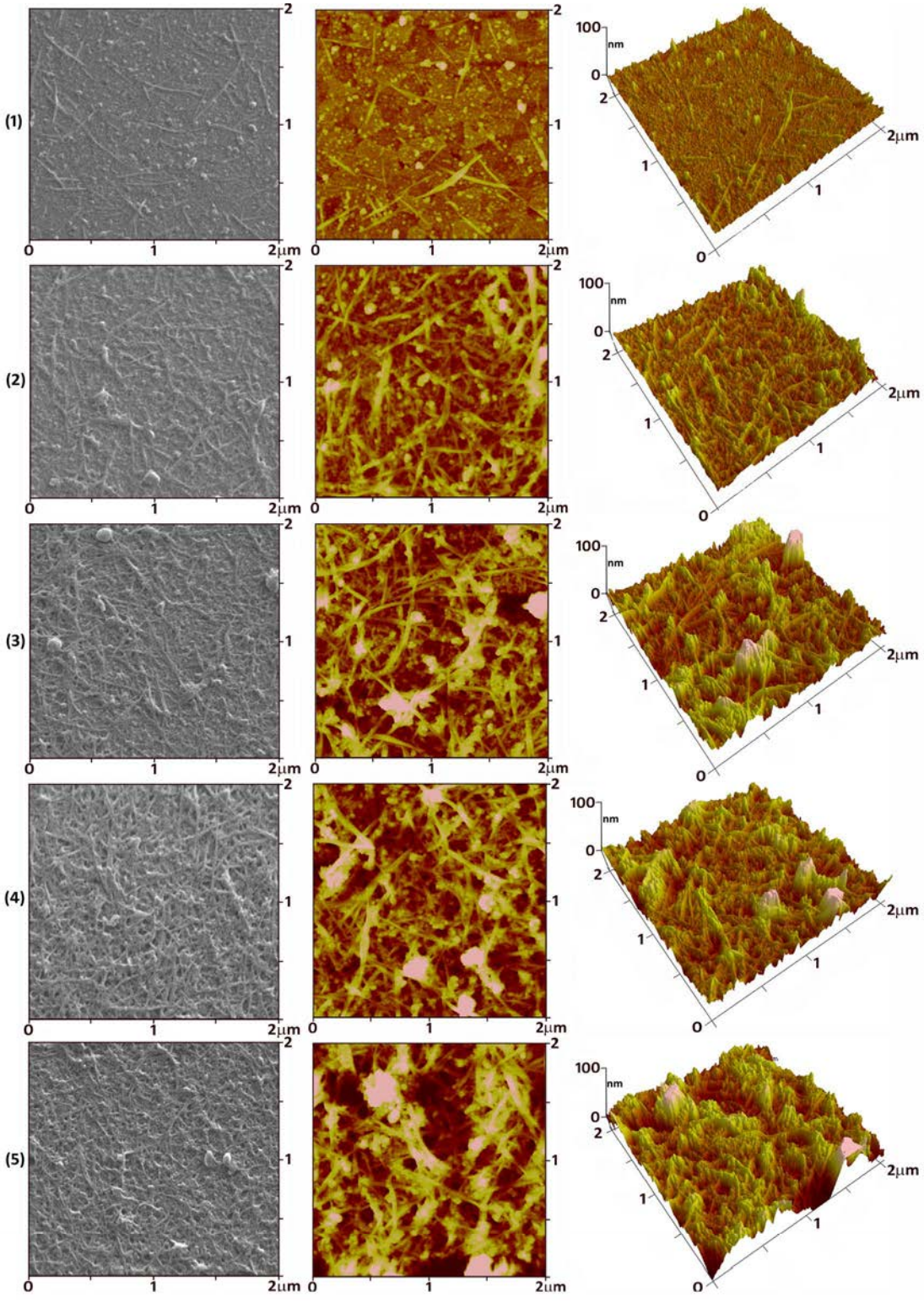

Figure 2.3 The SWCNT on ITO electrodes from 1 treatment (top) to 5 treatments (bottom). SEM images are shown in the left column, tapping mode AFM images are shown in the centre column and 3D representations of the AFM images are shown in the right column. The SEM and AFM images are not of the same location on the surface.

2.3 Results and Discussion

The morphology of the SWCNT on ITO electrode surfaces was investigated with AFM and SEM. Images showing electrodes with one to five treatments of SWCNTs are presented in **Figure 2.3**. There is no discernible difference between surfaces before and after treatment with EDA or dye. SWCNT bundle widths, obtained by measuring 25 bundles from each of four separate AFM images (100 bundles in total) were found to be 24 ± 7 nm. The AFM images and their 3D representations show a mixture of horizontally and vertically oriented SWCNT bundles. In **Figure 2.3** the ITO substrate is visible in both AFM and SEM images of surfaces after one or two SWCNT treatments due to incomplete coverage but cannot be seen after the third treatment as the cross-linked SWCNT network becomes denser. Correspondingly, the surface area increases for the first three SWCNT treatments but then plateaus (**Figure 2.4**). This is interpreted to mean that full coverage of the surface is achieved with three treatments, after which the network increases in thickness. The total surface area of the SWCNT network is increasing but the AFM tip can only penetrate so far into it, hence the plateau. Amorphous carbonaceous impurities remaining from the acid oxidation are also present and observed in the images as bright globules.

The sheet resistance of the ITO glass used in this work was measured with a two point probe to be 11 $\Omega\,sq^{-1}$ which is in accordance with the manufacturer specifications of 8-12 $\Omega\,sq^{-1}$. The same measurement protocol was used to measure the sheet resistance of each unsensitised SWCNT electrode giving values of 21 $\Omega\,sq^{-1}$, 23 $\Omega\,sq^{-1}$, 24 $\Omega\,sq^{-1}$, 26 $\Omega\,sq^{-1}$ and 28 $\Omega\,sq^{-1}$ for electrodes with 1-5 treatments of SWCNTs, respectively. This increase is consistent with a model in which sheet resistance is controlled by the number and type of junctions between SWCNTs and agrees well with the findings of Nirmalraj et al.[29] for acid treated SWCNT films. The sheet resistances of the dye sensitised SWCNT electrodes were 28 $\Omega\,sq^{-1}$, 29 $\Omega\,sq^{-1}$, 31 $\Omega\,sq^{-1}$, 33 $\Omega\,sq^{-1}$ and 35 $\Omega\,sq^{-1}$ for 1-5 treatments,

respectively. The marginally higher values for the dye sensitised electrodes are anticipated due to the slightly insulating effect of the EDA functionalisation.

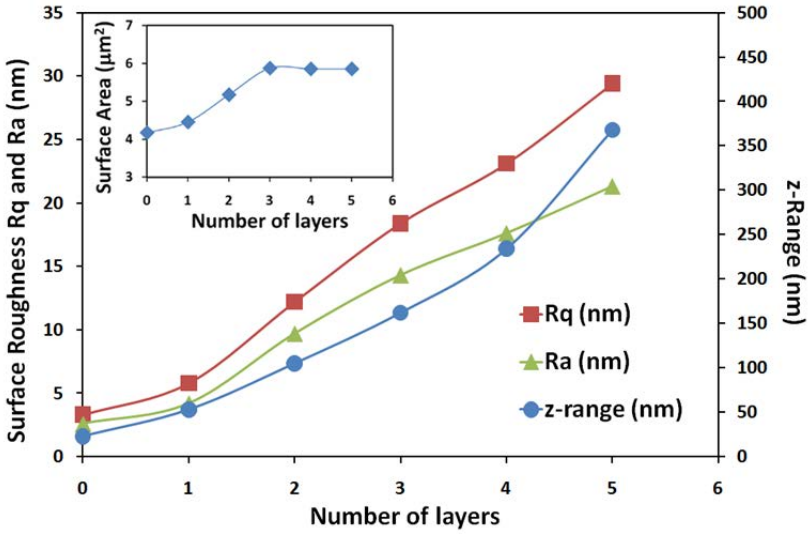

Figure 2.4 Surface analysis of the layered SWCNT electrodes taken from AFM images shown in Figure 3. Plots show the variation in *z*-range, RMS roughness (R_q) and mean roughness (R_a) with increasing treatments of SWCNTs. **Inset** shows the variation in surface area with subsequent SWCNT treatments.

UV-Visible spectra were recorded for the SWCNT electrodes prior to dye sensitisation, as shown in **Figure 2.5** (A-E). A broad increase in absorbance with additional treatments of SWCNTs can be clearly seen. A plot of absorbance versus the number of treatments yields a linear relationship at all wavelengths. However the slope of this relationship is greater at the positions of the absorbance maxima. The height of these maxima, taken as a percentage of the background, decreases with each successive treatment of SWCNTs. This indicates that with each additional treatment the scattering process (the background) becomes increasingly dominant with respect to the electronic excitation processes (the maxima).

The unsensitised SWCNT electrodes show a broad absorbance centred at ~ 460 nm, a much smaller one at ~ 750 nm and another broad absorbance centred at ~ 1050 nm. The positions of these absorption maxima agree well with the work of Fluerier et al.[30] using the same arc-discharge P2-SWCNT from Carbon Solutions, Inc. The absorbance at 1050 nm is attributed to v_2 - c_2 (S_{22}) interband transitions in

the DOS of s-SWCNTs. The low energy v_1 - c_1 (S_{11}) transitions near 1800 nm were not probed in this work. The presence of the absorbance at ~ 750 nm is characteristic of the primary M_{11} optical transition within m-SWCNTs. The presence of m-SWCNTs was unexpected in this work since the oxidative treatment in concentrated mixed acid under ultrasonication is generally thought to remove metallic characteristics from mixtures of m-SWCNTs and s-SWCNTs.[31-32]

The absorbance maximum ~ 460 nm is not present in UV-Vis spectra of the carboxylated SWCNTs in DMSO (**Figure 2.5**(F)), the ITO glass (**Figure 2.5**(H)) or when the hydroxylated ITO is immersed in the SWCNT solution without coupling agent (**Figure 2.5**(G)). This absorbance maximum must therefore be a property of the interface between the SWCNTs and the ITO. It may be that the covalent bonding between these two different semiconducting materials leads to the formation of a newly accessible electronic transition (at ~ 460 nm) in the region where the DOS of the two materials combine. The presence of this broad absorption maximum extending through the visible region of ~ 350 nm to ~ 600 nm could help to explain why the SWCNT-only cells are photoactive without any dye sensitisation. Other possible explanations include light scattering or reflectance, a change in ITO doping or stoichiometry, or thin film optical interference effects.

UV-Vis spectra were also recorded for the SWCNT electrodes after dye sensitisation. Compared to the spectra of the unsensitised SWCNT electrodes, they show a broad increase of ~ 3 - 5 % absorbance across all wavelengths. Difference spectra produced by subtracting ITO-x-SWCNT from ITO-x-SWCNT-N3 (where x is the number of treatments) display two distinct peaks at ~ 525 nm and ~ 380 nm as shown in **Figure 2.6**(a). This correlates very well with the UV-Vis spectrum of the N3 ruthenium dye shown in **Figure 2.6**(b), which displays two characteristic absorbance maxima at ~ 540 nm and ~ 405 nm corresponding to the two separate metal-to-ligand charge transfer (MLCT) pathways between the ruthenium centre and its dual bipyridine and thiocyanate ligands.[28, 33] There is a shift of the MLCT bands which can be attributed to the effect of the DMSO solvent used to obtain the

absorption spectrum of the dye compared to that of the SWCNT electrode which was obtained in air. SWCNTs display a strong absorbance near 260 nm due to π-π* transitions characteristic of extended aromatic systems[34] hence the high energy intraligand (π-π*) charge-transfer transitions of the dye near 300 nm were not measurable.

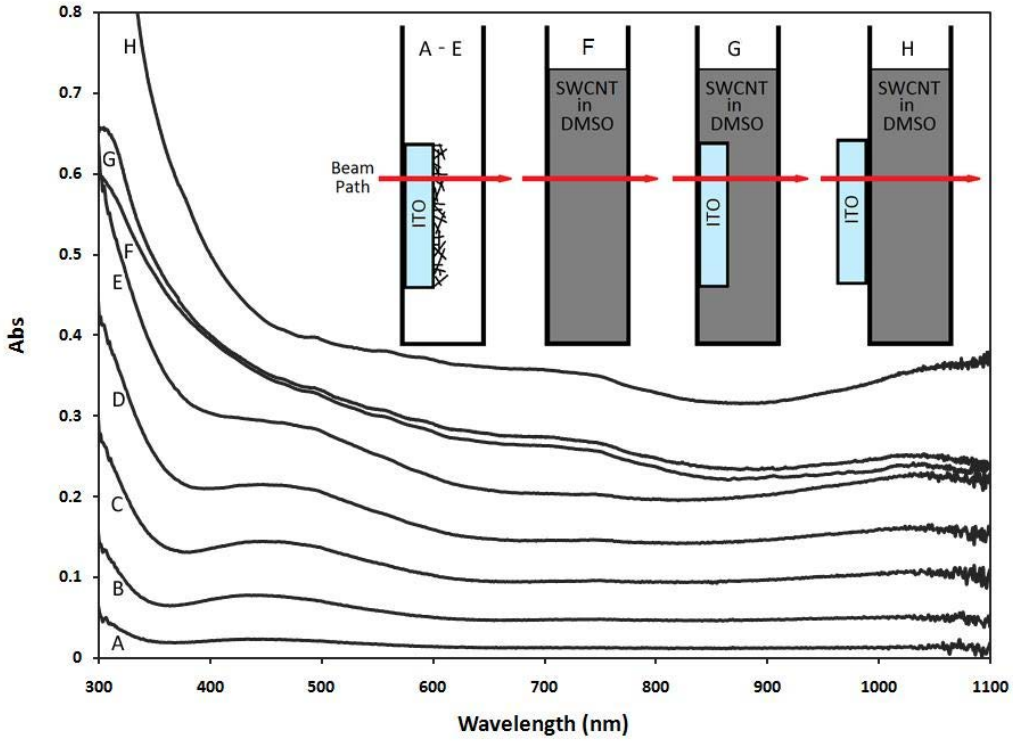

Figure 2.5 UV-Vis spectra of the layered SWCNT electrodes and control experiments; (A) ITO-1-SWCNT, (B) ITO-2-SWCNT, (C) ITO-3-SWCNT, (D) ITO-4-SWCNT, (E) ITO-5-SWCNT, (F) SWCNT in DMSO, (G) clean ITO internal, (H) clean ITO external. For (A-E) the beam passed through the quartz cuvette and the functionalised ITO sample; the quartz spectrum was removed as background. For (F) the beam passed through a quartz cuvette containing SWCNT in DMSO; the quartz + DMSO spectrum was removed as background. For (G) and (H) the beam passed through a quartz cuvette containing SWCNT in DMSO with a clean ITO sample either in contact with the solution (G) or external to the cuvette (H) and the quartz + DMSO spectrum was removed as background. Of note is the broad absorbance from ~ 350 nm to ~ 600 nm present only in (A-E). The greater absorbance displayed in (F), (G) and (H) is attributed to the larger number of SWCNTs sampled in solution than on the ITO surfaces in (A-E). The even higher absorbance displayed in (H) is due to additional scattering at the air-filled ITO/quartz interface.

The photovoltaic performance of solar cells fabricated using both sensitised and unsensitised SWCNT electrodes is presented in **Figure 2.7**(a), **Figure 2.7**(b) and **Table 1**. Importantly, the observed photocurrent of the SWCNT-based DSC flows

in the reverse direction to conventional DSCs i.e. they display a cathodic photocurrent. In titania-based cells the excited dye injects photo-generated electrons into the conduction band of the titania with the resultant holes in the dye being filled by oxidation of triiodide to iodide. In these SWCNT-based cells, photo-generated electrons must reduce the iodide to triiodide with resultant holes being refilled by electrons returning from the external circuit via the ITO and SWCNTs. This reversal of photocurrent is certainly a result of a substantial difference in the potential of SWCNTs conduction band(s) compared to that of titania and suggests a markedly different mechanism of electron transfer within and between the components of the DSC.

The dye sensitised electrodes (ITO-x-SWCNT-N3) also display a cathodic photocurrent indicating that electrons flow both directly from SWCNTs to the electrolyte (as before) and additionally now via the dye. However, dye sensitisation of the SWCNT electrodes after any number of treatments examined in this work does increase the magnitude of the observed photocurrent density (**Figure 2.7**(b)). For a single treatment of SWCNTs the observed photocurrent density was 2.0 μA cm^{-2} which is increased to 2.8 μA cm^{-2} by dye sensitisation – equating to a gain of 40 % (**Table 1**). Upon addition of further layers of SWCNT and EDA without dye sensitisation, additional increases in photocurrent density are observed up to a maximum of 4.9 μA cm^{-2} for five treatments. For the dye sensitised electrodes the increase is approximately linear with additional SWCNT treatments up to a maximum of 6.2 μA cm^{-2} for five treatments. For the SWCNT-only electrodes the increase is linear up to three treatments but then appears to approach a saturation level. This is likely due to an increased occurrence of electron-hole recombination in the denser networks due to (a) the increased distance between the point of photo-generation of charge carriers and the ITO electrode and/or (b) the greater number of (insulating) EDA links that must be traversed by the carriers or (c) scattering from the SWCNTs near the surface which means excitation of the SWCNTs further from the surface is limited.

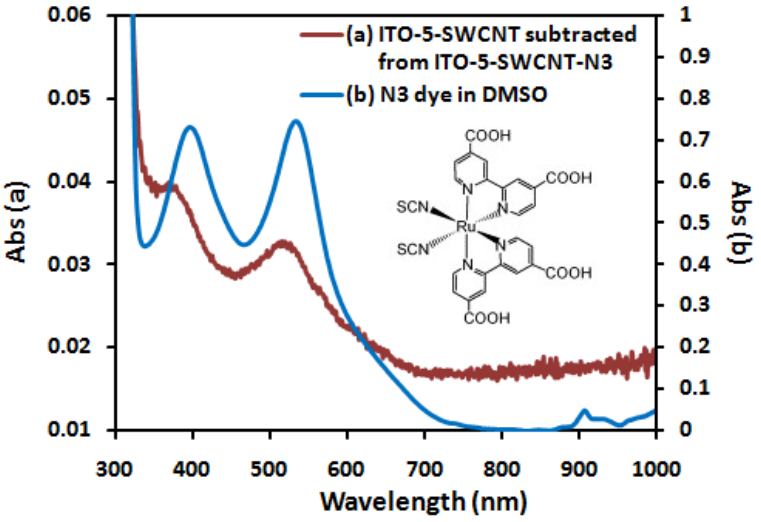

Figure 2.6 (a) The difference spectrum produced by subtracting ITO-3-SWCNT from ITO-3-SWCNT-N3 and (b) UV-Vis spectrum of the N3 ruthenium dye in DMSO. **Inset** shows the N3 molecular structure.

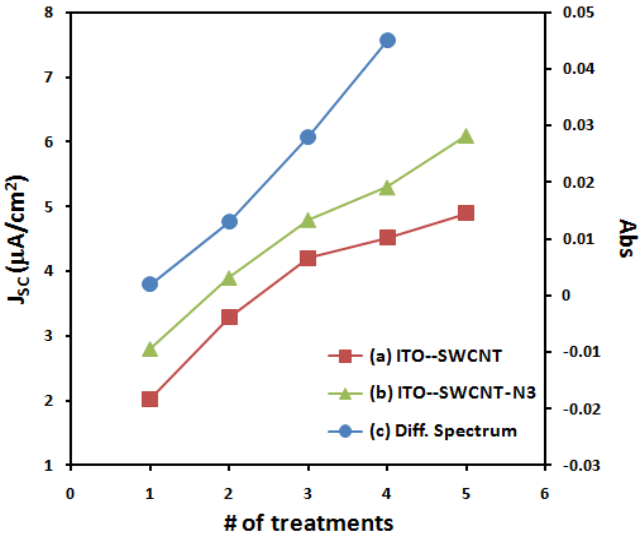

Figure 2.7 (a) Increase of J_{SC} with increasing number of SWCNT treatments without dye sensitisation, (b) Increase of J_{SC} with increasing number of SWCNT treatments with dye sensitisation, (c) Increase in the UV-Visible absorbance (at 450 nm) of difference spectra produced by subtracting the spectra of ITO-x-SWCNT from the spectra of ITO-x-SWCNT-N3. The standard deviation in each measurement is contained within the data points.

Addition of the N3 dye opens up a second mechanism for the generation of charge carriers - excitation of the dye. After dye excitation the two possible routes for the charge carriers are through the SWCNTs or direct transfer to the electrolyte. In all cases introduction of the dye increases the photocurrent observed. However, the magnitude of the increase in photocurrent density upon dye sensitisation is a constant for the first three treatments of SWCNTs but begins to increase for the fourth and fifth. This suggests that for the first three treatments the total number of attached dye molecules does not increase. However the difference in UV-Vis absorbance (at 450 nm) between the dye sensitised and SWCNT-only electrodes (**Figure 2.7**(c)), taken as a direct measure of the amount of dye on the surface, increased approximately linearly from ~ 0.2 for one treatment up to ~ 4.5 for four treatments. Therefore, further treatments subsequent to the first, increase the number of available sites for dye attachment and hence the amount of dye on the surface.

This increasing amount of dye is not reflected in the observed photocurrent for the first three treatments. This may be due to the position of the dye in the networks. It is well known that the ends of SWCNTs are more reactive and hence the location where one would expect the attachment of the dye. When there are few SWCNTs present as is the case for few treatments, one would expect a large fraction of the dye to be on the ends of the SWCNTs. Charge carriers are transported down the length of SWCNT much more efficiently than through the sidewalls.[35] Thus, for a few treatments, charge carriers generated by excitation of the dye will be very likely to transfer to the SWCNT where the electron-hole recombination within the EDA cross-linked networks discussed earlier will play an important role and limit the photocurrent produced. With four and five treatments it is likely that some of the ends of the SWCNTs will be unavailable for reaction and the increased surface area will mean more side wall defect sites will be available as points of attachment for dye molecules. Thus, now a large fraction of the dye molecules will be on the side walls of SWCNTs where transfer of the charge carriers to SWCNTs will be much harder. This will mean an increased rate of carriers transferred directly to the electrolyte

increasing the photocurrent observed. This indicates that charge separation due to the dye is beginning to dominate that occurring within the SWCNTs. An alternative possibility is that the large fraction of dye molecules at the SWNT-ends leads to formation of dye aggregates which could generate losses and so compete with charge transport. In contrast, along the SWNT sidewalls, the density of defects is less than at the nanotube ends, therefore fewer dyes attach and presumably lower amounts of dye aggregation occurs. Thus dyes attached to the sidewalls could potentially be more efficient in their charge transfer (relative to the SWNT ends).

Table 1 Photovoltaic properties of the SWCNT network electrodes.

Cell	V_{OC} (mV)	J_{SC} ($\mu A\ cm^{-2}$)	FF
ITO-1-SWCNT	47	2.0	0.28
ITO-2-SWCNT	46	3.3	0.30
ITO-3-SWCNT	44	4.2	0.32
ITO-4-SWCNT	43	4.5	0.31
ITO-5-SWCNT	43	4.9	0.31
ITO-1-SWCNT-N3	43	2.8	0.28
ITO-2-SWCNT-N3	41	3.9	0.27
ITO-3-SWCNT-N3	41	4.8	0.29
ITO-4-SWCNT-N3	39	5.3	0.32
ITO-5-SWCNT-N3	36	6.2	0.29

The voltages produced by the cells are on the order of mV, likely due to a combination of factors; incomplete coverage of the electrode surface, a significant back reaction caused by low shunt resistance at the ITO and/or SWCNT surfaces, electron-hole recombination within the network, poor matching of SWCNT and dye - effectively a high series resistance, and poor matching of SWCNT and electrolyte potentials limiting the maximum obtainable voltage. The SWCNTs used in this work are a combination of m-SWCNTs and s-SWCNTs and it is expected that the m-SWCNTs would lower the potential of the entire network by providing sites for exciton recombination. All these factors also contribute to the modest FF of ~ 0.3 for all the electrodes produced in this work. Of course, the quantity of photoactive material on the surface is miniscule compared to that in conventional DSCs so it was not expected that the power generated would be comparable.

The low photocurrent densities in the μA range can be attributed in part to the small quantities of material on the surface (the SWCNT networks are only a few microns thick) but also largely to charge recombination occurring either within the network or within the SWCNTs themselves. On comparison of J_{SC} and variations in UV-Vis absorption between cells with either a single treatment of unsensitised SWCNTs or two treatments, it is seen that while J_{SC} increased from 2.0 μA cm^{-2} to 3.3 μA cm^{-2}, a gain of 65 %, the UV-Vis absorption (at 500 nm) increased from 0.021 - 0.069, a gain of 228 %. A simple model takes the UV-Vis absorption as a measure of the amount of SWCNT on the surface, including both absorption and scattering. The disparity between the increases in J_{SC} and UV-Vis absorption with additional SWCNT treatments indicates a substantial drop in conversion efficiency going from one treatment of SWCNTs to two, and the trend is continued with subsequent treatments. Furthermore, it also suggests that charge recombination is more prevalent in the networks than in the individual SWCNTs.

2.4 Summary

Photoelectrochemical cells fabricated from SWCNTs covalently bound to ITO and sensitised with a Ru(II) dye have been produced and characterised. Randomly dispersed networks created by sequential treatments with SWCNTs and EDA were shown to increase the quantity of dye attached thus improving photocurrent density. Measurements from the unsensitised SWCNT electrodes (no dye) confirm that SWCNT networks on ITO are themselves photoactive with spectral evidence showing a broad absorbance spanning the visible region. The photovoltaic performance of solar cells containing both dye sensitised SWCNT and SWCNT-only electrodes was measured showing an appreciable, photoresponse. The source of the low power generated compared to conventional titania-based DSCs is largely due to far less photoactive material being present on the electrode surface, although a significant mismatch of potential energy levels between the different components of the cells is also implicated. A markedly reduced FF indicates substantial recombination within the cells. Both the dye sensitised and SWCNT-only network

based photoelectrochemical cells reported in this work may be promising for future low cost solar cell applications if the underlying mechanism of action is further understood. However, given the poor performance of this system, work was refocussed onto a new architecture.

2.5 References

[1] Ryu, K., Badmaev, A., Wang, C., Lin, A., Patil, N., Gomez, L., Kumar, A., Mitra, S., Wong, H.S.P., and Zhou, C., *Nano Letters,* **2008**. 9(1): p. 189-197.

[2] Yu, J., Shapter, J.G., Quinton, J.S., Johnston, M.R., and Beattie, D.A., *Physical Chemistry Chemical Physics,* **2007**. 9(4): p. 510-520.

[3] Flavel, B.S., Yu, J., Shapter, J.G., and Quinton, J.S., *Electrochimica Acta,* **2008**. 53(18): p. 5653-5659.

[4] Bin, K., Decai, Y., Yaodong, D., Shuquan, C., Da, C., and Yitao, D., *Small,* **2009**. 5(11): p. 1292-1301.

[5] Yusof, A.M., Buang, N.A., Yean, L.S., and Ibrahim, M.L. *The use of multi-walled carbon nanotubes as possible carrier in drug delivery system for aspirin*. in *Nanoscience & Nanotechnology: International Conference on Nanoscience and Nanotechnology*. 2009. Shah Alam, Selandor (Malaysia): AIP.

[6] Lynam, C., Gilmartin, N., Minett, A.I., O'Kennedy, R., and Wallace, G., *Carbon,* **2009**. 47(10): p. 2337-2343.

[7] Wang, J., Deng, X., Yang, S., Wang, H., Zhao, Y., and Liu, Y., *Nanotoxicology,* **2008**. 2(1): p. 28 - 32.

[8] Tseng, S.H., Tai, N.H., Hsu, W.K., Chen, L.J., Wang, J.H., Chiu, C.C., Lee, C.Y., Chou, L.J., and Leou, K.C., *Carbon,* **2007**. 45(5): p. 958-964.

[9] Kang, B., Dai, Y., Chang, S., and Chen, D., *Carbon,* **2008**. 46(6): p. 978-981.

[10] Liu, L., Barber, A.H., Nuriel, S., and Wagner, H.D., *Advanced Functional Materials,* **2005**. 15(6): p. 975-980.

[11] Coleman, J.N., Khan, U., Blau, W.J., and Gun'ko, Y.K., *Carbon,* **2006**. 44(9): p. 1624-1652.

[12] Zhang, J., Han, H., Wu, S., Xu, S., Yang, Y., Zhou, C., and Zhao, X., *Solid State Ionics,* **2007**. 178(29-30): p. 1595-1601.

[13] Hirscher, M., Buschow, K.H.J., Robert, W.C., Merton, C.F., Bernard, I., Edward, J.K., Subhash, M., and Patrick, V., *Hydrogen absorption in carbon nanotubes: A critical review*, in *Encyclopedia of materials: Science and technology*. 2006, Elsevier: Oxford. p. 1-4.

[14] Chen, Y., Wang, P., Liu, C., and Cheng, H.-M., *International Journal of Hydrogen Energy,* **2007**. 32(9): p. 1262-1268.

[15] Ugawa, A., Hwang, J., Gommans, H.H., Tashiro, H., Rinzler, A.G., and Tanner, D.B., *Current Applied Physics,* **2001**. 1(1): p. 45-49.

[16] Yu, J., Mathew, S., Flavel, B.S., Johnston, M.R., and Shapter, J.G., *Journal of the American Chemical Society,* **2008**. 130(27): p. 8788-8796.

[17] Lee, W., Jungwoo, L., Sangjin, L., Whikun, Y., Sung-Hwan, H., and Byung Won, C., *Applied Physics Letters,* **2008**. 92(15): p. 153510-153513.

[18] Ulbricht, R., Lee, S.B., Jiang, X., Inoue, K., Zhang, M., Fang, S., Baughman, R.H., and Zakhidov, A.A., *Solar Energy Materials and Solar Cells,* **2007**. 91(5): p. 416-419.

[19] Lee, W., Lee, J., Lee, S.H., Chang, J., Yi, W., and Han, S.H., *J. Phys. Chem. C,* **2007**. 111(26): p. 9110-9115.

[20] Lee, T.Y., Alegaonkar, P.S., and Yoo, J.-B., *Thin Solid Films,* **2007**. 515(12): p. 5131-5135.

[21] Lee, T.Y. and Yoo, J.-B., *Diamond and Related Materials,* **2005**. 14(11-12): p. 1888-1890.

[22] Camacho, R.E., Morgan, A.R., Flores, M.C., and McLeod, T.A., *JOM,* **2007**. 59(3): p. 39-42.

[23] O'Regan, B. and Gratzel, M., *Nature,* **1991**. 353(6346): p. 737-740.

[24] Lee, W., Jungwoo, L., Haiwon, L., Whikun, Y., and Sung-Hwan, H., *Applied Physics Letters,* **2007**. 91(4): p. 043515-043518.

[25] Bissett, M.A. and Shapter, J.G., *Journal of Physical Chemistry C,* **2010**. 114(14): p. 6778-6783.

[26] Marshall, M.W., Popa-Nita, S., and Shapter, J.G., *Carbon,* **2006**. 44(7): p. 1137-1141.

[27] Huang, M.e.a., *Chemical Communications,* **2005**. 44: p. 5560-5562.

[28] Nazeeruddin, M.K., Kay, A., Rodicio, I., Humphry-Baker, R., Mueller, E., Liska, P., Vlachopoulos, N., and Graetzel, M., *Journal of the American Chemical Society,* **1993**. 115(14): p. 6382-6390.

[29] Nirmalraj, P.N., Lyons, P.E., De, S., Coleman, J.N., and Boland, J.J., *Nano Letters,* **2009**. 10.1021/nl9020914.

[30] Fleurier, R., Lauret, J.-S., Lopez, U., and Loiseau, A., *Advanced Functional Materials,* **2009**. 19(14): p. 2219-2223.

[31] Zhang, Z.-B., Li, J., Cabezas, A.L., and Zhang, S.-L., *Chemical Physics Letters,* **2009**. 476(4-6): p. 258-261.

[32] Yang, C.-M., Park, J.S., An, K.H., Lim, S.C., Seo, K., Kim, B., Park, K.A., Han, S., Park, C.Y., and Lee, Y.H., *The Journal of Physical Chemistry B,* **2005**. 109(41): p. 19242-19248.

[33] Nazeeruddin, M.K., Zakeeruddin, S.M., Humphry-Baker, R., Jirousek, M., Liska, P., Vlachopoulos, N., Shklover, V., Fischer, C.-H., and Gratzel, M., *Inorganic Chemistry,* **1999**. 38(26): p. 6298-6305.

[34] Saito, R., Dresselhaus, G., and Dresselhaus, M.S., eds. *Physical properties of carbon nanotubes*. 1998, Imperial College Press.

[35] Yu, J., Shapter, J.G., Johnston, M.R., Quinton, J.S., and Gooding, J.J., *Electrochimica Acta,* **2007**. 52(21): p. 6206-6211.

Chapter 3
SWCNT front electrodes for silicon solar cells

In this chapter, the results of measurements on solar cells made from randomly aligned thin films of SWCNTs on n-type monocrystalline silicon are presented. The films are made by vacuum filtration from aqueous TritonX-100 suspensions of large diameter arc-discharge SWCNTs. The dependence of the solar cell performance on the thickness of the SWCNT film is shown in detail, as is the variation in performance due to doping of the SWCNT film with $SOCl_2$.

3.1 Introduction

As demonstrated in Chapter 1, there has been considerable work already in the field of SWCNT-silicon heterojunction solar cells. Several reports deal in part with the electrical and optical characteristics of the SWCNT film.[1-8] Because of the large variety of SWCNT films reported in the literature, the methods of their preparation, deposition and treatment, as well as physical, electrical and optical characteristics, it can sometimes be difficult to ensure the validity of comparisons between different devices. This chapter outlines in detail the methods used in this thesis and relevant film characteristics. As in other reports, the performance of SWCNT-silicon solar cells fabricated with such films will be shown to depend very strongly on the optical density and conductivity of the film. In the simplest sense, the best films are those with both the highest transmittance and lowest resistance however there is often a trade-off needed in the assessment of film quality. The best of SWCNT films reported here (~700 Ω sq^{-1} for T_{av} = 90 %) were certainly better than many earlier examples such as the high density films in early reports by Li[3] (10 - 100 kΩ sq^{-1} for T_{550} = 90 %) but were outperformed by the latest in very highly aligned films (~10 Ω sq^{-1} for T_{550} = 90 %)[9] using a modification of the super acid method of Saha.[10] The same vacuum filtration method described here has been used throughout the thesis, including recent work, to maintain test consistency and allow less ambiguous comparison between results.

3.2 Method

Vacuum filtration films of SWCNTs were used to fabricate solar cells and also deposited on glass to allow optical characterisation and measurement of the sheet resistance. Additionally, nine different optical densities of film were made by using varying volumes of SWCNT suspension. Each complete solar cell was made in duplicate and solar cell parameters were averaged from both devices with the standard deviation displayed by error bars in the plotted data.

3.2.1 Preparation of SWCNT suspension

Arc-discharge SWCNTs (5 mg, P3-SWCNT, Carbon Solutions Inc) were bath sonicated at ~ 50 W_{RMS} for 1 hr in an aqueous solution of TritonX-100 (50 mL, 1 % v/v, Sigma). The resulting suspension was centrifuged in 6 x 8 mL tubes for 1 hr at 17,500 g. This first supernatant was collected, combined and then centrifuged for a further 1 hr at 17,500 g. The upper 6 mL of the second supernatant (of each 8 mL tube) was collected and combined to yield a (very slightly red) black suspension (36 mL). The centrifuge residues were combined, filtered onto a pre-weighed polycarbonate membrane (0.45 μm, HTTP, Millipore), rinsed thoroughly with 250 mL of DI water and then dried in air for 1 hr at 80°C. The final mass of the unwanted residue was 3.2 mg, giving a process yield (into the suspension) of 36 %. The yield could be improved by using a high powered tip sonicator however the bath sonicator was used to minimise damage to the SWCNTs.

3.2.2 SWCNT film formation by vacuum filtration

Randomly aligned SWCNT membranes were prepared similarly to Wu[11] and Hu.[12] Volumes of 25, 50, 75, 150, 225, 300, 375, 450 or 600 μL cm^{-2} of filter membrane of the SWCNT suspension described in section 3.2.1 were first diluted in 250 mL of a 0.01 % v/v solution of TritonX-100 in DI water and then filtered onto large pore mixed cellulose ester (MCE) 'target' membranes (0.45 μm, HAWP, Millipore) over a smaller pored 'stencil' membrane (25 nm, VSWP, Millipore). The very large difference in flow rates between target and stencil allows the fabrication of well-defined film shapes on the target membrane, all with identical characteristics. The films made this way are highly reproducible and the thickness/optical density are precisely controllable by varying the concentration and/or volume of SWCNT solution, with the additional benefit of minimising wastage of SWCNT material. However, to get good long term reproducibility and control of films' optical and sheet resistance characteristics, it was found that the same apparatus (glass filter frit, etc) must be used with the same vacuum applied and the concentration of surfactant and age/bundle state of the suspension must all be

well controlled. The SWCNT films were rinsed thoroughly with 3 x 50 mL DI water then a further 250 mL DI water. Circular regions (0.32 cm^2) of the resulting SWCNT-MCE membrane were taken for device fabrication.

3.2.3 Device fabrication

Phosphorous doped n-type silicon wafers (CZ, 5-25 Ω cm, <100>, SSP, ABC GmbH) with a thermal oxide (100 nm) were diced into rectangular pieces (1 x 1.5 cm^2). UV photolithography was used to define circular regions (0.08 cm^2) in a positive resist (AZ1518, micro resist technology GmbH), which was developed and then the front metal contact (Ti/Au, 5/145 nm) was sputtered.

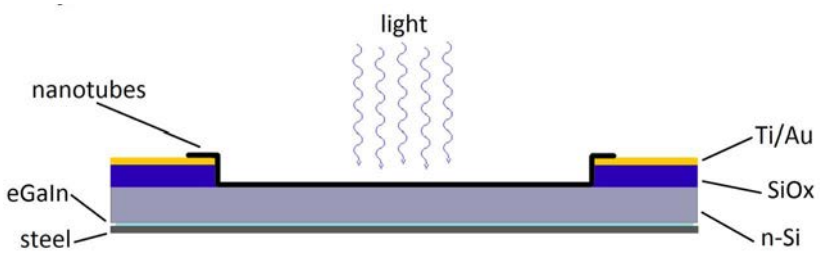

Figure 3.1 Schematic showing solar cell device structure.

Following photoresist lift off the 100 nm oxide in these regions was removed with buffered oxide etch (BOE). The SWCNT films were deposited onto the substrate surfaces by placing the circular SWCNT-MCE membranes, SWCNT side down, centred over the etched holes. The membranes were wetted with DI water then compressed and baked dry (80°C, 15 min). Following cooling, the substrates were immersed in acetone for 1 hr to dissolve the MCE. After being removed from this first acetone bath and dried with N_2, the devices were washed in a further 3 baths of fresh acetone for 1 hr each and with mild stirring of the solvent. After the final drying with N_2, substrates were obtained with SWCNT membranes tightly adsorbed onto their surfaces providing 0.08 cm^2 circular active areas surrounded by 0.24 cm^2 regions where the SWCNT membranes overlap the front metal contacts. After etching of the rear oxide the devices were completed with gallium indium eutectic (eGaIn) back contacts and mounted on steel plates (2 cm^2). The solar cells thus produced are called 'as-prepared', unless specified in the text.

3.2.4 Characterisation

UV-Visible-NIR absorbance spectra of the SWCNT films were measured using a spectrophotometer (Cary50, Varian) by passing the beam through films mounted on glass. Simple background subtraction was performed using the absorbance spectra of the glass substrates. Transmittance spectra were calculated post-measurement from the absorbance data. Sheet resistance measurements were taken from the same films using a four point probe (KeithLink) in linear geometry and a multimeter (GDM-8261, GW Instek).

The method used to calculate a reliable measure of the average optical depth is shown in detail in Chapter 5 where it is particularly important in the metallic/semiconducting SWCNT comparisons. Briefly, the absorbance was averaged from two points chosen so as to be outside the range of the SWCNT absorption peaks. This is because those regions are subject to large changes due to post fabrication film treatments, which would skew the absorbance values. For these large diameter arc-discharge SWCNTs the two wavelengths were 450 nm and 850 nm and the negative log of their average absorbance is the average transmittance i.e. $T_{av} = 10^{-x}$ where $x = (Abs_{450} + Abs_{850}) / 2$

Current-voltage data was collected with a Keithley 2400 source measure unit (SMU) and recorded using a custom Labview™ virtual instrument (see Appendix 2). For light experiments the cells were illuminated by collimated 100 mW cm^{-2} light from a xenon-arc source passed through an AM1.5G filter. The irradiance at the sample plane was measured with a silicon reference cell (PV Measurements, NIST-traceable calibration). Data was obtained by scanning from 1 V to -1 V and several curves were taken to verify the stability of the output characteristics.

The solar cell light IV parameters J_{SC}, V_{OC}, FF, and PCE were found as in section 2.2.8 and the series resistance (R_S) and shunt resistance (R_{SH}) were estimated from the inverse slopes of the light IV curves at V_{OC} and J_{SC}, respectively. The dark current characteristics were analysed using the diode equation;[14]

$$J = J_0 \left[e^{\frac{qV}{nkT}} - 1 \right] \qquad \textbf{Equation 3.1}$$

where J_0 is the reverse saturation current density, V the applied potential, q the elementary charge, k the Boltzmann constant, T the absolute temperature and n the ideality factor. For V > kT/q, the -1 term can be dropped since the exponential term becomes >>1. Taking the natural logarithm of both sides gives;

$$\ln J = \left(\frac{q}{nkT} \right) V + \ln J_0 \qquad \textbf{Equation 3.2}$$

Thus the semilog plot of the current-voltage data (*lnJ* vs. *V)* yields *n* and J_0 from the slope and intercept, respectively. This method works well for close-to-ideal diodes however in some of the SWCNT-silicon test cells the voltage drop due to high parasitic series resistance cannot be ignored. Thus, Equation 3.1 can be modified to give;[13]

$$J = J_0 \left[e^{\frac{q(V - JAR_S)}{nkT}} - 1 \right] \qquad \textbf{Equation 3.3}$$

where A is the active area of the junction and R_s is the combined series resistances of the device. In this case a plot of *lnJ* vs. (V-JAR_S) can be more accurate, assuming a reliable measure of the series resistance can be made. It can be estimated from the light JV data but possible light-induced effects must be taken into account. Another way to determine R_s, that will be used in Chapter 6 but which assumes a Schottky diode,[14] is to take the logarithm of Equation 3.3, differentiate with respect to J and rearrange terms to give;

$$\frac{d(V)}{d(\ln J)} = R_S A J + \frac{n}{\beta} \qquad \textbf{Equation 3.4}$$

where $\beta = kT/q$ and a plot of $d(V)/d(lnJ)$ vs. J yields the series resistance and a self-consistency check of the ideality factor from the slope and intercept, respectively. Regardless, as with all modelling of real data, it must be done with a good idea of what should be expected and an understanding of the limitations and alternatives of the model used.

3.2.5 Film treatments applied post fabrication

After characterisation, the as prepared devices were treated for 15 s with 2 % hydrofluoric acid (HF) to remove the native oxide. This was done by placing a single drop on the film surface, which was readily wetted, and then rinsing with water and then ethanol. HF dissolves glass thus it was not possible to use it on the glass-mounted films used for optical and sheet resistance measurements (such treatments meant the films slipped off and/or stretched/deformed/crumpled) and so 2 % HCl was used instead, in the same manner. For thionyl chloride ($SOCl_2$) treatment, two drops were applied to the SWCNT films, allowed to dry in air, and then rinsed briefly with ethanol and dried with N_2. A second HF treatment was applied in the same manner as the first.

3.3 The effect of front electrode thickness

For front gold electrodes of thickness > 145 nm the output of devices was consistent however a small increase in J_{SC} from devices with thinner front gold electrodes was found to be due to light penetration to the underlying silicon around the active area artificially enhancing the photocurrent (**Figure 3.2**). This was proven by the fact that an aperture placed over the cells such that only the active area was exposed to light had no effect for devices with front gold thickness > 145 nm, but reduced the output of the devices with the thinner electrodes.

3.4 The back junction

The function of the back junction in these test devices was to provide an ohmic contact to the steel backing plate. Gallium indium eutectic liquid (eGaIn) was used for this and for its ease and versatility of use. Highlighting the importance of an ohmic contact, a non-ohmic back contact is implicated in Chapter 4 as the cause of a misleading feature in the EQE of SWCNT-silicon solar cells.

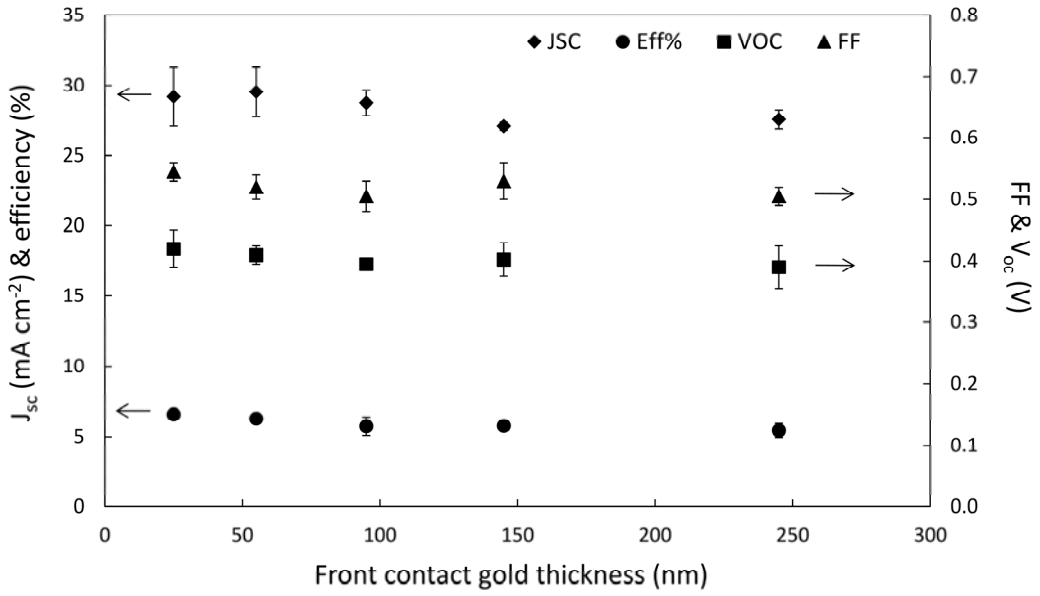

Figure 3.2 Variation of solar cell JV characteristics with thickness of front gold electrode under AM1.5 illumination.

3.5 SWCNT film thickness

The UV-Vis-NIR spectrum of an as prepared film of arc-discharge SWCNTs is shown in **Figure 3.3**. The low energy of the S_{11} transition (~ 0.7 eV) is consistent with large diameter SWCNTs and the broadness of the absorption features is indicative of both the polychirality of the material and the bundled state of the dispersion.[15] Following treatment with 2 % HCl the S_{11} absorption peak is slightly suppressed. This is expected due to mild p-type doping of the SWCNTs by transfer of charge during protonation by the acid as discussed further in section 3.5.3. Following treatment with $SOCl_2$ there is complete bleaching of the S_{11} absorption and a substantial decrease in the intensity of S_{22}, but an overall absorption increase for λ < 850 nm. Bleaching of S_{11} is consistent with electron transfer from the top of the SWCNT valance band to the organic oxidiser as previously observed.[16-17] The origin of the increase in the lower λ region is unknown and it was not always observed, but was always removed by the second acid treatment and may have been due to incomplete removal of $SOCl_2$ decomposition products. Importantly, there was no return of S_{11} after the second acid treatment.

The linear relationship between absorbance and volume of SWCNT suspension shown in **Figure 3.4**(a) is expected from the Beer law where the absorbance A is proportional to N, the number of absorbing units.[18] Although there is a logarithmic relationship between absorbance and transmittance, T_{av} is in the range of relative linearity (99 % > T > 40 %) with N. The very small difference between average absorbance before and after the various treatments is an indicator of the efficacy of the averaging process in removing the effect of the absorption peaks (see sections 3.2.4 and 5.2).

In **Figure 3.4**(b), the plot of sheet resistance, R_{sheet}, vs. film thickness (expressed here as T_{av}) shows the same apparent exponential increase seen as in prior reports.[3, 12] R_{sheet} is composed of two regions of resistance: one ($R_{junction}$) where conductance is limited by the number of tube-tube junctions and their contact resistance, and the other (R_{tube}) limited by the concentration of carriers and their mobility, such that; $R_{sheet} = R_{junction} + R_{tube}$. The R_{tube} term dominates for the thicker films, which are more metal-like, whilst $R_{junction}$ dominates for the sparsest films in which transport is governed by percolation theory.[12, 19-21] The point T_{th} is the threshold of transmittance/thickness/density at which the conductance of the film switches from being dominated by percolation to a more bulk metallic behaviour. T_{th} is a figure of merit for these films, with higher values indicating a better electrode film, and its effect will be clearly seen in the solar cell performance measurements that follow. R_{th} is R_{sheet} at T_{th} and clearly, the lower R_{th} is the better. Even though the acid treatment had little effect on the optical absorbance, T_{th} increased markedly from ~ 65 % to ~ 85 % when the SWCNT films on glass were exposed briefly to 2 % HCl, and this was coupled with an order of magnitude decrease in R_{th}. This initial improvement is likely due to removal of residual surfactant molecules by the acid. Another big increase in T_{th} up to 90 - 95 % is observed following the $SOCl_2$ treatment, as well as large reductions in R_{sheet} in the range 45 – 85 %. However no further improvements are seen following a second 2 % HCl treatment, indicating that any improvements observed in solar cell devices from the second HF treatment are due to the silicon.

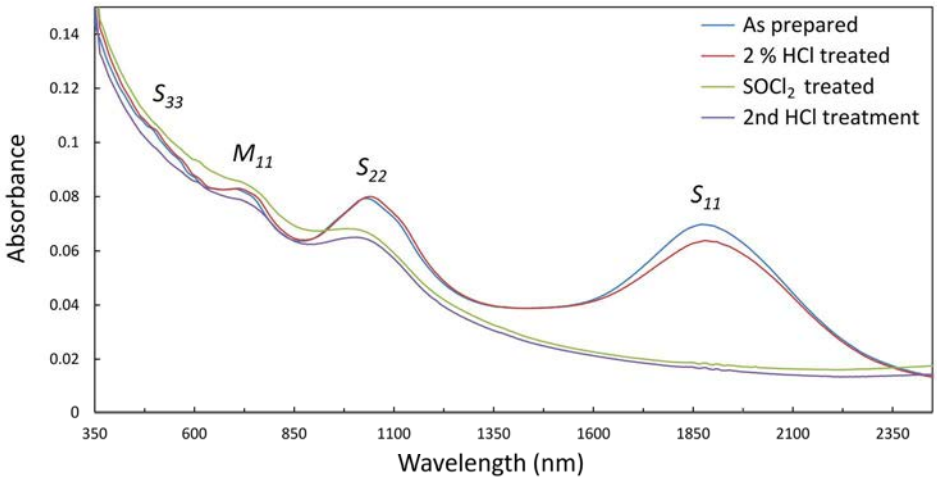

Figure 3.3 UV-Vis-NIR spectra of thin vacuum filtration films of SWCNTs on glass, made from aqueous TritonX-100 suspensions of large diameter arc-discharge material (section 3.2.1). Optical transitions are clearly seen and have been labelled in accordance with the DOS diagrams shown in Figure 1.8.

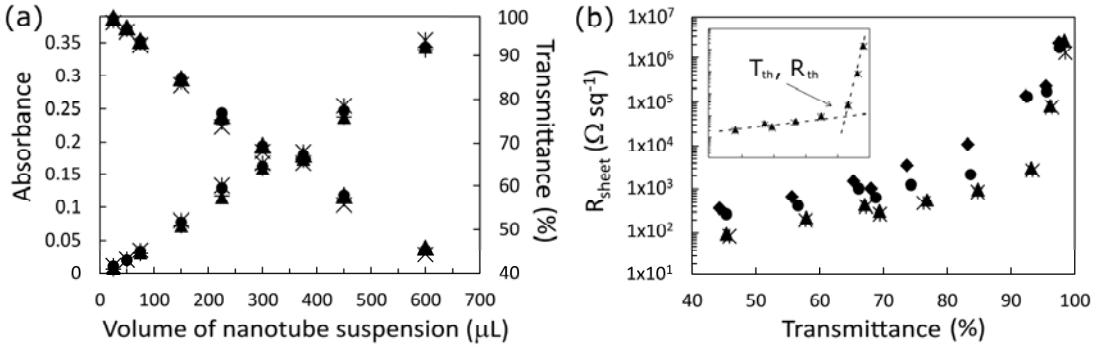

Figure 3.4 (a) Dependence of the SWCNT films' average optical depth (see 3.2.4) on the volume of SWCNT suspension used per square centimetre of filtration membrane. The different symbols represent different treatments and show very that there is very little effect on the baseline visible absorption. (b) Variation of the sheet resistance with film transmission for as prepared (◆), HCl treated (●), $SOCl_2$ treated (■) and HCl retreated (▲) devices. Inset shows the two regions of differing resistance for the doped films and the threshold transmittance (T_{th}) and corresponding sheet resistance (R_{th}).

3.5.1 As-prepared solar cells

The light and dark current-voltage characteristics of the as-prepared devices were measured as a function of the optical density, or thickness, of the SWCNT film (Appendix 3) and are summarised in **Figure 3.5**. The peak in J_{SC}, around T_{av} ~ 60 - 70 %, occurs due to a balancing of the decrease in the photon flux, J_{ph}, penetrating through to the silicon for the thicker films with T_{av} < 65 %, and the steep exponential rise in R_{sheet} above T_{th}. In fact, the same pattern of variation seen in R_{sheet} is exactly replicated here in the plot of R_S, for films with T_{av} > 75 % (**Figure 3.4**(b)). V_{OC} is remarkably consistent across the thickness range until the thinnest film with T_{av} = 97 %. The FF show a clear but modest decrease towards thinner films. There is a noticeable U-shape in R_{SH}, this can be easily explained for T_{av} > 75 % as it exactly mirrors the pattern of variation evident in R_{sheet}, R_S and overall efficiency, and is thus likely also due to increasingly limited percolation pathways. For T_{av} < 75 % the cause of the increase in R_{SH} is less obvious, but could be due to a better depletion region set up in the silicon as a result of the higher total carrier concentration in the thicker films. Li[3] and Kozawa[7] observed a peak in the performance of their SWCNT-silicon solar cells at ~ 60 % film transmittance, likely related to T_{th}. However, in other work performance kept increasing for increased transmittance up to the maximum used in that experiment (90.4 %)[5] likely indicating that T_{th} > 91 % for those films. The reverse saturation current density, J_0, is good (low) for the thickest films at ~ 10^{-8} A cm^{-2} but is also clearly dependent on the SWCNT film thickness.

Overall efficiency shows the same two distinct regions as seen in R_{sheet}, J_{SC}, R_S and part of R_{SH}, and strongly implicates the poor sheet resistance of the SWCNT films as the major limiting factor underlying the poor performance of all the devices measured (< 2 %). When considering that R_S of these devices was, at best, 1 kΩ, and that the typical area normalised series resistance of commercial cells can range from 0.5 - 2 Ω cm^2, that is not really surprising.

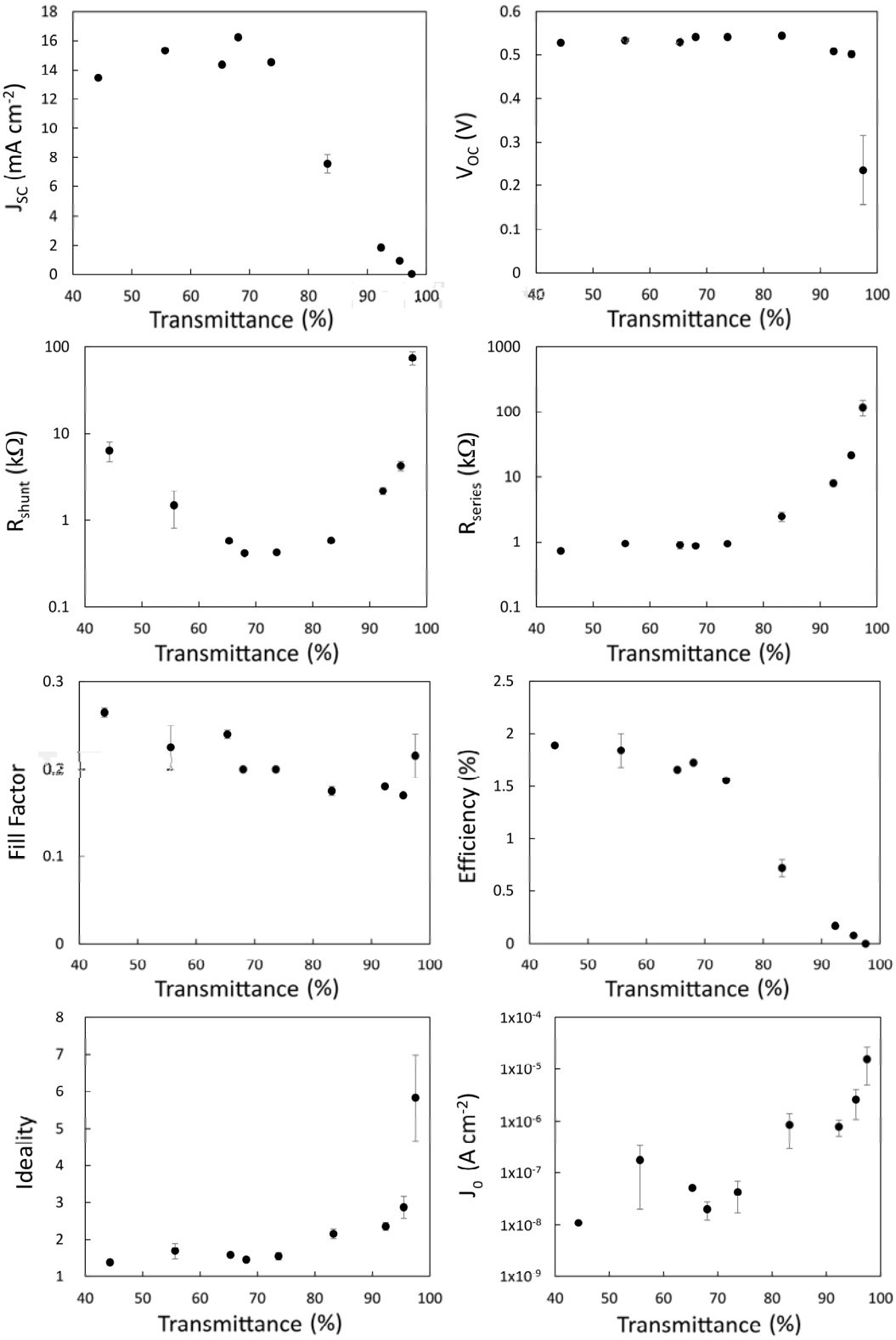

Figure 3.5 Solar cell parameters extracted from as-prepared SWCNT-Si devices with varying SWCNT film thickness. The full light and dark current-voltage plots can be found in Appendix 3.

3.5.2 The effect of HF treatment

The purpose of the HF treatment is to remove the relatively thick oxide present on the silicon surface between the silicon and the SWCNTs. This oxide would have likely been thickened somewhat during the wet and hot film deposition process (3.2.3). Measurements were not taken immediately following the HF treatment due to the observation of unpredictable and random results with large variations in output, sometimes even between consecutive measurements of the same device. Unlike the perfect silicon hydride that can be formed on an uncovered surface, the presence of the SWCNTs on these surfaces likely contributes to the formation of dangling bonds and trap states during the HF treatment. Measurements were observed to stabilise after an hour in air at room temperature (not long enough for the formation of an intermediate oxide > 1 nm).

Immediately apparent when comparing **Figure 3.5** and **Figure 3.6** is that J_{SC} is almost entirely unchanged, consistent with J_{SC} being dependent primarily on J_{ph}, which is not changed significantly by brief exposure to mild acid, as implied by **Figure 3.3** and on the shape of R_S. Importantly, V_{OC} now shows a definite dependence on the SWCNT film thickness and has been reduced by > 10 % in all cases. The FF has been improved; doubling for thicker films, whilst also now showing a stronger dependence on the film thickness than before. Improvements in FF give an increase in the highest efficiency from 1.8 – 2.5 %, although other factors combine to decrease the efficiency much faster with reducing film thickness. The effect of lower R_{sheet}, particularly in the range of 60 % < T_{av} < 90 %, is seen in the plot of R_S however there is little change to R_{SH} or J_0.

Overall, it appears that the rapid increase in R_{sheet} above T_{th} dominates all measures of the device IV characteristics for T_{av} > 70 %, and this occurs via its effect on R_S. Such strong dependence supports the hypothesis that, in these devices, the role of the SWCNT film is as a transparent, conducting front electrode that must also (clearly) establish an inversion layer/depletion region in the underlying silicon.

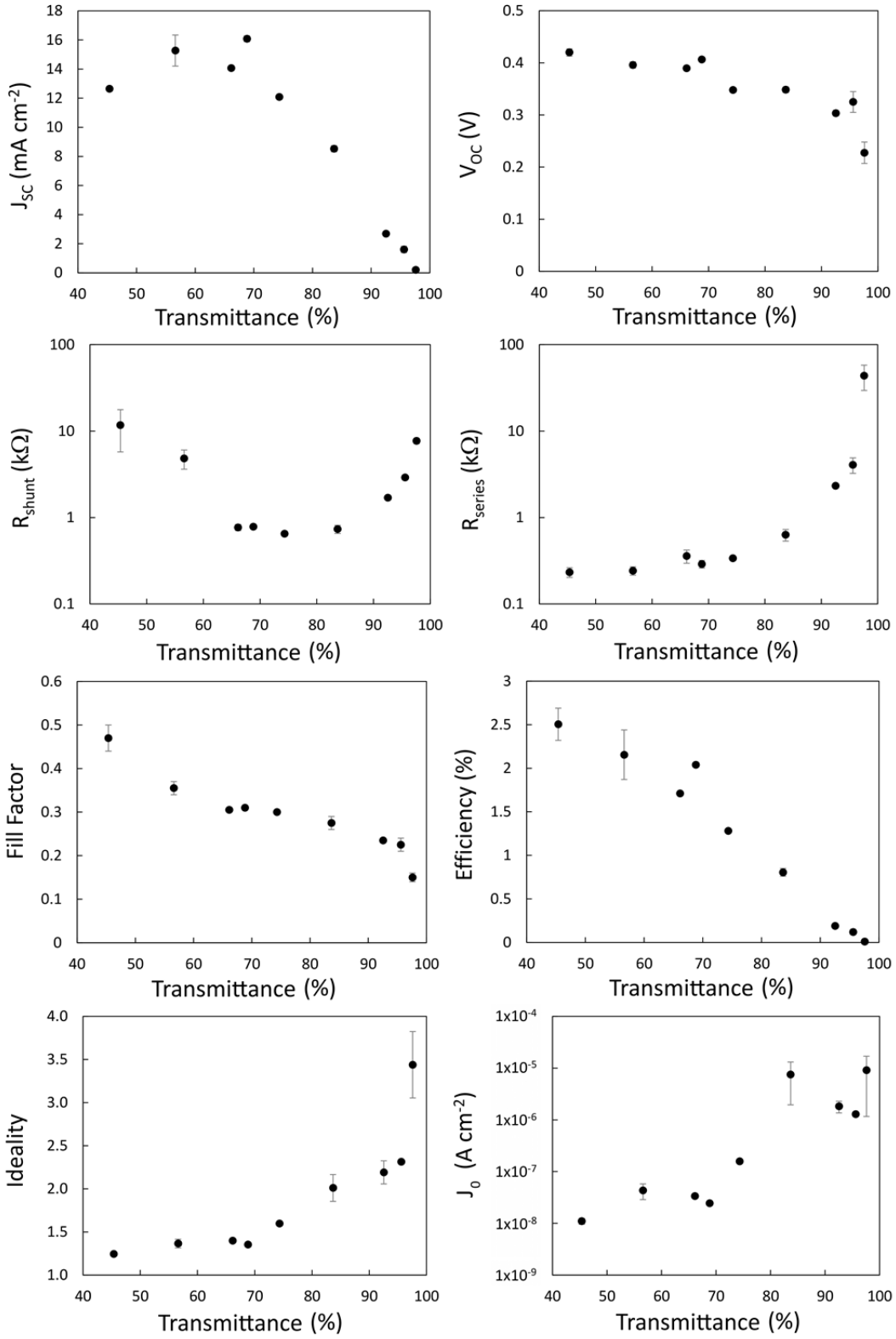

Figure 3.6 Solar cell parameters extracted from HF treated SWCNT-Si devices with varying SWCNT film thickness, 1 hr after treatment.

3.5.3 The effect of $SOCl_2$ treatment

A common method to reversibly improve the electrical properties of SWCNT films is to expose them to the powerful organic oxidiser, $SOCl_2$.[17, 22-27] This has the effect of hole doping the SWCNTs via the electron withdrawing nature of the decomposition reaction;

$$2SOCl_2 + 4e^- \rightarrow S + SO_2 + 4Cl^- \qquad \textbf{Equation 3.5}$$

Performance gains via $SOCl_2$ treatment of SWCNT-silicon solar cells have been reported previously.[2-3] The effect of $SOCl_2$ on SWCNTs has been relatively well-studied[17, 22-27] and is similar to HNO_3 doping.[28-29] $SOCl_2$ has been shown to be a very good p-type dopant for SWCNTs that increases conductivity in the SWCNTs by shifting the Fermi level into the valance band (as evidenced in this study by the bleaching of S_{11} absorption), and in the films by reducing barriers at the tube-tube junctions.[25, 28] After $SOCl_2$ treatment, the conduction mechanism of the SWCNT films switches from variable range hopping/thermionic emission over tube-tube barriers to tunnelling through them.[3, 25]

The J_{SC} peak in **Figure 3.7** has shifted to higher transmittance (~ 65 % to ~ 80 %) in line with the change observed in T_{th} (**Figure 3.4**(b)) as well as the magnitude of J_{SC} at each film thickness increasing to ~ 1.25 x the undoped value. The insensitivity of V_{OC} to film thickness (except for the 98 % film) has returned to exactly as it was before the HF treatment whilst the FF has been maintained or improved upon overall gains compared to the as prepared case. There has been a dramatic change in the behaviour of R_{SH}, with two distinct regions now separated by a sharp break at ~ 80 %, but J_0 and the ideality remain the same.

The increases in J_{SC} and V_{OC}, as well as modest improvement in FF and R_S, coupled with the large improvement of R_{SH} for 55 % < T_{av} < 80 %, lead to significant efficiency gains of up to 3.5 x the undoped values (for T_{av} ~ 75 %) and the pattern of variation in the efficiency is now clearly due to limited R_S.

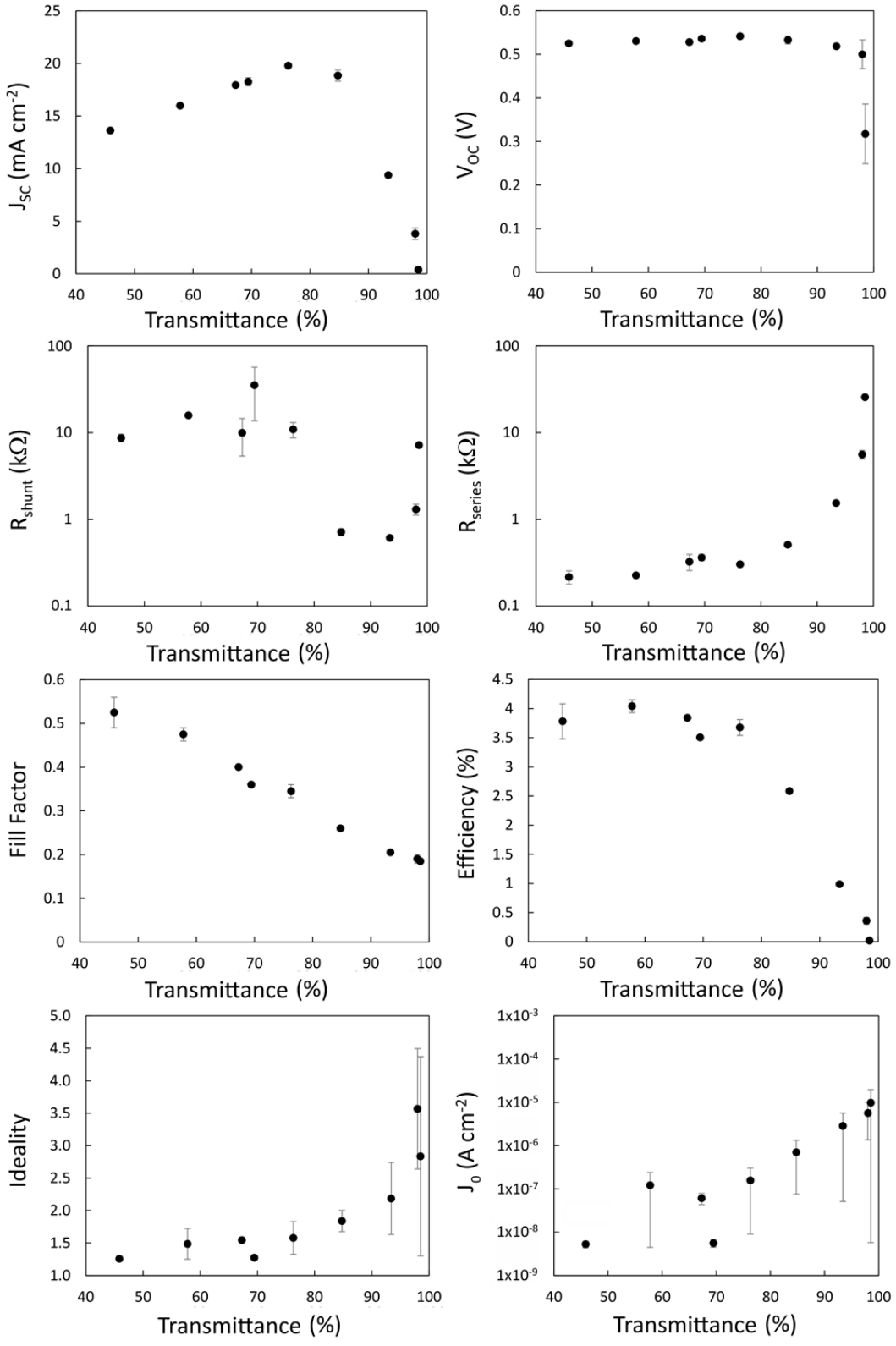

Figure 3.7 Solar cell parameters extracted from $SOCl_2$ treated SWCNT-Si devices with varying SWCNT film thickness.

3.5.4 The effect of a second HF treatment, with 1 hr or 4 hr oxide

Following the $SOCl_2$ treatment, a second brief HF treatment improves the FF (**Figure 3.8**), particularly for the thinner films, and this is likely due to lower R_S. V_{OC} has been reduced by ~ 10 % but is now reasonably high even for the device with the 98 % film. J_{SC} and J_0 are unchanged but the ideality is modestly improved in line with R_S for the thinner films. R_{SH} is markedly improved in the devices with the thicker films but unchanged for T_{av} > 80 %. It has been shown that the effect of acid doping on the conductance of SWCNT films sensitively depends on the film thickness[30] and a similar phenomenon exists here. The threshold at which R_S begins to increase rapidly has not increased as much as for R_{sheet}, and did not for the $SOCl_2$ case either, but this is consistent with a model in which the percolation factor ($R_{junction}$) contributing to R_S has an additional term that R_{sheet} does not, representing the dependence on the number of the SWCNT-silicon junctions.

The overall efficiency of these particular devices remained relatively unchanged by the 2nd HF treatment but it was often observed that this step was critical in attaining the best performance from devices following the $SOCl_2$ treatment. A third HF treatment immediately following the second had no noticeable effect however, after multiple consecutive HF treatments there comes a point where the undercutting of the oxide underneath the front gold electrode causes collapse of this onto the silicon and results in a very noticeable drop in performance. If left for several days, the performance of all devices returned to about the same as the as prepared state.

After 4 hr in ambient laboratory air there will certainly be a native oxide (**Figure 3.9**). The overall shape of J_{SC} is again unchanged and still peaks at ~ 75 – 80 % but the FF, R_S, R_{SH} and the PCE have all been affected to some degree, predominantly in the middle of the thickness range. The growth and removal of an interfacial oxide has been shown to reversibly improve the performance of some randomly aligned SWCNT-silicon solar cells[31-32] but this is not true of all reports.

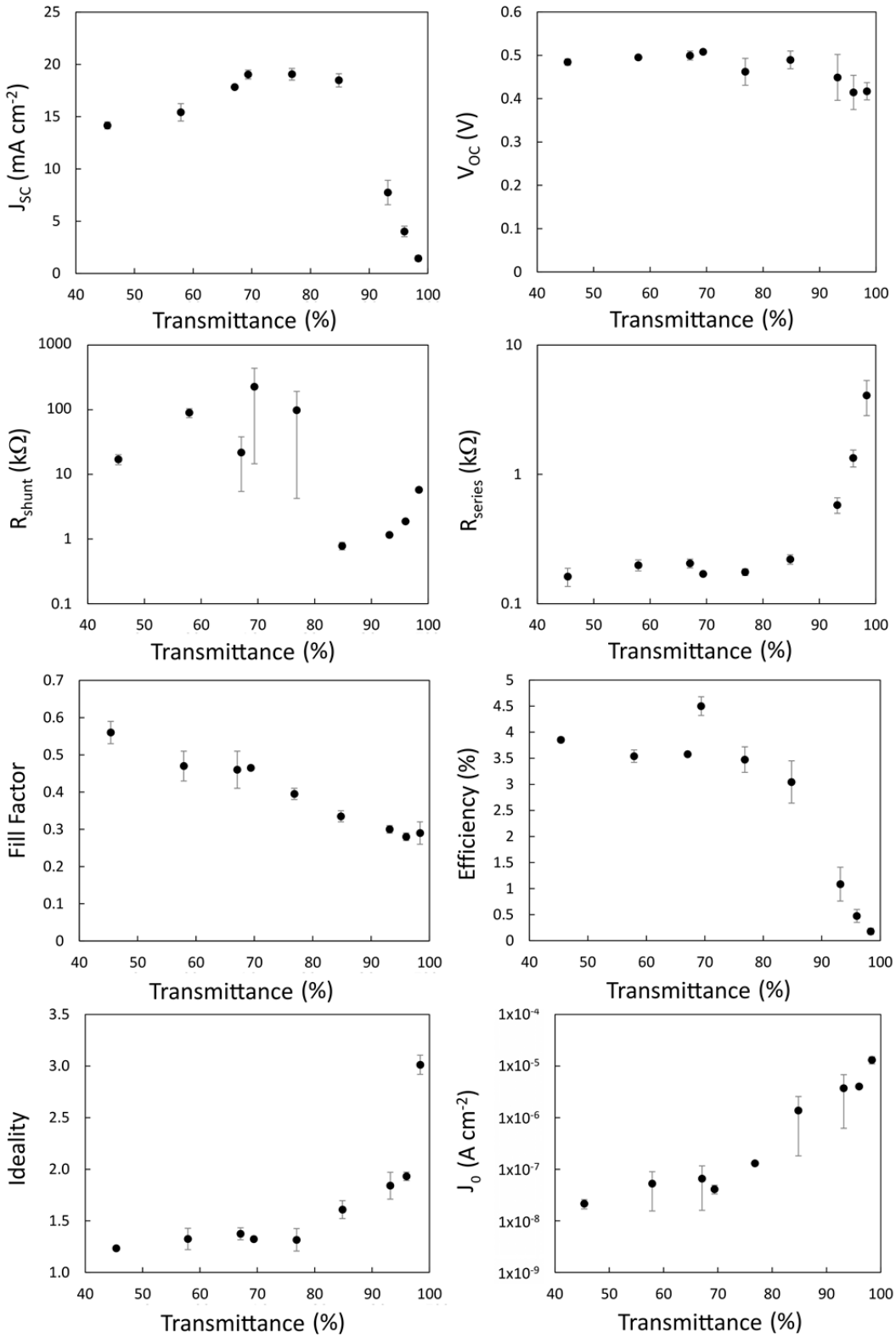

Figure 3.8 Solar cell parameters extracted from HF treated (second treatment) SWCNT-Si devices with varying SWCNT film thickness, 1 hr after treatment.

Jung reasons that the operating mechanism in their solar cells, made with highly aligned SWCNT films, is not that of a MS Schottky junction primarily because the very high activation energy, E_a, is equal to E_g, the energy gap of silicon (1.1 eV) and is far too high for a Schottky barrier, and because of the very long minority carrier lifetime in the microseconds.[33] It is also reasoned that the mechanism of action is the same as in pn not MIS solar cells because the growth of a thin oxide does not improve their devices' performance, contrary to the observations of Jia.[31-32] Although it does not resolve the issue, Chapter 4 will show that the SWCNTs do not contribute directly to the observed photocurrent.

Consistent with the results shown here, it may be that the thin oxide is required in between the sparse SWCNT junctions formed by randomly aligned films to prevent recombination at these uncovered surfaces and allow carriers time to find a nearby SWCNT-silicon junction in the imperfectly covering film. The ability of the devices to separate charge is thus governed primarily by the $Si:SiO_x$ junction, hence the relative insensitivity of V_{OC} towards SWCNT film thickness in the presence of the oxide and the $E_a = E_g$ observation. This is unnecessary with the very low resistance aligned films and the conformal covering they provide.

3.6 Summary

The results show a strong dependence on film thickness, as expected, particularly for films with average transmittance greater than ~ 70 % and the main cause of this is the sheet resistance of the SWCNT film. The effect of doping with $SOCl_2$ is primarily via a reduction in sheet resistance boosting J_{SC}, V_{OC} and FF of all devices. An interfacial oxide does not improve the devices with doped SWCNT films, but is essential for those with the undoped films, and particularly the thinner films with $T_{av} > 70$ %.

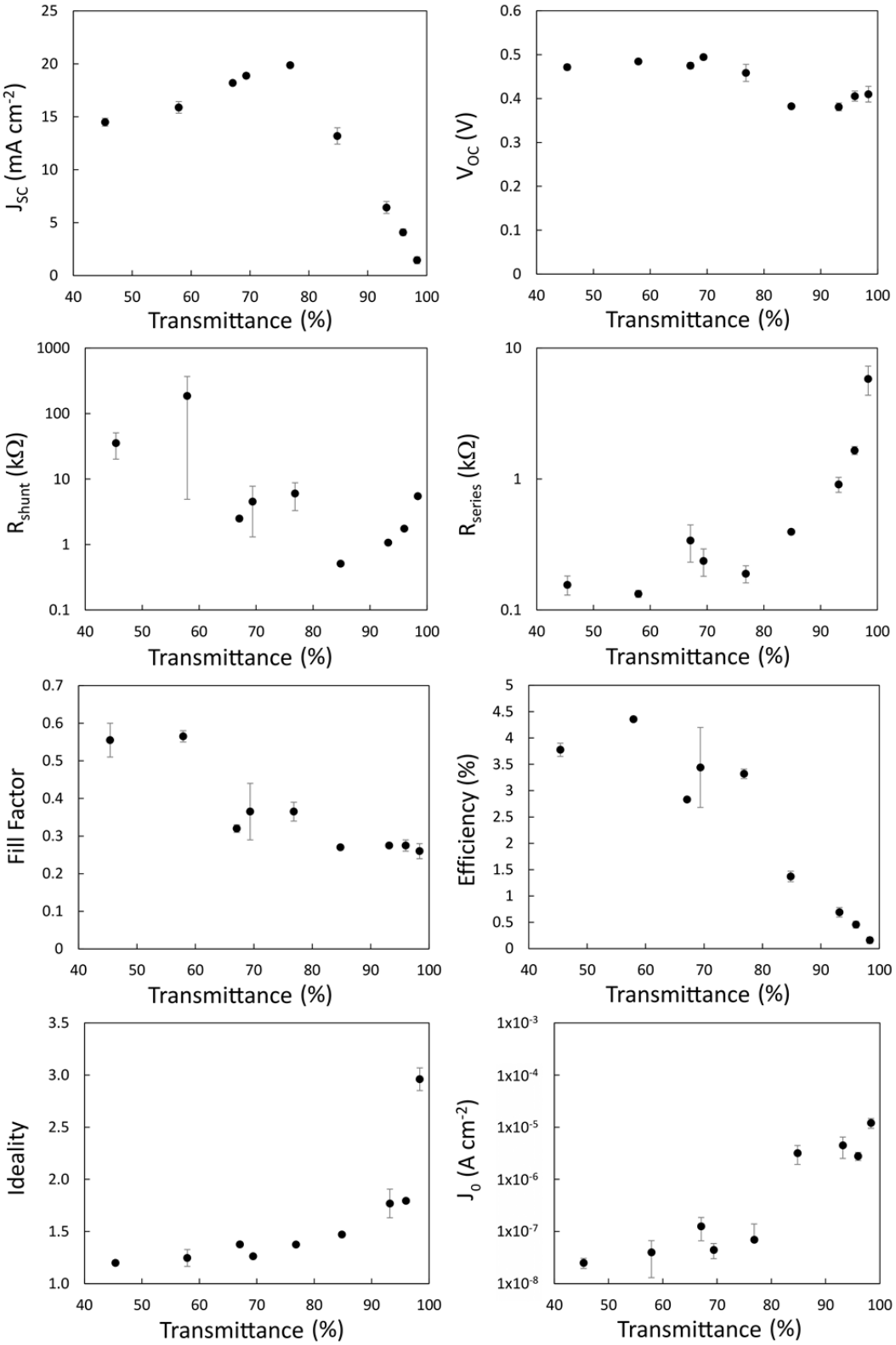

Figure 3.9 Solar cell parameters extracted from HF treated (second treatment) SWCNT-Si devices with varying SWCNT film thickness, 4 hr after treatment.

3.7 References

[1] Wei, J., Jia, Y., Shu, Q., Gu, Z., Wang, K., Zhuang, D., Zhang, G., Wang, Z., Luo, J., Cao, A., and Wu, D., *Nano Letters,* **2007**. 7(8): p. 2317-2321.

[2] Li, Z., Kunets, V.P., Saini, V., Xu, Y., Dervishi, E., Salamo, G.J., Biris, A.R., and Biris, A.S., *Applied Physics Letters,* **2008**. 93(24): p. 243117-3.

[3] Li, Z., Kunets, V.P., Saini, V., Xu, Y., Dervishi, E., Salamo, G.J., Biris, A.R., and Biris, A.S., *ACS Nano,* **2009**. 3(6): p. 1407-1414.

[4] Jia, Y., Li, P., Wei, J., Cao, A., Wang, K., Li, C., Zhuang, D., Zhu, H., and Wu, D., *Materials Research Bulletin,* **2010**. 45(10): p. 1401-1405.

[5] Li, Z., Jia, Y., Wei, J., Wang, K., Shu, Q., Gui, X., Zhu, H., Cao, A., and Wu, D., *Journal of Materials Chemistry,* **2010**. 20(34): p. 7236-7240.

[6] Del Gobbo, S., Castrucci, P., Scarselli, M., Camilli, L., De Crescenzi, M., Mariucci, L., Valletta, A., Minotti, A., and Fortunato, G., *Applied Physics Letters,* **2011**. 98(18): p. 183113-3.

[7] Kozawa, D., Hiraoka, K., Miyauchi, Y., Mouri, S., and Matsuda, K., *Applied Physics Express,* **2012**. 5(4): p. 042304.

[8] Zhao, Y., Yang, L., Chen, S., Wang, X., Ma, Y., Wu, Q., Jiang, Y., Qian, W., and Hu, Z., *Journal of the American Chemical Society,* **2013**. 10.1021/ja310566z.

[9] Li, X., Jung, Y., Sakimoto, K., Goh, T.-H., Reed, M.A., and Taylor, A.D., *Energy & Environmental Science,* **2013**.

[10] Saha, A., Ghosh, S., Weisman, R.B., and Martí, A.A., *ACS Nano,* **2012**. 10.1021/nn302092b.

[11] Wu, Z., Chen, Z., Du, X., Logan, J.M., Sippel, J., Nikolou, M., Kamaras, K., Reynolds, J.R., Tanner, D.B., Hebard, A.F., and Rinzler, A.G., *Science,* **2004**. 305(5688): p. 1273-1276.

[12] Hu, L., Hecht, D.S., and Grüner, G., *Nano Letters,* **2004**. 4(12): p. 2513-2517.

[13] Sze, S.M. and Ng, K.K., *Physics of semiconductor devices*. 3 ed. 10.1002/0470068329. 2006: Wiley Interscience.

[14] Cheung, S.K. and Cheung, N.W., *Applied Physics Letters,* **1986**. 49(2): p. 85-87.

[15] Ryabenko, A.G., Dorofeeva, T.V., and Zvereva, G.I., *Carbon,* **2004**. 42(8-9): p. 1523-1535.

[16] O'Connell, M.J., Eibergen, E.E., and Doorn, S.K., *Nature Materials,* **2005**. 4(5): p. 412-418.

[17] Dettlaff-Weglikowska, U., Skákalová, V., Graupner, R., Jhang, S.H., Kim, B.H., Lee, H.J., Ley, L., Park, Y.W., Berber, S., Tománek, D., and Roth, S., *Journal of the American Chemical Society,* **2005**. 127(14): p. 5125-5131.

[18] Beer, A., *Annalen der Physik und Chemie,* **1852**. 86: p. 78-88.

[19] Pike, G.E. and Seager, C.H., *Physical Review B,* **1974**. 10(4): p. 1421-1434.

[20] Yi, Y.B. and Sastry, A.M., *Physical Review E,* **2002**. 66(6): p. 066130.

[21] Nirmalraj, P.N., Lyons, P.E., De, S., Coleman, J.N., and Boland, J.J., *Nano Letters,* **2009**. 10.1021/nl9020914.

[22] Parekh, B.B., Fanchini, G., Eda, G., and Chhowalla, M., *Applied Physics Letters,* **2007**. 90(12): p. 121913-3.

[23] Geng, H.-Z., Kim, K.K., So, K.P., Lee, Y.S., Chang, Y., and Lee, Y.H., *Journal of the American Chemical Society,* **2007**. 129(25): p. 7758-7759.

[24] Blackburn, J.L., Barnes, T.M., Beard, M.C., Kim, Y.-H., Tenent, R.C., McDonald, T.J., To, B., Coutts, T.J., and Heben, M.J., *ACS Nano,* **2008**. 2(6): p. 1266-1274.

[25] Barnes, T.M., Blackburn, J.L., van de Lagemaat, J., Coutts, T.J., and Heben, M.J., *ACS Nano,* **2008**. 2(9): p. 1968-1976.

[26] Tantang, H., Ong, J.Y., Loh, C.L., Dong, X., Chen, P., Chen, Y., Hu, X., Tan, L.P., and Li, L.-J., *Carbon,* **2009**. 47(7): p. 1867-1870.

[27] Kim, D.H., Lee, J.K., Huh, J.H., Kim, Y.H., Kim, G.T., Roth, S., and Dettlaff-Weglikowska, U., *physica status solidi (b),* **2011**. 248(11): p. 2668-2671.

[28] Znidarsic, A., Kaskela, A., Laiho, P., Gaberscek, M., Ohno, Y., Nasibulin, A.G., Kauppinen, E.I., and Hassanien, A., *The Journal of Physical Chemistry C,* **2013**. 117(25): p. 13324-13330.

[29] Jia, Y., Cao, A., Bai, X., Li, Z., Zhang, L., Guo, N., Wei, J., Wang, K., Zhu, H., Wu, D., and Ajayan, P.M., *Nano Letters,* **2011**. 11(5): p. 1901-1905.

[30] Zhang, Z.-B., Li, J., Cabezas, A.L., and Zhang, S.-L., *Chemical Physics Letters,* **2009**. 476(4-6): p. 258-261.

[31] Jia, Y., Li, P., Gui, X., Wei, J., Wang, K., Zhu, H., Wu, D., Zhang, L., Cao, A., and Xu, Y., *Applied Physics Letters,* **2011**. 98(13): p. 133115-3.

[32] Jia, Y., Cao, A., Kang, F., Li, P., Gui, X., Zhang, L., Shi, E., Wei, J., Wang, K., Zhu, H., and Wu, D., *Physical Chemistry Chemical Physics,* **2012**. 14(23): p. 8391-6.

[33] Jung, Y., Li, X., Rajan, N.K., Taylor, A.D., and Reed, M.A., *Nano Letters,* **2012**. 13(1): p. 95-99.

Chapter 4
The role of nanotubes in SWCNT - silicon solar cells

The mechanism of action of SWCNT-silicon heterojunction solar cells is under discussion with literature reports suggesting either pn or Schottky junction characteristics. A crux of this issue is whether or not the SWCNTs contribute to the observed photocurrent or not. In order to further understand the mechanism of action of the solar cells fabricated in this thesis, devices were fabricated using SWCNTs sorted by (n,m) species, such that the excitonic transition was well defined and was outside the range of absorption of silicon and such that any contribution to the photocurrent from the SWCNTs should be easily resolved from the silicon by analysis of the photocurrent spectrum. The devices exhibited the photocurrent spectra of silicon only, indicating that the SWCNTs do not contribute to the photocurrent. However, by changing the back contact electrode material from gallium indium eutectic to silver, results can be obtained that appear to show such a contribution.

4.1 Introduction

As shown in Chapter 1, SWCNT-silicon solar cells have seen growing research interest in recent years with advances made in just the last year bringing the current maximum power conversion efficiency to 11.5 % in the dry state,[1] 15 % with a TiO_2 antireflective layer[2] and > 18 % in the wet state.[3] In this architecture, a thin film of SWCNTs is placed in contact with the surface of a silicon wafer to produce a photoactive junction. The two main mechanisms suggested for how these devices convert light to electrical power are; the devices work in the manner of 1) a pn heterojunction solar cell, with the SWCNTs contributing as photoactive material[4-10] or, 2) a MS Schottky junction solar cell or the structurally related MIS solar cell, where the SWCNTs operate as transparent conducting electrodes.[11-17] SWCNTs have been shown to a) produce a photocurrent when exposed to light,[18-19] b) be capable of forming photoactive pn junctions[20] and c) be capable of contributing to photocurrent generation in photoactive donor-acceptor pairs.[21-22] Additionally, it is well known that air-exposed s-SWCNTs are p-type due to oxygen adsorption.[23] Considering this, it is not unreasonable to assume that SWCNT-silicon solar cells could function in the manner of a pn junction. Indeed, the literature contains reports that suggest exactly that; recent measurements on SWCNT-silicon devices by Jung et al. preclude the MIS or MS mechanism.[1] However, other measurements on similar SWCNT-silicon devices show greatly enhanced (500 x) performance with an interfacial oxide layer, indicating an MIS-type mechanism.[24]

A more direct probe of the mechanism of action in relation to SWCNT contribution is to use photocurrent spectroscopy to measure the EQE of the devices. Contribution from the SWCNTs to the photocurrent would rule out a standard MS mechanism. In the work of Tzolov,[4] photocurrent spectroscopy of SWCNT-silicon devices shows a broad feature in the IR that is attributed to the SWCNTs. However this feature is very similar to the free carrier absorption profile of the silicon substrate,[25] confounding the issue. Also, in the EQE data of Ong[10]

there is a feature that is attributed to photocurrent generation by the SWCNTs. However this small feature in the EQE, which roughly corresponds to the optical gap of the (7,6) nanotubes used in the study (~ 1150 nm), sits right on the edge of the silicon absorption spectrum (~ 1200 nm) thus the conclusion of device pn junction characteristics based solely on this feature is uncertain.

To determine more conclusively whether or not SWCNTs contribute to photocurrent generation in SWCNT-silicon solar cells, devices were fabricated using two different s-SWCNT samples enriched in either small or large diameter tubes. These were chosen since the first excitonic transition (S_{11}) of the major (6,5) chirality in the small diameter SWCNTs lies at ~ 980 nm and overlaps the silicon spectrum similarly to the (7,6) nanotubes used by Ong,[10] whereas for the larger diameter tubes the gap is ~ 1320 nm, well above the absorption onset wavelength of silicon. Any contribution to the photocurrent from the larger diameter SWCNTs should thus be easily resolved by analysis of the photocurrent spectrum.

4.2 Method

Two types of SWCNT raw materials were used for this study: (i) CoMoCat SWCNTs (Sigma-Aldrich) and (ii) SWCNTs prepared in-house by pulsed laser vaporisation (PLV) in an argon atmosphere using carbon targets doped with 1 atom% Ni and Co catalyst and an oven operated at 1000 °C.[26] For the starting suspensions each of the SWCNT material (typically 10 mg) was suspended with sodium dodecyl sulphate (SDS) (1 % w/v) in DI water (15 ml) using a tip sonicator (Bandelin, 200 W maximum power, 20 kHz, in pulsed mode with 100 ms pulses) applied for 2 hr at 20 % power. The resulting dispersion was then centrifuged at 100,000 g for 1 hr (Beckmann Coulter) to remove larger agglomerates. To sort SWCNTs, gel filtration was performed as described by Moshammer[27] using Sephacryl S-200 gel filtration medium (Amersham Biosciences) in a glass column of 20 cm length and 2 cm inner diameter. After filling the glass column with the filtration medium, the gel was slightly compressed to yield a final height of

approximately 14 cm. For the separation, SWCNT starting suspension (10 mL) was applied to the top of the column and subsequently a solution of SDS (1 % w/v) in DI water as eluent was pushed through the column by applying sufficient pressure with compressed air to ensure a flow of ~ 1 mL min^{-1}. After ~ 10 mL of this eluent had been added most of the m-SWCNTs had moved through the column whereas the s-SWCNTs remained trapped in the upper part of the gel. After applying a total of 20 mL of SDS solution in this fashion, the m-SWCNTs were completely removed from the gel. By then changing the eluent from SDS (1 % w/v) in DI water to aqueous sodium cholate (2 % w/v) the s-SWCNTs also subsequently eluted completely from the column and were collected separately in fractions of approximately 1 mL.

Vacuum filtration films were prepared and deposited onto glass and silicon substrates (for optical measurements) and the test solar cells as in section 3.2. Phosphorous doped n-type silicon wafers (CZ, 1-20 Ω cm, <100>, SSP, ABC GmbH) with a thermal oxide (100 nm) were diced into pieces (2 cm^2). E-beam lithography (Raith) was used to define square regions (0.09 cm^2) in the negative resist (maN-2403, micro resist technology GmbH, Germany), which was developed and then the front metal contact (Ti/Au, 5/55 nm) was sputtered. Following lift off the oxide in these regions was etched with a reactive ion etcher (50 sccm CHF_3, 5 sccm O_2, 140 W) (Plasmalab 80 Plus, Oxord). This process produced substrates with 0.09 cm^2 square active areas surrounded by 0.23 cm^2 regions where the SWCNT films overlap the front metal contacts.

UV-Vis-NIR absorption spectra of films of sorted SWCNT material in this chapter were recorded with a Varian Cary 500 spectrophotometer. Photoluminescence excitation (PL) maps of sorted SWCNT material in solution were measured in the emission range of ~ 900 - 1700 nm and excitation range of 500 - 950 nm (scanned in 3 nm steps) using a modified FTIR spectrometer (Bruker IFS66) equipped with a liquid nitrogen cooled Ge photodiode and a monochromatised excitation light source as described elsewhere.[28] The EQE was measured using a setup consisting of

a 450 W xenon light source, an optical chopper (47.7 Hz), a 300 mm monochromator (LOT-Oriel), a custom designed current amplifier (DLPCA-S, Femto Messtechnik) and a digital lock-in amplifier (eLockin 203, Anfatec). A modified photoreceiver (OE-200-S, Femto Messtechnik) with a Si/InGaAs sandwich diode was used to monitor the stability of the monochromatic light beam. Initial calibration was carried out with reference silicon and germanium diodes (Thorlabs, NIST traceable calibration).

4.3 Results and discussion

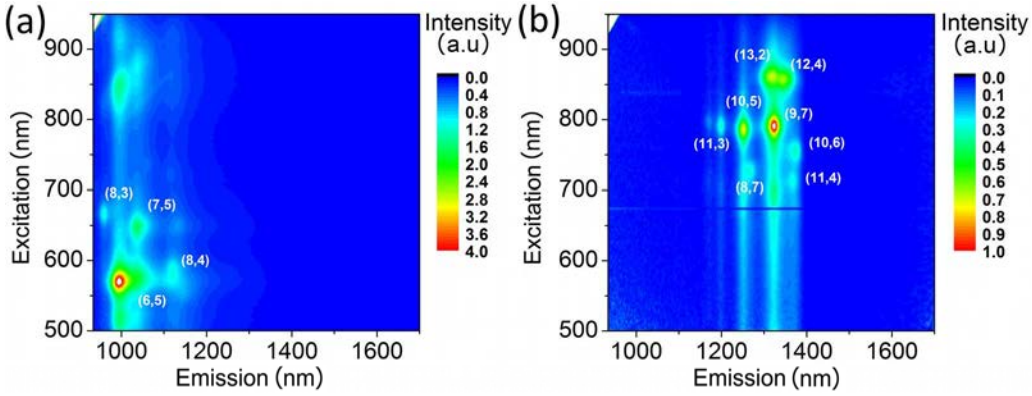

Figure 4.1 Photoluminescence spectra SWCNT material produced by either the a) CoMoCat or b) laser ablation methods.

Figure 4.1 shows PL measurements of the semiconducting fractions of SWCNTs produced by either the a) CoMoCat or b) laser ablation methods (hereafter referred to as COM and LAB), where the excitation and emission energies correspond to the second (S_{22}) and first (S_{11}) excitonic transitions, respectively. As clearly seen, the two samples are composed of markedly different populations of SWCNT chiralities. The smaller diameter COM sample contains a very high proportion of the (6,5) species whilst the larger diameter LAB material has the (9,7) species and smaller quantities of (10,5), (13,2) and (12,4). Absorption of emitted photons by the inner filter effect of water for $\lambda > 1400$ nm prevents any larger diameter SWCNT species from being observed. Although the LAB material contains a larger number of species it is clear that the LAB material will still have its first excitonic transitions, S_{11}, corresponding to wavelengths $\lambda > 1250$ nm, well outside that of any of the COM material

(~ 950 - 1150 nm) and, importantly for this study, well outside the range of silicon absorption.

UV-Vis-NIR absorption spectra of SWCNT films on glass (**Figure 4.2,** dash-dotted lines) support the PL measurements, with the COM material displaying a dominant S_{11} absorption peak at ~ 1030 nm and the LAB material showing a broad absorption band spanning ~ 1300 - 1800 nm. The sharp peak present in the absorption spectrum of the COM material are indicative of the (n,m) purity of the SWCNT

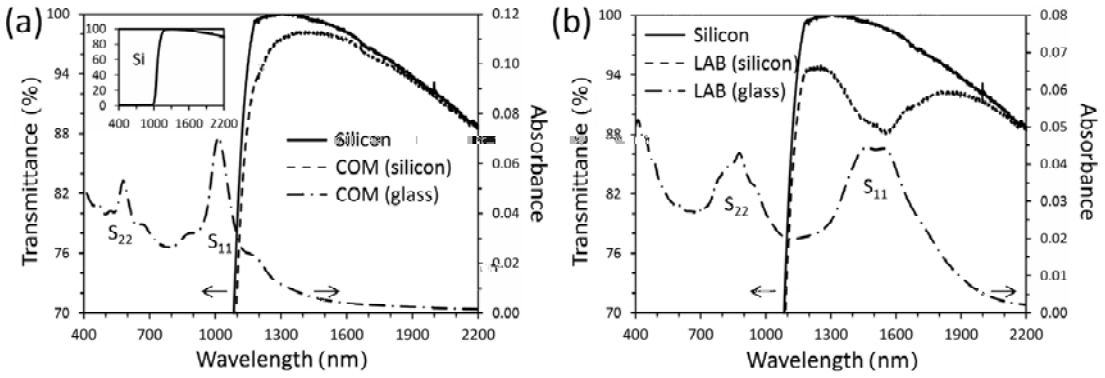

Figure 4.2 UV-Vis-NIR spectra of films prepared from the semiconducting fractions of (a) COM and (b) LAB SWCNTs. Transmittance spectra are shown for films on silicon and absorption spectra are shown for films on glass. **Inset** of (a) shows the full silicon transmittance spectrum in the same wavelength range.

sample as also measured by the PL. This differs from the broad band present in the spectrum of the LAB material that is a convolution of several peaks relating to the four major (n,m) species shown in the PL measurements. Closer inspection reveals a substantial difference between the positions of the S_{11} transitions as measured by PL and UV-Vis-NIR. The PL yields an S_{11} of ~ 980 nm for the (6,5) species and ~ 1320 nm for the (9,7) species whereas the absorption spectra yield ~ 1030 nm for the (6,5) and at least ~ 1490 nm for the (9,7). This apparent shift in the energy of S_{11} has been reported in the literature and, in the case of the (6,5) nanotube, exactly matches that observed elsewhere.[29]

Here it is important to note that the PL measurements are performed on highly disperse, aqueous solutions of surfactant-wrapped s-SWCNT material immediately

following the sorting process. However, the transmittance spectra are obtained from dry SWCNT films on glass substrates, prepared from the sorted fractions, wherein the relatively surfactant-free SWCNTs are present as bundles. Since the excitonic properties of SWCNTs are greatly affected by many body interactions, Coulomb interaction and charge transfer between adjacent SWCNTs in bundles significantly distorts the thin film transmittance measurements. Additionally, in the dry transmittance measurements, the filter effect of water is not an issue thus the contribution of the larger diameter SWCNTs is observable, yielding a much larger apparent shift in S_{11} of the more polychiral LAB material than for the purer COM material. Therefore, if there is a contribution from the SWCNTs then the S_{11} features in the transmittance measurement of the dry films (not those in the PL of the aqueous suspensions) should be represented in the EQE of solar cell devices that employ the same dry films.

The UV-Vis-NIR transmittance properties of SWCNT films on silicon (**Figure 4.2**, dotted lines) are dominated by silicon absorption due to a) the fundamental bandgap (λ < 1200 nm, steep onset) and b) free carrier absorption (λ > 1400 nm, slow onset). Since the wavelength of light corresponding to the first excitonic transition, S_{11}, of the major (6,5) chirality in the COM material is well above that corresponding to silicon's fundamental bandgap, the major absorption features due to (6,5) material are not discernible. Still, a small contribution to the absorption can be seen in the region 1000 - 1400 nm (**Figure 4.2**(a), dotted lines) arising from the shoulder on the higher wavelength side of the main (6,5) peak. In the case of the LAB material, the S_{11} absorption energies of the major chiralities are well below silicon's bandgap. Consequently, the S_{11} absorption features of this material are clearly visible in the range 1300 - 1800 nm (**Figure 4.2**(b), dotted lines) and exactly match the corresponding features in the absorbance spectra of LAB films on glass (**Figure 4.2**(b), dash-dotted lines).

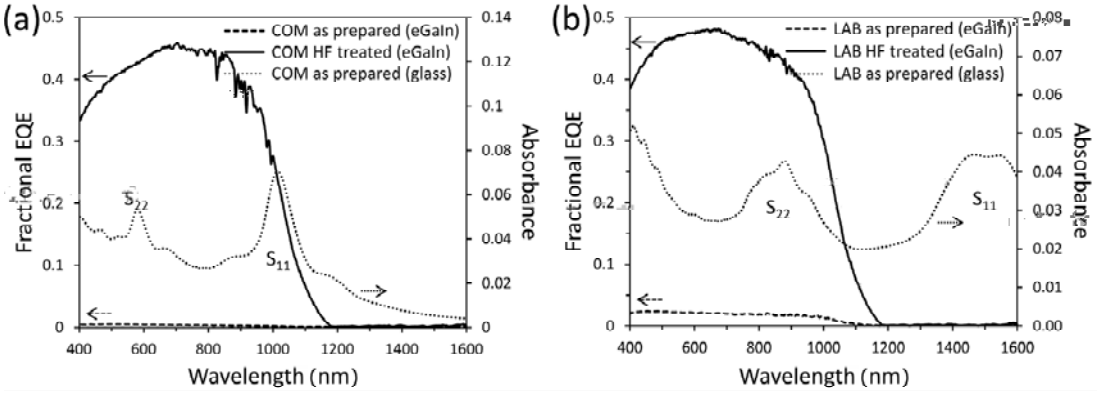

Figure 4.3 EQE of SWCNT-silicon devices fabricated with films of either (a) COM or (b) LAB s-SWCNTs with eGaIn back contact electrodes. UV-Vis-NIR spectra of corresponding films on glass are shown for comparison.

SWCNT-silicon solar cells were fabricated with semiconducting COM and LAB SWCNT material (the same thickness films as those used for the optical measurements), with eGaIn back contact electrodes, and the EQE of as prepared and HF treated devices was measured (**Figure 4.3**). Immediately apparent is the poor response of the as prepared devices due to a thick oxide formed on the silicon during the SWCNT film deposition. On the other hand, the HF treated device shows a significant improvement in EQE. The high porosity of the SWCNT film means that the acid can penetrate through to the underlying silicon allowing the oxide to be removed without harm to the SWCNTs.[30] Indeed, the presence of an S_{11} absorption feature in the UV-Vis-NIR spectra of the LAB SWCNT films on silicon show that they are still present and their electronic properties unchanged after the HF treatment although adsorbed oxygen will have been largely replaced with fluorine.[30]

Comparison of the EQE of COM solar cell devices with the UV-Vis-NIR absorption spectra of COM films on glass shows no correlation between the position of S_{11} and any features in the EQE. Importantly, a similar comparison of the EQE of LAB solar cell devices with the UV-Vis-NIR absorption spectra of LAB films on silicon also shows no such correlation. Any contribution to photocurrent generation resulting from photons absorbed via the S_{11} transition of the SWCNTs should be clearly visible in the EQE in the range corresponding to the observed peak in the

UV-Vis-NIR. Even though the photocurrent response of the COM nanotubes would be obscured by the silicon response however, a) EQE measurements are extremely sensitive by design and, b) none of the devices gave an EQE of 100 %, leaving plenty of room for the SWCNT response to be observed over that of the silicon. In fact, the EQE of both COM and LAB devices are very similar to each other and show no significant deviation from what would be expected from a silicon Schottky junction solar cell, which is in apparent disagreement with Ong et al.[10]

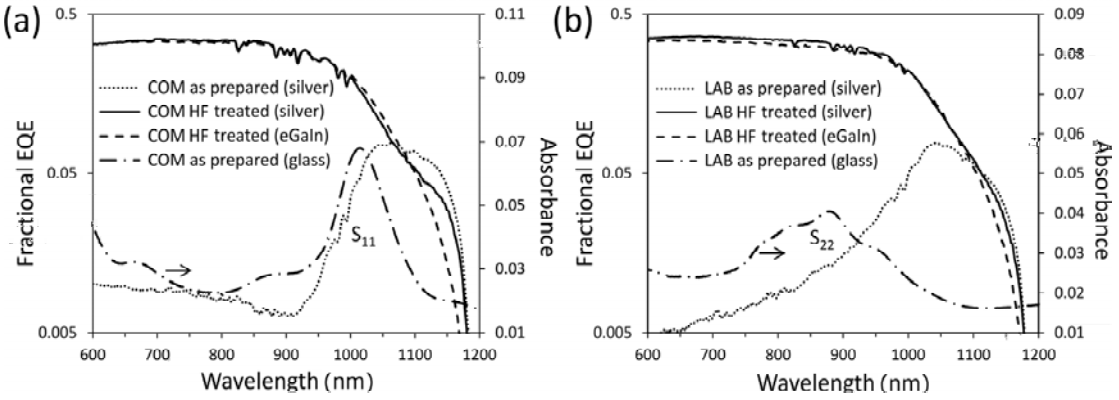

Figure 4.4 EQE of SWCNT-silicon devices fabricated with either (a) COM or (b) LAB s-SWCNTs with silver paint or eGaIn back contact electrodes, note log scale. UV-Vis-NIR absorption spectra of the corresponding films on glass are shown for comparison.

It is possible that different mechanisms apply to devices made with different SWCNT species due to variations in band alignment with the silicon substrate thus the lack of a response from the LAB devices cannot be interpreted to mean that there can be no response from devices using larger bandgap material such as the COM (6,5) and the (7,6)-enriched material used by Ong et al.[10] However no response is observed from either the smaller bandgap LAB or the larger bandgap COM devices used in this study and the LUMO of the (7,6) nanotube is only ~ 80 meV below (6,5). The light (AM1.5G) and dark IV measurements for the devices shown in the EQE measurements yielded V_{OC} = 410 mV, J_{SC} = 9.4 mA cm^{-2}, FF = 0.35, R_S = 95 Ω sq^{-1}, n = 1.46 and PCE = 1.4 % for LAB and V_{OC} = 395 mV, J_{SC} = 17.4 mA cm^{-2}, FF = 0.35, R_S = 150 Ω sq^{-1}, n = 1.26 and PCE = 2.4 % for COM and that these are comparable with the V_{OC} = 370 mV, J_{SC} = 14.6 mA cm^{-2}, FF = 0.3, R_S = 150 Ω sq^{-1}, n = 3.75 and PCE = 1.7 % by Ong et al.[10]

It was demonstrated that the SWCNTs do not contribute to the photocurrent in these devices but then the influence of the back contact was studied by fabricating otherwise identical solar cell devices using silver paste as the back contact electrode instead of eGaIn, and measuring the EQE (**Figure 4.4**). The work function of eGaIn is $\phi \sim 4.16$ eV whereas for silver paste $\phi \sim 4.5$ - 4.8 eV and eGaIn makes a good ohmic contact to n-type silicon ($\phi \sim 4.26$ eV) whereas silver paste does not. In the spectra of as prepared COM (silver) devices (**Figure 4.4**(a), dotted line) there is a prominent feature in the range ~ 900 - 1200 nm that is not present in devices where eGaIn is used as the back contact (**Figure 4.4**(a), dashed line). A similar feature is also present in the EQE of the as prepared, silver-backed LAB devices (**Figure 4.4**(b), dotted line) and even after both of these devices have been treated with HF this feature remains apparent as a shoulder in **Figure 4.4**(a) and (b), solid lines. This is especially obvious when comparing the eGaIn and silver backed devices, and particularly in the case of the COM devices in **Figure 4.4**(a). Importantly, the feature does not appear to be correlated with any of the SWCNT absorption characteristics shown for comparison in **Figure 4.4**(a) and **Figure 4.4**(b), dash-dotted lines.

The decrease in the EQE towards shorter wavelengths (900 - 1000 nm) is typical of a back-illuminated Schottky junction solar cell.[31] Here it is important to note that the terms 'front-illuminated' and 'back-illuminated' refer to whether the rectifying contact is illuminated directly, or indirectly through the device substrate, respectively. To determine whether or not this is the origin of the 900 - 1200 nm feature in **Figure 4.4**, the IQE of a back-illuminated solar cell with an ohmic contact and a rectifying contact, as shown in **Figure 4.5**(a), has been calculated using the analytical model of Basu and Saha.[31] Equation (9) in that work uses as fitting parameters the thickness of the semiconducting layer, t, the width of the depletion layer, d, the minority carrier diffusion length, L, the minority carrier diffusion coefficient, D, the surface recombination velocity, s, and the wavelength-dependent absorption coefficient, $\alpha(\lambda)$. This work used t = 525 µm,

L = 500 µm, D = 10^{-3} m^2 s^{-1}, for 525 µm thick n-type silicon with a donor density of 10^{14} cm^{-3},[32] used $\alpha(\lambda)$ from Green[33] and $d \leq 10^{-6}$ m and s = 1 m s^{-1} were set as best fit to the photocurrent spectra of the as-prepared cells with silver back contacts. The IQE of a front-illuminated solar cell with a rectifying contact and an ohmic contact, as shown in **Figure 4.5**(b), has also been calculated, based on the analytical model of Soukoup and Akers[34] requiring only L and $\alpha(\lambda)$ as parameters, which was chosen identical to the back-illuminated case. **Figure 4.5**(c) shows the IQE modeling results for front- and back-illuminated solar cells. The non-monotonic behavior for the back-illuminated cell is due to the enhanced absorption of shorter wavelength light by the substrate and the limited diffusion of the minority carrier towards the charge separating back contact. Hence a back-illuminated device can generate photocurrent only in the long wavelength range.

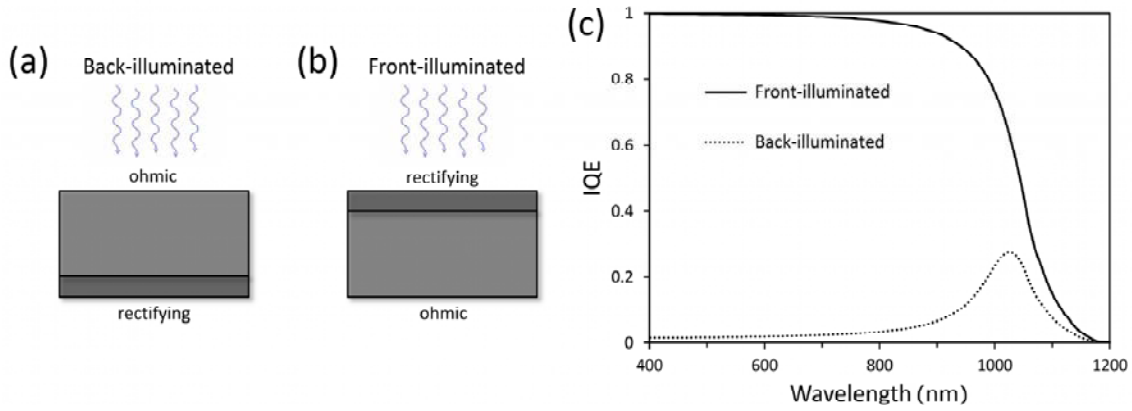

Figure 4.5 Schematics of the modelled front (a) and back (b) illuminated cells and (c) the calculated IQE of front and back illuminated solar cells with rectifying or ohmic front and back contacts.

Comparing the IQE spectrum of the modelled back-illuminated silicon Schottky junction solar cell, **Figure 4.5**(c), with the feature observed in the EQE of the silver-backed SWCNT-silicon solar cell, **Figure 4.5**(a), solid line and dotted line, it seems likely that the enhanced EQE in the wavelength range close to the absorption edge of silicon arises due to the contribution of a rectifying back contact rather than as a result of contribution to the photocurrent from the nanotubes. The presence of this contact leads to predictably poor solar IV parameters of V_{OC} = 180 mV, J_{SC} = 0.5 mA cm^{-2}, FF = 0.14, R_S = 24 kΩ sq^{-1}, n = 1.97 and efficiency = 0.01 % for

LAB and V_{OC} = 226 mV, J_{SC} = 3.1 mA cm^{-2}, FF = 0.17, R_S = 53 kΩ sq^{-1}, n = 2.06 and PCE = 0.12 % for COM. This is despite the fact that the silver backed devices were otherwise identical to the eGaIn devices and the silver paste itself is conductive.

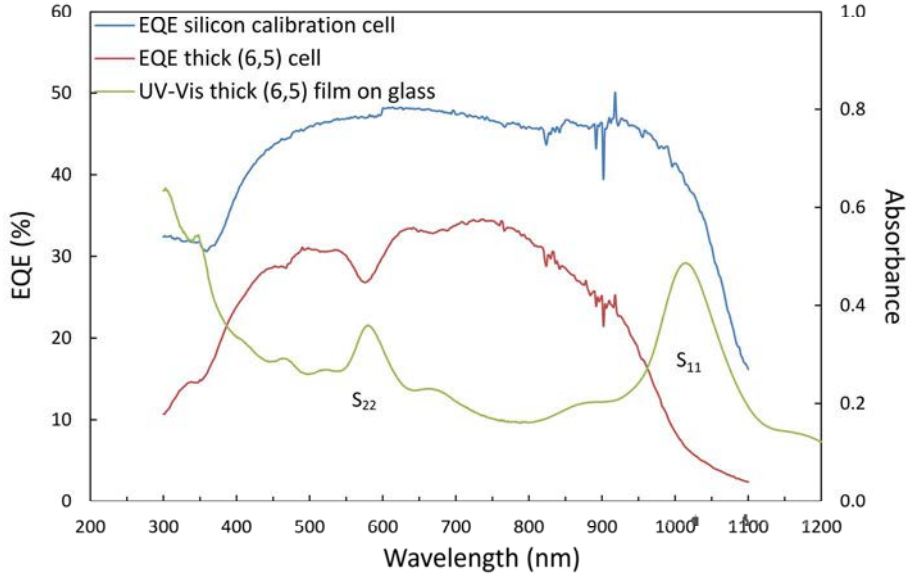

Figure 4.6 EQE (red) and UV-Vis (green) data corresponding to a device made with a very thick film of COM (6,5) nanotubes. The reduction in efficiency in the region of the nanotube S_{22} is quite clearly a result of light absorption by the nanotubes. The EQE of a silicon calibration cell (blue) displays no such features. Also apparent by comparison are the effects of the nanotube S_{11} in the 1050 nm region and π-π* absorption in the UV. The sharp features in the 800 - 1000 nm region are spectral artefacts from the instrument.

The SWCNT films used in this study and others are, by design, very thin and it may be that the contribution of such a film is so small that it was not observed. However, a device made with a much thicker film not only does not show a contribution from the SWCNTs but, rather, shows distinct reductions in efficiency in the regions of the S_{11}, S_{22} and π-π* absorptions (**Figure 4.6**). This is expected though since any exciton produced in the film away from a SWCNT-silicon junction would have no driving force for separation and cannot percolate far through the SWCNT network in the manner of free charges.[35] Any contribution could only come from the nanotubes in a thin region close to the silicon surface and so a thicker film effectively just gets in the way. An alternative explanation is that in a s-SWCNT-Si heterojunction, it may be possible to have a pn junction (with the

SWCNTs taking the role of the p-type material) even without observing a photocurrent response from the SWCNTs if the conduction band energy offset at the SWCNT-Si heterojunction is large enough to allow for rectification, but not large enough to overcome the exciton binding energy. In other words if the change in electron affinity between the s-SWCNT and Si does not exceed the SWCNT exciton binding energy then there should be no driving force for splitting the exciton into separable charge, but the change in electron affinity may be sufficient to establish a pn diode. In which case, photocurrent measurements are of no assistance.

If the SWCNTs do not contribute to the photocurrent then they function primarily as transparent front electrodes. This is possible even for a device made with high purity s-SWCNT material as, even without the presence of fluorine resulting from intentional acid treatment, adsorbed oxygen molecules act as p-type dopants. Indeed, for electrode purposes, it has been argued that one would ideally like to use highly doped s-SWCNTs (with a Fermi level pushed into the valence or conduction band) in preference to m-SWCNTs.[36] Even if the SWCNTs do not contribute to the photocurrent or take the role of p-type material in a pn junction, this does not necessarily mean that the mechanism of action of the devices is not that of a pn junction. Measurements by Jung et al.[1] on their SWCNT-silicon solar cells indicate that the mechanism is similar to that of a single crystal silicon pn homojunction. In those devices, removal of the native oxide significantly improved device performance. However, measurements by Jia et al.[24] on similar devices showed the opposite; that the presence of an interfacial oxide layer improved device performance, indicating an MIS mechanism. These differing results may be related to the structure of the SWCNT films in the different devices. In Jia's devices the SWCNT bundles were present as a porous, randomly aligned membrane but in Jung's the bundles were very highly aligned by design. The difference could also be due to the different types of SWCNT material, their (n,m) species purity or the effects of treatments they received during fabrication. Such apparently conflicting data further illustrates the complexity and diversity of SWCNT films and their

properties and underscores the need for more work to determine the effect of various films' nanostructure and component SWCNT type/species.

4.4 Summary

The photocurrent spectra of SWCNT-silicon solar cells fabricated with small and large diameter s-SWCNTs do not show any features that could be attributed to photocurrent generation by the SWCNTs. This is despite the fact that the SWCNTs used in this work were deliberately chosen so that any such contribution should be clearly discernible. Thus the SWCNTs in the devices reported herein are not contributing elements of a pn junction-type solar cell. Photocurrent spectra of SWCNT-silicon solar cells fabricated with non-ohmic back contact electrodes do show a similar feature to that which has been elsewhere attributed to photocurrent generation by the SWCNTs. However the data herein strongly suggests that this feature arises due to the choice of back contact electrode material. With this understanding in mind, future research endeavours in this field should be largely directed towards exploiting and optimising the application of SWCNTs as front contact electrodes. With very high transparency and excellent conductivity, SWCNTs are well suited to this purpose and could have the potential to surpass the performance of the current generation of front metallisation strategies via reduced optical shading and enhanced carrier collection over the full solar cell surface.

4.5 References

[1] Jung, Y., Li, X., Rajan, N.K., Taylor, A.D., and Reed, M.A., *Nano Letters,* **2012**. 13(1): p. 95-99.

[2] Shi, E., Zhang, L., Li, Z., Li, P., Shang, Y., Jia, Y., Wei, J., Wang, K., Zhu, H., Wu, D., Zhang, S., and Cao, A., *Scientific reports,* **2012**. 2: p. 884.

[3] *See reference 10 in [2].*

[4] Tzolov, M.B., Kuo, T.-F., Straus, D.A., Yin, A., and Xu, J., *The Journal of Physical Chemistry C,* **2007**. 111(15): p. 5800-5804.

[5] Wei, J., Jia, Y., Shu, Q., Gu, Z., Wang, K., Zhuang, D., Zhang, G., Wang, Z., Luo, J., Cao, A., and Wu, D., *Nano Letters,* **2007**. 7(8): p. 2317-2321.

[6] Arena, A., Donato, N., Saitta, G., Galvagno, S., Milone, C., and Pistone, A., *Microelectronics Journal,* **2008**. 39(12): p. 1659-1662.

[7] Li, Z., Kunets, V.P., Saini, V., Xu, Y., Dervishi, E., Salamo, G.J., Biris, A.R., and Biris, A.S., *Applied Physics Letters,* **2008**. 93(24): p. 243117-3.

[8] Li, Z., Kunets, V.P., Saini, V., Xu, Y., Dervishi, E., Salamo, G.J., Biris, A.R., and Biris, A.S., *ACS Nano,* **2009**. 3(6): p. 1407-1414.

[9] Li, Z., Saini, V., Dervishi, E., Kunets, V.P., Zhang, J., Xu, Y., Biris, A.R., Salamo, G.J., and Biris, A.S., *Applied Physics Letters,* **2010**. 96(3): p. 033110-3.

[10] Ong, P.L., Euler, W.B., and Levitsky, I.A., *Nanotechnology,* **2010**. 21(10): p. 105203.

[11] Behnam, A., Johnson, J.L., Choi, Y., Ertosun, M.G., Okyay, A.K., Kapur, P., Saraswat, K.C., and Ural, A., *Applied Physics Letters,* **2008**. 92(24).

[12] Jia, Y., Wei, J., Wang, K., Cao, A., Shu, Q., Gui, X., Zhu, Y., Zhuang, D., Zhang, G., Ma, B., Wang, L., Liu, W., Wang, Z., Luo, J., and Wu, D., *Advanced Materials,* **2008**. 20(23): p. 4594-4598.

[13] Jia, Y., Li, P., Wei, J., Cao, A., Wang, K., Li, C., Zhuang, D., Zhu, H., and Wu, D., *Materials Research Bulletin,* **2010**. 45(10): p. 1401-1405.

[14] Li, Z., Jia, Y., Wei, J., Wang, K., Shu, Q., Gui, X., Zhu, H., Cao, A., and Wu, D., *Journal of Materials Chemistry,* **2010**. 20(34): p. 7236-7240.

[15] Wadhwa, P., Liu, B., McCarthy, M.A., Wu, Z., and Rinzler, A.G., *Nano Letters,* **2010**. 10(12): p. 5001-5005.

[16] Jia, Y., Li, P., Gui, X., Wei, J., Wang, K., Zhu, H., Wu, D., Zhang, L., Cao, A., and Xu, Y., *Applied Physics Letters,* **2011**. 98(13): p. 133115-3.

[17] Wadhwa, P., Seol, G., Petterson, M.K., Guo, J., and Rinzler, A.G., *Nano Letters,* **2011**. 11(16): p. 2419-2423.

[18] Fujiwara, A., Matsuoka, Y., Suematsu, H., Ogawa, N., Miyano, K., Kataura, H., Maniwa, Y., Suzuki, S., and Achiba, Y., *Japanese Journal of Applied Physics, Part 2: Letters,* **2001**. 40(11 B): p. L1229-L1231.

[19] Freitag, M., Martin, Y., Misewich, J.A., Martel, R., and Avouris, P., *Nano Letters,* **2003**. 3(8): p. 1067-1071.

[20] Lee, J.U., *Applied Physics Letters,* **2005**. 87(7): p. 073101-3.

[21] Bindl, D.J., Wu, M.-Y., Prehn, F.C., and Arnold, M.S., *Nano Letters,* **2011**. 11(2): p. 455-460.

[22] Švrček, V., Cook, S., Kazaoui, S., and Kondo, M., *The Journal of Physical Chemistry Letters,* **2011**. 2(14): p. 1646-1650.

[23] Collins, P.G., Bradley, K., Ishigami, M., and Zettl, A., *Science,* **2000**. 287(5459): p. 1801-1804.

[24] Jia, Y., Cao, A., Kang, F., Li, P., Gui, X., Zhang, L., Shi, E., Wei, J., Wang, K., Zhu, H., and Wu, D., *Physical Chemistry Chemical Physics,* **2012**. 14(23): p. 8391-6.

[25] Spitzer, W. and Fan, H.Y., *Physical Review,* **1957**. 108(2): p. 268.

[26] Lebedkin, S., Schweiss, P., Renker, B., Malik, S., Hennrich, F., Neumaier, M., Stoermer, C., and Kappes, M.M., *Carbon,* **2002**. 40(3): p. 417-423.

[27] Moshammer, K., Hennrich, F., and Kappes, M.M., *Nano Research,* **2009**. 2: p. 599-606.

[28] Lebedkin, S., Hennrich, F., Kiowski, O., and Kappes, M.M., *Physical Review B,* **2008**. 77(16): p. 165429.

[29] Jain, R.M., Howden, R., Tvrdy, K., Shimizu, S., Hilmer, A.J., McNicholas, T.P., Gleason, K.K., and Strano, M.S., *Advanced Materials,* **2012**. 24(32): p. 4436-9.

[30] Kim, K., Ryu, J., Lee, C., Jang, J., and Park, K., *Journal of Materials Science: Materials in Electronics,* **2009**. 20(1): p. 120-124.

[31] Basu, P. and Saha, H., *physica status solidi (a),* **1976**. 37(2): p. 625-631.

[32] del Alamo, J.A. and Swanson, R.M., *Solid-state Electronics,* **1987**. 30(11): p. 1127-1136.

[33] Green, M.A. and Keevers, M.J., *Progress in Photovoltaics: Research and Applications,* **1995**. 3(3): p. 189-192.

[34] Soukup, R.J. and Akers, L.A., *Journal of Applied Physics,* **1978**. 49(7): p. 4031-4034.

[35] Mehlenbacher, R.D., Wu, M.-Y., Grechko, M., Laaser, J.E., Arnold, M.S., and Zanni, M.T., *Nano Letters,* **2013**. 13(4): p. 1495-1501.

[36] Rinzler, A.G. and Donoghue, E.P., *ACS Nano,* **2011**. 5(5): p. 3425-3427.

Chapter 5
The effect of film metallicity on SWCNT-silicon solar cells

This chapter explores the effect of the semiconducting/metallic nature, or 'metallicity' of the SWCNT film on solar cell properties and performance. Solar cells are fabricated using films of either unsorted SWCNTs, or SWCNTs sorted by metallicity. The sorted material is produced by gel chromatography and is highly purified in either m-SWCNT or s-SWCNT species. The effect of chemical doping of the SWCNTs is also investigated.

5.1 Introduction

Reliance on silicon is ubiquitous in the modern world however material limitations require the incorporation of a range of other, newer materials with desirable properties that can be exploited at the nanoscale where the drawbacks of bulk silicon dominate. The technologically important SWCNT-silicon heterojunctions have broad application in a variety of fields and are receiving increasing attention.[1] Although there have been major advances there is still much to be understood to enable a fruitful marriage between established silicon technology and the carbon newcomer. A factor that has limited progress in the understanding and application of SWCNT-silicon heterojunctions has been the polydispersity of as-produced SWCNT material. Whilst technological routes to the separation of SWCNTs by (n,m) species have been known for some time,[2-7] production has predominantly been in small research quantities and there has been slow progress in scale-up, although recent refinements to chromatographic separation methods may offer practical solutions. These include tailoring the tube-gel interaction through temperature control,[8] pH variation[9] and surfactant concentration.[10]

As outlined in Chapter 1, a promising applications of SWCNT-silicon heterojunctions is in photovoltaic devices. SWCNT-silicon solar cells have seen very significant performance gains with recent reports of reasonable dry-state, small area efficiencies from Jia[11] (2011, 10.9 %), Jung[12] (2012, 11.2 %) and Shi[13] (2012, 15 %). There has been work revealing the mechanism of action of these devices[14-18] and other reports of novel ways to improve upon the basic SWCNT-silicon design.[18-20] However, as discussed in Chapters 1 and 4, in some respects the data is apparently conflicting, likely as a result of the complexity and diversity of SWCNT films, their metallicity, various nano- and microstructures, component species and the effect of any treatments they receive during device fabrication. Resolving the contribution of these different factors from the literature can be further complicated by inadequate SWCNT and film characterisation. As a step towards more fully understanding the role of SWCNT film metallicity in these devices this chapter

reports the first direct comparison between SWCNT-silicon heterojunction solar cells fabricated with unsorted SWCNTs and sorted m-SWCNT and s-SWCNT material. Additionally, the effect on these systems of $SOCl_2$ and HF treatments is also reported.

5.2 Method

The test solar cells were fabricated, and films deposited on both glass and silicon substrates to allow film characterisation, as in section 3.2. Additionally, for each material type, three different optical densities were used; roughly corresponding to T_{av} = 96 %, 90 % and 84 %. Each such solar cell was made in duplicate and solar cell parameters are averaged from both devices with the standard deviation most often contained within the extent of the data point markers. SWCNT dispersions were generated from 25 mL solutions of either 2 or 0.5 % w/v SDS containing 1 mg mL^{-1} HiPCO SWCNTs via tip ultrasonication (Sonics VCX 750 W) for 45 min. Sonication was performed at 20 kHz with a 6.5 mm Ti microtip operating at 22 % of the maximum amplitude (corresponding to a power input of approximately 0.4 W mL^{-1}).[21] Samples were cooled with ice water during exposure to ultrasound and were ultracentrifuged directly after sonication. Ultracentrifugation was carried out at fixed angle for 90 min at 40500 rpm (~ 120 x 10^3 g) in a Ti rotor (Type 70) mounted in an ultracentrifuge (Optima L-100XP, Beckman-Coulter), with the upper 75 - 85 % of the supernatant collected via pipette. Unsorted SWCNT films were prepared from this centrifuged supernatant; however the SWCNT solution was diluted 1:5 in DI water before creation of the unsorted films to account for the very large difference in concentration between this and the sorted fractions. This is because such a large concentration difference introduces unacceptably high uncertainty in the film thickness calibration process used to ensure consistent optical density between films.

For metal-semiconductor separation, the gel chromatography technique was used.[22-24] SWCNTs dispersed in DI water at an SDS concentration of 0.5 % w/v were used

as a starting solution. This concentration was selected as it has been found to provide the best metal-semiconductor separation for the HiPCO SWCNT distribution.[10] A glass column with a fritted disc was filled with 30 mL of Sephacryl S-200 HR (N,N'-methylenebisacrylamide cross linked allyl-dextran; 25 - 75 μm diameter) gel bead solution to give a bed height of approximately 22 cm. The gel was first washed with 30 mL of DI water followed by 30 mL of 0.5 % w/v SDS before addition of the SWCNT solution (10 mL). Elution was facilitated by application of unregulated nitrogen flow to the top of the column, giving a variable flow rate of 0.5 - 0.8 mL min^{-1}. The flow through eluate was collected with the addition of 15 mL 0.5 % w/v SDS solution to the column until the coloured mobile band was observed to be completely eluted. This flow through solution is very highly enriched in metallic species and was therefore used to prepare m-SWCNT films.

Although it is possible to collect the s-SWCNT fraction in this process by further eluting the SWCNT material that is adsorbed to the gel, this would provide a large number of different SWCNT species with varied optical properties. To obtain a semiconducting fraction of significantly reduced chirality distribution, the gel separation process was performed again in a manner similar to Liu et al.[22] In this case, SWCNTs dispersed in 2 % w/v SDS were used as the starting suspension with only 0.6 mL of gel beads, providing a thin gel bed. The gel was washed with DI water and 2 % w/v SDS prior to addition of 10 mL of SWCNT solution, which was passed through the gel bed and collected. The gel was then washed by 6 mL of 2 % w/v SDS before changing the eluent to 0.5 % w/v sodium deoxycholate (DOC). The s-SWCNTs are desorbed from the gel in this surfactant and were collected in a 3 mL aliquot. The gel bed was then flushed by DI water and 2 % w/v SDS before repeating this procedure, re-using the same original SWCNT dispersion to generate a second semiconducting fraction. Three such fractions were collected before replacing the gel and collecting additional fractions. Suspensions of the unsorted material and the enriched fractions were diluted in DI water at a concentration of 1 μL mL^{-1} and then used to prepare solar cells as in section 3.2.

To determine the optical density of the SWCNT films, the absorbance at two points on the spectra of each material was averaged as shown in **Figure 5.1** and then converted to transmittance. The points were chosen to be at wavelengths least affected by the changes to the S_{11}, S_{22} or M_{11} optical transitions that are caused by chemical doping, as well as providing a meaningful comparison between the films within this thesis and with the T_{550} values given in other work. Since the absorption features of the different films occur at different wavelengths, the two points chosen are different for each film type.

As discussed in section 3.2, considerable care must be taken to ensure the reproducibility of vacuum filtration SWCNT films. **Figure 5.2** shows the calibration data used to achieve this, where the slope gives a relative measure of the concentration of the SWCNT source suspension. As can be seen, the unsorted suspension (already diluted 1:5) is almost twice as concentrated as the metallic fraction and ~ 7 x more concentrated than the semiconducting fraction. **Figure 5.3** shows the variation in R_{sheet} of the SWCNT films with the volume of starting suspension, where the slope gives a relative measure of 'resistivity', here denoted ρ^* and having the units of $k\Omega\ \mu L\ sq^{-1}$ but different to resistivity in its usual form, which has the units of Ω cm. The metallic material starts out with ρ^* ~ 2 orders of magnitude lower than the unsorted material, itself ~ 20 x lower than the semiconducting material but this changes with $SOCl_2$ doping, as will be discussed in the next section. An anomaly exists in that the slopes of the m-SWCNTs before and after doping appear to show that the doping makes the m-SWCNT material more resistive. This is untrue, as shown in **Table 5.1** and discussed in the next section, and is most likely due to the m-SWCNT data point with the highest R_{sheet} being an outlier (before doping).

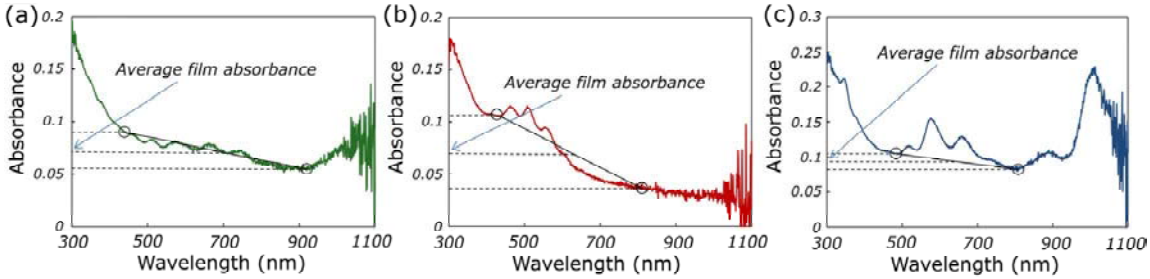

Figure 5.1 Method used to estimate average film absorbance for the three types of SWCNT material whilst avoiding any distortion due to the absorption peaks, (a) unsorted, 450 nm & 930 nm, (b) metallic, 440 nm & 800 nm, (c) semiconducting, 495 nm & 800 nm.

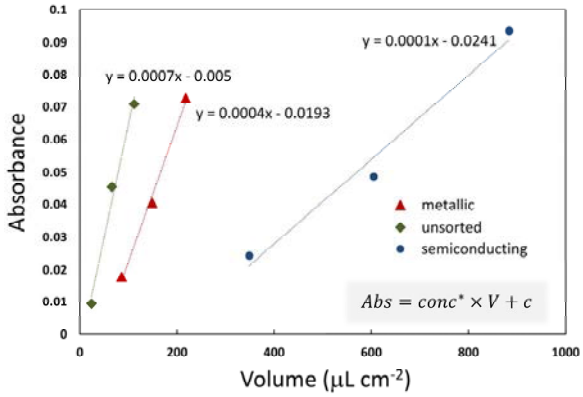

Figure 5.2 Calibration of SWCNT films showing the variation in optical density with the volume of SWCNT suspension used per area of filter membrane.

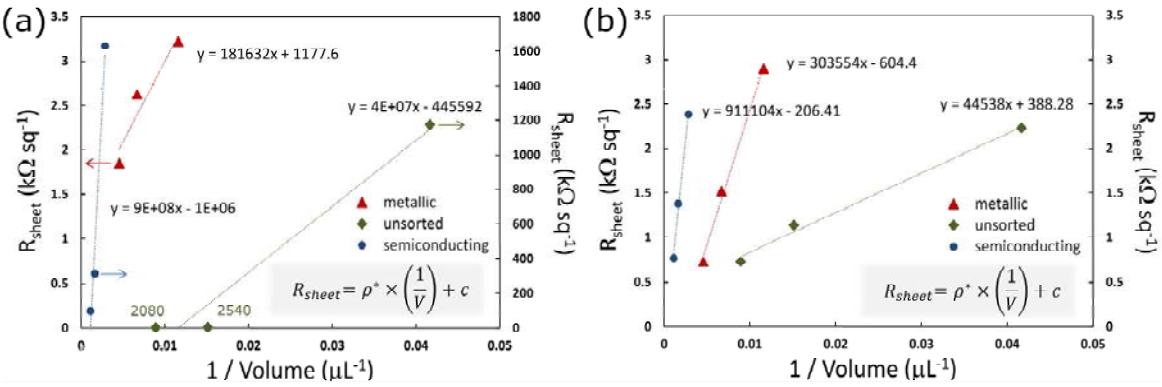

Figure 5.3 Variation in sheet resistance with the volume of SWCNT suspension used per area of filter membrane and corresponding to (a) as prepared devices and (b) $SOCl_2$ doped devices

5.3 Results and discussion

PL measurements performed on aqueous suspensions of the unsorted SWCNTs and the two sorted fractions that were used (**Figure 5.4**) show that the three types of SWCNT material are composed of distinctly different populations. The unsorted material contains the expected large range of chiralities with S_{11} < 1400 nm (the measurement cut-off due to water absorption). The PL process involves absorption of a high energy photon through S_{22}, followed by decay of the excited state to S_{11} and then radiative relaxation down to the ground state. Naturally, m-SWCNTs cannot be observed by this technique (no M_{22} in the practical range of measurement) but the m-SWCNT PL data is still important in that it indicates the metallic purity of the m-SWCNT fraction or, more correctly, the lack of semiconducting species. The s-SWCNT fraction is dominated by the (6,5) nanotube, but also with significant amounts of (6,4), (7,5), (7,6) and traces of others.

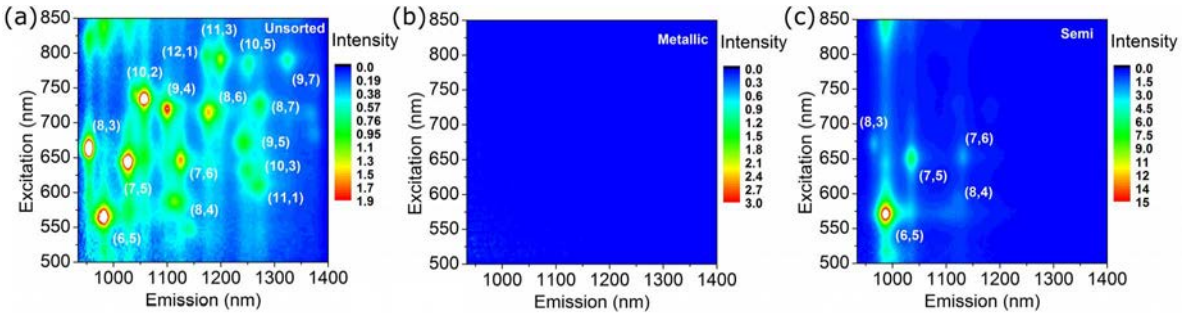

Figure 5.4 PL maps of (a) unsorted (denoted "U"), (b) metallic (M) and (c) semiconducting (S) SWCNT material used in the devices. Note that m-SWCNTs cannot be observed by this measurement, see text.

Current-voltage measurements obtained from solar cells fabricated with the three different kinds of SWCNT starting material (**Figure 5.5**(a-c)) show markedly different output characteristics (**Table 5.1**). The devices made with m-SWCNTs clearly outperform their semiconducting and unsorted counterparts. This is despite great care being taken to ensure that the amount of material (optical density) in the different films is comparable (**Figure 5.5**(d-f)). In the case of the semiconducting material and the devices with the thinnest of the unsorted films, it can easily be argued that this is due to the very high R_{sheet} of the films, in the MΩ range

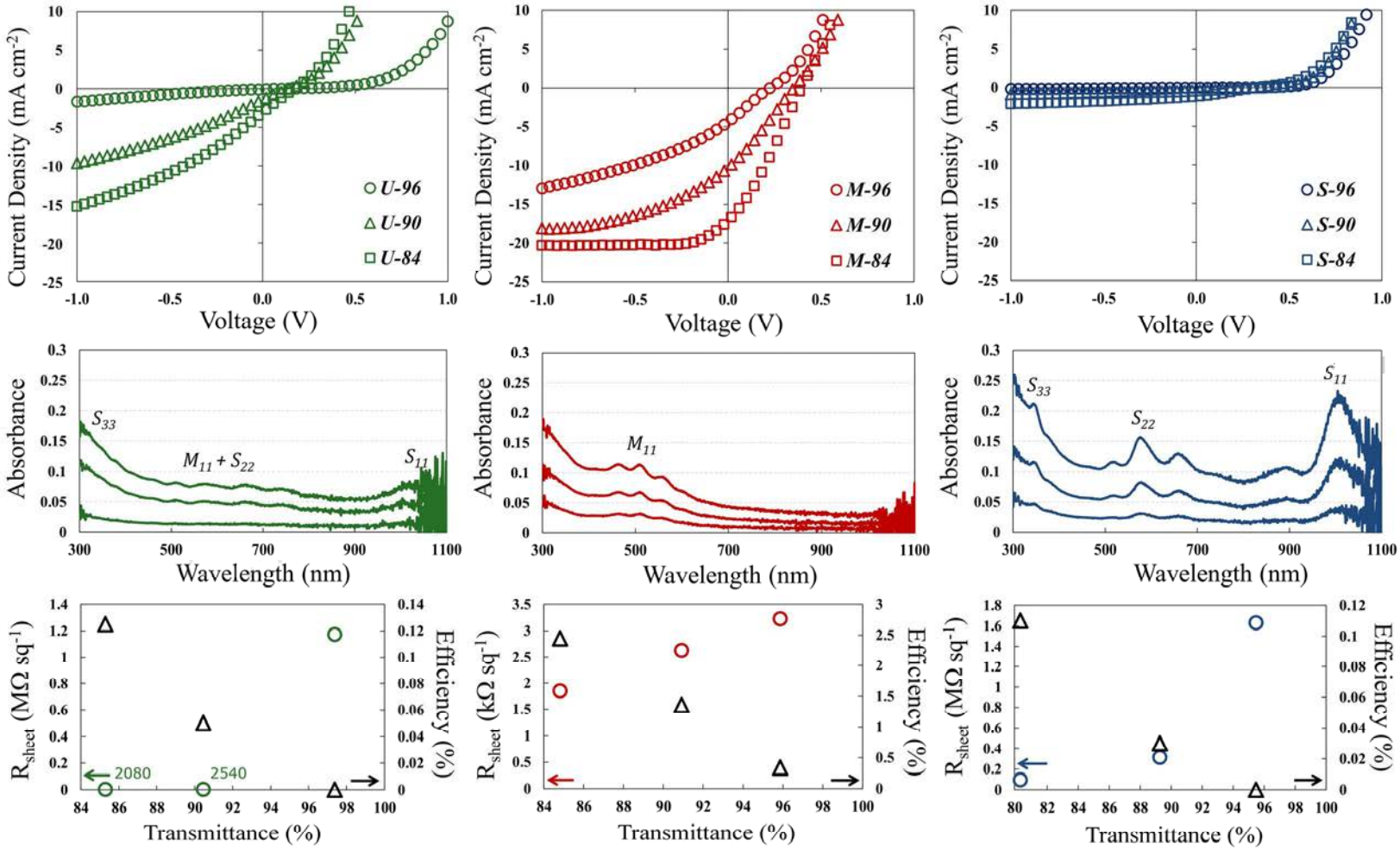

Figure 5.5 Current-voltage characteristics of solar cell devices made with either (a) unsorted (denoted 'U') (b) metallic (M) or (c) semiconducting (S) SWCNT material at three different optical densities (approximately 96 %, 90 % and 84 % transmittance). (d-f) show the corresponding UV-Vis-NIR absorption spectra (obtained from SWCNT films on glass) and (g-i) show the variation of R_S and PCE as a function of SWCNT film transmittance.

Table 5.1 Summary of measured and calculated photovoltaic performance and device parameters as well as optical transmittance and R_{sheet} of the SWCNT films used pre- and post-treatment with $SOCl_2$.

	U-96		U-90		U-84		M-96		M-90		M-84		S-96		S-90		S-84	
	pre-	post-	pre-	post-	pre-	post-	pre-	post-	pre-	post-	pre-	post-	pre-	post-	pre-	post-	pre-	post-
J_{sc} (mA cm^{-2})	0.08	1.06	1.46	18.48	3.12	21.68	5.05	13.93	11.51	17.89	18.03	19.71	0.02	1.63	0.39	5.98	1.17	11.00
V_{oc} (V)	0.14	0.46	0.14	0.53	0.18	0.54	0.27	0.48	0.41	0.50	0.44	0.50	0.18	0.44	0.32	0.49	0.33	0.50
FF	0.24	0.27	0.23	0.36	0.23	0.39	0.25	0.34	0.29	0.38	0.31	0.47	0.25	0.33	0.24	0.37	0.28	0.37
PCE (%)	0.00	0.13	0.05	3.58	0.13	4.51	0.34	2.28	1.36	3.39	2.45	4.51	0.00	0.26	0.03	1.08	0.11	2.01
R_{SH} (Ω)*	2.25E+04	1.17E+04	1.12E+03	8.29E+02	6.53E+02	1.51E+03	7.94E+02	9.13E+02	7.09E+02	3.94E+03	6.57E+02	1.28E+04	1.06E+05	1.01E+04	1.17E+04	2.30E+03	6.06E+03	1.23E+03
R_S (Ω)*	2.73E+04	7.14E+03	1.30E+03	1.75E+02	7.70E+02	1.47E+02	7.42E+02	2.49E+02	4.15E+02	2.00E+02	2.55E+02	1.48E+02	1.14E+05	3.47E+03	1.41E+04	4.96E+02	4.53E+03	2.67E+02
Ideality†	3.07	2.45	1.61	1.62	1.59	1.57	1.55	1.71	1.50	1.25	1.45	1.30	3.20	2.58	3.03	2.10	2.47	1.89
J_0 (mA cm^{-2})†	1.99E-03	2.09E-04	2.27E-03	1.45E-05	1.19E-03	9.13E-06	2.82E-04	1.01E-04	6.00E-05	2.03E-06	7.76E-05	7.63E-06	5.67E-03	8.97E-03	5.54E-03	1.54E-03	7.63E-03	8.36E-04
Φ_{SBH} (eV)†	0.70	0.76	0.71	0.71	0.72	0.84	0.75	0.78	0.81	0.88	0.81	0.86	0.76	0.76	0.74	0.77	0.73	0.79
Transmittance (%)	97.4	98.3	90.4	90.5	85.3	85.5	95.9	95.7	90.9	90.9	84.8	84.7	95.5	95.0	89.3	89.4	80.4	80.6
R_{sheet} (Ω sq^{-1})	1.17E+06	2.23E+03	2.54E+03	1.14E+03	2.08E+03	7.26E+02	3.22E+03	2.90E+03	2.62E+03	1.52E+03	1.85E+03	7.27E+02	1.63E+06	2.38E+03	3.14E+05	1.38E+03	9.56E+04	7.68E+02

* = calculated from the current-voltage curves, † = calculated from semilog plot of current-voltage

((**Figure 5.5**(g-i)), which causes a high R_{sheet}. However this reasoning fails when trying to rationalise the ~ 20 x improvement in PCE when using metallic vs. unsorted SWCNTs in the thicker film devices, which have comparable R_{sheet}. Furthermore, the fact that R_{sheet} is relatively the same for the unsorted and metallic devices with the thicker films (U-84 and M-84), yet R_S is ~ 3 x greater in the unsorted, means that there are other factors involved.

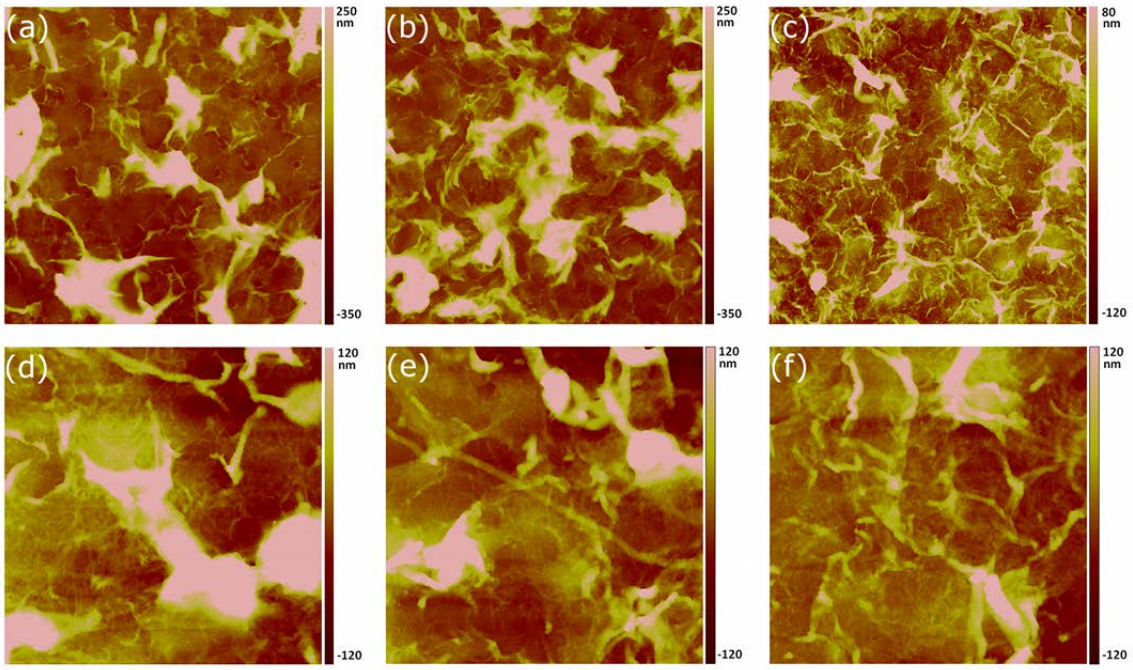

Figure 5.6 AFM images (15 x 15 µm) from films of (a) unsorted SWCNTs, (b) m-SWCNTs and (c) s-SWCNTs. (d-f) show the same films as (a-c) on a 5 x 5 µm scale.

AFM measurements (**Figure 5.6**) show the morphology of the films, including thickness, bundle size, level of connectivity and degree of alignment (none), is also comparable for similar thicknesses. There are differences in the height range seen in **Figure 5.6**(a-c), where the unsorted and metallic films show a greater range, but on a smaller scale **Figure 5.6**(d-e) it can be seen that the films are very similar. In fact the smaller height range of the s-SWCNT films should produce a more conformal coverage of the silicon surface and thus provide a better interface. If not due to morphological differences in the films, the substantial difference in output characteristics must therefore arise as a direct result of the intrinsic differences in the SWCNT films used.

Correlation of the first transition peak positions shown in the UV-Vis-NIR (**Figure 5.5**(e) and (f)) with Haroz et al.[25] and Weismann, et al.[26] shows that the most likely species in the m-SWCNT material are the (7,7), (8,8) and (9,9), and confirms the PL measurements for the s-SWCNTs. Thus, although the unsorted material contains a distribution of SWCNT diameters, the m-SWCNT and s-SWCNT diameters are relatively the same. Also, since they are all derived from the same starting material, the strong dependence of the film conductivity on SWCNT length is not an issue. The unsorted material was suspended with SDS and the m-SWCNT material was suspended and eluted with SDS, however the s-SWCNT material was suspended in SDS but eluted by the addition of DOC and it is conceivable that this may in some way give rise to the observed JV differences. However it must be noted that, a) the films were thoroughly rinsed with a very large volume of DI water, and this is expected to remove most surfactant, b) films produced with DOC have been shown to outperform, in terms of electrical characteristics, those made with SDS due to improved fine structure (smaller bundles, better connectivity),[27] although this was not observed for these filtered films (**Figure 5.5**(d-e)) where the inherent effect of aggregation due to filtering through defined pores dominates the effect of different surfactants on the film structure, c) the brief HF treatment and ethanol rinse applied to the films/devices prior to measurement is expected to, if anything, desorb any remaining surfactant molecules, and, d) a visual inspection of the JV characteristics suggests that the performance of the unsorted devices is intermediate between that of the metallic and semiconducting devices, which indirectly suggests that the performance of the semiconducting devices is not anomalous relative to that of the unsorted or metallic devices (and no DOC was present in the unsorted films). Thus, if the different output characteristics are not caused by differences in the SWCNT films, they must arise due to inherent differences in the SWCNTs.

Considering the DOS of s-SWCNTs, silicon and m-SWCNTs shown in **Figure 5.7**(a), (b) and (c), respectively, elucidating an energy diagram for these devices is not a trivial matter. One may (boldly) draw up the energy diagram of the s-SWCNT-silicon interface as a classical pn junction and, as discussed in Chapter 4,

this is possible even without the observation of contribution to the photocurrent from the SWCNTs, if the offset at the junction is just right. In the work of Jung et al.,[12] the observation of a very long minority carrier lifetime does indeed indicate a pn mechanism. Also in that work, the activation energy, E_a, of the SWCNT-silicon solar cells was determined to be 1.12 eV, the same as the silicon bandgap, which indicates that it is the silicon that produces the photocurrent. However, this also indicates that it is not the s-SWCNTs that take the role of the p side of the active junction because $E_a = E_g$ should only occur for a silicon pn homojunction[28] (or if the bandgap of the nanotubes just happens to be exactly the same as silicon, which is unlikely in general and certainly not the case in the Jung et al. work, which used mixed SWCNTs). If the SWCNTs do not act as the p-type material, this does not necessarily preclude an underlying pn mechanism for the devices because this mechanism also underlies the MIS system,[29] where the active region exists between the silicon bulk and the inversion layer created adjacent to the oxide. In fact, the MIS mechanism is consistent with published work in this field as described in Chapter 1 and best represented in Jia et al.,[15] as well as with the observations in this thesis, in which an appropriate thickness of oxide is seen to be highly beneficial. The exception is the very recent work from the Reed group,[12, 17] in which it is reported that the removal of the oxide has a negative effect on device performance. Compared to the rest of the field, that work is peculiar in that very highly aligned films were used and it may be that this is the cause of the unusual observation.

In the case of m-SWCNTs, the M_{11} transition shown in **Figure 5.7**(c) is an optical transition only – despite the existence of the VHSs this is not a semiconducting material and should never form a pn junction. Thus, it appears unlikely that either the m-SWCNT or s-SWCNT devices (and, by extension, the unsorted SWCNT devices) operate by a classical pn mechanism, with the SWCNTs acting as the p-type material. Furthermore, the single particle model shown in **Figure 5.7**(a) and **Figure 5.7**(c) is a simplification; the SWCNTs absorption properties are in fact entirely excitonic in nature.[30] Although unlikely, it may even be that in such a simplified model the junction-defining characteristics are not retained.

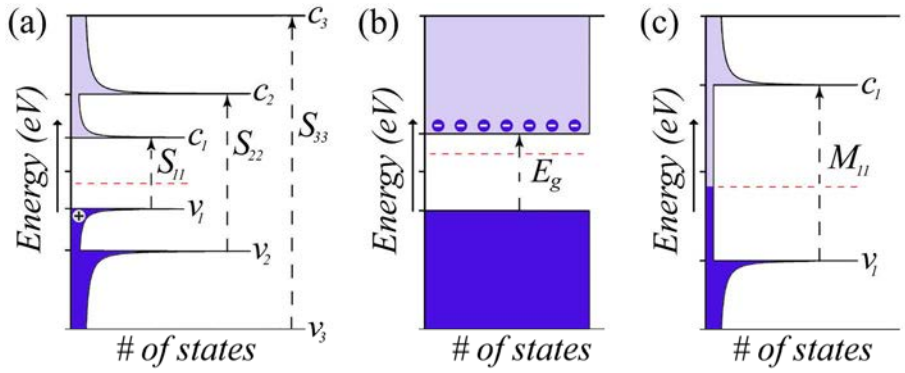

Figure 5.7 Density of states of the (a) s-SWCNTs, (b) bulk silicon and (c) m-SWCNTs used in devices. The valance (v_i) and conduction (c_i) states are indicated in the SWCNTs, as are the optical transitions giving rise to the S_{ii} and M_{11} excitons. The bandgap energy (E_g) of silicon is 1.12 eV and the Fermi energy is indicated by dashed red lines. The alignment of the silicon bands with the VHS in the s-SWCNT and m-SWCNTs is shown to form. The Fermi energy in the silicon is shifted up ~ 0.25 eV due to the moderate n-doping whilst that of the SWCNTs is shifted down slightly to account for p-type doping by adsorbed oxygen molecules.[31]

If unavoidable p-type doping of the SWCNTs by adsorbed oxygen molecules is assumed to shift the SWCNT Fermi energy down by a modest ~ 100 meV (a reasonable figure for large bandgap SWCNTs)[31] then the difference in Fermi energies between the moderately doped n-type silicon and the (6,5) s-SWCNTs is ~ 4.6 eV - 4.26 eV ≈ 0.34 eV. This difference causes the formation of a built-in potential, V_{bi}, upon contact between the materials, which in turn sets an approximate limit on V_{OC} and correlates well with that measured from devices (0.33 V for S-84 devices). The V_{OC} of the metallic devices tended towards a higher value of 0.45 V with increasing film thickness. The distribution of species in the unsorted material, and thus conduction/valance state and first excitonic transition energies, will surely give rise to the formation of intertube energy barriers and localised charge traps in the film. This would contribute to an enhanced recombination current that would reduce the device potential under illumination. This is both the likely cause of the lower V_{OC} of 0.19 V and a likely contributor to the ~ 3 x greater device series resistance in the thicker unsorted vs. metallic devices, which have very similar R_{sheet} of $2.08 \times 10^3\ \Omega\ sq^{-1}$ and $1.85 \times 10^3\ \Omega\ sq^{-1}$, respectively. The FF is roughly the same for all three kinds of SWCNTs (likely limited by the high R_S). However, J_0, which depends on the quality of the diode,

through the metallic devices is over an order of magnitude lower than through the unsorted, and over two orders lower than through the semiconducting devices i.e. it follows the trend m-SWCNT < unsorted SWCNT < s-SWCNT. This is consistent with the observation that, whatever the operating mechanism, the width and homogeneity of the space charge region set up in the silicon, and thus the quality of the diode, will depend heavily on the initial carrier concentration at the Fermi level of the SWCNT, which follows the trend m-SWCNT > unsorted SWCNT > s-SWCNT. As well, a visual inspection of the current-voltage curves in the reverse bias regime suggests that, at least in the thicker film devices, the m-SWCNT devices are doing a better job of maintaining charge separation (slope ~ 0). In short summary, the performance of the solar cells follows the trend in SWCNT film metallicity with the m-SWCNT solar cells significantly outperforming the unsorted devices, which in turn outperform the semiconducting devices.

The situation becomes remarkably different after the application of the powerful organic oxidiser, $SOCl_2$, to the SWCNT films (**Figure 5.8**). Following treatment with $SOCl_2$ there is almost complete bleaching of the S_{11} absorption and a substantial decrease in the intensity of S_{22} and this is consistent with electron transfer from the top of the SWCNT valance states to the organic oxidiser.[32] As discussed in Chapter 3, the electron withdrawing nature of this treatment has a strong p-type doping effect on the SWCNTs and has been repeatedly shown to greatly improve SWCNT film conductivity, and the performance of similar solar cells made with them. This is clearly in evidence here; the s-SWCNT films underwent decreases in R_{sheet} of 2 - 3 orders of magnitude, depending on film thickness, similarly with the unsorted SWCNT films. Concurrently, a ~ 20 x improvement in s-SWCNT device PCE (0.11 % - 2.01 % for S-84) was observed, and a ~ 35 x improvement in unsorted SWCNT device PCE (0.13 % - 4.51 % for U-84), accompanied by relatively similar increases for the thinner film devices. It should not be possible to p-dope the m-SWCNTs down into the VHS by chemical doping alone (an increase in the work function of ~ 1.2 eV!) and this is confirmed by

the lack of observation of M_{11} bleaching seen in the UV-Vis-NIR (**Figure 5.8**(e)). Therefore, unlike in the case of unsorted and s-SWCNTs, the p-doping should not significantly alter the density of states at the Fermi level (see **Figure 5.7**(c)). As discussed in Chapter 3, the $SOCl_2$ lowers the contact resistance at the tube-tube junctions, tightening the bundles as observed by M_{11} peak broadening in **Figure 5.8**(e). These two effects should improve the conductivity of the film, but not nearly to the same degree as shifting the Fermi energy fully into a VHS. This is commensurate with the observation of only relatively minor improvements in R_{sheet} (~ 10 - 70 %, depending on thickness) and PCE (2.45 % - 4.51 % for M-84) for the m-SWCNT films/devices. The improvements in PCE are well correlated with measured improvements in the R_{sheet} of the SWCNT films and the changes in the trends in PCE with film transmittance exactly match changes in the corresponding trends in R_{sheet}, i.e. the very noticeable change for the unsorted and semiconducting films from nonlinear before treatment to distinctly linear after (the trend in the m-SWCNT film R_{sheet} with transmittance remained linear).

The $SOCl_2$ treatment greatly increases carrier (hole) density, reducing energy barriers at tube-tube junctions[33] and switching the conduction mechanism from thermionic emission over tube-tube barriers to tunnelling through them.[34] The fact that R_{sheet} of the thinner m-SWCNT films' remained relatively unaffected compared to the other films is consistent with the fact that the conductivity of those films was not limited to any great degree by low carrier density at the Fermi level like the semiconducting and unsorted films. Rather it may be that they were already limited by the density, degree of alignment and level of connectivity in the film, which then also become limiting factors in the semiconducting and unsorted SWCNT films after the $SOCl_2$ treatment. However, despite the obvious huge changes in SWCNT film conductivity, R_{sheet} of the three thicker films is, conveniently, almost identical (726, 727 and 768 Ω sq^{-1} for unsorted, metallic and semiconducting, respectively). This precludes the improved conductivity due to the $SOCl_2$ treatment as the only contributor to the observed differences between device types.

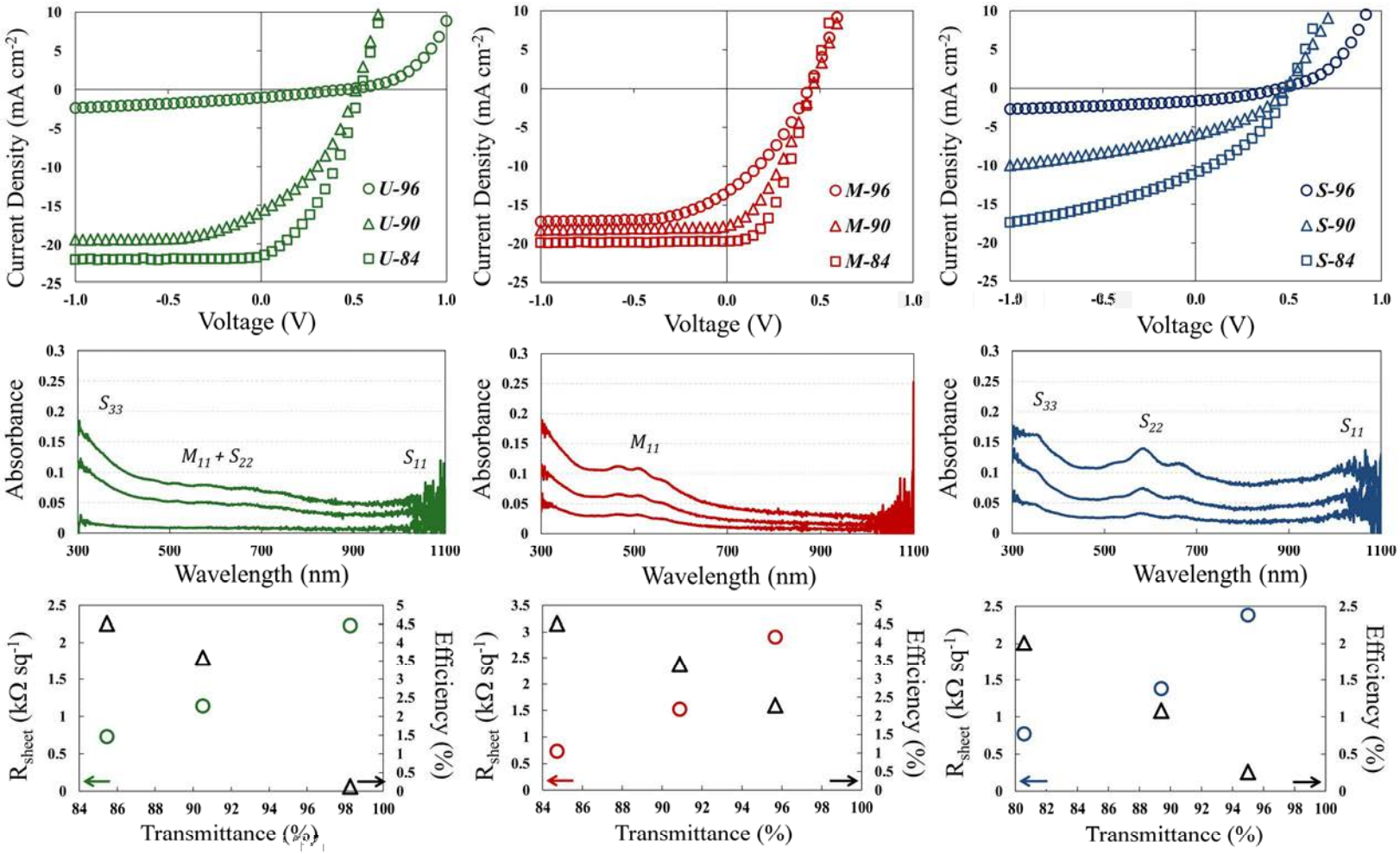

Figure 5.8 Current-voltage output of solar cells, optical absorption and R_{sheet} of SWCNT films, after doping with $SOCl_2$.

One of the most striking differences is that both J_{SC} and V_{OC} of the unsorted SWCNT solar cells are now better than of the m-SWCNT ones, although the FF are poorer in the unsorted, which results in solar cells of both types being equally 4.5 % efficient. A probable cause can be found in the ρ* changes observed in **Figure 5.3** where ρ* of the m-SWCNTs starts out much better than the unsorted ρ* (182 kΩ μL sq^{-1} vs. 40 MΩ μL sq^{-1}) but then, after $SOCl_2$ treatment, ρ* of the unsorted SWCNTs becomes better than that of the m-SWCNTs (44 kΩ μL sq^{-1} vs. 304 kΩ μL sq^{-1}). This may be because the complex mixing of states in the films' DOS means that the average carrier density in the unsorted films is now higher at the new Fermi energy since these films contain a proportion of s-SWCNT doped into their VHS. Considering the nanoscale dimension of the basic material elements and their presumably homogeneous physical mixing in the film as well as their high conductivity, particularly after doping, it is not unreasonable that the bulk material properties may be an average of those of the individual SWCNT species. It may also be that in some respects the SWCNT films behave like an alloy – where the electrical properties can exhibit features not found in any single component. In this case, it should be possible to fabricate SWCNT films with specifically tailored properties provided by defined compositional ratios of two or more SWCNT species. With a plethora of SWCNT species, each with their own peculiar electronic structure and resulting SWCNT-silicon heterojunction properties, there is great opportunity for exploration, exploitation and leverage of such characteristics in future solar cells and electronic devices.

5.4 Summary

In summary, the first ever direct comparison is presented between SWCNT-silicon heterojunction solar cells fabricated with unsorted SWCNTs, m-SWCNTs or s-SWCNTs. It is clear that the resistivity of the SWCNT film is a primary factor determining the performance of these solar cells. However, as discussed, it is evident that the metallicity of the SWCNT film also plays a highly significant role.

5.5 References

[1] De Volder, M.F.L., Tawfick, S.H., Baughman, R.H., and Hart, A.J., *Science,* **2013**. 339(6119): p. 535-539.

[2] Ghosh, S., Bachilo, S.M., and Weisman, R.B., *Nat Nano,* **2010**. 5(6): p. 443-450.

[3] Arnold, M.S., Green, A.A., Hulvat, J.F., Stupp, S.I., and Hersam, M.C., *Nat Nano,* **2006**. 1(1): p. 60-65.

[4] Tu, X., Manohar, S., Jagota, A., and Zheng, M., *Nature,* **2009**. 460(7252): p. 250-253.

[5] Arnold, M.S., Stupp, S.I., and Hersam, M.C., *Nano Letters,* **2005**. 5(4): p. 713-718.

[6] Moshammer, K., Hennrich, F., and Kappes, M., *Nano Research,* **2009**. 2(8): p. 599-606.

[7] Blum, C., Stürzl, N., Hennrich, F., Lebedkin, S., Heeg, S., Dumlich, H., Reich, S., and Kappes, M.M., *ACS Nano,* **2011**. 5(4): p. 2847-2854.

[8] Liu, H., Tanaka, T., Urabe, Y., and Kataura, H., *Nano Letters,* **2013**. 13(5): p. 1996-2003.

[9] Flavel, B.S., Kappes, M.M., Krupke, R., and Hennrich, F., *ACS Nano,* **2013**. 7(4): p. 3557-64.

[10] Blanch, A.J., Quinton, J.S., and Shapter, J.G., *Carbon,* **2013**. DOI: 10.1016/j.carbon.2013.04.064(0).

[11] Jia, Y., Li, P., Gui, X., Wei, J., Wang, K., Zhu, H., Wu, D., Zhang, L., Cao, A., and Xu, Y., *Applied Physics Letters,* **2011**. 98(13): p. 133115-3.

[12] Jung, Y., Li, X., Rajan, N.K., Taylor, A.D., and Reed, M.A., *Nano Letters,* **2012**. 13(1): p. 95-99.

[13] Shi, E., Zhang, L., Li, Z., Li, P., Shang, Y., Jia, Y., Wei, J., Wang, K., Zhu, H., Wu, D., Zhang, S., and Cao, A., *Scientific reports,* **2012**. 2: p. 884.

[14] Jia, Y., Cao, A., Bai, X., Li, Z., Zhang, L., Guo, N., Wei, J., Wang, K., Zhu, H., Wu, D., and Ajayan, P.M., *Nano Letters,* **2011**. 11(5): p. 1901-1905.

[15] Jia, Y., Cao, A., Kang, F., Li, P., Gui, X., Zhang, L., Shi, E., Wei, J., Wang, K., Zhu, H., and Wu, D., *Physical Chemistry Chemical Physics,* **2012**. 14(23): p. 8391-6.

[16] *See Chapter 4.*

[17] Li, X., Jung, Y., Sakimoto, K., Goh, T.-H., Reed, M.A., and Taylor, A.D., *Energy & Environmental Science,* **2013**.

[18] Wadhwa, P., Seol, G., Petterson, M.K., Guo, J., and Rinzler, A.G., *Nano Letters,* **2011**. 11(16): p. 2419-2423.

[19] *See Chapter 6.*

[20] Wadhwa, P., Liu, B., McCarthy, M.A., Wu, Z., and Rinzler, A.G., *Nano Letters,* **2010**. 10(12): p. 5001-5005.

[21] Blanch, A.J., Lenehan, C.E., and Quinton, J.S., *Carbon,* **2011**. 49(15): p. 5213-5228

[22] Liu, H., Nishide, D., Tanaka, T., and Kataura, H., *Nature Communications,* **2011**. 2: p. 309.

[23] Tanaka, T., Urabe, Y., Nishide, D., and Kataura, H., *Appl. Phys. Express,* **2009**. 2(12): p. 125002.

[24] Moshammer, K., Hennrich, F., and Kappes, M.M., *Nano Research,* **2009**. 2: p. 599-606.

[25] Hároz, E.H., Lu, B.Y., Nikolaev, P., Arepalli, S., Hauge, R.H., and Kono, J., *Journal of the American Chemical Society,* **2011**. 10.1021/ja209333m.

[26] Weisman, R.B. and Bachilo, S.M., *Nano Letters,* **2003**. 3(9): p. 1235-1238.

[27] Shimizu, M., Fujii, S., Tanaka, T., and Kataura, H., *The Journal of Physical Chemistry C,* **2013**. 10.1021/jp3113254.

[28] Sze, S.M. and Ng, K.K., *Physics of semiconductor devices*. 3 ed. 10.1002/0470068329. 2006: Wiley Interscience.

[29] Shewchun, J., Singh, R., and Green, M.A., *Journal of Applied Physics,* **1977**. 48(2): p. 765-770.

[30] Spataru, C.D., Ismail-Beigi, S., Benedict, L.X., and Louie, S.G., *Physical Review Letters,* **2004**. 92(7): p. 077402.

[31] Collins, P.G., Bradley, K., Ishigami, M., and Zettl, A., *Science,* **2000**. 287(5459): p. 1801-1804.

[32] O'Connell, M.J., Eibergen, E.E., and Doorn, S.K., *Nature Materials,* **2005**. 4(5): p. 412-418.

[33] Barnes, T.M., Blackburn, J.L., van de Lagemaat, J., Coutts, T.J., and Heben, M.J., *ACS Nano,* **2008**. 2(9): p. 1968-1976.

[34] Li, Z., Kunets, V.P., Saini, V., Xu, Y., Dervishi, E., Salamo, G.J., Biris, A.R., and Biris, A.S., *ACS Nano,* **2009**. 3(6): p. 1407-1414.

Chapter 6
SWCNT - polyaniline - silicon solar cells

SWCNT-silicon heterojunction solar cells can be quite underperforming and this may be in part due to incomplete coverage of the silicon surface by the SWCNTs. It is possible to fabricate silicon heterojunction solar cells with a thin film of the conductive polymer, polyaniline (PANI), but these devices can perform poorly, being perhaps limited by the low lateral current carrying capacity of very thin polymer films. In this chapter, the fabrication and characterisation of well performing silicon solar cells with a new type of front electrode is reported. The devices use a hybrid PANI-SWCNT layered electrode, combining the conformal coverage given by the polymer and the excellent electrical properties of SWCNT films. The hybrid SWCNT-PANI-silicon heterojunction solar cells significantly outperform both of the individual PANI-silicon and SWCNT-silicon counterparts.

6.1 Introduction

In the short time since initial reports, the field of SWCNT-solar cells has seen power conversion efficiencies of up to 14 % for small area research cells.[1-3] Similar efficiencies have been achieved with novel strategies involving ionic liquid mediated gating of the SWCNT-silicon junction electrostatics.[4-6] In addition to process improvements, the much improved performance of the most recent devices compared to earlier reports is a result of either the build-up of negative ions adjacent to the silicon surface[4-6] or the presence of a thin oxide layer.[2-3] Both of these have the effect of creating a more complete depletion region in the silicon compared to the relatively inhomogeneous region that exists when no ionic liquid/oxide is present. The effect of the oxide on device performance has been discussed in Chapter 3 and Chapter 5. Recently, hybrid solar cells of PEDOT:PSS on an n-type silicon surface modified with a regular nanocone structure have been demonstrated with ~ 11 % PCE.[7] This chapter examines high efficiency heterojunction solar cells in which a thin layer of PANI is placed between the silicon and the SWCNTs. PANI-silicon heterojunction solar cells have been reported previously[8-9] but such devices can suffer from poor performance for silicon photovoltaics.

6.2 Method

SWCNT-silicon solar cells were fabricated in the manner of section 3.2. To make the spin coating solution, PANI (emeraldine base, 10,000 M_w, Sigma-Aldrich) was sonicated in DMF (Sigma-Aldrich) at a concentration of 1 mg mL^{-1} for 30 min and then centrifuged at 20,000 g for 30 min. The supernatant was filtered through 1 μm Teflon filters (Millipore) and then, for the devices with PANI, 3 drops of the filtrate were spin coated onto substrates at a spin speed of 3000 rpm and the resulting films were baked in air at 130°C for 2 hr. For PANI devices the spin coating was performed immediately after HF etching. For devices with SWCNTs, films were deposited onto the substrate surfaces as in section 3.2 (**Figure 6.1**). SEM images of

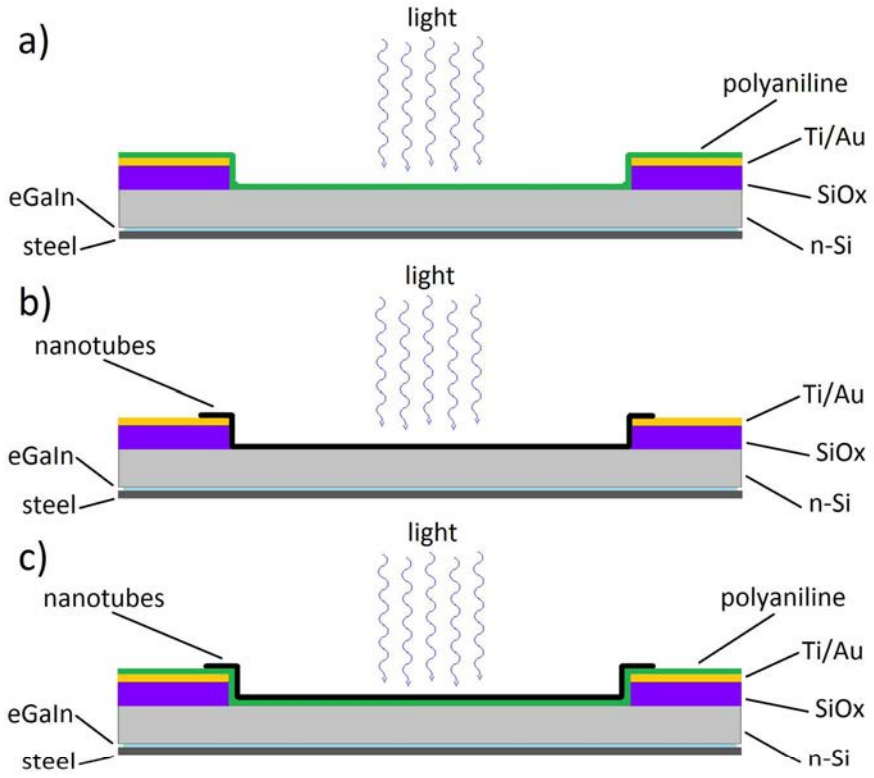

Figure 6.1 Schematics of silicon solar cell devices with (a) only PANI, (b) only SWCNTs and (c) hybrid devices of SWCNTs and PANI.

the SWCNT electrodes in this chapter were obtained on an FEI Helios and prior to imaging all samples were sputtered with 5 nm platinum. Before measurement, cells without PANI were briefly exposed to 2 % HF to remove native oxide and then rinsed with ethanol and dried with N_2.

6.3 Results and discussion

Figure 6.2(a-c) show SEM and AFM images of the solar cell surface. **Figure 6.2**(a) shows the edge of the circular active area where the SWCNT film contacts both the silicon (left) and the gold front electrode (right). The film has an uneven topography which could be an imprint from the filter paper or contraction due to the evaporation of water during the SWCNT film immobilisation step. AFM measurements of the give an average film thickness of ~ 35 nm (**Figure 6.2**(b)). The morphology shown in **Figure 6.2**(c) is that of a relatively isotropic, randomly aligned network containing bundles of ~ 15 nm in diameter.

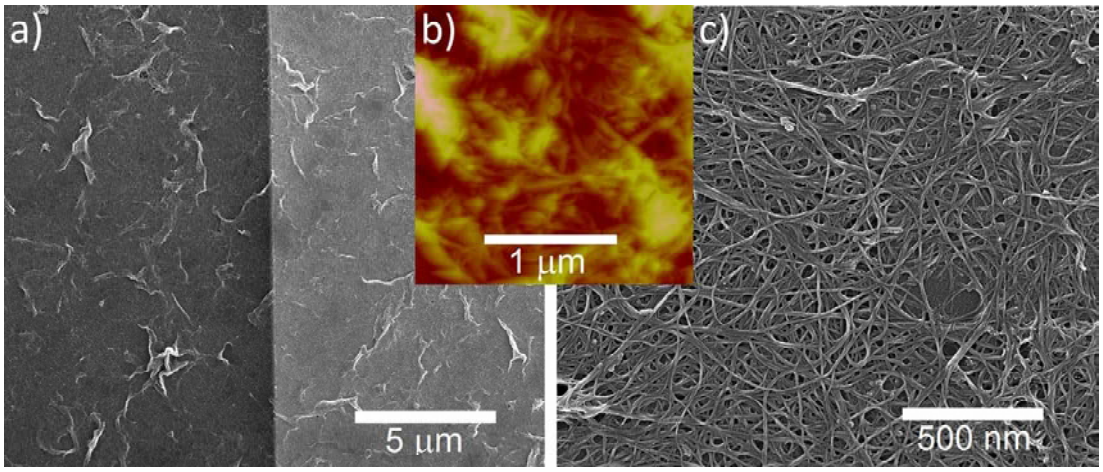

Figure 6.2 (a) SEM image of the SWCNT coated silicon surface showing the edge of the active area (silicon on the left, gold on the right) (b) AFM image of the SWCNT film from which thickness measurements were obtained (c) magnified SEM image of the SWCNT film shown in (a).

The UV-Visible-NIR absorption properties of PANI and SWCNTs are shown in **Figure 6.3**. As in Chapter 3, HCl was used in lieu of HF to remove oxide whilst preventing damage to the surface of the glass substrate and/or peeling of the SWCNT film. The presence of broad, weak peaks in the spectra of SWCNTs (**Figure 6.3**(a)) indicates that they are not highly dispersed, which is in agreement with the bundle sizes observed in the SEM micrographs.

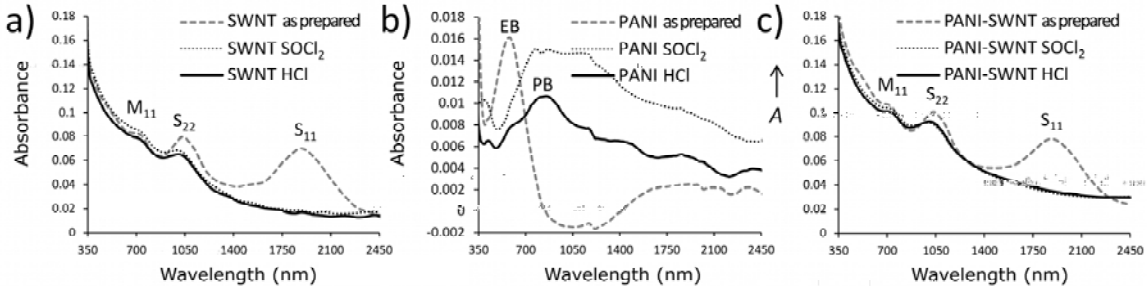

Figure 6.3 UV-Visible-NIR absorption spectra of (a) SWCNT film, (b) PANI film and (c) SWCNT film on PANI film.

Before treatment the PANI films (**Figure 6.3**(b)) show the expected π-π^* absorption in the UV and the emeraldine base singlet peak at 550 nm corresponding to a molecular exciton associated with the quinone diimine structure of partially protonated polymer in the compact coil conformation.[10-11] The compacted coil conformation is expected since, as described in section 6.2, the PANI is spin coated from DMF onto the highly hydrophobic silicon hydride surface.[12] After $SOCl_2$

treatment this well resolved peak at 550 nm is replaced by a broad absorption tail corresponding to a Peierl's gap in the expanded coil conformation of the pernigraniline base, beginning at ~ 500 nm, with a peak at ~ 800 nm and extending well into the IR.[13] The spectra of PANI-SWCNT hybrid films (**Figure 6.3**(c)) are a summation of the individual component spectra as expected.

Measurements of R_{sheet} from thin films of PANI, SWCNTs, and PANI with SWCNTs on top are shown in **Table 6.1**. Regardless of post treatment, the PANI films all exhibit values in the range of MΩ sq^{-1}, confirming the poor lateral conductivity of the films in this study. In contrast, the untreated SWCNTs films have R_{sheet} smaller by a factor of ~ 10^4 and these are reduced further following treatment with $SOCl_2$ and dilute acid. The hybrid films of PANI and SWCNTs begin with R_{sheet} almost double that of films containing only SWCNTs (1300 Ω sq^{-1} compared to 850 Ω sq^{-1}), but after treatment these films exhibit similar values to the SWCNT-only films (310 Ω sq^{-1} compared to 270 Ω sq^{-1}).

Table 6.1 Summary of measurements for the three films/device types.

		V_{OC} (V)	J_{SC} (mA cm^{-2})	FF	PCE (%)	R_{sheet} (Ω sq^{-1})	T_{550} (%)	R_{SH} (Ω)	R_S (Ω)
PANI	fresh	0.26	0.087	0.22	0.005	1.9 x10^6	96.4	32845	35169
	$SOCl_2$	0.13	0.17	0.22	0.005	1.7 x10^6	98	9792	11590
	HF/HCl	0.17	0.11	0.22	0.004	2.5 x10^6	98.4	18235	20777
SWCNT	fresh	0.25	2.76	0.19	0.13	8.5 x10^2	79.8	748	1873
	$SOCl_2$	0.35	11.41	0.22	0.89	1.8 x10^2	79.7	370	764
	HF/HCl	0.39	21.71	0.4	3.36	2.7 x10^2	81.3	680	93
PANI-SWCNT	fresh	0.4	19.54	0.14	1.11	1.3 x10^3	75.2	176	2460
	$SOCl_2$	0.53	27.1	0.37	5.25	3.1 x10^2	76.8	10291	468
	HF/HCl	0.52	27.38	0.68	9.66	3.1 x10^2	77.5	6077	37

The JV characteristics of cells fabricated with only PANI (**Figure 6.4**(a)) show very poor performance, with a PCE of ~ 0.005 %. This is likely due to the poor lateral conductivity of the PANI films used in this study, the effect of which is evident in the series resistance in the range of ~ kΩ. However, the PANI films on silicon do exhibit diode-like behaviour. After treatment with $SOCl_2$ the behaviour tends more

towards ohmic whereas after the HF treatment, the device returns to a more diode-like behaviour, although with a reduced V_{OC}.

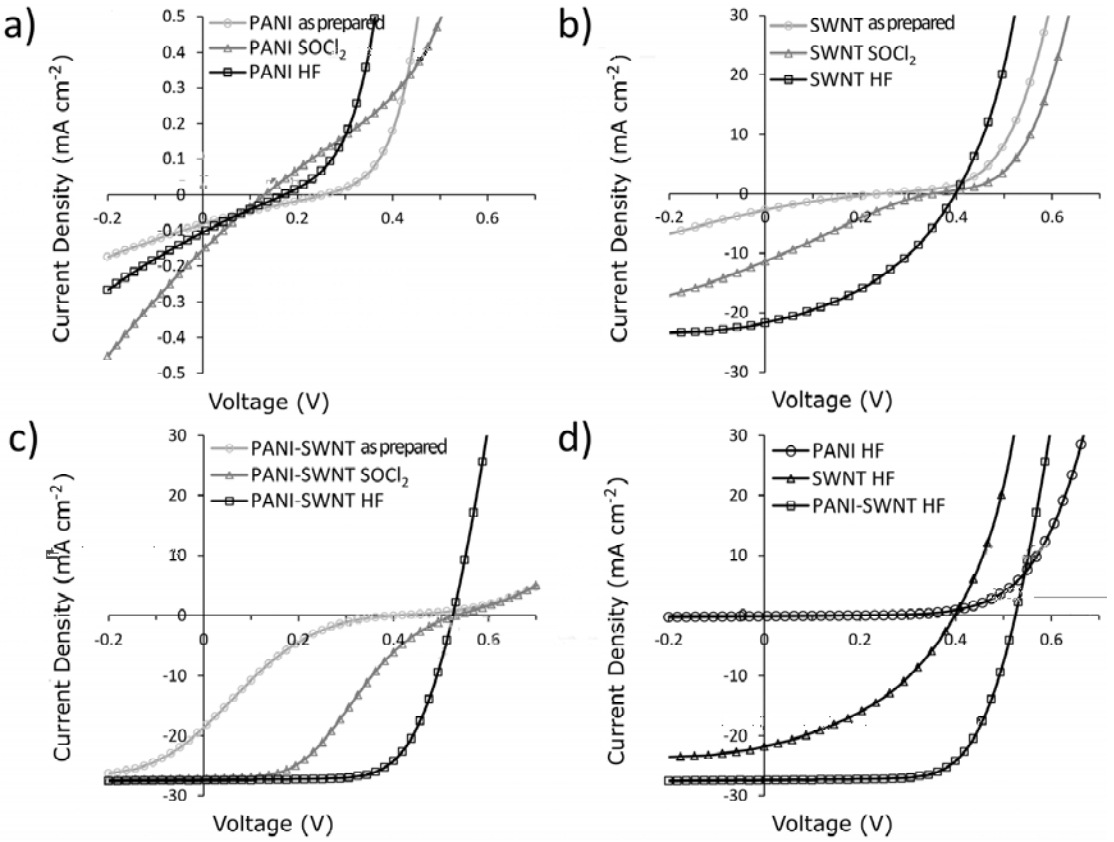

Figure 6.4 Light JV characteristics of solar cell devices with (a) only PANI (note different scale), (b) only SWCNTs, (c) hybrid devices of PANI and SWCNTs and (d) comparison of all three devices after all post treatments.

The JV characteristics of cells fabricated with only SWCNTs (**Figure 6.4**(b)) initially show a PCE of ~ 0.13 %, which is better than the PANI cells by a factor of ~ 10^2. However, the poor FF indicates that the cell is substantially underperforming. One reason for this can be seen in the S-bend kink feature in the JV curves which has been investigated theoretically and shown to be a result of limited interfacial electron transfer[14] which could be due to the formation of an oxide layer during SWCNT deposition. After treatment of the SWCNT films with $SOCl_2$ the PCE is increased to ~ 0.9 %, predominantly via an increase in J_{SC} but with a small increase in V_{OC}. The performance enhancing effect of $SOCl_2$ is discussed in detail in section 3.5.3. A further brief treatment with dilute HF yields a doubling of both J_{SC} and FF which results in a substantial increase in device

performance up to ~ 3.4 %. The S-bend kink feature is now absent in accordance with an improved interfacial electron transfer rate, however the FF is still rather low.

The JV characteristics of hybrid devices using both PANI and SWCNTs are shown in **Figure 6.4(c)**. Immediately apparent is the increased V_{OC} in all PANI-SWCNT devices compared to either PANI or SWCNT devices, regardless of treatment. Also apparent is that all the hybrid devices, regardless of treatment, produce about the same J_{SC} at small reverse bias (- 0.2 V). However, they differ considerably in the FF. Since the FF can be thought of as a measure of the ability of devices to maintain charge separation, this indicates a greater level of recombination occurring in the untreated devices. Specifically, in the fresh devices under illumination, the series resistance is very high (2.46 kΩ) and the shunt resistance is very low (176 Ω). Neglecting any small contribution from the thin PANI film in the vertical plane, the series resistance can be attributed to the poor electrical properties of the SWCNT film before $SOCl_2$ treatment. As shown in **Table 6.1**, R_{sheet} decreases substantially from 1300 - 310 Ω sq^{-1} while the transmittance may increase very slightly from 75.2 - 76.8 % with the $SOCl_2$ treatment. The S-bend kink feature is present in the fresh hybrid devices and after $SOCl_2$ treatment but, as with the SWCNT devices, disappears after the second acid treatment. If the PANI is assumed to somewhat protect the silicon from oxidation then the origin must result from some change to the PANI, the SWCNT film or the SWCNT-PANI junction. It is known that protonation of PANI-graphene junctions improves interfacial charge transfer[15] and this is likely also the case for SWCNTs.

Compared to the solar cells without PANI, the use of PANI may have an effect on the silicon depletion region similar to that in the ionic liquid modified devices of Wadhwa.[4-5] In this model the SWCNT devices suffer from the fact that the SWCNT film, being a porous network, does not make a complete, conformal covering on the silicon surface. This produces an incomplete and non-homogeneous depletion region in the silicon, reducing performance. However the PANI does

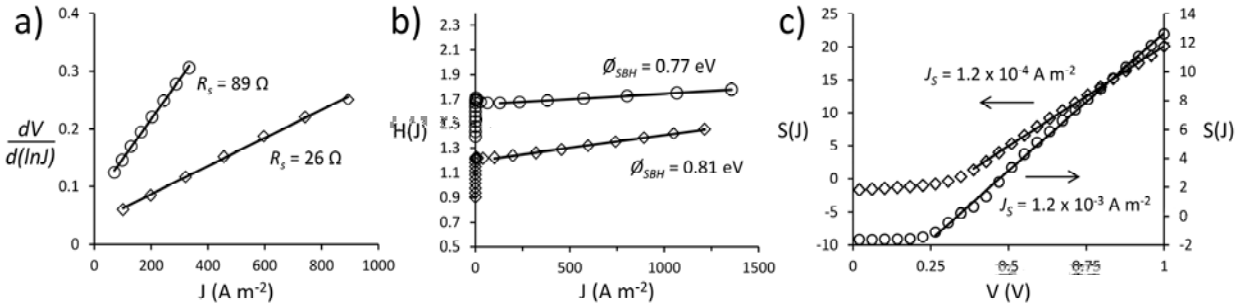

Figure 6.5 Dark current analysis of SWCNT (circles) and SWCNT-PANI (diamonds) devices; (a) *dV/d(lnJ)* vs. *J*, (b) *H(J)* vs. *J*, (c) *S(J)* vs. *V*.

form a complete conformal covering, producing a much better depletion region and also serving the additional function of maintaining a physical separation between photogenerated holes travelling through the SWCNT film and electrons in the underlying silicon.

To obtain the Schottky diode parameters the device dark JV characteristics were analysed as in 3.2.4. Briefly, R_S and the ideality factor were obtained from the plot of *d(V)/d(lnJ)* vs. *J* (**Figure 6.5**(a))[16] and then, as in [16] a new parameter H(J) was defined such that;

$$H(J) = V - \left(\frac{n}{\beta}\right) \ln\left(\frac{J}{A^{*}T^{2}}\right) = RAJ + n\emptyset_{SBH} \qquad \textbf{Equation 6.1}$$

where *V* is the applied potential, *n* the ideality factor, $\beta = kT/q$, *k* the Boltzmann constant, *T* the absolute temperature, and *q is* the elementary charge, *A** is the Richardson constant, *A* the interfacial area. A plot of *H(J)* vs. *J* yields the Schottky barrier height, $Ø_{SBH}$, and a self-consistency check via a second measure of R_s (**Figure 6.5**(b)). Taking the natural log of **Equation 3.1** and rearranging to define;

$$S(J) = \ln J + \frac{qJAR}{nkT} = \left(\frac{q}{nkT}\right) V + \ln J_0 \qquad \textbf{Equation 6.2}$$

A plot of *S(J)* vs. *V* yields a straight line and extrapolation to zero bias, using *n* and R_S from **Equation 3.4**, yields J_0 (**Figure 6.5**(c)) which can then be used as an additional estimation of the Schottky barrier height since, in **Equation 3.3**;[17]

$$J_0 = A^* T^2 e^{\left(\frac{-q\emptyset_{SBH}}{kT}\right)}$$ **Equation 6.3**

The results of the dark current analysis are shown in **Table 6.2** with the PCE and FF calculated from the light measurements. The analysis reveals a significant decrease (~ 10^3) in J_0 in the hybrid devices compared to the SWCNT devices and a concurrent improvement in ideality factor from ~ 2 to ~ 1.43.

Table 6.2 Change in device characteristics before (fresh) and after (HF) film treatment.

	SBH (eV)	n	R_S (Ω)	J_0 (A m^{-2})	PCE (%)	FF
PANI	0.81 - 0.81	2.16 - 2.05	33 - 33	3.4×10^{-4} - 2.8×10^{-4}	0.005 - 0.004	0.22 - 0.22
SWCNT	0.64 - 0.77	3.68 - 2.02	242 - 89	1.3×10^{-1} - 4.5×10^{-3}	0.13 - 3.36	0.19 - 0.4
PANI-SWCNT	0.68 - 0.81	3.3 - 1.43	112 - 26	7.5×10^{-2} - 3.6×10^{-4}	1.11 - 9.66	0.14 - 0.68

The hole-doping effect of $SOCl_2$ can be seen in the increased Schottky barrier heights and 2 orders of magnitude decrease in J_0 for the SWCNT and SWCNT-PANI devices after treatment. The ability of $SOCl_2$ to also improve film conductivity can be seen in the reduced series resistance and concurrent decrease in ideality factor towards unity. The modelled increases in barrier heights are consistent with the measured increases in V_{OC}; for SWCNT devices $\emptyset_{SBH}$ increases by 0.13 eV whilst V_{OC} increases by 0.14 V, and for PANI-SWCNT devices $\emptyset_{SBH}$ also increases by 0.13 eV whilst V_{OC} increases by 0.12 V. Comparison of $\emptyset_{SBH}$ in PANI and PANI-SWCNT devices seems to suggest that the maximum effective barrier height of these devices is limited by the PANI-Si interface to 0.81 eV. This is consistent with a model in which the PANI-Si interface is the photoactive junction and the nanotubes function as efficient transporters of holes to the external circuit. The superior depletion region of the PANI-SWCNT devices compared to the SWCNT devices is also evidenced in the order of magnitude decrease in J_0 when PANI is present and in the increased shunt resistance of the PANI-SWCNT devices compared to SWCNT only. The devices in this study show very good performance

but it is important to note that they have not been highly optimised. For example, compared to state of the art literature examples, the electrical characteristics of the PANI films used here were very poor and there is much that could be to improve this. Also, UV-Vis-NIR spectra show clearly that the SWCNTs used in these devices comprise a range of SWCNT chiralities including both metallic and semiconducting varieties.

In Chapter 4 it was shown that, contrary to the assumption in some reports, light absorption by SWCNTs does not contribute to photocurrent generation in SWCNT-silicon solar cells. Rather, as shown in Chapter 5, such devices perform better as the metallicity of the SWCNT film is increased and indeed, that is exactly the effect that the $SOCl_2$ treatment has. So, presumably devices fabricated using chirality sorted m-SWCNTs will outperform those fabricated with mixed SWCNTs. Devices fabricated with doped, chirality sorted s-SWCNTs may outperform either the mixed or m-SWCNT devices, whether they are doped or not. This is due to the fact that conductivity scales with carrier density and a s-SWCNT, with a Fermi level doped up to the conduction band, has a much higher electron density at that point than at any point accessible in a m-SWCNT.[18-19] In the ideal case of SWCNT-PANI-silicon hybrid devices fabricated with state of the art PANI films and highly doped, single chirality SWCNT films, very considerable gains in performance over that reported here are not at all unreasonable. The SWCNT films could be significantly thinner and more transparent and these SWCNT films are also intrinsically antireflective, being excellent scatterers of light over a broad range of energies. In this situation, such hybrid films as those reported here could provide improved front contact performance over current metallisation strategies via reduced optical shading and enhanced carrier collection over the entire front solar cell surface and, considering the very rapidly dropping cost of SWCNT material and relative ease of processing, potential cost savings as well.

6.4 Summary

Hybrid SWCNT-PANI-silicon heterojunction solar cells were fabricated and shown to clearly outperform their SWCNT-silicon and PANI-silicon counterparts. Other reports of SWCNT-silicon solar cells used controlled oxide growth or the introduction of an ionic liquid to improve the performance; however, the use of an intermediate layer of conductive polymer is a new step with a demonstrated positive effect. Furthermore, the use of a layer of SWCNTs to improve the electrical properties of an underlying conductive polymer film clearly has broad applications, ranging from solar cells and organic light-emitting diodes to touch-sensitive interfaces and more. The increased performance from the hybrid devices reported in this chapter is attributed to the synergistic combination of an improved silicon depletion region due to conformal surface covering by the polymer and the high conductivity and current-carrying capacity of the SWCNT film. These devices show good photovoltaic performance, and optimization of device components could lead to significant performance gains. The hybrid PANI-SWCNT films thus show potential as improved front-side electrodes for current and future generations of commercial silicon solar cells photodetectors and more.

6.5 References

[1] *See Chapter 1.*

[2] Jia, Y., Cao, A., Bai, X., Li, Z., Zhang, L., Guo, N., Wei, J., Wang, K., Zhu, H., Wu, D., and Ajayan, P.M., *Nano Letters,* **2011**. 11(5): p. 1901-1905.

[3] Jia, Y., Li, P., Gui, X., Wei, J., Wang, K., Zhu, H., Wu, D., Zhang, L., Cao, A., and Xu, Y., *Applied Physics Letters,* **2011**. 98(13): p. 133115-3.

[4] Wadhwa, P., Liu, B., McCarthy, M.A., Wu, Z., and Rinzler, A.G., *Nano Letters,* **2010**. 10(12): p. 5001-5005.

[5] Wadhwa, P., Seol, G., Petterson, M.K., Guo, J., and Rinzler, A.G., *Nano Letters,* **2011**. 11(16): p. 2419-2423.

[6] Chen, W., Seol, G., Rinzler, A.G., and Guo, J., *Applied Physics Letters,* **2012**. 100(10): p. 103503.

[7] Jeong, S., Garnett, E.C., Wang, S., Yu, Z., Fan, S., Brongersma, M.L., McGehee, M.D., and Cui, Y., *Nano Letters,* **2012**. 12(6): p. 2971-6.

[8] Wang, W. and Schiff, E.A., *Applied Physics Letters,* **2007**. 91(13): p. 133504.

[9] Cárdenas, J.R., de Vasconcelos, E.A., de Azevedo, W.M., da Silva, E.F., Pepe, I., da Silva, A.F., Ribeiro, S.S., and Silva, K.A., *Applied Surface Science,* **2008**. 255(3): p. 688-690.

[10] de Albuquerque, J.E., Mattoso, L.H.C., Balogh, D.T., Faria, R.M., Masters, J.G., and MacDiarmid, A.G., *Synthetic Metals,* **2000**. 113(1–2): p. 19-22.

[11] MacDiarmid, A.G., *Synthetic Metals,* **1997**. 84(1–3): p. 27-34.

[12] Avlyanov, J.K., Min, Y., MacDiarmid, A.G., and Epstein, A.J., *Synthetic Metals,* **1995**. 72(1): p. 65-71.

[13] de Albuquerque, J.E., Mattoso, L.H.C., Faria, R.M., Masters, J.G., and MacDiarmid, A.G., *Synthetic Metals,* **2004**. 146(1): p. 1-10.

[14] Nelson, J., Kirkpatrick, J., and Ravirajan, P., *Physical Review B,* **2004**. 69(3): p. 035337.

[15] Wang, R.-X., Huang, L.-F., and Tian, X.-Y., *The Journal of Physical Chemistry C,* **2012**. 116(24): p. 13120-13126.

[16] Cheung, S.K. and Cheung, N.W., *Applied Physics Letters,* **1986**. 49(2): p. 85-87.

[17] Sze, S.M. and Ng, K.K., *Physics of semiconductor devices*. 3 ed. 10.1002/0470068329. 2006: Wiley Interscience.

[18] Blackburn, J.L., Barnes, T.M., Beard, M.C., Kim, Y.-H., Tenent, R.C., McDonald, T.J., To, B., Coutts, T.J., and Heben, M.J., *ACS Nano,* **2008**. 2(6): p. 1266-1274.

[19] Barnes, T.M., Blackburn, J.L., van de Lagemaat, J., Coutts, T.J., and Heben, M.J., *ACS Nano,* **2008**. 2(9): p. 1968-1976.

Chapter 7
The potential sunlight harvesting efficiency of SWCNT solar cells

Laboratory-scale solar cells have been demonstrated which show clear evidence of the successful exploitation of s-SWCNTs as primary absorbers of sunlight energy. The unique properties of SWCNTs may allow for high efficiency solar cell devices however little progress has been made to quantify this. Herein the best currently available data is used to simulate the absorption properties of different s-SWCNT species and thus calculate a species-dependent sunlight harvesting potential. The same model is then used to simulate relevant tandem cell scenarios, predicting a conservative estimate of the potential harvesting efficiency of ~ 28 % for a multijunction device absorbing in the visible and ~ 19 % for a similar device absorbing primarily in the infrared, whilst minimising absorption in the visible.

7.1 Introduction

Shockley and Queisser used detailed balance calculations to establish a thermodynamic limit to the power conversion efficiency of a single junction, bulk semiconductor solar cell and determined the dependence of this limit on the semiconductor bandgap.[6] However, two of the assumptions upon which those calculations are based do not apply in the case of s-SWCNTs. The first is that all photons with energy greater than the semiconductor bandgap are absorbed. This assumes a smooth continuum of states above and below the gap, which is the case for bulk semiconductors such as silicon but not so for s-SWCNTs with their sharp VHS in the DOS, yielding discrete optical transitions between complementary states above and below the gap (**Figure 5.7**). Such transitions are denoted S_{ii}, where ii denotes a transition from the i^{th} VHS below the gap to the i^{th} VHS above it i.e. S_{11}, S_{22}, etc. The second assumption is that the absorption of one photon produces one exciton. Whilst this is true for bulk semiconductors, s-SWCNTs have been shown to exhibit quantum efficiencies greater than unity, indicating multiple exciton generation from single photons.[7-8]

Among other factors, the breakdown of the Shockley/Quiesser model due to the non-monotonic nature of the SWCNT DOS limits the establishment of a detailed balance limit of efficiency for SWCNT-based solar cells. However, the absorption properties of SWCNTs are known, as is the spectrum of solar radiation. Thus, with some reasonable assumptions, it is possible to estimate what portion of the solar spectrum can be harvested by a particular s-SWCNT species. There not only exists a variety of s-SWCNT species with bandgaps within the useful range of the Sun's radiation but this range is spanned almost entirely by the different species' individual absorption features. This suggests the possibility of tailoring a SWCNT-based solar cell's absorption profile to suit demand, if functional solar cell device architectures can be engineered to exploit SWCNTs for light harvesting. A candidate structure for this was the carbon SWCNT-silicon solar cell but the measurements reported in Chapter 4 indicate that the SWCNT do not contribute to photocurrent generation

in those devices. Considering the recent successful realisation of other SWCNT-based solar cells,[1-5] the inadequacies of the SQ model for SWCNT-based photovoltaics and the growing interest in the field, there is a clear need for quantitative analysis and comparison of the potential of different s-SWCNT species to absorb sunlight.

This work presents a numerical simulation of s-SWCNT absorption properties, based on empirical measurement, and then a careful analysis of the overlap between the simulated absorption properties of 70 different s-SWCNTs and the terrestrial solar spectrum. This is then used to predict the optimal (n,m) species composition of two SWCNT based tandem solar cells with real world significance. An analysis of critical photovoltaic device parameters such as the open circuit voltage, exciton dissociation probability, series resistance, etc., would also be helpful but such parameters are very much device and architecture-specific, whereas this work is necessarily device-independent. For example, the exciton dissociation probability will depend on the nature, geometry and quality of the junction where exciton dissociation occurs, and on the physical and electronic characteristics of whatever material the other element of the junction is composed of. The component of the series resistance arising due to the SWCNT layer(s) will depend on such things as the thickness, density, composition, metallicity and degree of alignment of the SWCNT and, of course, the component of the series resistance arising due to the other components of a particular device in question will depend on what those components are and how they are physically and electronically related to the SWCNT. Other characteristics of a SWCNT based solar cell device will similarly depend greatly on the specific photovoltaic architecture employed in fabrication e.g. photoelectrochemical, organic, polymer, solid state, etc. The absorption characteristics of the SWCNT as simulated, the relative differences between the different SWCNT species, and their overlap with the terrestrial solar spectrum should, however, be the same whatever the particular device structure.

7.2 Method

Sunlight (AM1.5G) was modelled according to the ASTM G-173-03 reference solar spectral irradiance data set.[9] An ideal solar cell was considered, consisting of a s-SWCNT absorber layer, a mechanism for separating photogenerated excitons into free electrons and holes and a mechanism for extracting these into an external circuit to do work. All s-SWCNTs with bandgaps greater than 0.7 eV and diameters greater than 0.45 nm were modelled, with the transition energies $E_{11}^{(n,m)}$ and $E_{22}^{(n,m)}$ taken from refs. [10] and [11], respectively. As per ref. [12], each SWCNT absorption peak corresponding to an optical transition was modelled in energy space as a Voigt line profile ($V_{ii}^{(n,m)}(E)$); a convolution of a Lorentzian ($L_{ii}^{(n,m)}(E)$), representing natural line broadening due to uncertainty in particle lifetimes, and a Gaussian ($G_{ii}^{(n,m)}(E)$), representing Doppler broadening due to the distribution of particle velocities. These were expressed as $L_{ii}^{(n,m)}(E) = \gamma/\pi\left(\left(E-E_{ii}^{(n,m)}\right)^2+\gamma^2\right)$ and $G_{ii}^{(n,m)}(E) = \left(1/\sigma\sqrt{2\pi}\right)e^{-\left(E-E_{ii}^{(n,m)}\right)^2/2\sigma^2}$ where γ is the half-width-at-half-maximum (hwhm) and where σ is the standard deviation. The transition energy, $E_{ii}^{(n,m)}$, is thus the median of the Lorentzian component and the mean of the Gaussian component. The full-width-at-half-maxima (fwhm) of the Gaussian ($\Gamma_{G,ii}$) and Lorentzian ($\Gamma_{L,ii}$) components are related to the fwhm of the Voigt ($\Gamma_{V,ii}$) by:[13] $\Gamma_{V,ii} = 0.5436\Gamma_{L,ii} + \sqrt{0.2166\Gamma_{L,ii}^2 + \Gamma_{G,ii}^2}$. The broadening processes are energy dependent however the fwhm of SWCNT absorption peaks are not explicitly known thus they were set, empirically, as $\Gamma_{V,ii} = 0.067 \times E_{ii}^{(n,m)} - 0.02$ yielding ~ 27 meV for $E_{ii}^{(n,m)} = 0.7$ eV, increasing to ~ 114 meV for $E_{ii}^{(n,m)} = 2$ eV, which is in agreement with ref. [14]. Each SWCNT absorption peak was thus simulated as; $V_{ii}^{(n,m)}(E) = w_l \times L_{ii}^{(n,m)}(E) + w_g \times G_{ii}^{(n,m)}(E)$ where w_l and w_g are the weightings of the Lorentzian and Gaussian components, respectively, and w_g=0.1 was used as an empirical fit to measurements.

An assumption that must be made is the optical depth, τ, of the absorber layer (at $E_{ii}^{(n,m)}$). A semi-infinite τ could be chosen so as to maximise absorption in the simulation but this would be impractical in a real device. One could simply set τ equal to unity however a more realistic situation would be that an optically deeper absorber layer is used such that the maximum absorption is marginally more than that required to absorb all incident radiation at the peak energy, thus $\tau = 1 + 1/e$ ($\tau \sim 1.36$) was used. The S_{11} and S_{22} optical transitions were considered, thus the absorption profile of the s-SWCNT absorber layer is; $\chi_{SWCNT}^{(n,m)}(E) = \alpha_{11} \times V_{11}^{(n,m)}(E) + \alpha_{22} \times V_{22}^{(n,m)}(E)$ where α_{11} is a scaling factor applied such that $V_{11}^{(n,m)}(E)_{max} = \tau$ and where the total absorptance at any energy could, of course, have a maximum value no greater than unity. Note that the absorption profile is necessarily expressed as *absorptance* – the direct ratio of absorbed to incident radiation, not *absorbance* – the negative logarithm of the transmittance. This is because the simulation multiplies the solar spectral irradiance at each energy by the SWCNT absorption to yield the power harvested at that energy and thus requires the linear absorptance scale. The more familiar absorbance plot is commonly used in optical transmittance measurements to enhance peak to valley ratio of smaller features.

In ref. [12] the ratio of S_{11}/S_{22} peak heights was determined to show some dependence on (n,m) species, however the dependence was not quantified for all the (n,m) species considered in this work and neither was a general form of the relationship determined (or indeed apparent) thus it could not be incorporated into the present model. The ratio of S_{11}/S_{22} peak heights is assumed to be constant for all (n,m) species. Thus the scaling factor α_{22} was applied such that $V_{22}^{(n,m)}(E)_{max} = {}^{7}/_{8} \times V_{11}^{(n,m)}(E)_{max}$ where the ratio 7/8 on an absorptance scale is that value which gives an empirically determined ratio of ~ 2/7 on an absorbance scale (**Figure 7.1**). Because the relaxation of the S_{22} exciton to S_{11} occurs on the picosecond to sub-picosecond timescale[15] and involves energy loss, and since the solar cell is considered to be optimised for extraction of carriers from S_{11}, the energy

harvested from carriers photogenerated via S_{22} was considered to be no more than from an S_{11} carrier. Due to the oscillator strength of the S_{33} exciton being small compared to S_{11} or S_{22}, and since a complete dataset of the S_{33} transition energies is unavailable, light harvesting through S_{33} was not considered in this work. For the purposes of this analysis, the SWCNTs were considered to be in the fully isolated, or debundled state, thus it was assumed that there were no energy-dependent scattering processes contributing to a sloping background and since only s-SWCNTs were considered then it was assumed there would be no broad m-SWCNT π-π^* contribution either, giving a flat background[16] upon which $\chi_{SWCNT}^{(n,m)}(E)$ was superimposed.

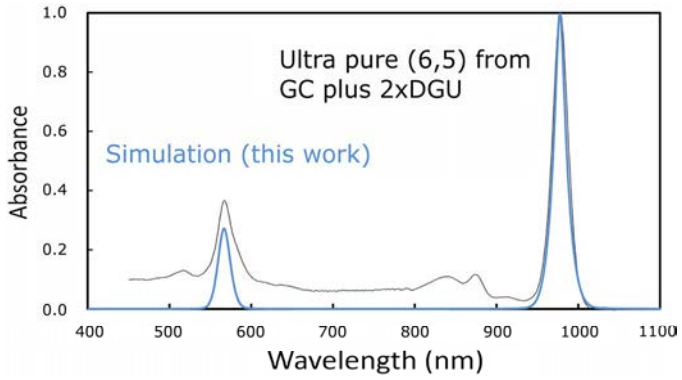

Figure 7.1 Comparison of the simulation output (blue) with measured absorbance data from ultra-pure (6,5) s-SWCNTs (black). Spectrum kindly provided by Dr B. Flavel.

The simulation of tandem cells involved simple addition of the component $\chi_{SWCNT}^{(n,m)}(E)$ to yield $\chi_{SWCNT}^{(Tandem)}(E)$ whilst still allowing the combined absorptance to have a maximum value no greater than unity. Only SWCNT species which are known to be stable in the isolated form (not as inner walls of MWCNTs) were considered for inclusion in the tandem cells (see Appendix 4 for list). The multijunction model does not include the effects of optical shadowing by SWCNT S_{33} absorption which would reduce the irradiance impinging on the underlying absorber layer, thus reducing the potential harvesting efficiency. However, if the resulting excited states decay radiatively (unlikely since fluorescent yields are typically less than 10 %) then some of the emitted photons may be recaptured via S_{22} or S_{11} in adjacent SWCNT in the same absorber layer or another. The shadowing is not an issue in the simulated

tandem cells as the energies of the S_{33} transitions (known or predicted) are, by design, outside the range of any of the S_{22}. Similarly, although electron-hole recombination would reduce the efficiency, since these are tandem cells the resulting electroluminescence would allow that loss to be partially regained. The model also does not include shadowing by, or sunlight harvesting due to other solar cell elements which may be present such as fullerenes[1, 3-5] or silicon nanocrystals[2] and which could significantly increase the harvesting potential if the SWCNTs are correctly matched to the absorption profile of these elements. To find the portion of the solar spectrum that could potentially be harvested by a particular (n,m) species (or tandem cell), the spectral irradiance of the Sun was multiplied by the SWCNT absorptance at each energy and then integrated over all energies; $P_{SWCNT}^{(n,m)} = \int E_{e\lambda}^{Sun}(E) \times \chi_{SWCNT}^{(n,m)}(E)\ dE$. The integration was performed numerically as a middle Riemann sum with a partition width equivalent to 0.5 nm, over the region 0.309 eV < *E* < 4.428 eV (280 - 4000 nm). The ASTM G-173-03 reference was linearly interpolated as required to obtain a solar spectral irradiance dataset with the necessary 0.5 nm resolution.

7.3 Results and discussion

Figure 7.2 shows an example of the simulation output, using one of the most commonly purified and investigated s-SWCNT species - the (6,5) nanotube. Combining the results from simulations of 70 different SWCNT species, and considering only S_{11} absorption (**Figure 7.3**), there is an obvious dependence of the potential sunlight harvesting efficiency on bandgap energy, with the higher bandgap species generally exhibiting a greater efficiency. This is expected since the power contained in the solar radiation is more concentrated in the higher energy region. However, there are some significant deviations from the trend. For example, the (n,m) species found in a vertical line from (13,0) to (9,8) (roughly corresponding to SWCNTs of the same diameter/bandgap) show markedly reduced efficiency compared to their adjacent species. These species all have a tube diameter ~ 1 nm and $E_{11}^{(n,m)}$ of ~ 0.9 eV, which overlaps the region of reduced irradiance due to atmospheric absorption effects (water and CO_2) in the terrestrial solar spectrum.

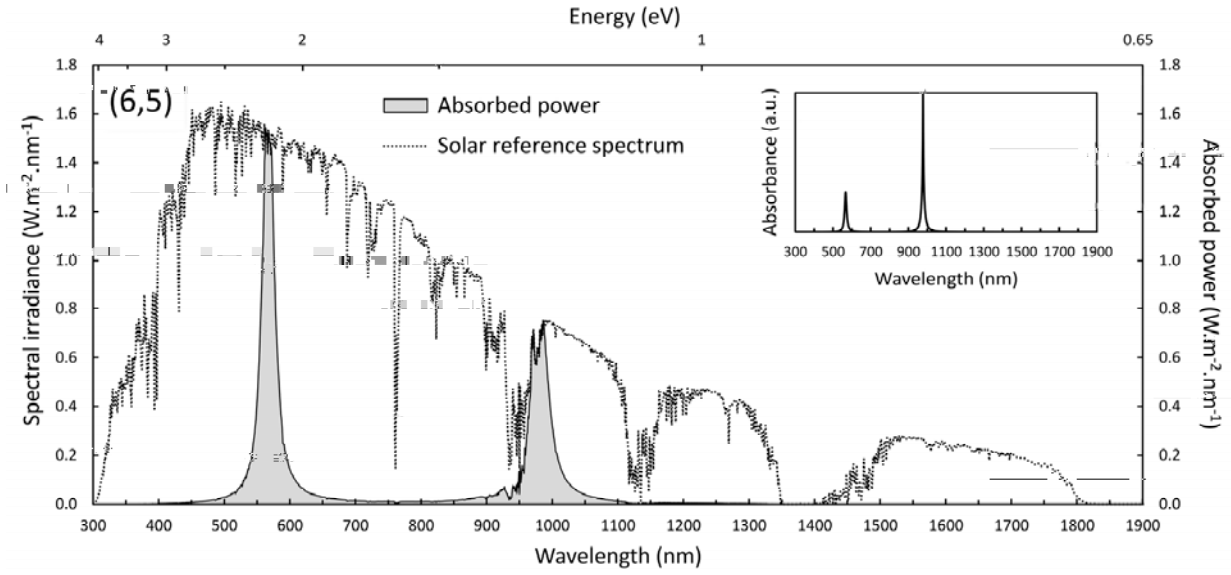

Figure 7.2 The simulation output for the (6,5) nanotube species showing both S_{11} and S_{22} absorption features overlaid with the terrestrial solar reference spectrum (AM1.5G). The apparent height of the S_{22} peak is much larger than S_{11}, however this is simply due to the SWCNT absorptance being multiplied by larger values of the spectral irradiance in the higher energy region. A full graphical list of the simulation output for all of the (n,m) species considered herein can be found in Appendix 3. Note that the SWCNT absorption profile is necessarily expressed as *absorptance* (see section 7.2). **Inset** The same SWCNT absorption profile presented on the more familiar logarithmic *absorbance* scale.

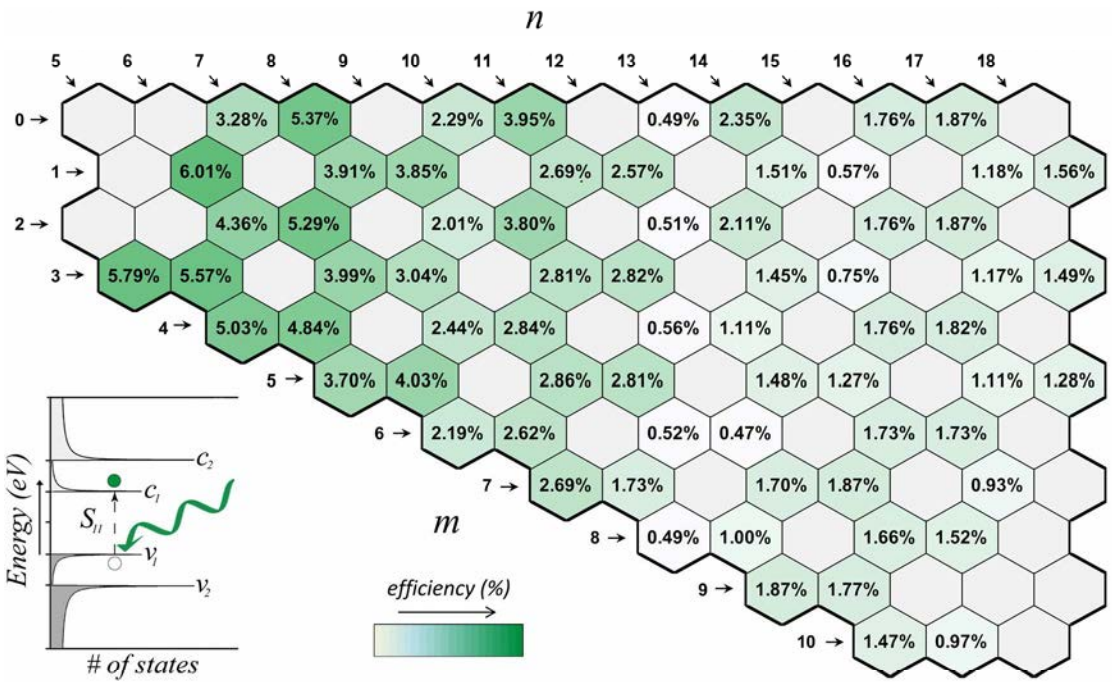

Figure 7.3 The potential efficiency, or percentage of AM1.5G sunlight harvested, as a function of (n,m) species for carriers photogenerated via the S_{11} optical transition. **Inset** Schematic of the one dimensional density of states of a s-SWCNT showing the S_{11} optical transition between the upper valance band (v_1) and lower conduction band (c_1).

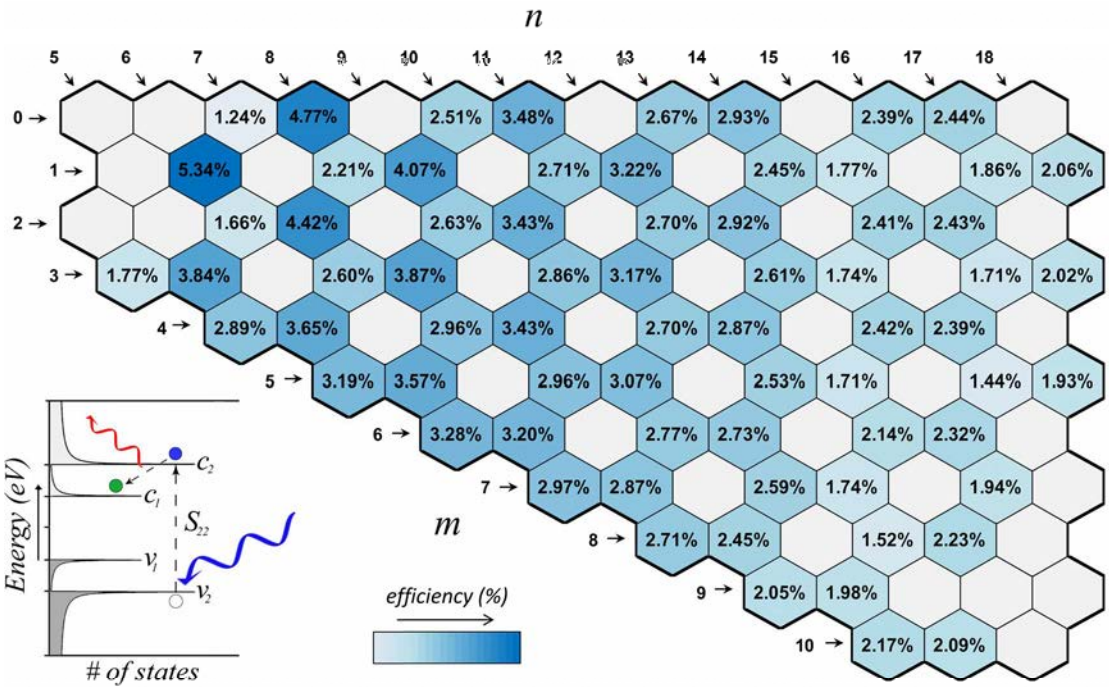

Figure 7.4 The harvesting potential as a function of (n,m) species for carriers photogenerated via the S_{22} optical transition (then radiatively relaxed back to S_{11} before extraction). **Inset** Schematic of the one dimensional density of states of a s-SWCNT showing the S_{22} optical transition between the second valance (v_2) and conduction (c_2) bands.

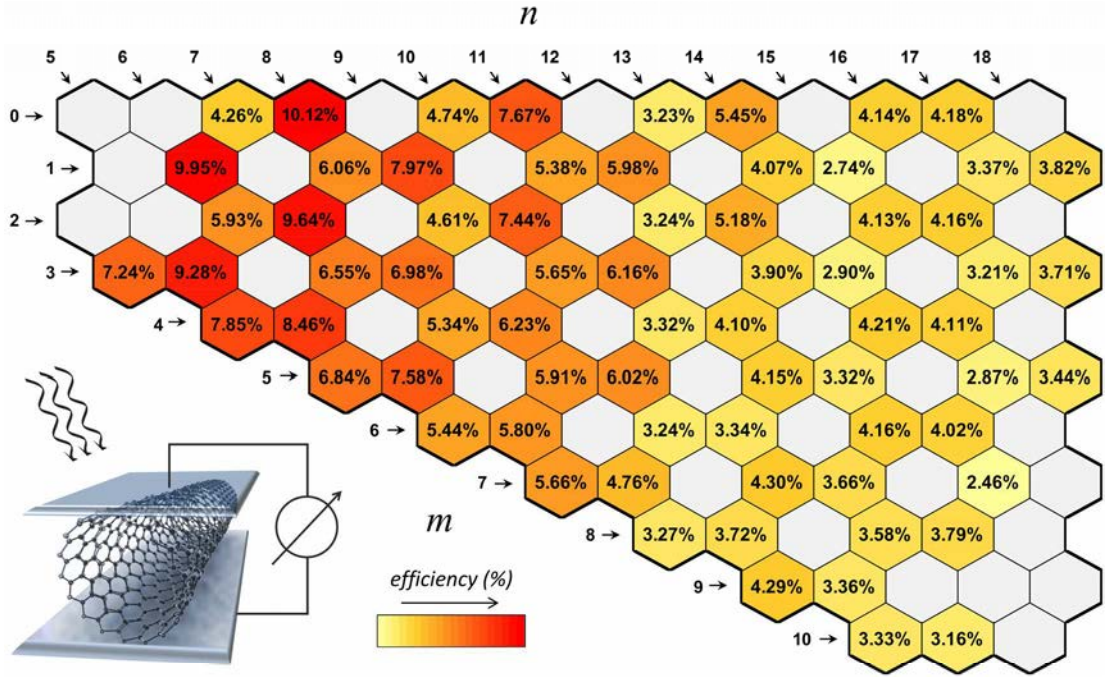

Figure 7.5 The harvesting potential as a function of (n,m) species, if the solar cell is considered to be capable of simultaneously extracting carriers photogenerated via both the S_{11} and S_{22} optical transitions. **Inset** Schematic of the ideal s-SWCNT solar cell considered in the model, consisting simply of a s-SWCNT absorber layer, a mechanism for separating photogenerated excitons into free electrons and holes and a mechanism for extracting these into an external circuit to do work.

A consideration of only S_{22} absorption (**Figure 7.4**) also shows a strong dependence on the transition energy. More so than for S_{11}, there are some species for which the transition energy is high enough into the blue/UV region to elicit a reduced efficiency due to overlap with the region of the terrestrial solar spectrum where irradiance is reduced by ozone. Naturally, when combining S_{11} and S_{22} (**Figure 7.5**), there is the dependence on transition energy and the species which exhibited a poor efficiency in one or both of the previous analyses are similarly poor in the combined analysis.

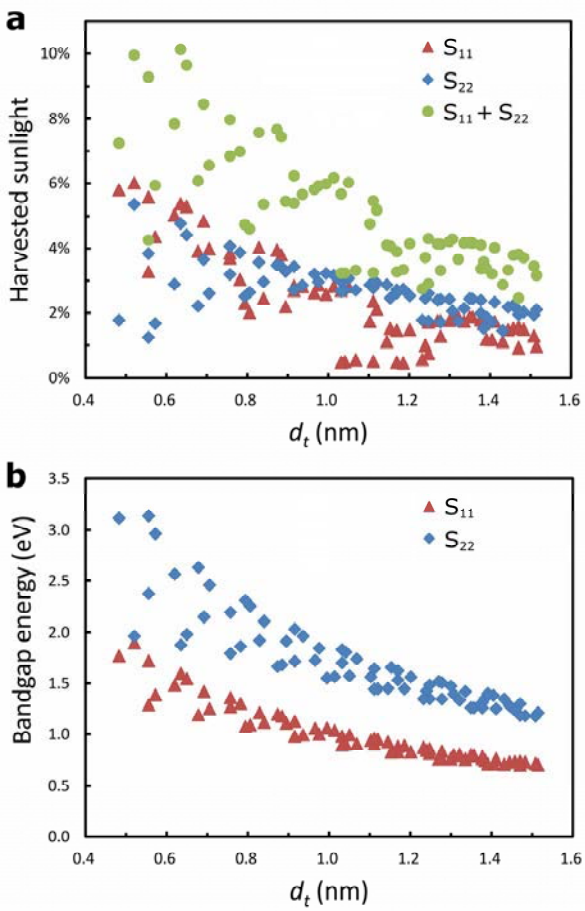

Figure 7.6 **a**, The dependence of the potential sunlight harvesting efficiency on SWCNT diameter. **b**, The dependence of the S_{11} and S_{22} transition energies on SWCNT diameter.

The dependence of the efficiency on diameter (**Figure 7.6**(a)) clearly illustrates large deviations from the familiar bandgap/diameter relationship seen in the Kataura plot (**Figure 7.6**(b). In fact, although the combination of S_{11} and S_{22} has reduced the difference between the extremes of the efficiency found when considering only S_{11} or S_{22}, it has exaggerated the differences between some SWCNTs with almost identical

diameters. This large difference in sunlight harvesting potential between SWCNTs of almost identical diameter dramatically demonstrates the importance of choosing appropriate (n,m) species to maximise performance in solar cell applications. Since the difference is caused by the absorption of different regions of the solar spectrum, this could be advantageous in the context of providing a degree of choice in the absorption profile whilst maintaining compatibility with other elements of the solar cell which may limit the range of SWCNT diameters that can be used e.g. ensuring steric compatibility with wrapping polymers in organic photovoltaics.

It is necessary for the absorber layer not to contain SWCNTs of differing bandgap or, depending on the structure of the particular device in question, either all carriers will be extracted at a maximum electric potential corresponding to the smallest bandgap (after losing any extra energy) or the species with the smallest gap will act as a trap for the others. Thus, mixing species to increase the absorption range of a single absorber layer is unhelpful. However, SWCNTs could be deployed in multijunction devices with other absorber layers composed of different species, or in conjunction with entirely different absorbing materials. A SWCNT-based solar cell with the appropriate (n,m) species could be fabricated behind an organic bulk heterojunction solar cell to scavenge energy from regions of the solar spectrum that cannot be captured by the primary cell, or to recapture a portion of the energy lost from the primary cell via electroluminescence.[17] The large range of SWCNT species allows for a high degree of flexibility in matching absorption profiles to maximise overall device efficiency.

To examine the multijunction proposition, two s-SWCNT tandem solar cells were simulated (**Figure 7.7** and **Figure 7.8**), with component species chosen for either maximum or infrared absorption. It is important to note here that although there will be an unavoidable recombination rate that will surely lower device efficiency, there will be no losses associated with the relaxation of excitons to the fundamental band edge as with bulk semiconductors. This is because, naturally in the case of S_{11},

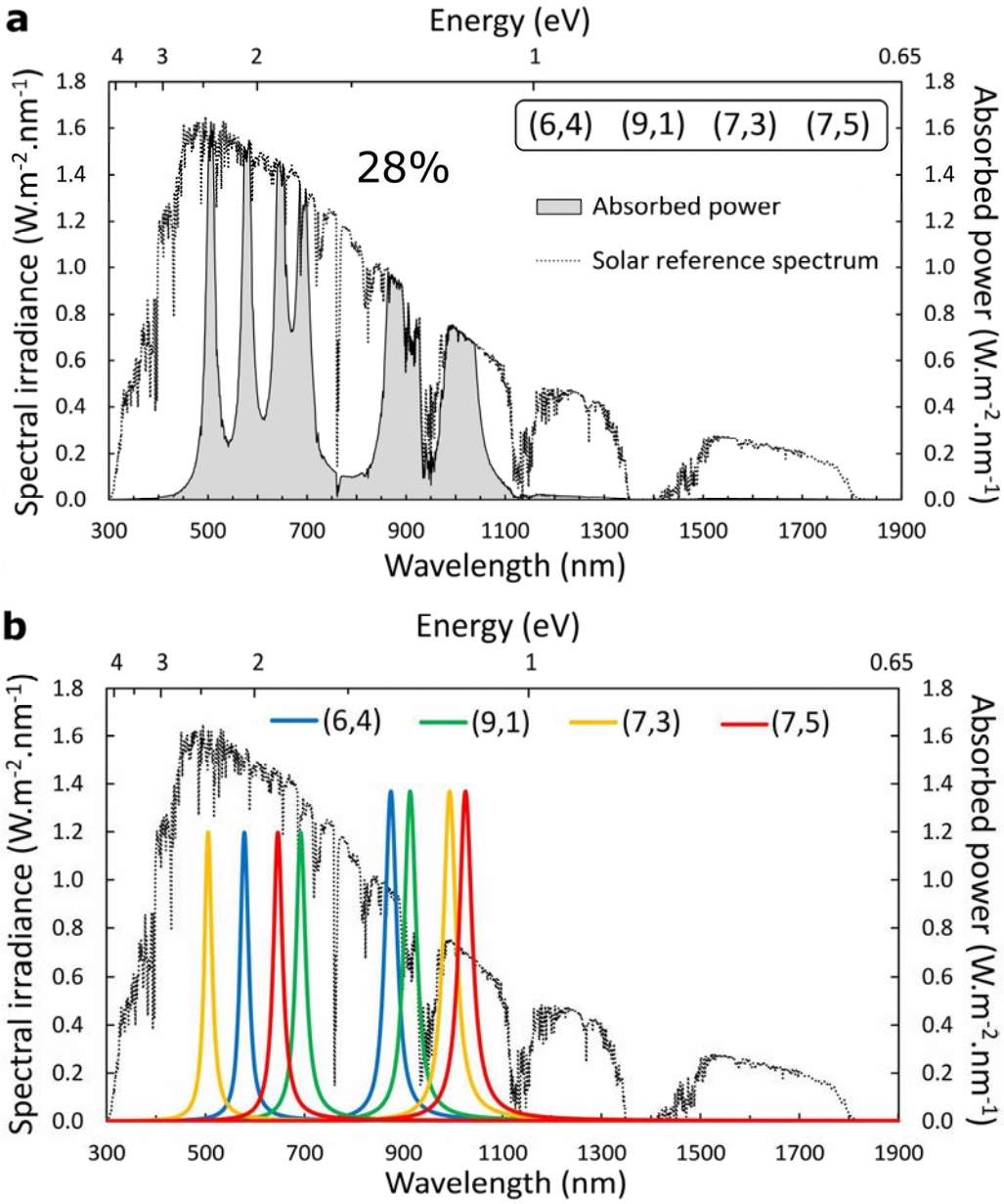

Figure 7.7 **a**, A tandem solar cell consisting of four individual cells of different (n,m) species, where the combination of species has been chosen to provide maximum power absorption, yielding a calculated efficiency of 28.3 % in this analysis. **b** shows the contributions of the different component SWCNT species which give rise to the combined tandem cell absorption profiles shown in **a**.

this is not an issue and, in the case of S_{22}, such relaxation losses have already been taken into account in the simulation. It must also be noted that the model is deliberately conservative in setting the optical depth, $\tau = 1.36$ and keeping the fwhm of the absorption features to a minimum corresponding to a singly dispersed approximation. In a real device, such single tube dispersion is unlikely and any bundling of SWCNTs will significantly increase the fwhm. A doubling of τ in the first device, corresponding to increasing the thickness or nanotube density of the absorber layers in a real device, would increase the efficiency to 41.9 % whilst a tripling would yield 49.5 %. A doubling of τ in the second tandem cell would increase the calculated efficiency from 19.0 % to 30.0 %, without significantly altering the range of the absorption, although it would also increase undesirable S_{33} absorption in the visible. A tripling of τ in this case would yield 35.7 %. Considering the deliberately conservative nature of the model used and the ease with which the absorption by SWCNTs could be increased in real devices, the simulated tandem solar cell efficiencies clearly demonstrate the impressive potential of SWCNT-based solar cells and sunlight-harvesting devices.

7.4 Summary

Whilst these simulations are the first attempts to quantify the potential of the different s-SWCNT species to harvest sunlight they do not, and are not intended to, provide a definitive limit on SWCNT-based solar cell efficiency. Rather, they constitute a comparison between species to inform and direct future research in this area. Among the many practical challenges to realising the promise of SWCNT-based solar cells indicated in this work are; refining and scaling up the processes to separate SWCNTs by (n,m) species, incorporating the effects of the observed transition energy red shifts and peak broadening for SWCNTs in bundles[18] and the necessary control of these in real devices via bundle size optimisation, as well as suppression or exploitation of the efficient nonradiative exciton recombination pathways that lead to the observed low quantum yields in s-SWCNT photoluminescence[19] and will presumably hamper efforts to obtain high quantum

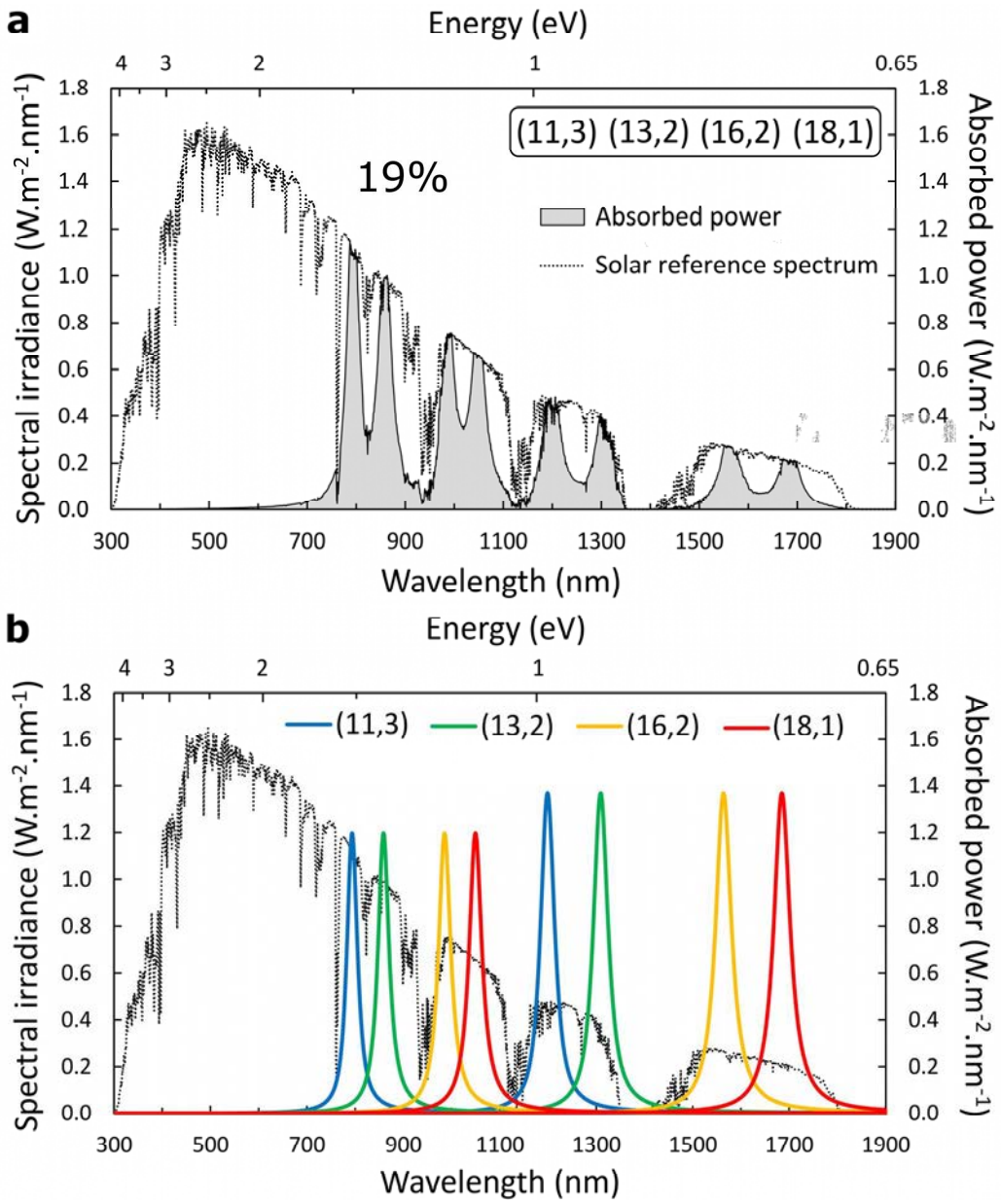

Figure 7.8 **a**, A similar tandem solar cell to Figure 7.7, but where the combination of species has been chosen to maximise absorption in the infrared, yielding 19.0% efficiency, whilst minimising absorption of visible light (remembering that there will still be some absorption in the visible due to S_{33} which is not considered herein). This is not possible with bulk semiconductors since, if the bandgap is in the IR, then the material will be opaque to visible light. Such capability could allow for the fabrication of IR absorbing, building integrated photovoltaic windows. **b** shows the contributions of the different component SWCNTs which give rise to the combined tandem cell absorption profiles shown in **a**.

efficiencies from solar cell devices. However, despite these challenges, the simulations presented herein indicate great potential and it is hoped that they will provide a powerful resource for the practical development of future SWCNT-based photovoltaics.

7.5 References

[1] Bindl, D.J., Wu, M.-Y., Prehn, F.C., and Arnold, M.S., *Nano Letters,* **2010**. 11(2): p. 455-460.

[2] Švrček, V., Cook, S., Kazaoui, S., and Kondo, M., *The Journal of Physical Chemistry Letters,* **2011**. 2(14): p. 1646-1650.

[3] Jain, R.M., Howden, R., Tvrdy, K., Shimizu, S., Hilmer, A.J., McNicholas, T.P., Gleason, K.K., and Strano, M.S., *Advanced Materials,* **2012**. 24(32): p. 4436-9.

[4] Ramuz, M.P., Vosgueritchian, M., Wei, P., Wang, C., Gao, Y., Wu, Y., Chen, Y., and Bao, Z., *ACS Nano,* **2012**. 6(11): p. 10384-95.

[5] Bindl, D.J., Shea, M.J., and Arnold, M.S., *Chemical Physics,* **2012**. 413: p. 29-34.

[6] Shockley, W. and Queisser, H.J., *Journal of Applied Physics,* **1961**. 32(3): p. 510-519.

[7] Gabor, N.M., Zhong, Z., Bosnick, K., Park, J., and McEuen, P.L., *Science,* **2009**. 325(5946): p. 1367-1371.

[8] Wang, S., Khafizov, M., Tu, X., Zheng, M., and Krauss, T.D., *Nano Letters,* **2010**. 10(7): p. 2381-6.

[9] *ASTM G-173-03 standard tables for reference solar spectral irradiances: direct normal and hemispherical on 37° tilted surface*. 2008.

[10] Bachilo, S.M., Strano, M.S., Kittrell, C., Hauge, R.H., Smalley, R.E., and Weisman, R.B., *Science,* **2002**. 298(5602): p. 2361-2366.

[11] Maultzsch, J., Telg, H., Reich, S., and Thomsen, C., *Physical Review B,* **2005**. 72(20): p. 205438.

[12] Nair, N., Usrey, M.L., Kim, W.-J., Braatz, R.D., and Strano, M.S., *Analytical Chemistry,* **2006**. 78(22): p. 7689-7696.

[13] Olivero, J.J. and Longbothum, R.L., *Journal of Quantitative Spectroscopy and Radiative Transfer,* **1977**. 17(2): p. 233-236.

[14] Ohmori, S., Saito, T., Tange, M., Shukla, B., Okazaki, T., Yumura, M., and Iijima, S., *The Journal of Physical Chemistry C,* **2010**. 114(22): p. 10077-10081.

[15] Ma, Y.-Z., Stenger, J., Zimmermann, J., Bachilo, S.M., Smalley, R.E., Weisman, R.B., and Fleming, G.R., *The Journal of Chemical Physics,* **2004**. 120(7): p. 3368-3373.

[16] Naumov, A.V., Ghosh, S., Tsyboulski, D.A., Bachilo, S.M., and Weisman, R.B., *ACS Nano,* **2011**. 5(3): p. 1639-1648.

[17] Vos, A.D., *Journal of Physics D: Applied Physics,* **1980**. 13(5): p. 839.

[18] Fantini, C., Jorio, A., Souza, M., Strano, M.S., Dresselhaus, M.S., and Pimenta, M.A., *Physical Review Letters,* **2004**. 93(14): p. 147406.

[19] Kinder, J.M. and Mele, E.J., *Physical Review B,* **2008**. 78(15): p. 155429.

Chapter 8
Conclusion

Throughout this thesis the results of new investigations into the use of SWCNTs in photovoltaics have been presented. The goal of exploring further applications of SWCNTs in photovoltaics was achieved, with the results of experiments helping to shed light on some of the issues. In Chapter 2, it was shown that DSCs can be fabricated with SWCNT working electrodes, that output is increased with successive additions of EDA-linked SWCNTs and that such interconnected networks can be used as the scaffold for dye molecules. As discussed, similar structures have since been reported with very promising efficiencies. However, in addition to the problem of the apparent resistance of the EDA links, the architecture faces a fundamental challenge of maintaining charge separation; in the nanotube only case, the channel for delivering charge from the photoexcited SWCNTs to the electrolyte is also the most likely recombination pathway. In a conventional DSC this problem is mitigated by applying a monolayer of photoactive dye to the surface of the TiO_2, which also extends the range of absorption from UV down into the visible, but it is not possible to apply a monolayer dye coating to the nanotubes. This means that there will always be some possible contact between the redox species in the electrolyte and charges travelling through the SWCNT network. Recombination will likely occur at any defects in the tube walls, but those defects are required to form the diamide (tube-tube) and ester (tube-surface) links. With these issues in mind the work was refocussed onto different solar cell architectures.

Chapter 3 detailed the effect on the performance and various solar cell parameters of changing the thickness of the SWCNT film, as well as treatments and doping steps involved in fabricating complete devices. As proof of principle and observation of trends this work was not really new, with most of the measurements already reported by the Wu group and collaborators, among others. Nevertheless, considering that the SWCNTs used here were of a different type/mixture than those reported elsewhere, as well as the fact that every lab's processes have their own peculiarities, it was absolutely necessary to make these investigations anew on the specific systems and processes reported in this thesis. In the future, many of the advances already made in silicon solar cell technology can be applied to the SWCNT-silicon system including

antireflection texturisation or coating, back surface fields and buried contacts. This thesis was careful to stay focussed on monocrystalline silicon technology but it must be mentioned that there is a lot of good work being done investigating the use of carbon nanotubes in amorphous silicon photovoltaics.

A reasonable hypothesis, and one found also in the literature, was that perhaps SWCNTs may contribute to photocurrent generation in SWCNT-silicon heterojunction solar cells. Chapter 4 reported an experiment designed to measure the contribution to photocurrent generation by the SWCNTs that was suggested by the results of other reports. A contribution was not observed, but the deliberate formation of a non-ohmic back contact caused a feature to appear in the photocurrent spectra that bore a striking resemblance to what might be expected, if such a contribution existed. Furthermore, when the optical density of the SWCNT film was increased, rather than seeing contribution from the SWCNTs, significant reductions in photocurrent were observed in the wavelength regions corresponding to the SWCNT absorption features. It is not an assertion of this thesis that this is the end of the matter. In future work, one of at least two sets of experiments is required to completely rule out contribution from the nanotubes; either a repeat of the Chapter 4 experiment but using a much larger range of significantly purer SWCNT species to mitigate possible band gap mismatch effects or, a similar experiment, but on the single tube device level. Since only a small number of SWCNT species can be produced in very high purity and in useful quantity, and then only by a few groups, such experiments will have to wait.

Although a lack of contribution from the SWCNTs strongly suggests that the SWCNT-silicon system is not operating in the manner of a pn junction, with the nanotubes taking the role of the p-type emitter, it is certainly not conclusive proof of any particular operating mechanism. As discussed, almost all published results obtained from SWCNT-silicon solar cells are confounded by the fact that the SWCNTs are present as a mixture of metallic and various bandgap semiconducting species. Considering that the use of silicon limits the choice of operating

mechanisms to MS, MIS or pn (an "SS" system), this has added an extra layer of difficulty to the problem of elucidating the true mechanism. Chapter 5 reported the outcomes of an experiment that took some steps to address this issue by fabricating devices with very high purity s-SWCNTs or m-SWCNTs. The results show that solar cells fabricated with m-SWCNTs significantly outperform those made with s-SWCNTs or the unsorted SWCNTs from which the semiconducting and metallic material was derived; however the situation became less clear after doping of the SWCNTs. Considering these results, and the clearly conflicting data to be found in the literature, the issue of which mechanism underlies the operation of these devices is still very much unresolved. In future work, an experiment could follow on from the observation that the unsorted SWCNT devices functioned in some ways better than the m-SWCNT devices after doping. This would involve a series of solar cells made with SWCNT films having controlled compositional ratios of m-SWCNTs and s-SWCNTs (i.e. 10:0, 9:1, 8:2 … 0:10). As a next step in bringing the issue of the operating mechanism to resolution, a repeat of the Chapter 5 experiments using very highly aligned SWCNT films will be revealing. On a fundamental level, it would be helpful to have more work done to solidify understanding of the photophysics of the SWCNT-silicon interface whilst, on a more practical level, much larger area devices will need to be demonstrated before this 'nanotubes as front electrodes of silicon cells' concept is really taken seriously by industry.

One of the issues with SWCNT-silicon solar cells is the lack of complete coverage of the silicon surface by the SWCNT film (excepting the recent highly aligned work coming out of the Reed group) and the resulting non-ideality of the interface. As well as adding an extra layer of confusion to the already tricky issue of operating mechanisms, it was hypothesised that this may be a cause of poor efficiencies as measured during this work and reported in the literature at that time. It was also hypothesised that the observation of poor FF may be due to recombination between electrons in the silicon and holes travelling through the SWCNT film. To address this issue, a thin layer of conducting polymer was deposited onto the silicon surface prior to the addition of the SWCNT film. This greatly improved device

performance compared to using only SWCNTs or only the conducting polymer. Since that time there has been much progress in the field and now high FF, good efficiency devices are being reported for SWCNT only systems. Thus it seems that the problems addressed by the inclusion of the polymer no longer limit currently reported devices. However, the work reported here on the SWCNT-polymer-silicon system was essentially a proof of principle plus some characterisation and there remains much that should be investigated in future work. For example, other polymers that could be used include polypyrrole, polythiophene, their derivatives e.g. PEDOT and more. Also, the choice of dopant ion, species of SWCNTs, method of polymer deposition (e.g. ex situ polymerisation then spin coat or in situ electropolymerisation) as well as optimisation of polymer/nanotube layer thicknesses are all interesting factors to be considered.

Although the secondary goal of finding photovoltaic systems that directly exploit light absorption by the SWCNTs was not achieved here, it was achieved elsewhere during the same period, primarily by the Arnold group but also with valuable contributions by others. The importance of this development in the field of photovoltaics, which has been discussed and predicted by many authors over many years, can hardly be understated and has opened up a new field of possibilities. As discussed in Chapter 7, in bulk semiconductors there is a single, fixed bandgap which allows for the renowned Shockley/Quiesser analysis of the optimal bandgap criterion for solar cell applications. In organic and dye sensitised photovoltaic systems such analysis is less relevant because the absorption properties can be very finely tuned by altering the chemical structure of the absorber e.g. adding a methyl group to a polymer side chain or exchanging ligands in a metal-centred dye complex. At least one of the assumptions of the generalised SQ analysis do not apply for SWCNTs, but because their absorption properties cannot be tuned in the same way as in organic systems, similar analyses are still needed to direct and inform research in this area. It is hoped that the numerical simulations and discussion that were presented herein will form a solid foundation for the further development and refinement of such analyses. In future work, the following factors should be

incorporated into the model and simulations: the S_{33} transitions, absorption due to phonon-exciton coupling (the other features observed in the experimental data in Figure 7.1), variations in S_{22}/S_{11} peak heights, variations in the oscillator strength of all the transitions with chirality, the background absorption of s-SWCNTs (the existence of which is evidenced by a background in excitation spectra of PLE maps), as well as the (diameter and chirality dependent) effects of bundling e.g. red/blue shifting of different transitions, trapping/quenching of excited states, broadening of the fwhm and altering of the shape of the absorption features between Lorentzian and Gaussian, as well as the vital issue of current matching in the tandem devices.

Glossary

AAO	anodised aluminium oxide
AFM	atomic force microscopy
BCP	bathocuproine
BHJ	bulk heterojunction
BIPV	building integrated photovoltaics
BOS	balance of system
CCS	carbon capture and storage
COM	CoMoCat (cobalt molybdenum catalysed, nanotube growth)
CVD	chemical vapour deposition
DCC	dicyclohexylcarbodiimide
DGU	density gradient ultracentrifugation
DI	deionised
DMAP	4-dimethylaminopyridine
DMF	dimethylformamide
DMSO	dimethylsulphoxide
DOC	deoxycholate
DSC	dye solar cell
DWCNT	double walled carbon nanotube
EDA	ethylenediamine
EMI-BTI	1-ethyl-3-methylimidazolium bis(trifluoromethylsulphonyl)imide
EQE	external quantum efficiency
FF	fill factor
FM	figure of merit
FTO	fluorine-doped tin oxide
GC	gel chromatography

GDP	gross domestic product
HDI	human development index
HOMO	highest occupied molecular orbital
IQE	internal quantum efficiency
ITO	indium tin oxide
J_{SC}	short circuit current density
J_0	reverse saturation current density
LAB	laser ablation
LUMO	lowest unoccupied molecular orbital
MCE	mixed cellulose ester
MEG	multiple exciton generation
MIS	metal-insulator-semiconductor
MLCT	metal to ligand charge transfer
MPN	3-methoxypropionitrile
m-SWCNT	metallic single walled carbon nanotube
MWCNT	multiwalled carbon nanotube
OPV	organic photovoltaic
P3HT	poly(3-hexylthiophene)
PCBM	[6,6]-phenyl-C_{61}-butyric acid methyl ester
PCE	power conversion efficiency
PDMS	polydimethylsiloxane
PEDOT	poly(3,4-ethylenedioxythiophene)
PFO	poly(9,9-di-n-octyl-fluorenyl-2,7-diyl)
PLV	pulsed laser vaporisation
PSS	poly(styrene sulphonate)
QCM	quartz crystal microbalance
rGO	reduced graphene oxide
R_S	series resistance
R_{SH}	shunt resistance
R_{sheet}	sheet resistance
SDS	sodium dodecyl sulphate
SEM	scanning electron microscopy
SMU	source measure unit

s-SWCNT	semiconducting single walled carbon nanotube
UV-Vis-NIR	ultraviolet visible near infrared
V_{OC}	open circuit voltage

Appendix 1
Summary of SWCNT-silicon solar cell literature reports

Publication details						Cell properties									Silicon					
#	Year	Author	Group	Journal	Subject	Active area (cm^2)	J_{SC} ($mA\ cm^{-2}$)	V_{OC} (V)	FF	η (%)	R_S (Ω)	R_{SH} (kΩ)	Rectification ratio	Ideality Factor n_1	Ideality Factor n_2	J_0 ($mA\ cm^{-2}$)	Plane	Dopant conc. (cm^{-3})	Resistivity (Ω cm)	Treatment	Thickness (μm)	Oxide (nm)
1	2007	Wei	Wu*	Nano.Lett.	DWNT Solar Cells	0.49	13.8	0.5	0.19	1.4	30 - 200	-	$5x10^2$	-	-	0.03	-	-	-	HF	525	-
2	2008	Arena	Pistone	Micro.elec.J	Photo props of MWNT/n-Si cells	0.01	2.7	0.29	0.46	~3 #	-	-	30	-	-	-	-	-	-	HF	-	-
3	2008	Jia	Wu*	Adv.Mat.	SWCNT-Si Solar Cells	0.49	26	0.54	0.53	7.4	13	20	10^3	3.68	2.62	-	-	10^{15}-10^{16}	2-3	HF	-	-
4	2008	Li	Biris	Appl.Phys.Lett.	$SOCl_2$ enhanced photo of SWCNT-Si cells	0.25	21	0.48	0.28	~1.3	-	-	10^2	-	-	0.05	-	-	-	-	-	-
5	2009	Li	Biris	ACS Nano	Light harvest high density SWCNT-Si cells	0.25	26.5	0.49	0.35	4.5	16	-	$4x10^2$	-	-	0.03	-	-	-	-	-	-
6	2010	Jia	Wu*	Mat.Res.Bull.	CNT films filtration SWCNT-Si cells	0.49	18.6	0.53	0.42	4.1	-	-	-	-	-	-	-	-	-	HF	-	-
7	2010	Ong	Levitsky	Nanotechnology	Hybrid SWCNT-Si cells	0.25	14.6	0.37	0.3	1.7	150	7	-	3.75	-	-	<100>	10^{19}	0.01	HF	-	-
8	2010	Wadhwa	Rinzler†	Nano.Lett.	Electronic junction control SWCNT-Si cells	0.08	25	0.55	0.79	10.9	-	-	-	-	-	-	-	10^{14}-10^{15}	4-20	BOE	-	-
9	2010	Li	Wu*	J.Mat.Chem	Large area spiderweb electrodes	0.49	25.1	0.53	0.55	7.3	-	-	-	-	-	-	-	10^{15}-10^{16}	3-5	-	-	-
10	2011	Jia	Ajayan*	Nano.Lett.	High eff. SWCNT-Si cells acid doping	0.09	36.3	0.53	0.72	13.8	25	-	-	1.4	-	-	-	10^{15}-10^{16}	2-4	HF	-	-
11	2011	Jia	Xu*	Appl.Phys.Lett.	Encapsulated SWCNT-Si MIS cells 10%	0.09	29	0.56	0.68	10.9	65	-	$1.2x10^5$	1.44	-	-	-	10^{15}-10^{16}	2-5	HF	-	-
12	2011	Wadhwa	Rinzler†	Nano.Lett.	Electrolyte induced inversion Schottky	0.08	29.8	0.55	0.73	12.0	-	-	-	-	-	-	<111>	10^{15}	4	BOE	-	-
13	2012	Jia	Wu*	PCCP	Reversible performance oxide interlayer	0.09	24.3	0.54	0.67	8.8	34	3000	-	1.4		0.005	-	10^{15}-10^{16}	2-5	HF	-	300
14	2012	Kozawa	Matsuda	Appl.Phys.Ex	Photo props of SWCNT-Si cells	-	14.6	0.39	0.43	2.4	56	2	-				-	-	-	-	-	-
15	2012	Shi	Cao*	Sci.Reps.	TiO_2 -coated SCNT-Si cells	0.15	32	0.61	0.77	15.1	-	-	-	-	-	-	-	10^{16}-10^{18}	0.05-0.2	HF	400	400
16	2012	Chen	Guo†	Appl.Phys.Lett.	Carrier dynamics/optimisation electrolyte induced inversion	-	-	-	-	-	-	-	-	-	-	-	-	10^{15}	4	-	10	1000
17	2012	Jung	Reed	Nano.Lett.	High eff. SWCNT-Si	-	28.6	0.53	0.74	11.2	-	-	-	1.05~1.15	-	$7x10^{-8}$	-	10^{15}-10^{16}	2-5	HF	-	500
18	2013	Li	Reed	EES	Improved eff. smooth aligned SWCNT film	-	29.3	0.53	0.74	11.5	-	-	-	1.08	-	$3x10^{-6}$	<100>	10^{14}-10^{16}	1-10	HF	-	500
19	2013	Tune	Shapter‡	ChemSusChem	SWCNT/PANI/Si cells	0.08	27.4	0.52	0.68	9.7	37	6	-	1.38	-	$1.2x10^{-5}$	<100>	10^{14}-10^{15}	1-20	BOE	525	100
20	2013	Tune	Flavel‡	Adv.En.Mat.	Role of tubes in SWCNT-Si cells	0.08	-	-	-	-	-	-	-	-	-	-	<100>	10^{14}-10^{15}	5-25	BOE	525	100
21	2013	Cui	Murayama	J.Phys.Chem.Lett.	Honeycomb network SWCNT-Si cells	0.09	25	550	0.73	10.0	-	-	-	-	-	-	<100>	10^{14}-10^{15}	7.5-12.5	NaOH	-	100

‡ † * indicate work from the same research or collaborative groups

#	Nanotubes								Front Contact		Back Contact		Notes
	Type	Source	Chirality (n,m)	Diameter (nm)	Thickness (nm)	R_{sheet} (Ω sq^{-1})	Depostion Method	Treatment	T_{550} (%)	Type	Thickness (nm)	Type	Thickness (μm)	
1	DWCNT	CVD	-	-	50	0.5 - 5	Aqueous Film transfer	H_2O_2/HCl	>60	Ag	-	Ti/Pd/Ag	2	Series resistance reduced by deposited Ti/Pd/Ag on back contact instead of silver paint
2	MWCNT	CVD	-	~12	-	-	Drop coat DCB 80^{o}C	HCl	-	Probe	-	Probe	-	Bad eff% calculation, 0.9 mW cm^{-2} light, SDS surfactant still present in CNT film
3	DWCNT	CVD	-	2	20-50	-	Aqueous Film transfer	H_2O_2/HCl	>60	Ag	-	Au/Ti	0.01	Improvement over #1 through replacing 2 μm Ti/Pd/Ag with 10 nm Au/Ti, energy diagram
4	SWCNT	HiPCO	-	0.6 - 1.1	-	170	Spray	$SOCl_2$	69	-	-	-	-	Improvement via $SOCl_2$ doping
5	SWCNT	-	(6,5) (7,5)	-	~250	~500	Spray	$SOCl_2$	57	Ag	-	Ag	-	Carrier density and effective mobility measurements (Hall effect) before and after $SOCl_2$
6	DWCNT	CVD	-	-	-	282	MCE	-	91	Ag	-	Ti/Au	50	Correlation of figure of merit (FM) for transparent, conductive thin films with PCE of SWCNT-Si solar cells
7	SWCNT	HiPCO	(7,6) (8,6)	0.9	20000 ~30000	1000	Spray	-	83	Ag	-	Cr/Au	0.02/0.15	Proof that SWNT take part in photogeneration, compare centrifugation fractions, energy diagram
8	SWCNT	-	-	-	~45	-	MCE	-	-	Cr/Au	5/80	GaIn	-	Electronically gated with IL
9	SWCNT	CVD	-	1 ~ 2	20-40	~200	Free Transfer	HNO_3	>85	Ag	~1000	Ti/Au	-	Focussed on CVD growth of tubes
10	SWCNT	CVD	-	-	-	<200	Aqueous Film transfer	HNO_3	>85	-	-	Ti/Au	-	Nitric acid soaked nanotubes (0.1-0.5M)
11	SWCNT	CVD	-	-	-	97	Free Transfer	HNO_3	-	-	-	Ti/Au	-	Oxide interlayer MIS design, energy diagram, PDMS encapsulation
12	SWCNT	-	-	-	~45	-	Free Transfer	-	-	Cr/Au	5/80	GaIn	-	Electronically gated with IL, line-etched CNT's
13	SWCNT	CVD	-	-	10~20	<200	Free Transfer	HNO_3	>85	Ag	-	Ti/Au	-	Grow/remove oxide, oxide required
14	SWCNT	CoMoCat	(6,5)	0.78	-	5000	Spray	-	70	-	-	-	-	SWCNT thickness optimisation
15	SWCNT	CVD	-	-	-	-	Transfer	HNO_3/H_2O_2	-	Ag	~1000	GaIn	-	TiO_2 antireflective coating
16	SWCNT	-	-	-	-	-	-	-	80	-	-	-	-	Modelling of carrier dynamics in silicon + BSF/HBL
17	SWCNT	-	-	-			Aqueous Film transfer	$HNO_3/HAuCl_4$		Cr/Au	-	Al	-	Extensive heterojunction characterisation appears to rule out the Schottky mechanism
18	SWCNT	CoMoCat	(6,5)	0.78	30-50	-	Aqueous Film transfer	$HNO_3/HAuCl_4$	-	Cr/Au	5/80	Cr/Au or Al	-	Compare superacid/mayer rod, wet/dry, Au vs. Al backside, effect of HAuCl4
19	SWCNT	CVD	(10,9) (11,10) (12,10)	1.5	~35	310	MCE	$SOCl_2$	78	Ti/Au	5/145	HF/GaIn/Steel	-	PANI interlayer, low FF (0.2) due to high series resistance -- FF = 0.7 ==> PCE ~9 %
20	SWCNT	-	-	-	-	-	MCE	-	>80	Ti/Au	5/145	GaIn or Ag	-	No contribution from SWCNTs to photocurrent, effect of non-ohmic back contact
21	SWCNT	CoMoCat	-	2	-	105	Thermocapillary	HNO_3	48.5	Pt	100	Ti/Pt	0.01/0.05	Exceptional performance without doping (values for doped), stable over many days

Appendix 2
Custom Labview™ virtual instrument for solar cell testing

The following program was written initially to reduce the workload involved in curve fitting of dark current data and streamline the process of obtaining and analysing solar cell output. Modules such as automated time lapsing and the ability to reanalyse old data have continued to be added and the program has evolved to become the workhorse of our solar IV testing facility. Apart from the basic code available from Keithley to interface with their 2400 SMU hardware, the program was conceived, designed and built by the Author.

The program's main features are:

- Source voltage, measure current and log current data to file
- Sweep voltage, measure current, log current-voltage data to file, display
- Analyse light IV data, log data to file, display plot and parameters
- Analyse dark IV data and fit linear regions of the semilog plot of current-voltage data, the plot of dV/d(lnI) vs. I, the plots of the parameters S(J) vs. V and H(J) vs. J, log data to file and display plots, linear fits and calculated parameters
- IV data analysis can be performed on data just obtained, or loaded from any .csv file of voltage and current
- As well as IV data analysis being conducted automatically as data is obtained, fitting parameters can be adjusted 'live' with resulted data saved to a new file
- Automated time lapsing of measurements with live display update

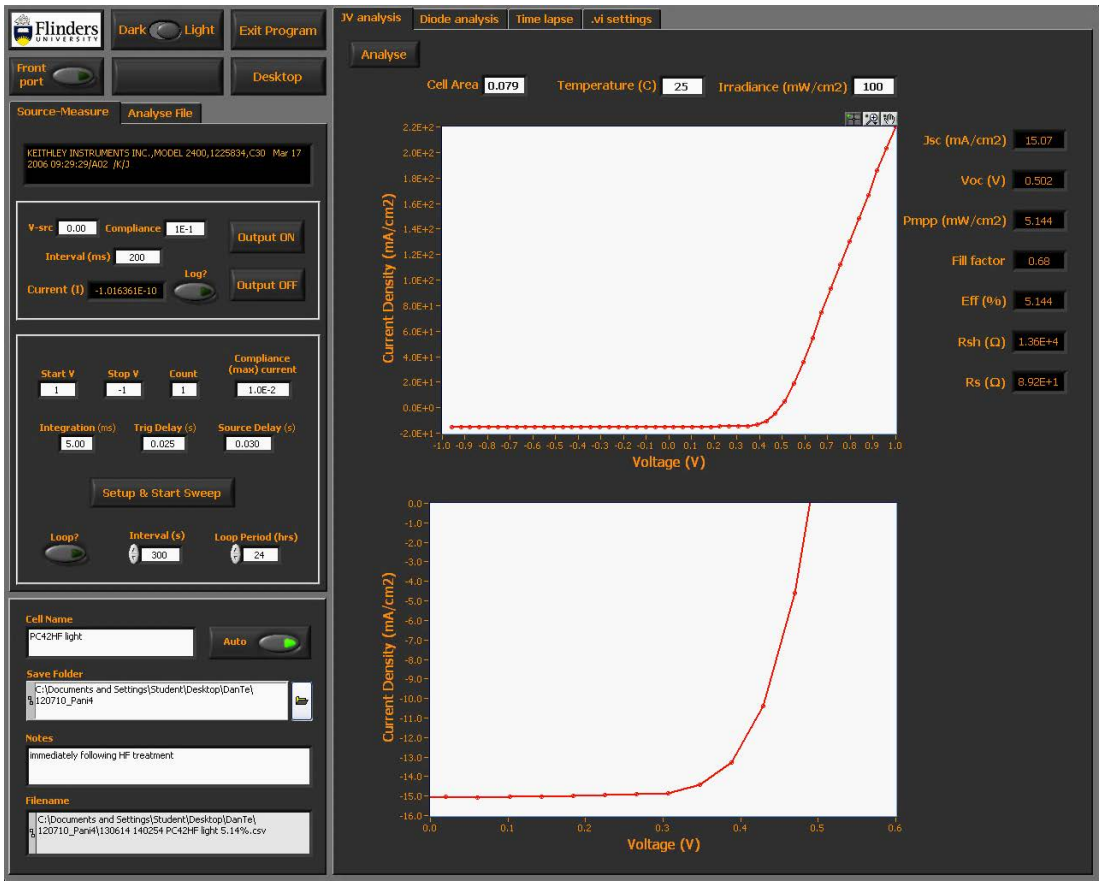

Figure A2.1 Screenshot of J-V analysis tab

Figure A2.2 Screenshot of dark current analysis tab

Figure A2.3 Screenshot of time lapsed light IV measurements

List of virtual instrument components

'Magic IV.vi' – Main program, GUI, File I/O and time lapsing

- 'Keithley 2400 SMU controller.vi' – adapted from Keithley's basic freeware including 'Wait Until Buffer Full - Serial.vi' and 'Display Table and Log.vi'
- 'Light IV curve analysis.vi' – Calculates V_{OC}, J_{SC}, etc from a simple plot of the light current-voltage data
- 'LnJ vs. V.vi' – uses shared components to calculate diode parameters from the semilog plot of the dark current-voltage data
- 'dV-dlnI.vi' - uses shared components to calculate diode parameters from the dV/d(lnI) vs. I plot of the dark current-voltage data
- 'S(J).vi' and 'S(J) vs. V.vi' - together use shared components to calculate diode parameters from a plot of the parameter S(J) vs. voltage data (see Chapter 6 for derivation)
- 'H(J).vi' and 'H(J) vs. J.vi' - together use shared components to calculate diode parameters from a plot of the parameter H(J) vs. current density data (see Chapter 6 for derivation)
- 'Find Linear.vi', 'LinearPtbyPt.vi', 'Replace Zeroes.vi', 'Within Range or Replace With.vi' and 'Within Range Array.vi' – shared components

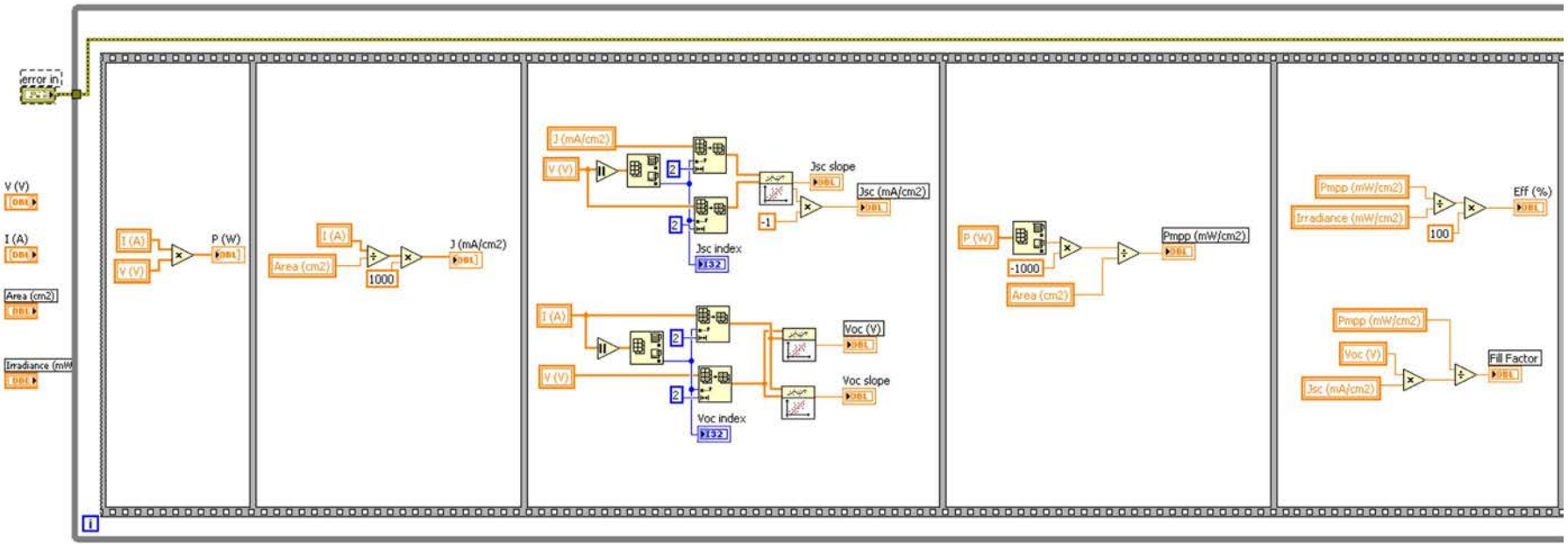

Figure A2.4 Block diagram showing left sequence of 'Light curve analysis.vi' (continued next page ..)

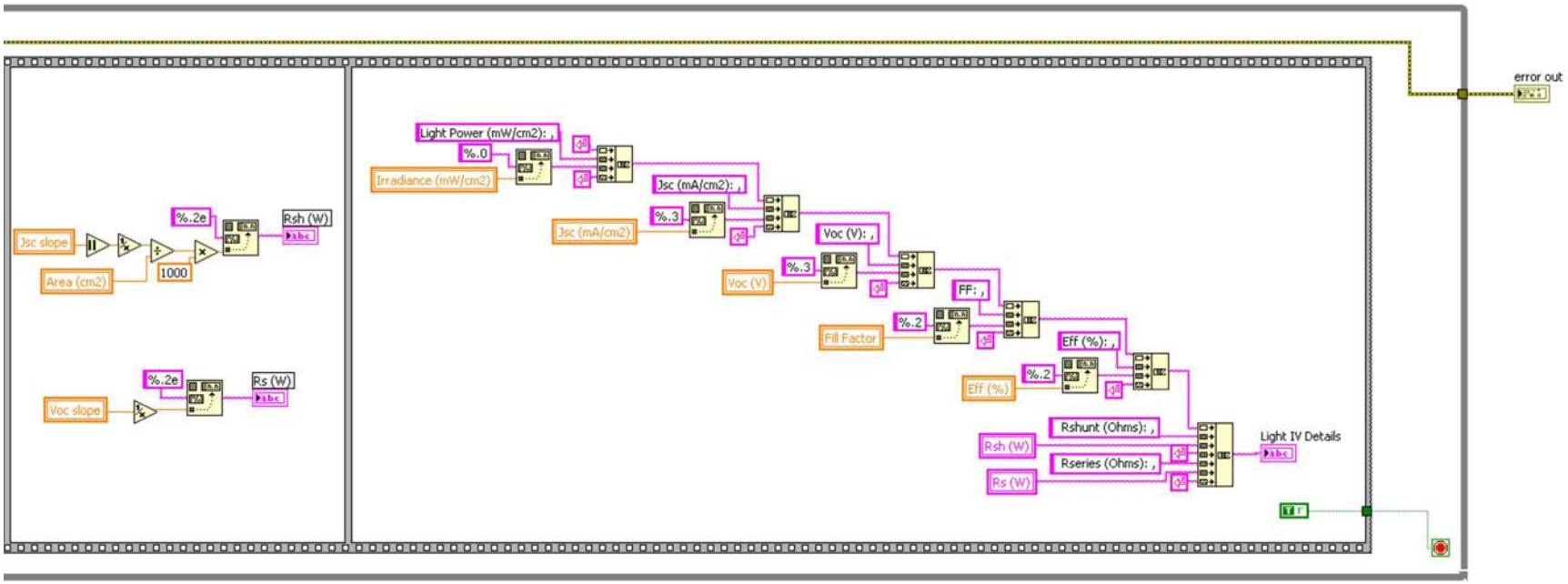

Figure A2.5 Block diagram showing right sequence of 'Light curve analysis.vi'

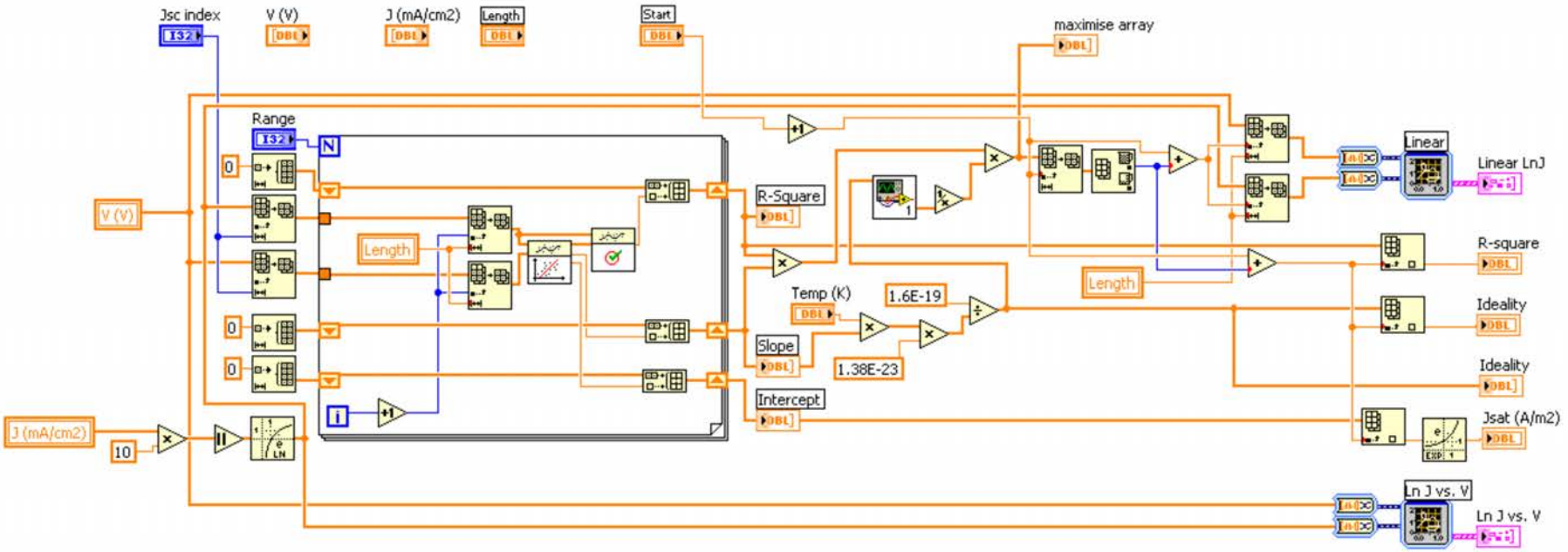

Figure A2.6 Block diagram showing 'LnJ vs. V.vi'

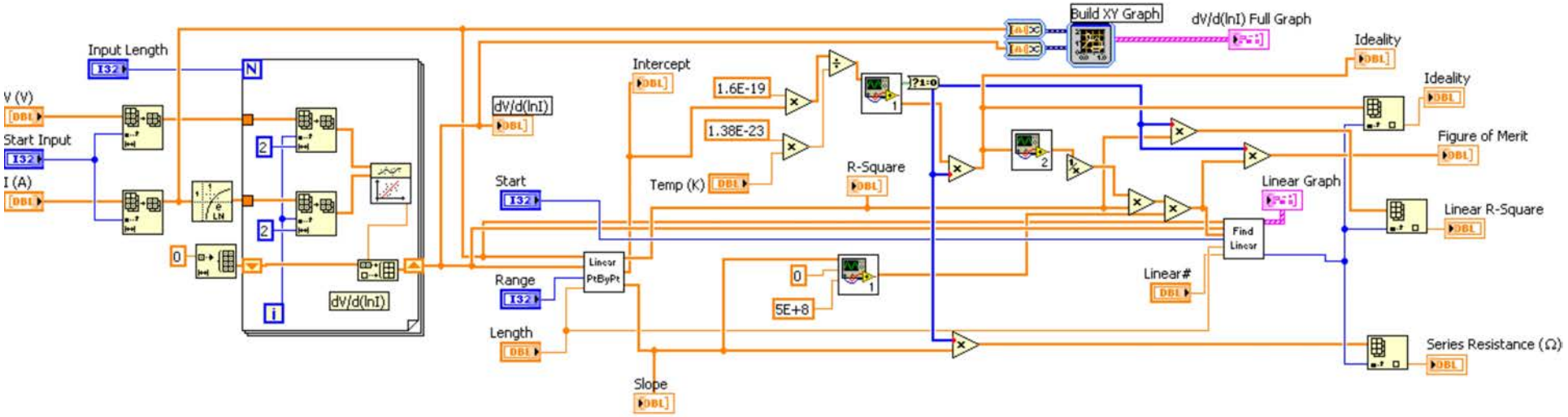

Figure A2.7 Block diagram showing 'dVdlnI vs I.vi'

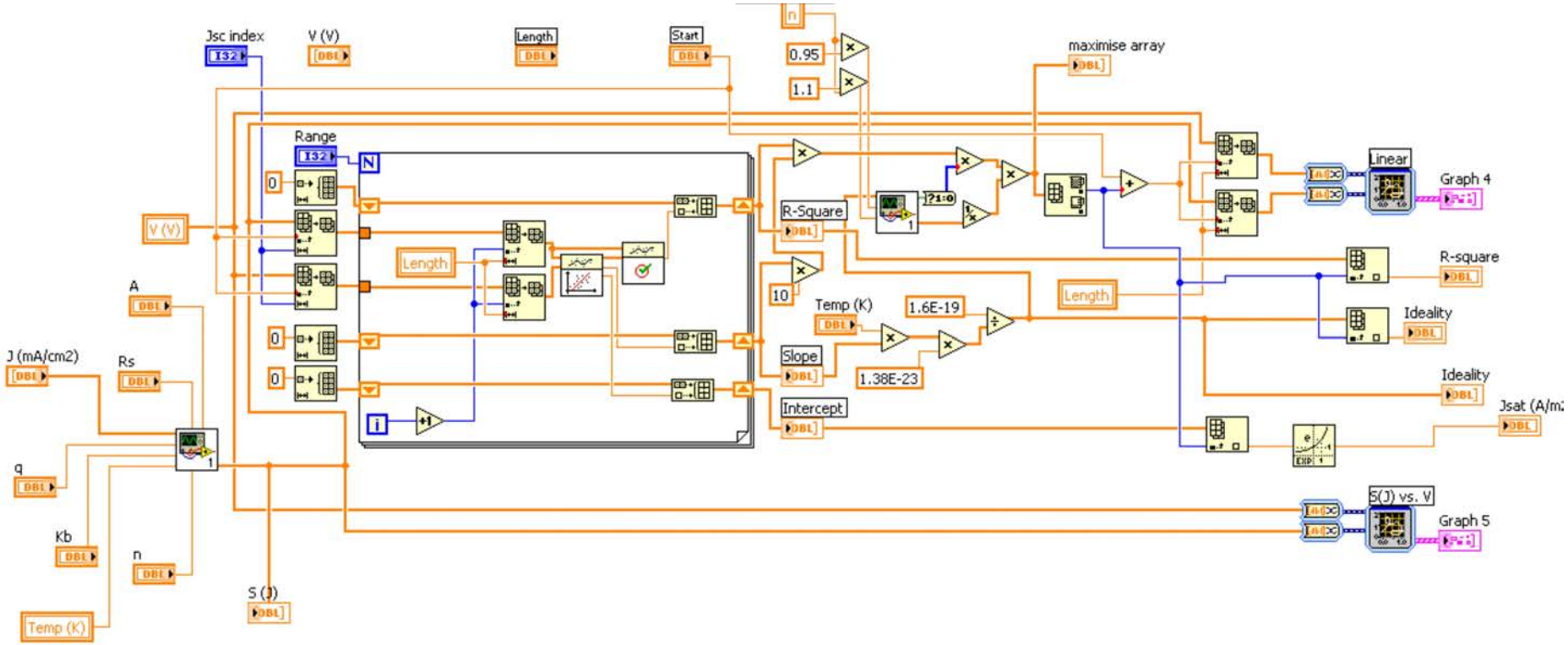

Figure A2.8 Block diagram showing 'S(J) vs. V.vi'

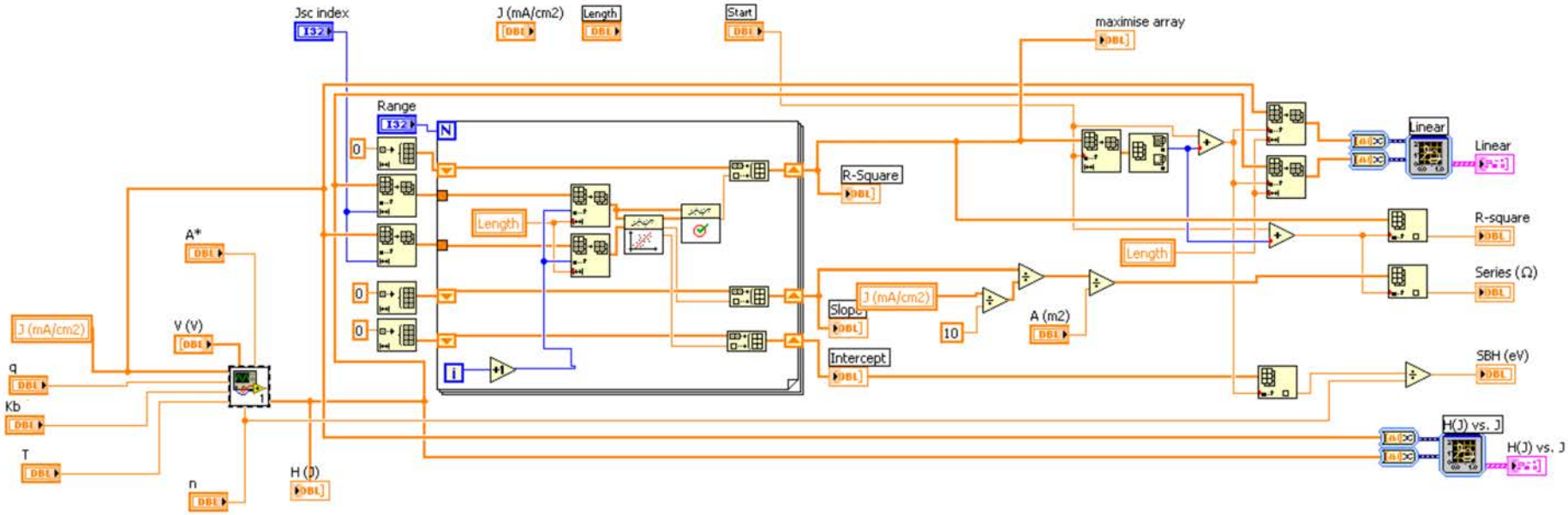

Figure A2.6 Block diagram showing 'H(J) vs. J.vi'

Appendix 3
Light and dark JV curves underlying the data presented in Chapter 3

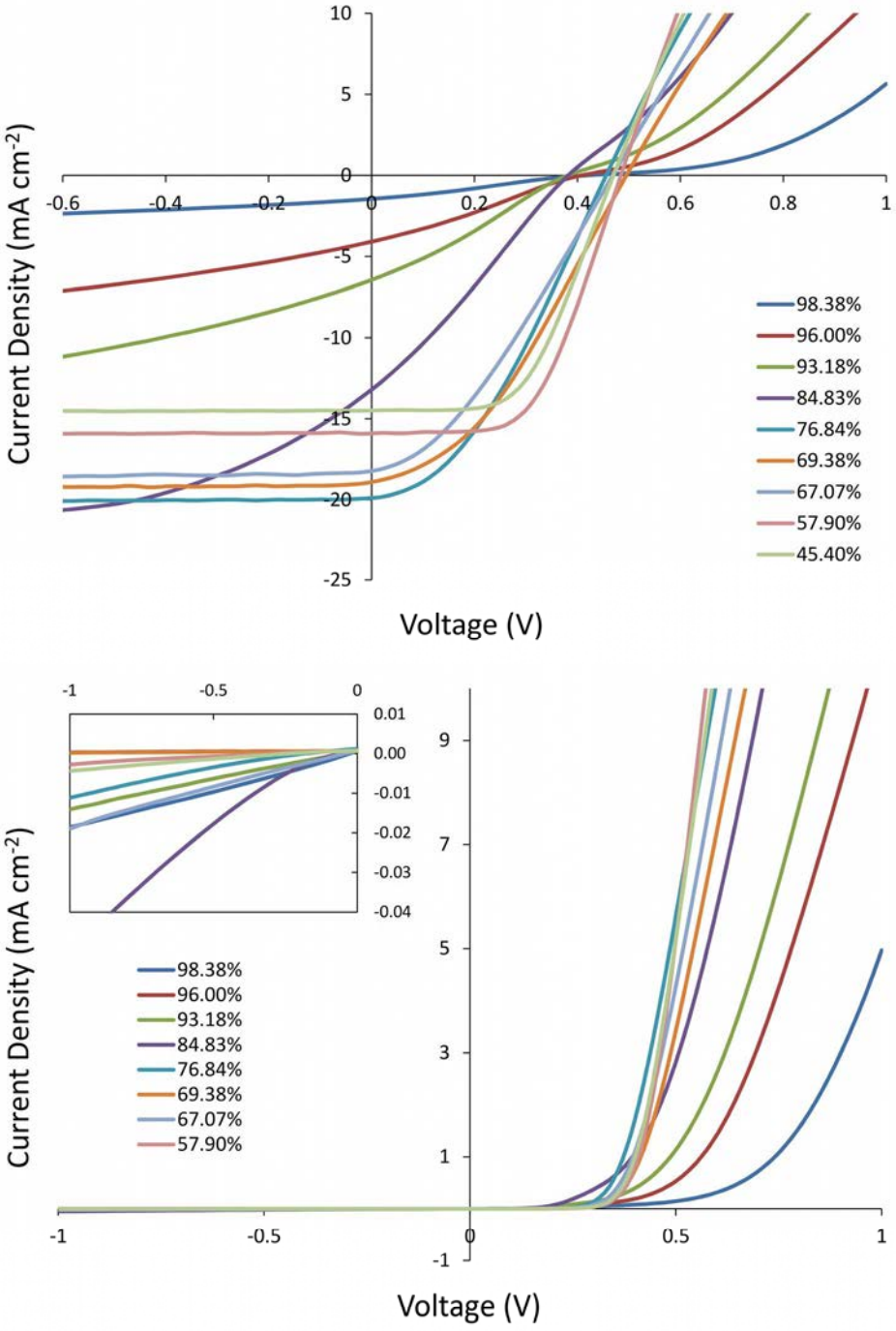

Figure A3.1 Light and dark JV curves corresponding to the data in **Figure 3.5** (as prepared devices)

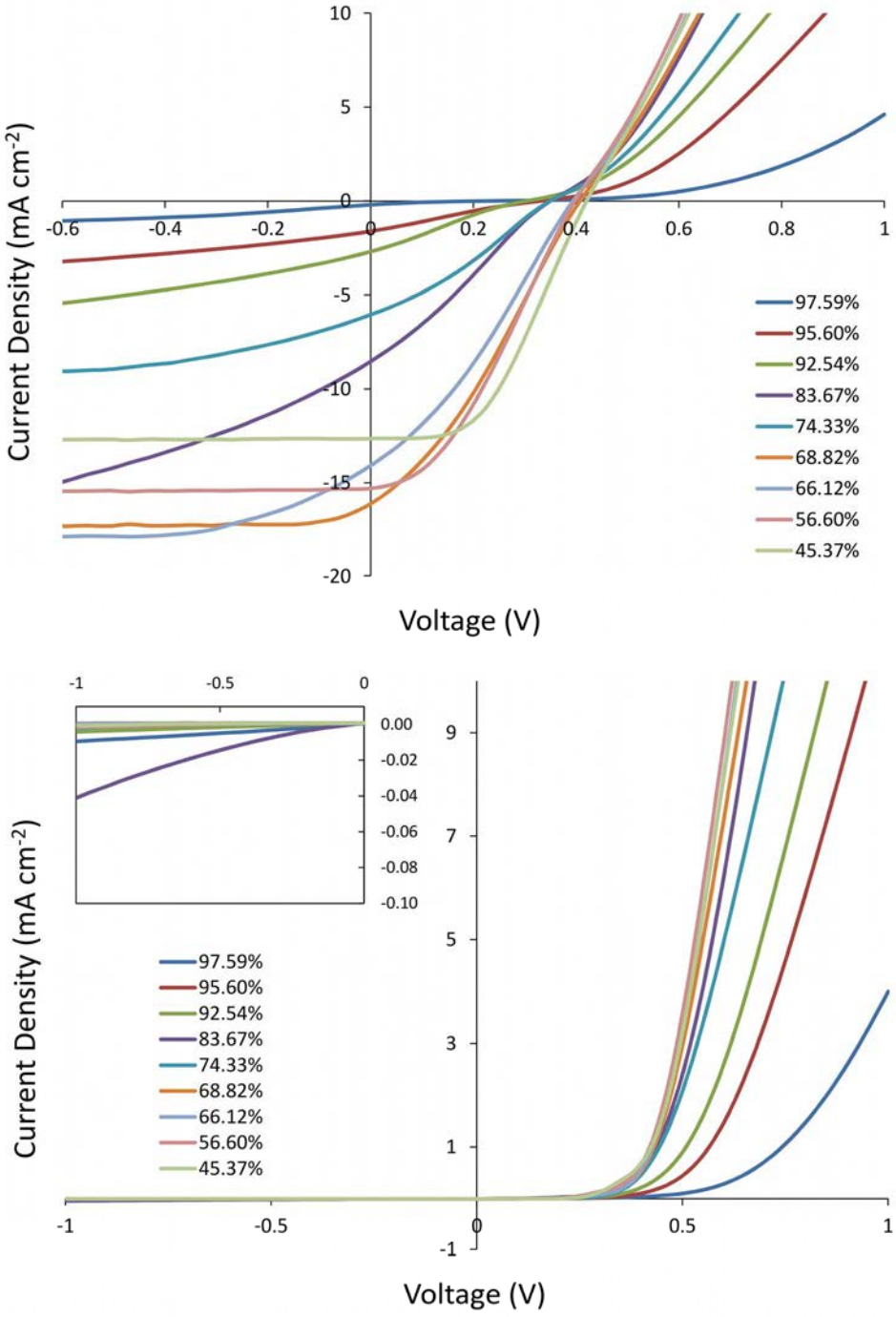

Figure A3.2 Light and dark JV curves corresponding to the data in **Figure 3.6** (HF treated devices)

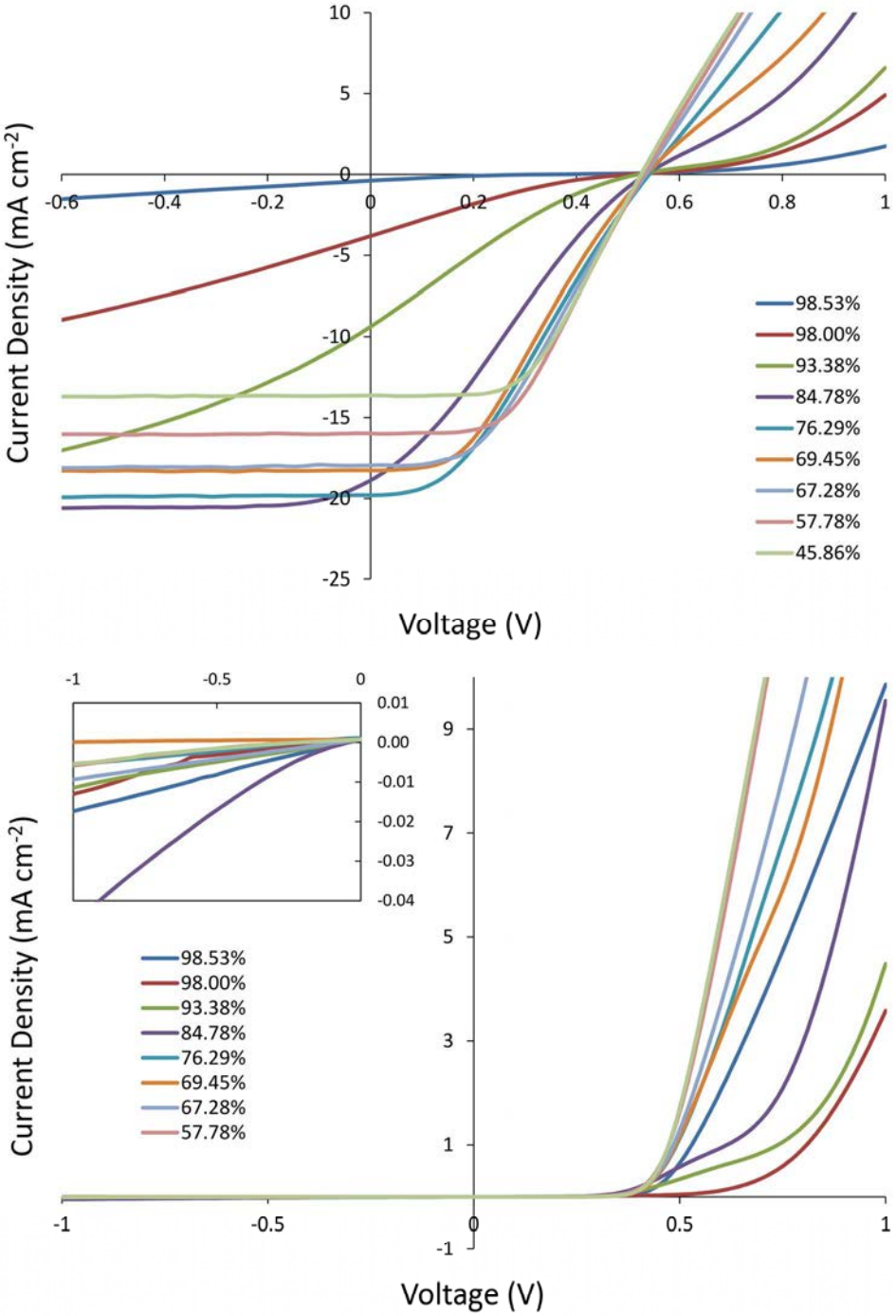

Figure A3.3 Light and dark JV curves corresponding to the data in **Figure 3.7** ($SOCl_2$ treated devices)

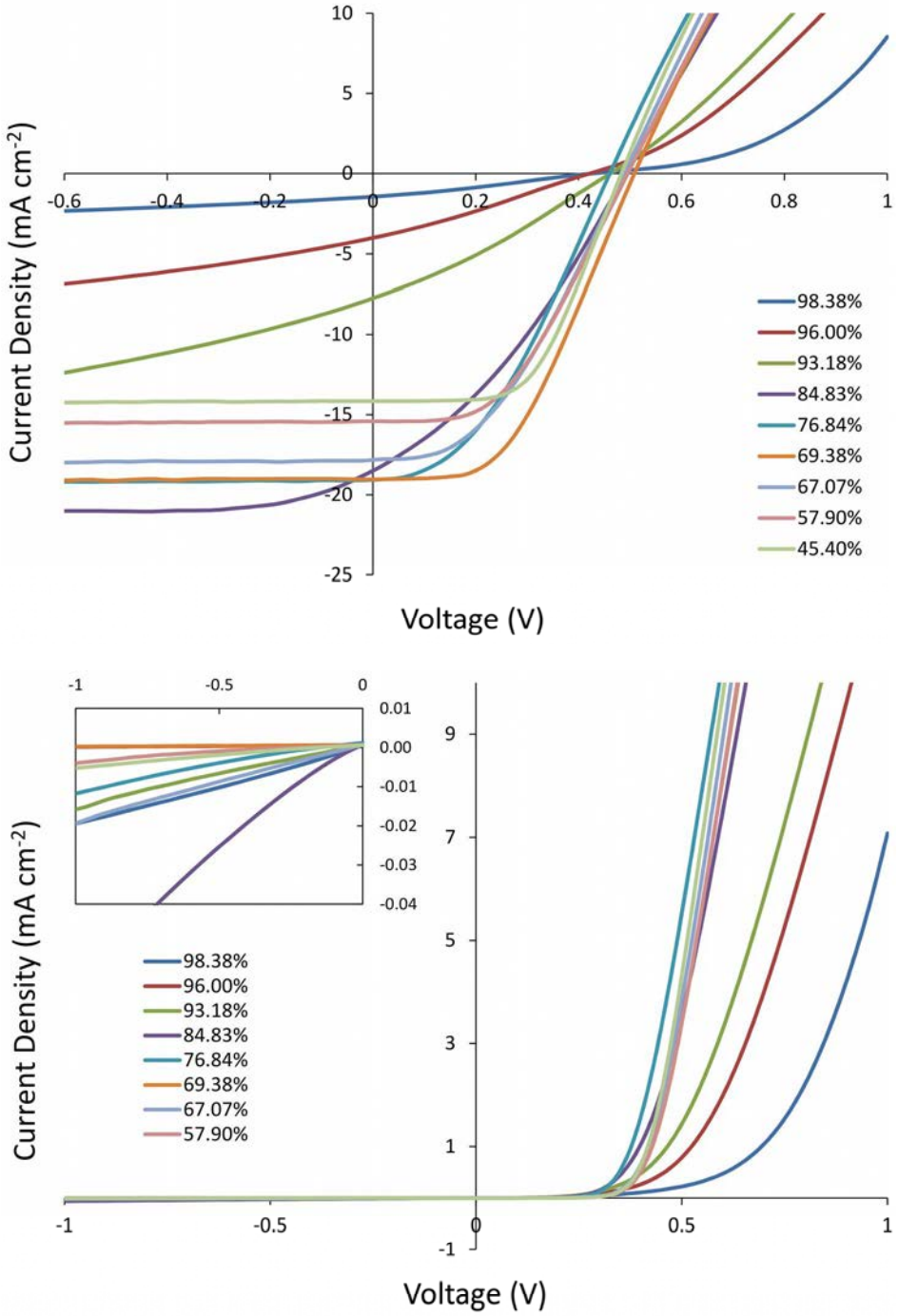

Figure A3.4 Light and dark JV curves corresponding to the data in **Figure 3.8** (HF retreated devices, 1 hr after treatment)

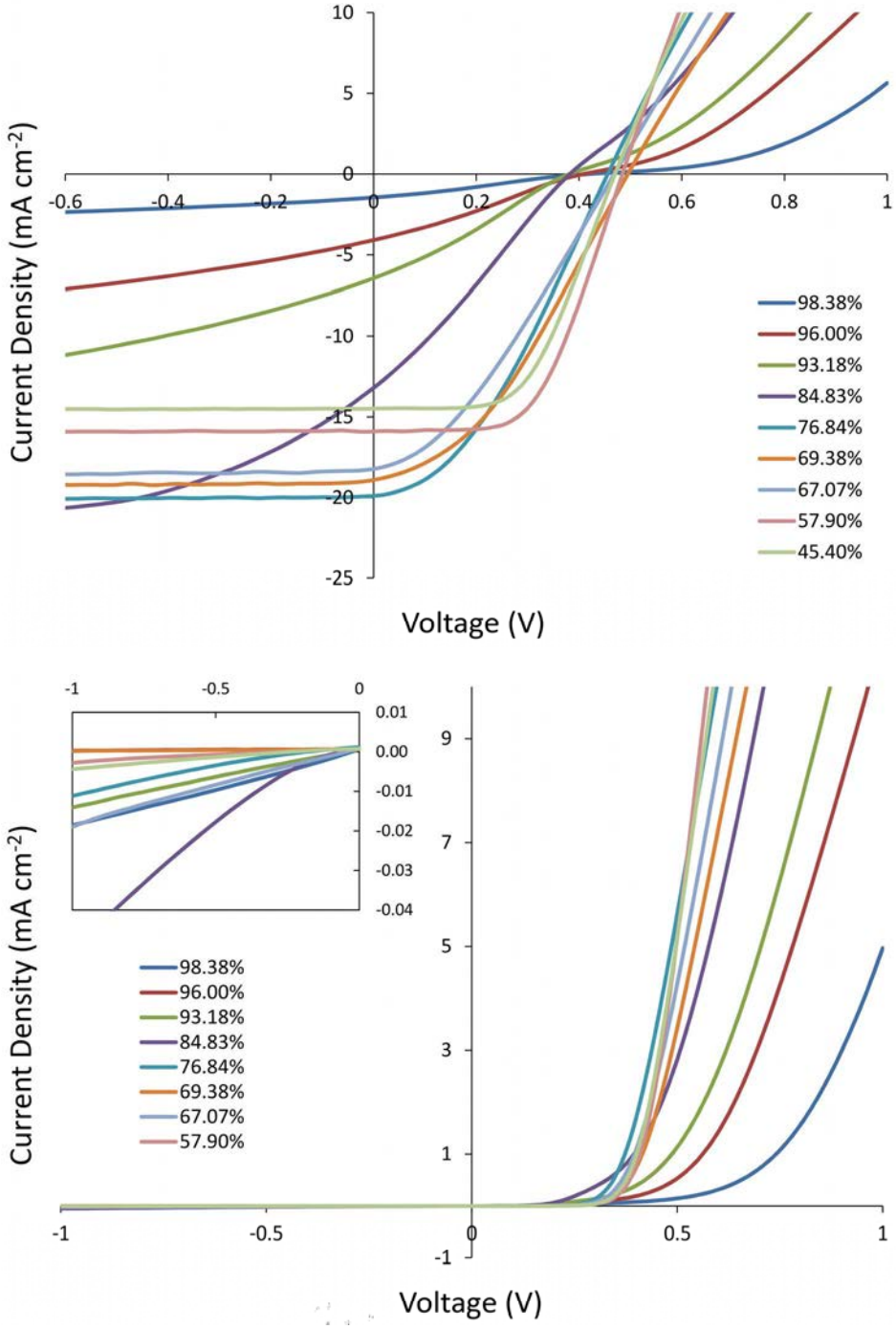

Figure A3.5 Light and dark JV curves corresponding to the data in **Figure 3.9** (HF retreated devices, 4 hr after treatment)

Appendix 4
Simulation of s-SWCNT absorption properties

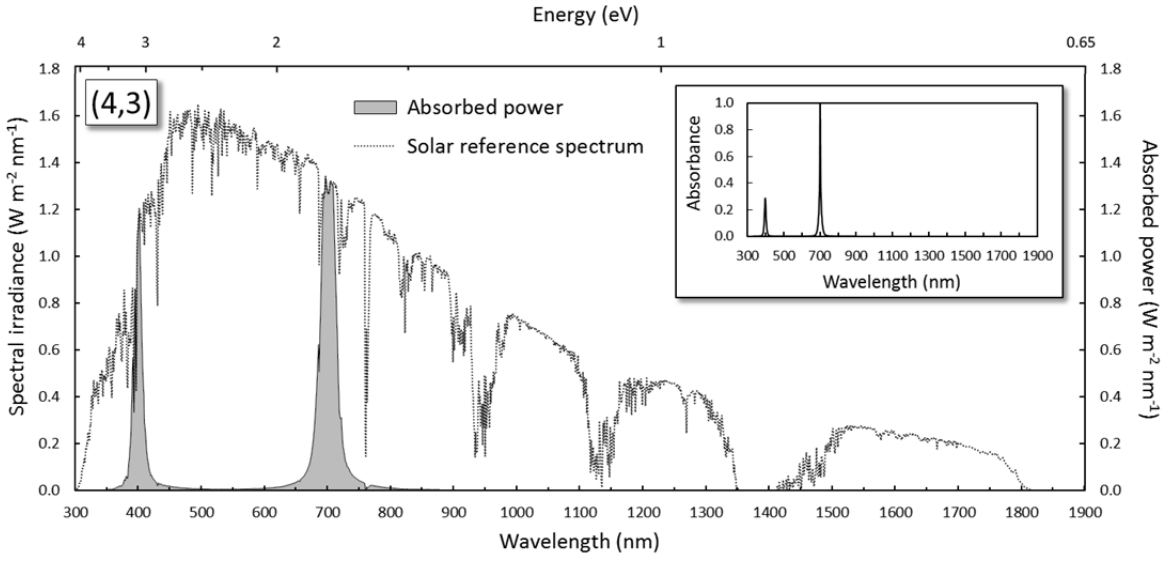

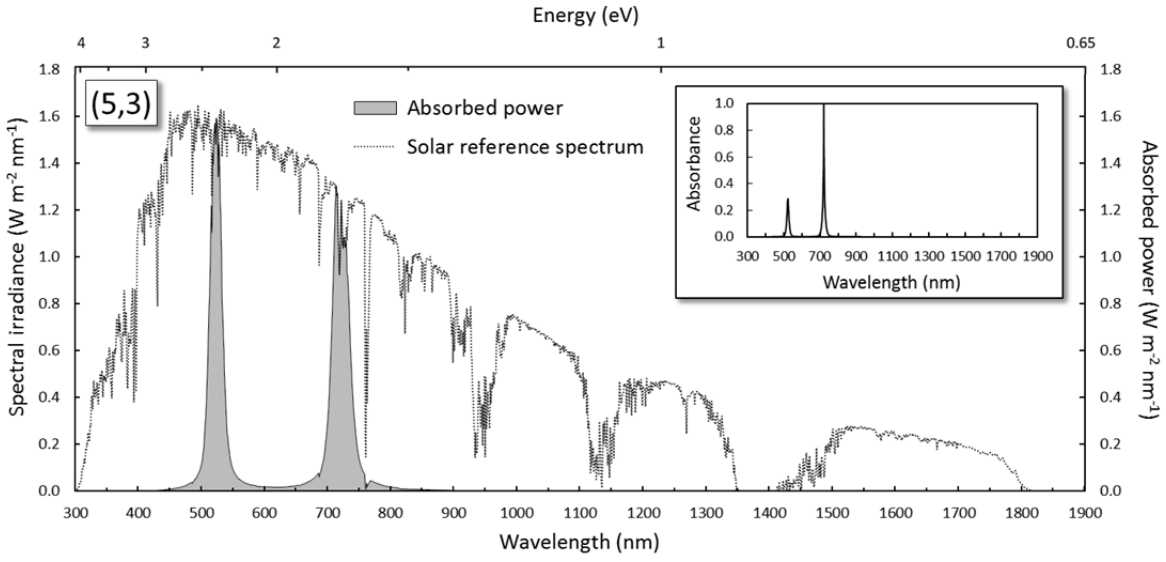

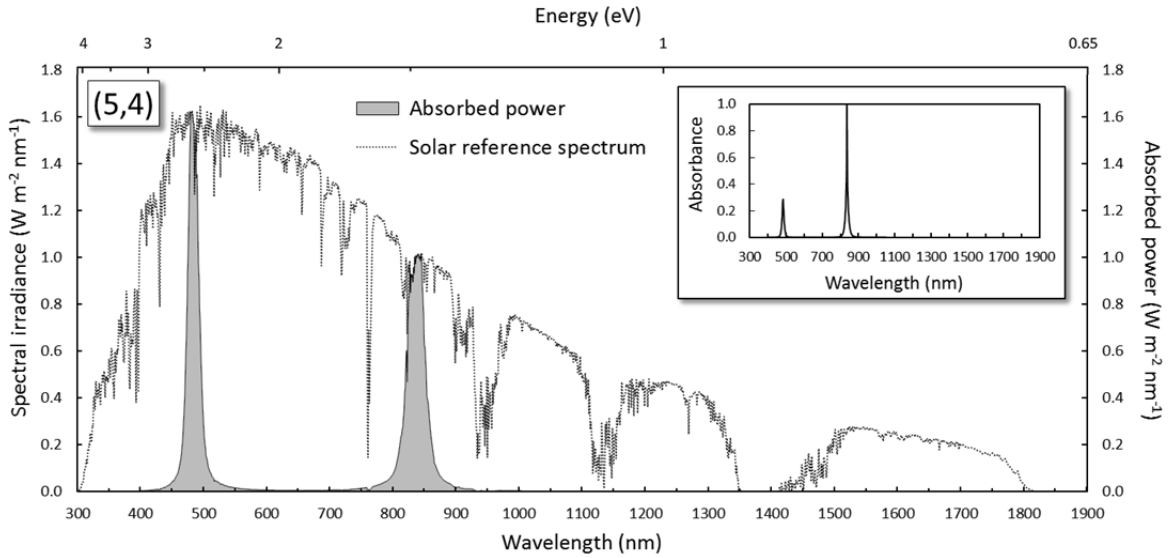
Energy (eV)
(5,4)
Absorbed power
Solar reference spectrum
Absorbance
Wavelength (nm)
Spectral irradiance (W m-2 nm-1)
Absorbed power (W m-2 nm-1)
Wavelength (nm)

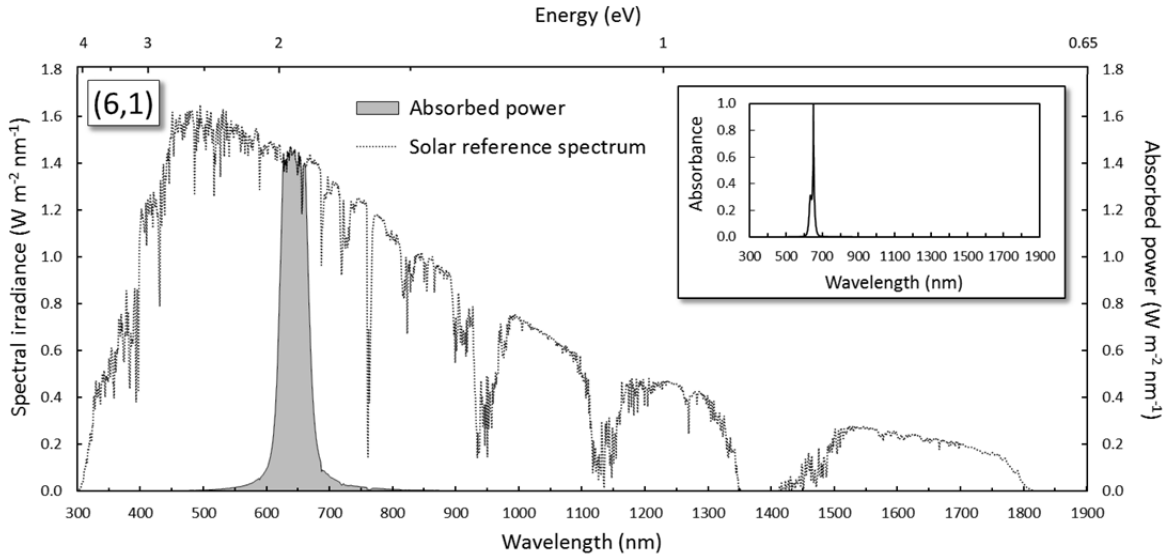
Energy (eV)
(6,1)
Absorbed power
Solar reference spectrum
Absorbance
Wavelength (nm)
Spectral irradiance (W m-2 nm-1)
Absorbed power (W m-2 nm-1)
Wavelength (nm)

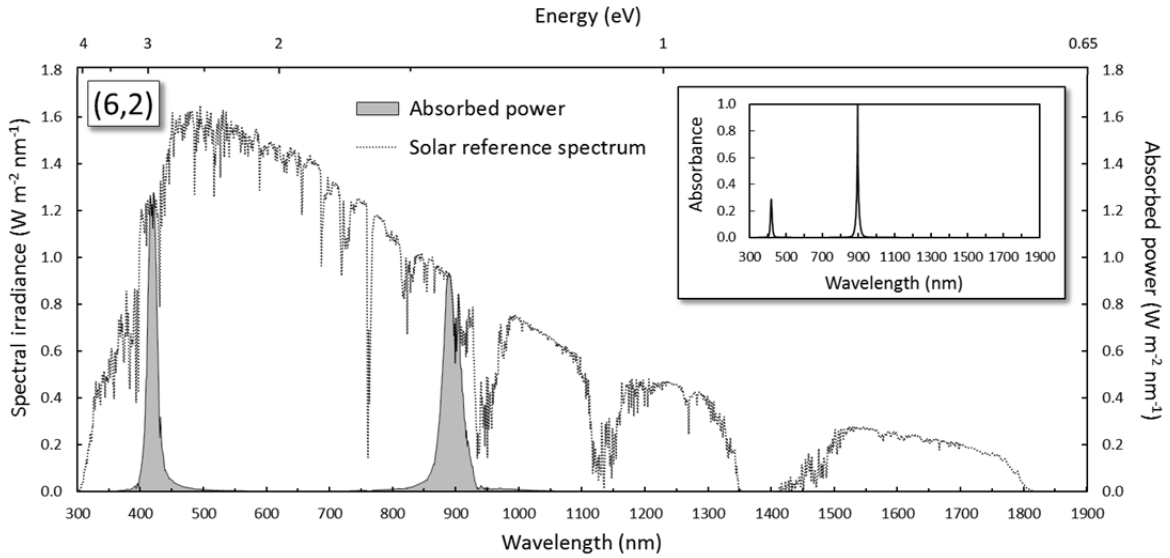
Energy (eV)
(6,2)
Absorbed power
Solar reference spectrum
Absorbance
Wavelength (nm)
Spectral irradiance (W m-2 nm-1)
Absorbed power (W m-2 nm-1)
Wavelength (nm)

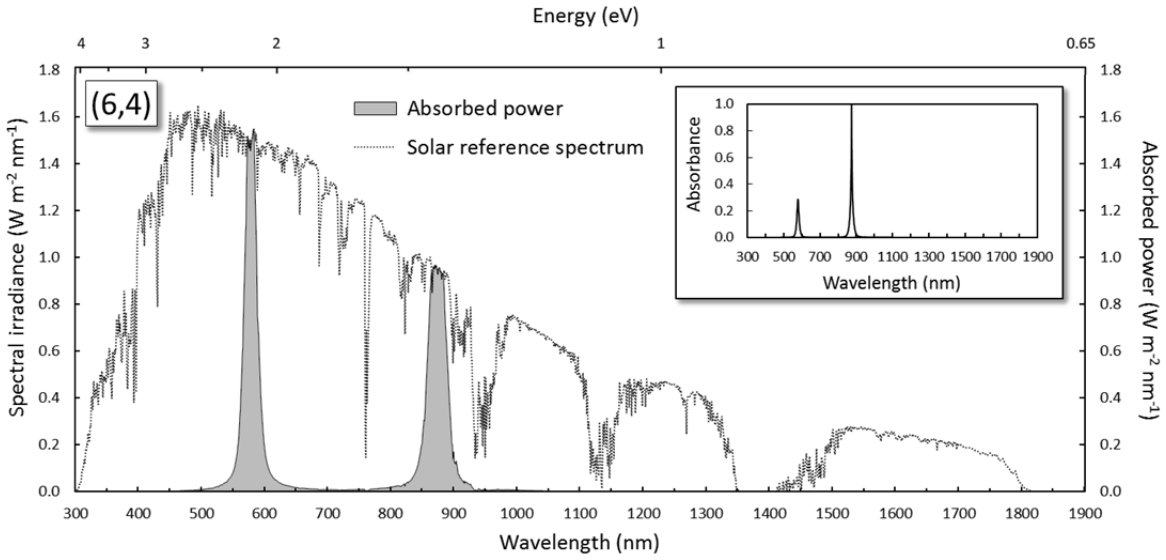
Energy (eV)
(6,4)
Absorbed power
Solar reference spectrum
Absorbance
Wavelength (nm)
Spectral irradiance (W m-2 nm-1)
Absorbed power (W m-2 nm-1)
Wavelength (nm)

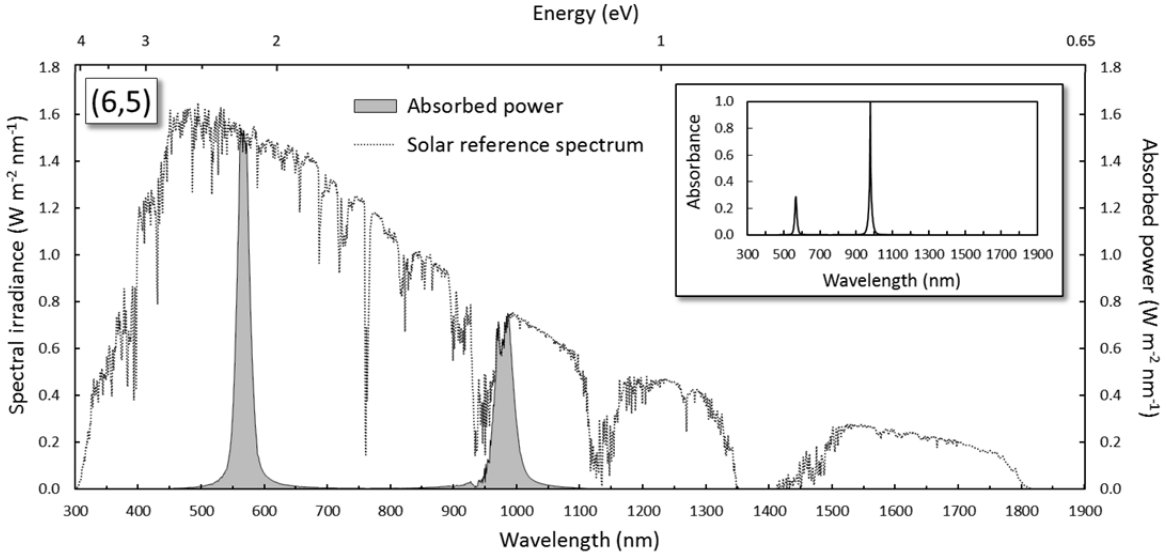
Energy (eV)
(6,5)
Absorbed power
Solar reference spectrum
Absorbance
Wavelength (nm)
Spectral irradiance (W m-2 nm-1)
Absorbed power (W m-2 nm-1)
Wavelength (nm)

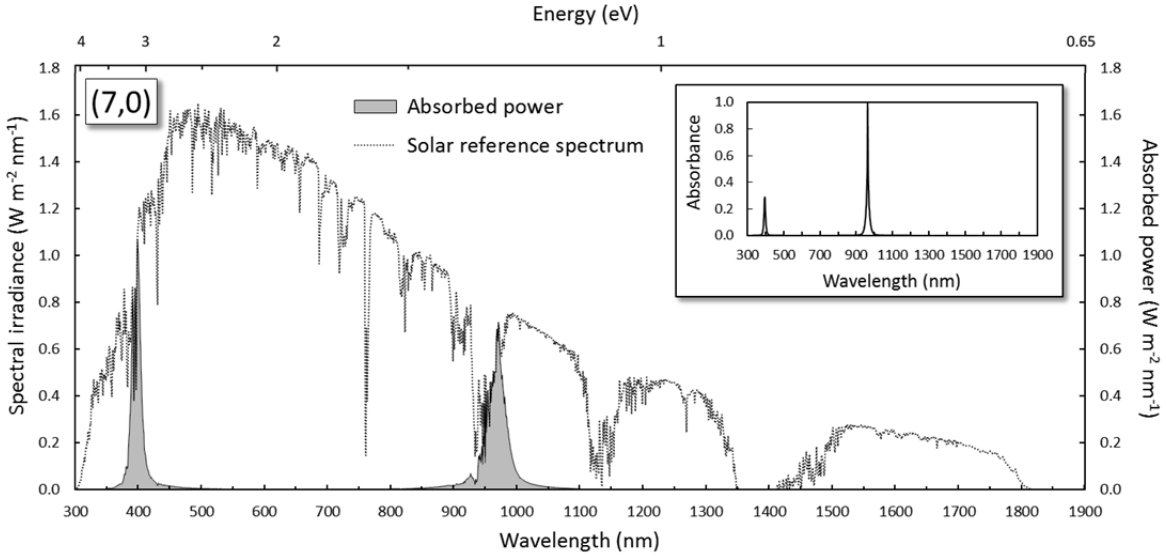
Energy (eV)
(7,0)
Absorbed power
Solar reference spectrum
Absorbance
Wavelength (nm)
Spectral irradiance (W m-2 nm-1)
Absorbed power (W m-2 nm-1)
Wavelength (nm)

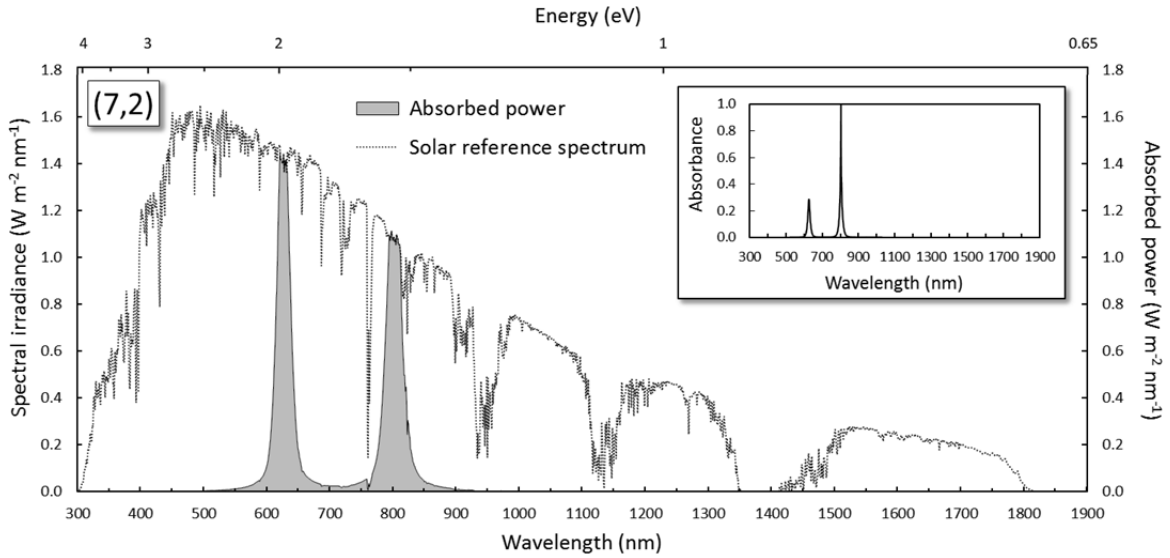
Energy (eV)
(7,2)
Absorbed power
Solar reference spectrum
Absorbance
Wavelength (nm)
Spectral irradiance (W m-2 nm-1)
Absorbed power (W m-2 nm-1)
Wavelength (nm)

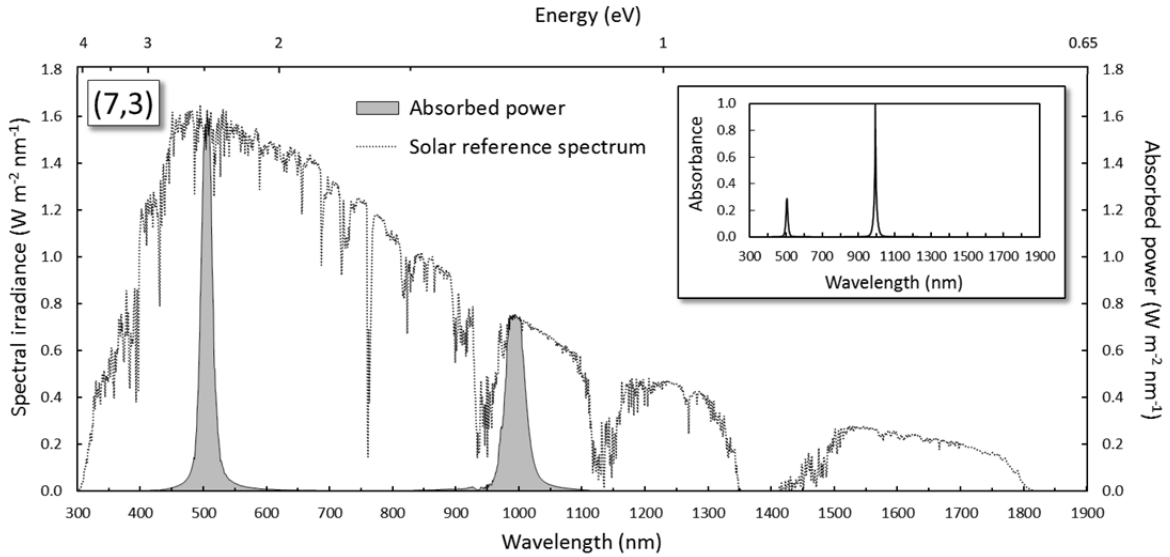
Energy (eV)
(7,3)
Absorbed power
Solar reference spectrum
Absorbance
Wavelength (nm)
Spectral irradiance (W m-2 nm-1)
Absorbed power (W m-2 nm-1)
Wavelength (nm)

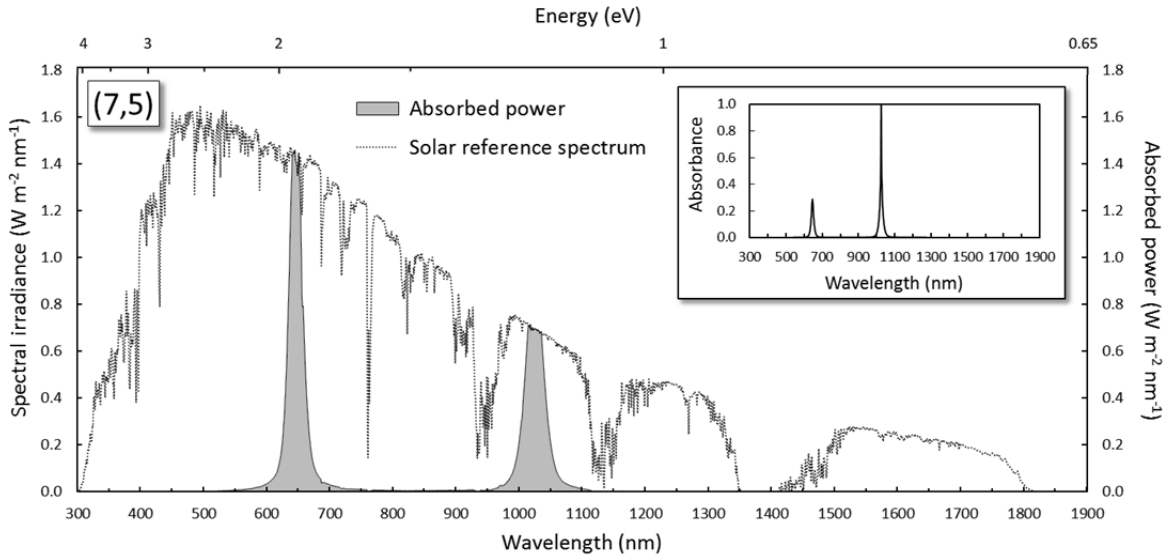
Energy (eV)
(7,5)
Absorbed power
Solar reference spectrum
Absorbance
Wavelength (nm)
Spectral irradiance (W m-2 nm-1)
Absorbed power (W m-2 nm-1)
Wavelength (nm)

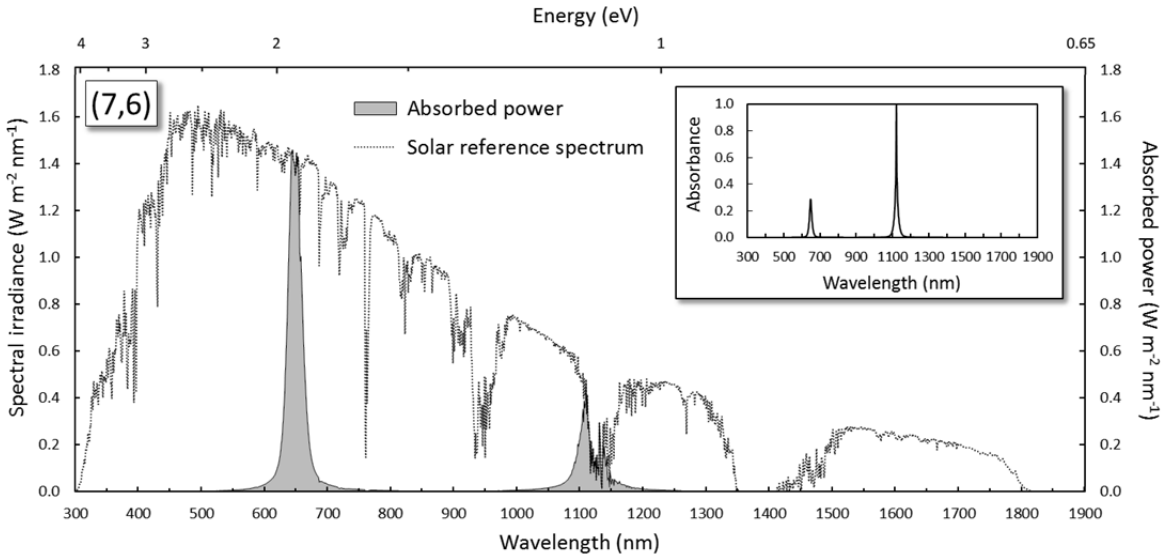
Energy (eV)
(7,6)
Absorbed power
Solar reference spectrum
Absorbance
Wavelength (nm)
Spectral irradiance (W m-2 nm-1)
Absorbed power (W m-2 nm-1)
Wavelength (nm)

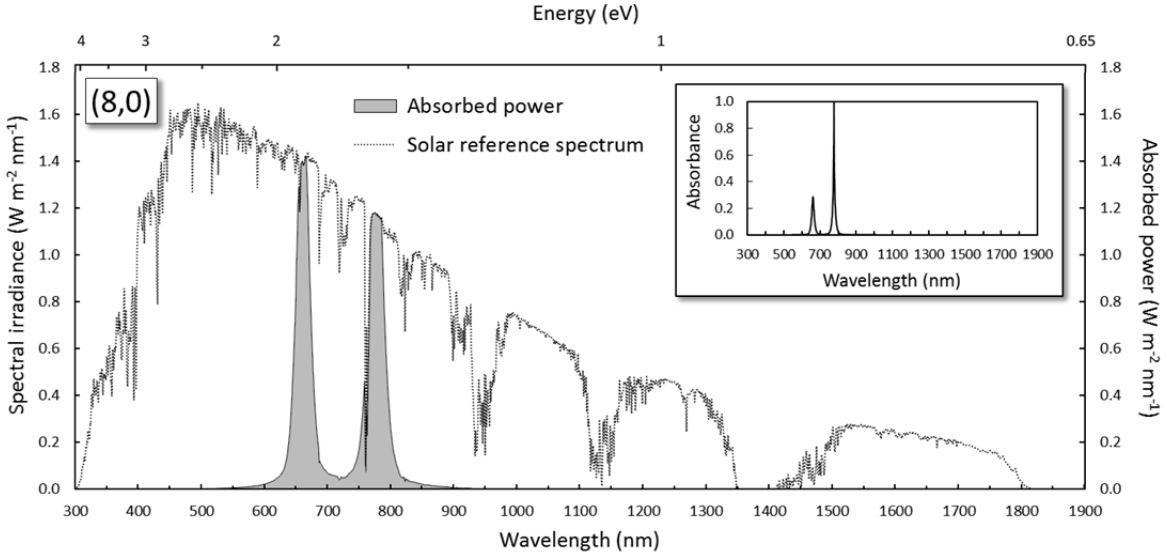
Energy (eV)
(8,0)
Absorbed power
Solar reference spectrum
Absorbance
Wavelength (nm)
Spectral irradiance (W m-2 nm-1)
Absorbed power (W m-2 nm-1)
Wavelength (nm)

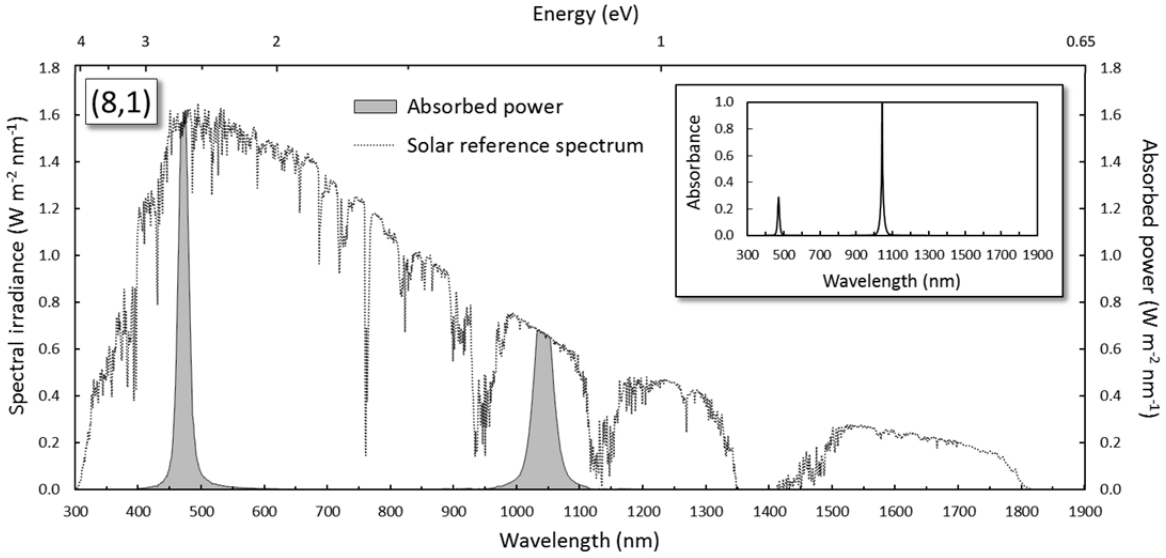
Energy (eV)
(8,1)
Absorbed power
Solar reference spectrum
Absorbance
Wavelength (nm)
Spectral irradiance (W m-2 nm-1)
Absorbed power (W m-2 nm-1)
Wavelength (nm)

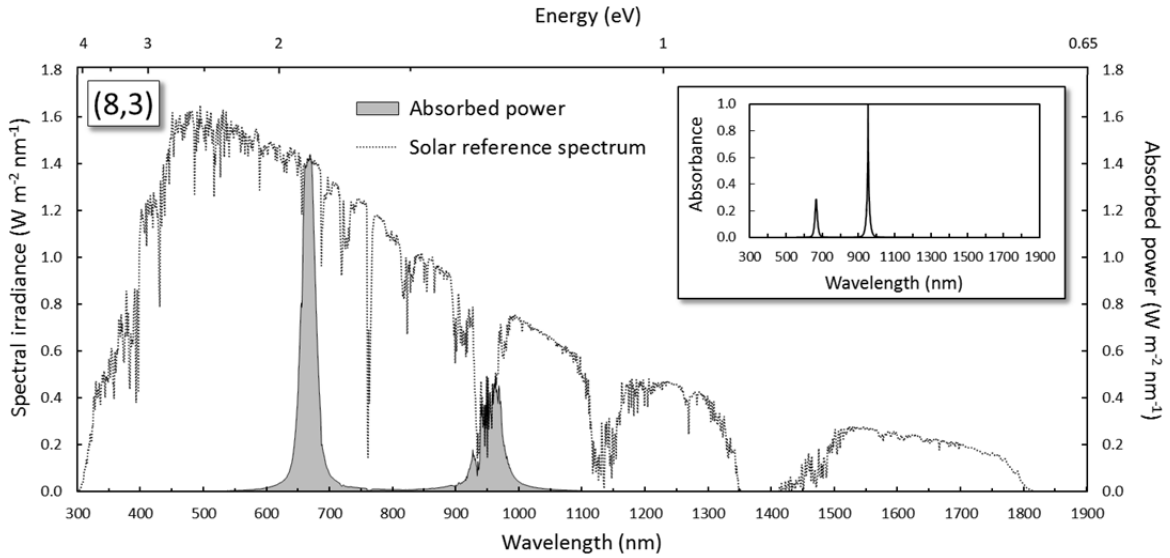
Energy (eV)
(8,3)
Absorbed power
Solar reference spectrum
Absorbance
Wavelength (nm)
Spectral irradiance (W m-2 nm-1)
Absorbed power (W m-2 nm-1)
Wavelength (nm)

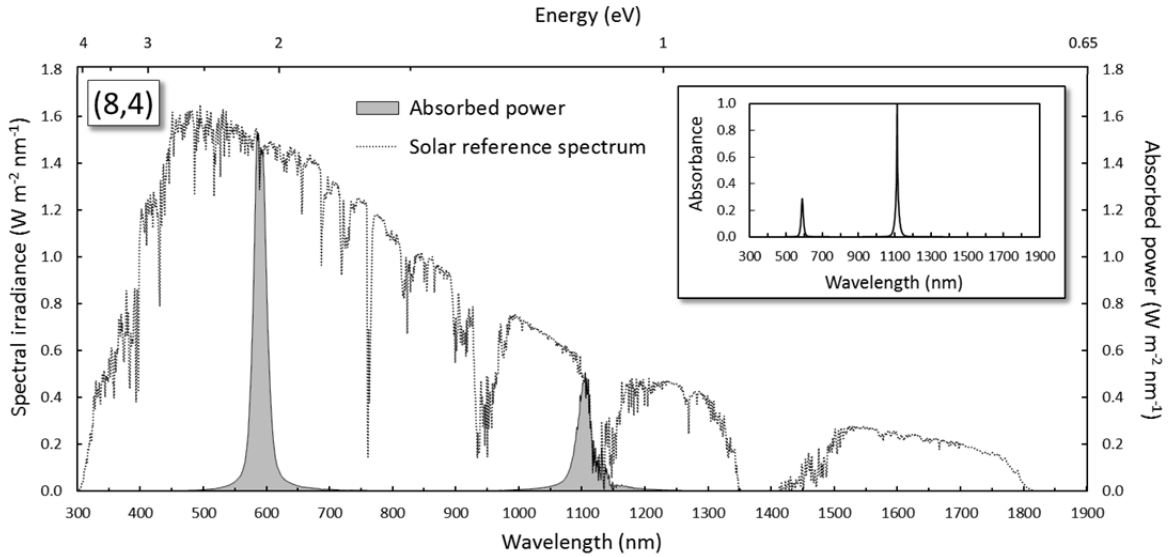
Energy (eV)
(8,4)
Absorbed power
Solar reference spectrum
Absorbance
Wavelength (nm)
Spectral irradiance (W m-2 nm-1)
Absorbed power (W m-2 nm-1)
Wavelength (nm)

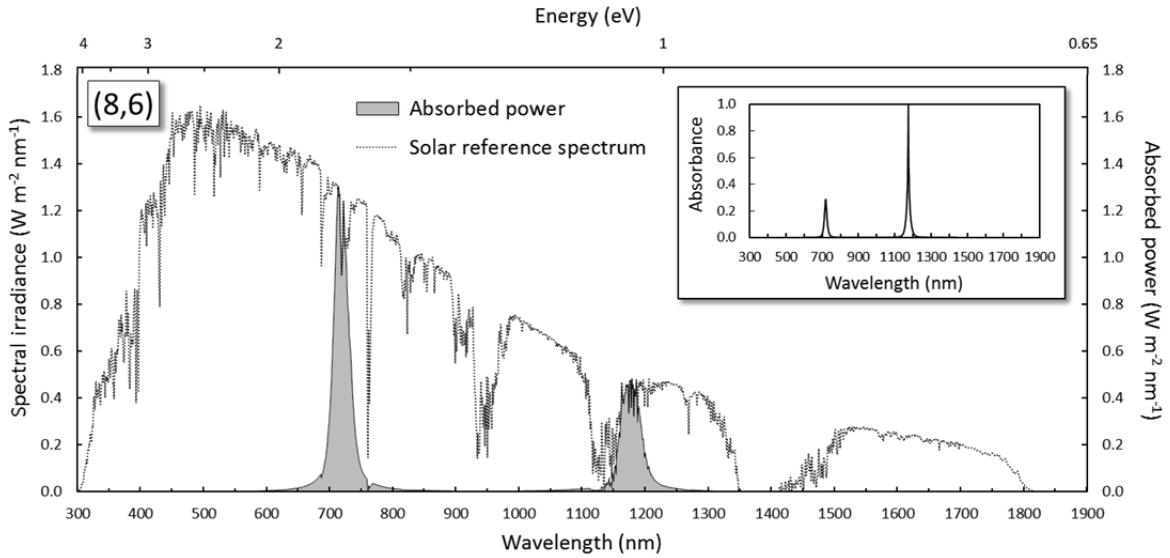
Energy (eV)
(8,6)
Absorbed power
Solar reference spectrum
Absorbance
Wavelength (nm)
Spectral irradiance (W m-2 nm-1)
Absorbed power (W m-2 nm-1)
Wavelength (nm)

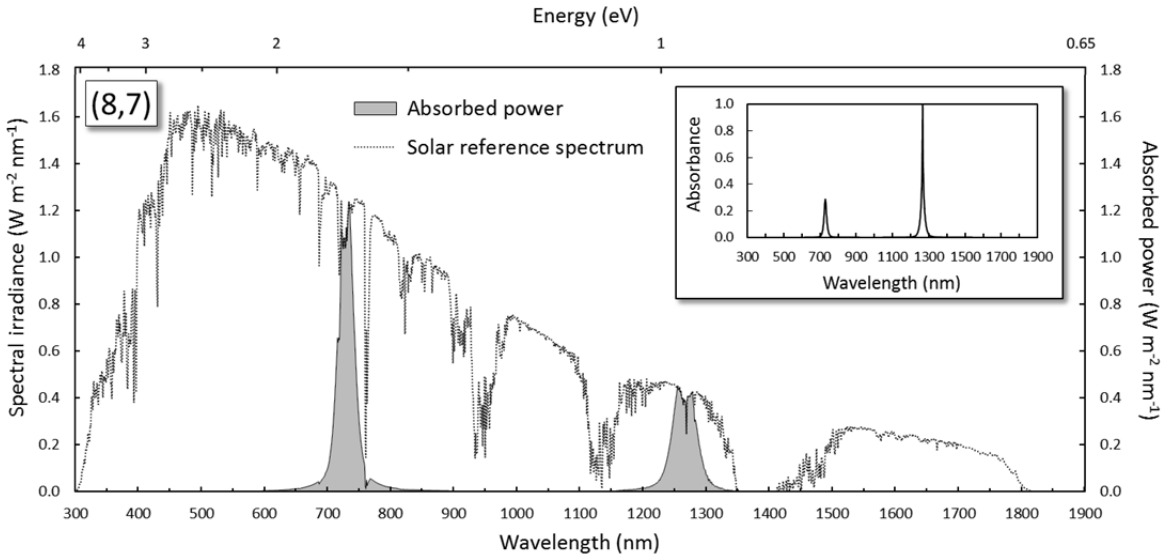
Energy (eV)
(8,7)
Absorbed power
Solar reference spectrum
Absorbance
Wavelength (nm)
Spectral irradiance (W m-2 nm-1)
Absorbed power (W m-2 nm-1)
Wavelength (nm)

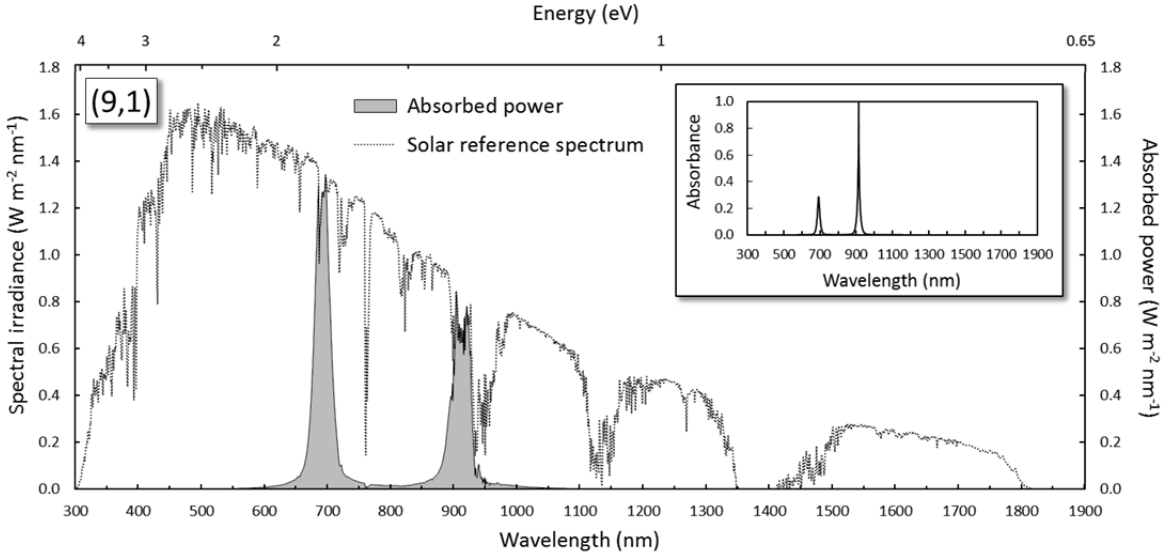
Energy (eV)
(9,1)
Absorbed power
Solar reference spectrum
Absorbance
Wavelength (nm)
Spectral irradiance (W m-2 nm-1)
Absorbed power (W m-2 nm-1)
Wavelength (nm)

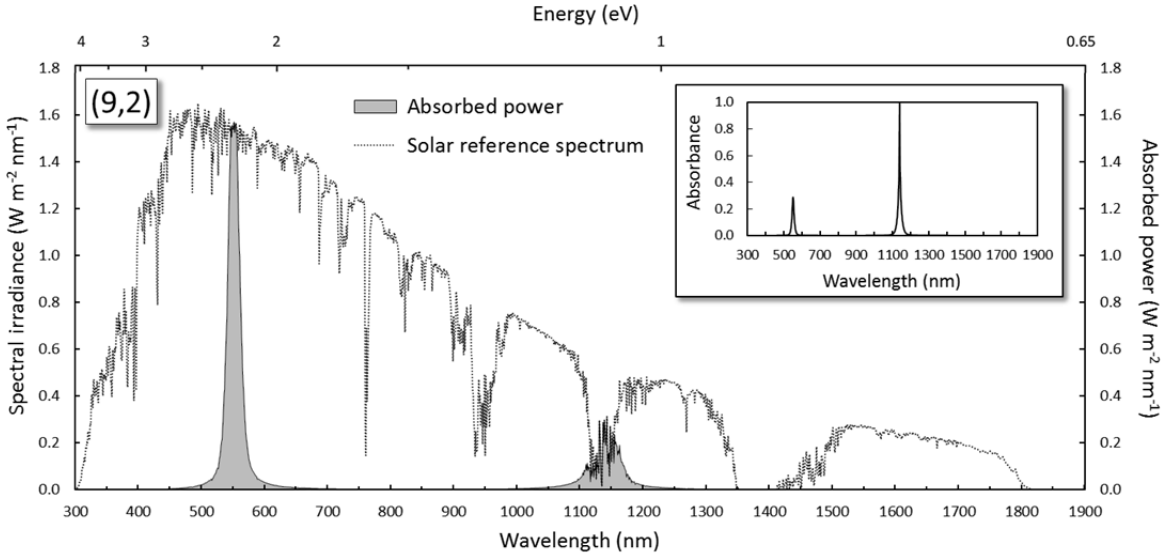
Energy (eV)
(9,2)
Absorbed power
Solar reference spectrum
Absorbance
Wavelength (nm)
Spectral irradiance (W m-2 nm-1)
Absorbed power (W m-2 nm-1)
Wavelength (nm)

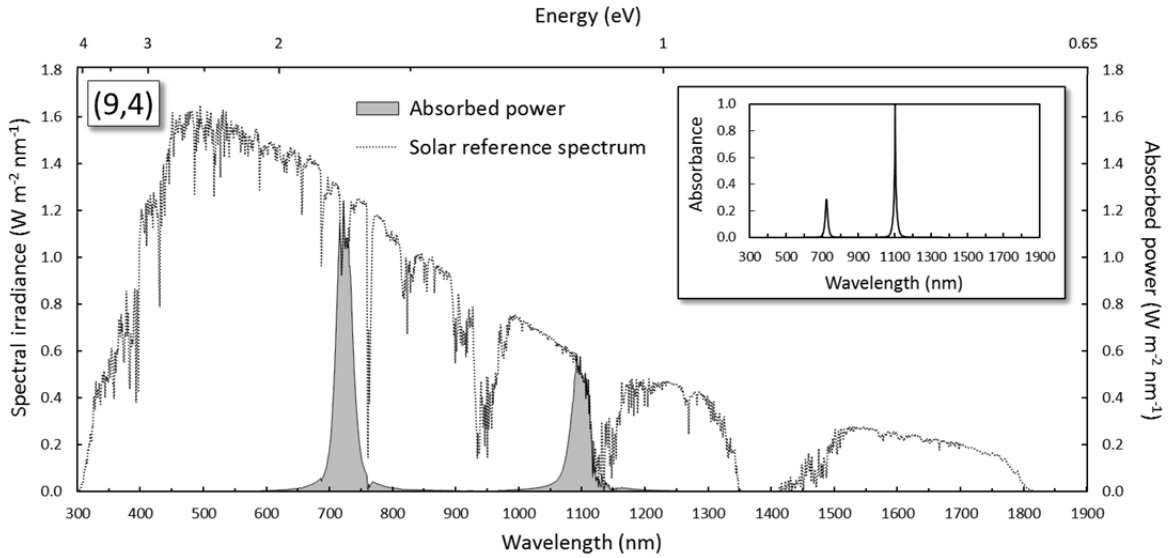
Energy (eV)
(9,4)
Absorbed power
Solar reference spectrum
Absorbance
Wavelength (nm)
Spectral irradiance (W m-2 nm-1)
Absorbed power (W m-2 nm-1)
Wavelength (nm)

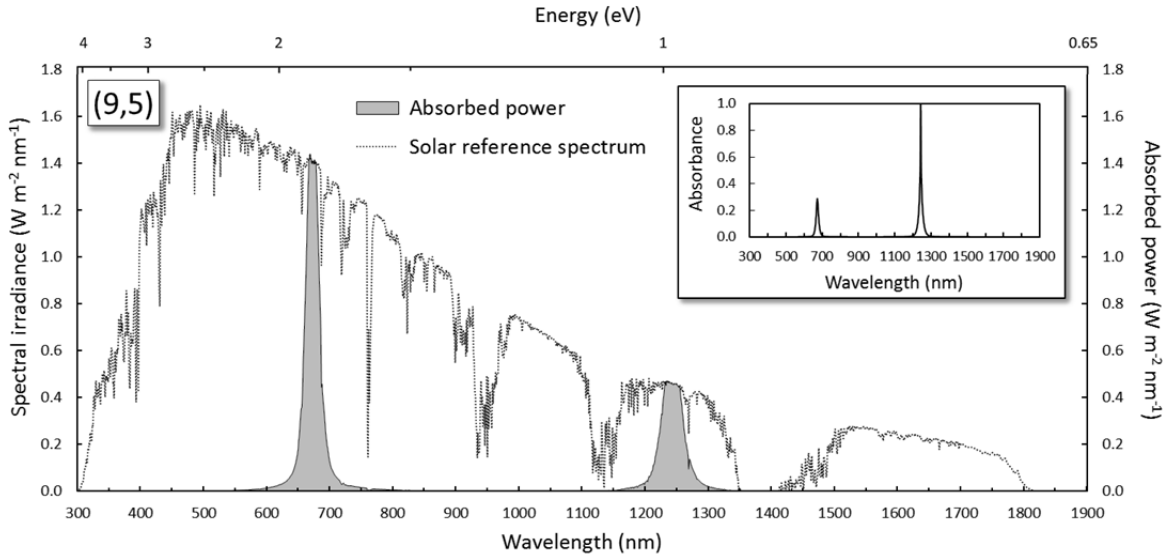
Energy (eV)
(9,5)
Absorbed power
Solar reference spectrum
Absorbance
Wavelength (nm)
Spectral irradiance (W m-2 nm-1)
Absorbed power (W m-2 nm-1)
Wavelength (nm)

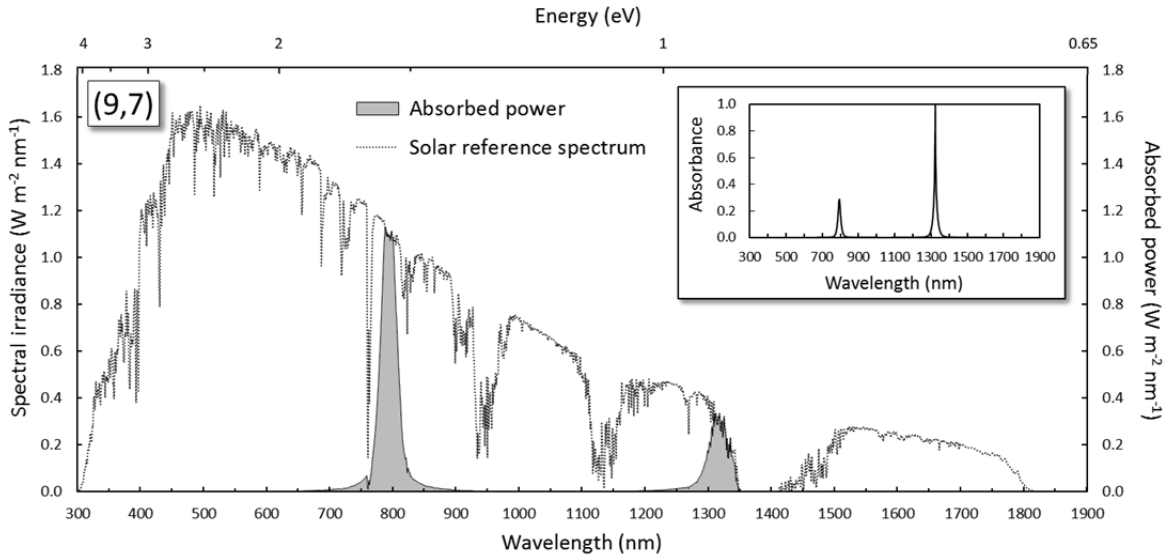
Energy (eV)
(9,7)
Absorbed power
Solar reference spectrum
Absorbance
Wavelength (nm)
Spectral irradiance (W m-2 nm-1)
Absorbed power (W m-2 nm-1)
Wavelength (nm)

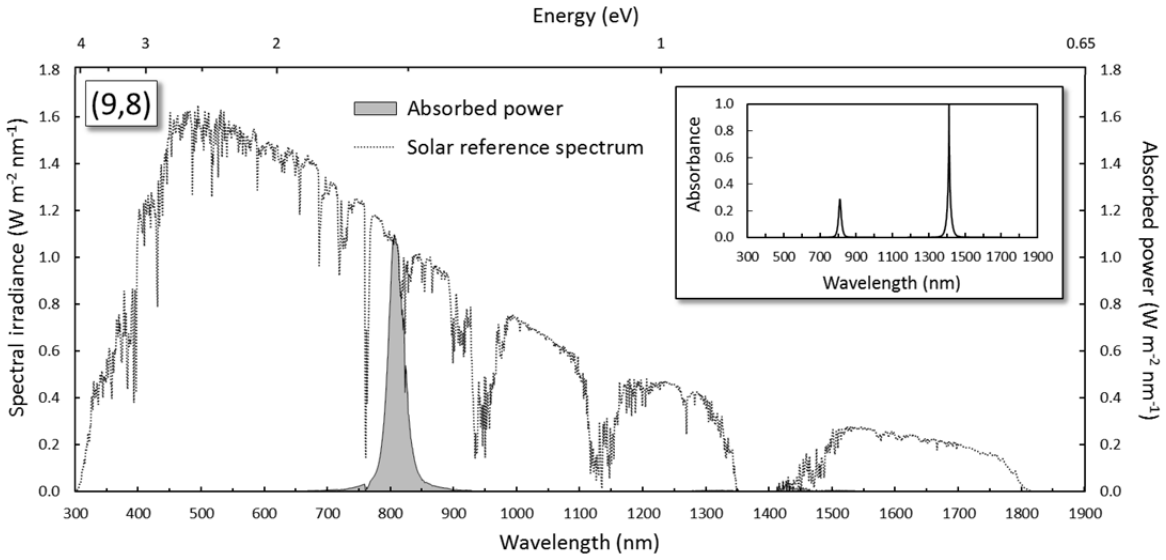
Energy (eV)
(9,8)
Absorbed power
Solar reference spectrum
Absorbance
Wavelength (nm)
Spectral irradiance (W m-2 nm-1)
Absorbed power (W m-2 nm-1)
Wavelength (nm)

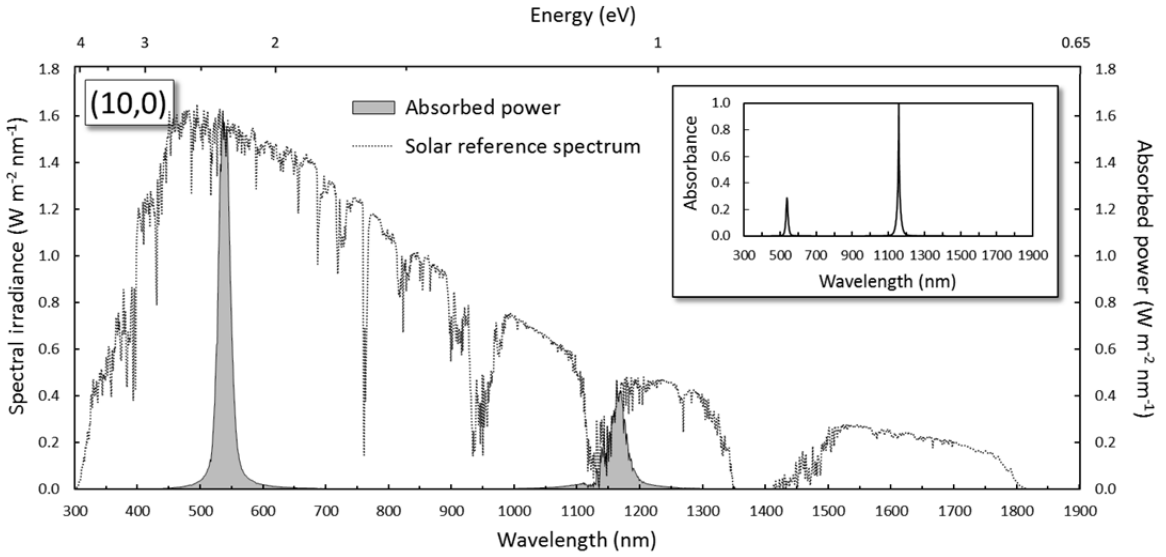
Energy (eV)
(10,0)
Absorbed power
Solar reference spectrum
Absorbance
Wavelength (nm)
Spectral irradiance (W m-2 nm-1)
Absorbed power (W m-2 nm-1)
Wavelength (nm)

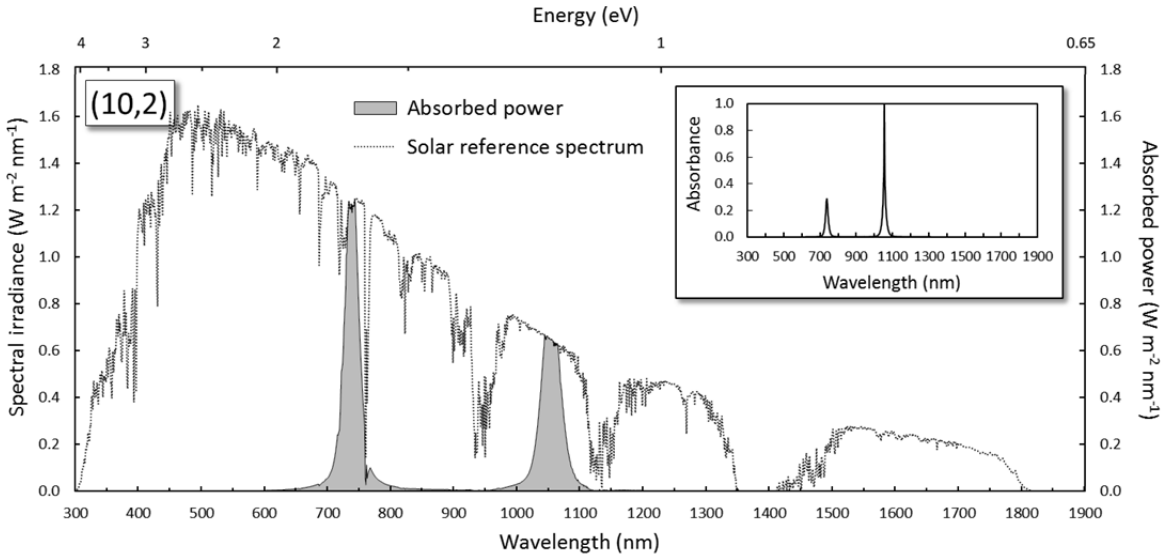
Energy (eV)
(10,2)
Absorbed power
Solar reference spectrum
Absorbance
Wavelength (nm)
Spectral irradiance (W m-2 nm-1)
Absorbed power (W m-2 nm-1)
Wavelength (nm)

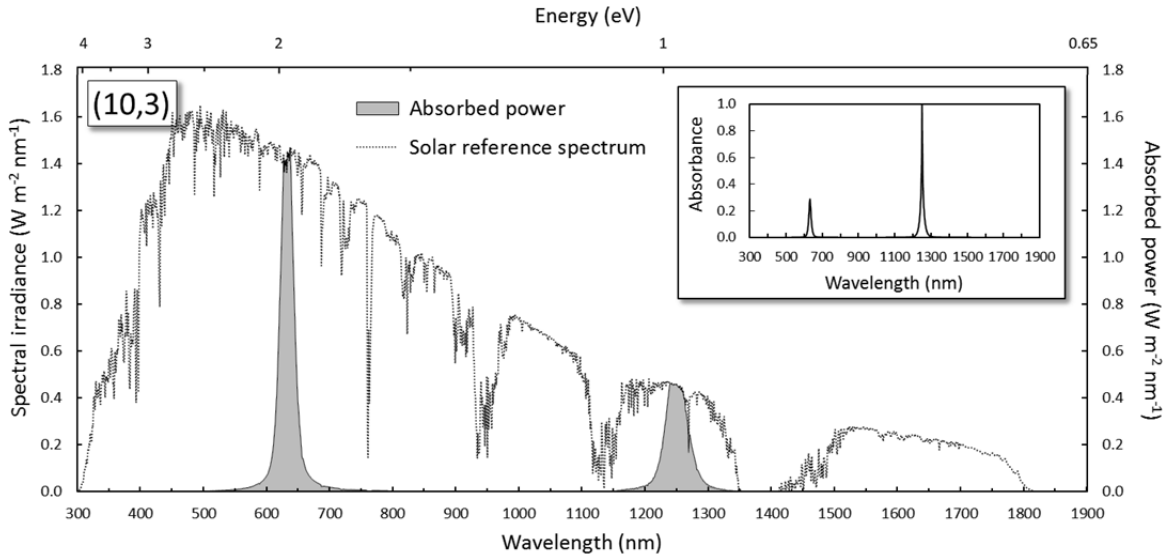
Energy (eV)
(10,3)
Absorbed power
Solar reference spectrum
Absorbance
Wavelength (nm)
Spectral irradiance (W m-2 nm-1)
Absorbed power (W m-2 nm-1)
Wavelength (nm)

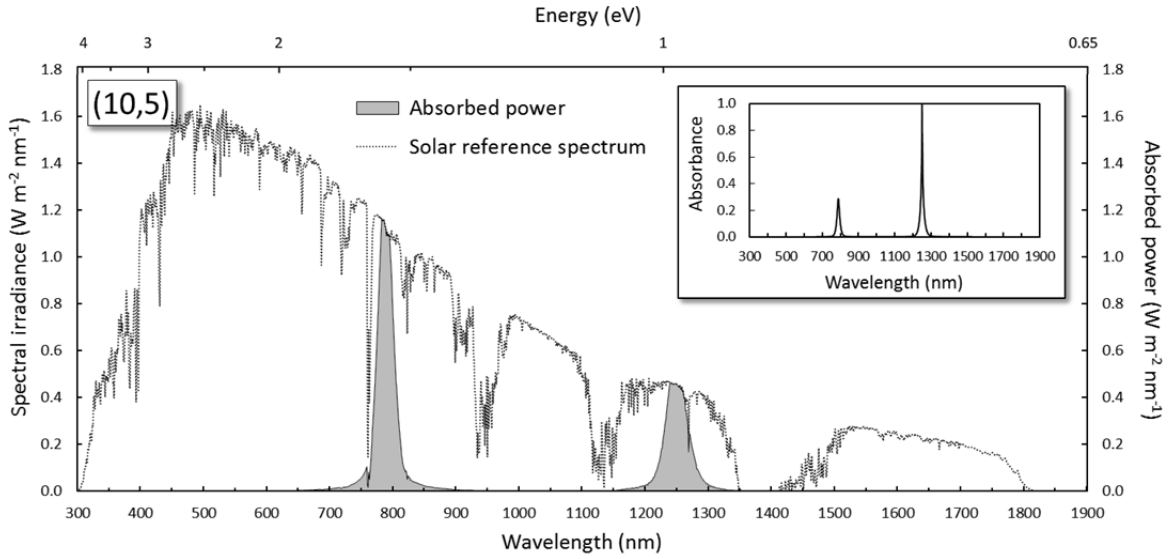
Energy (eV)
(10,5)
Absorbed power
Solar reference spectrum
Absorbance
Wavelength (nm)
Spectral irradiance (W m-2 nm-1)
Absorbed power (W m-2 nm-1)
Wavelength (nm)

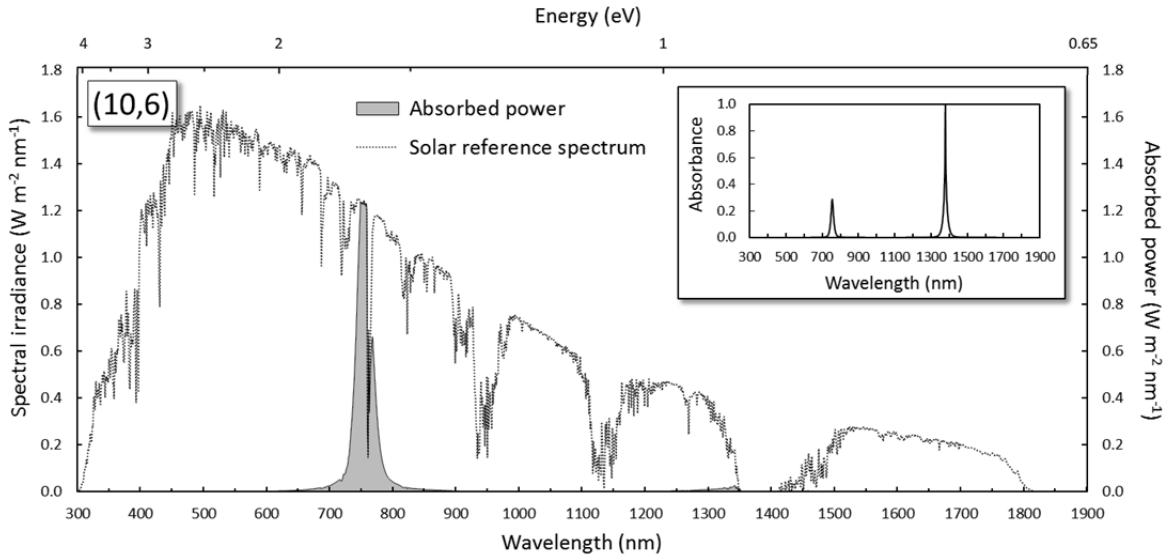
Energy (eV)
(10,6)
Absorbed power
Solar reference spectrum
Absorbance
Wavelength (nm)
Spectral irradiance (W m-2 nm-1)
Absorbed power (W m-2 nm-1)
Wavelength (nm)

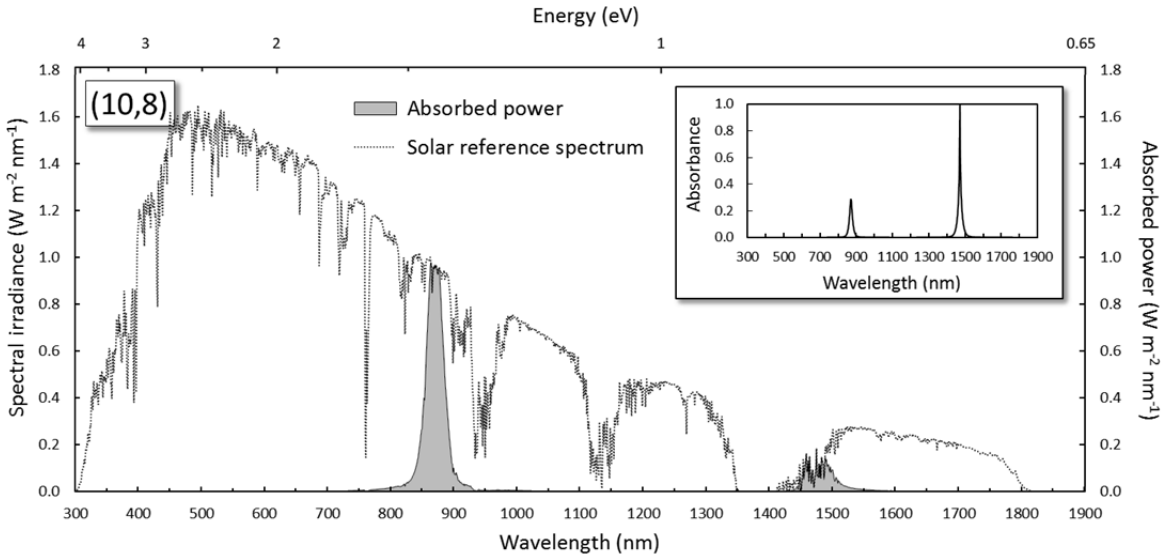
Energy (eV)
(10,8)
Absorbed power
Solar reference spectrum
Absorbance
Wavelength (nm)
Spectral irradiance (W m-2 nm-1)
Absorbed power (W m-2 nm-1)
Wavelength (nm)

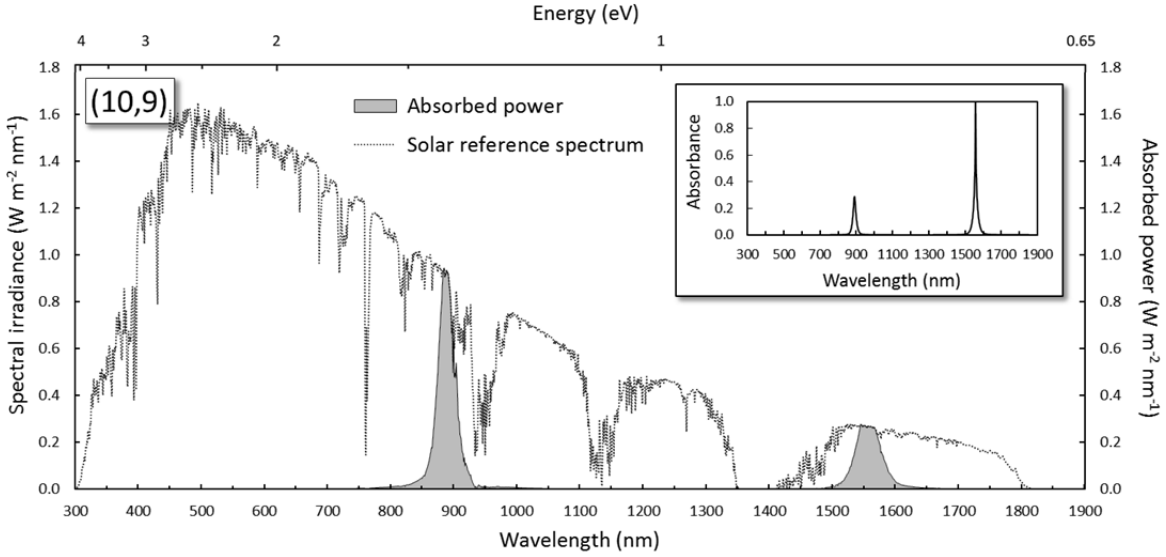
Energy (eV)
(10,9)
Absorbed power
Solar reference spectrum
Absorbance
Wavelength (nm)
Spectral irradiance (W m-2 nm-1)
Absorbed power (W m-2 nm-1)
Wavelength (nm)

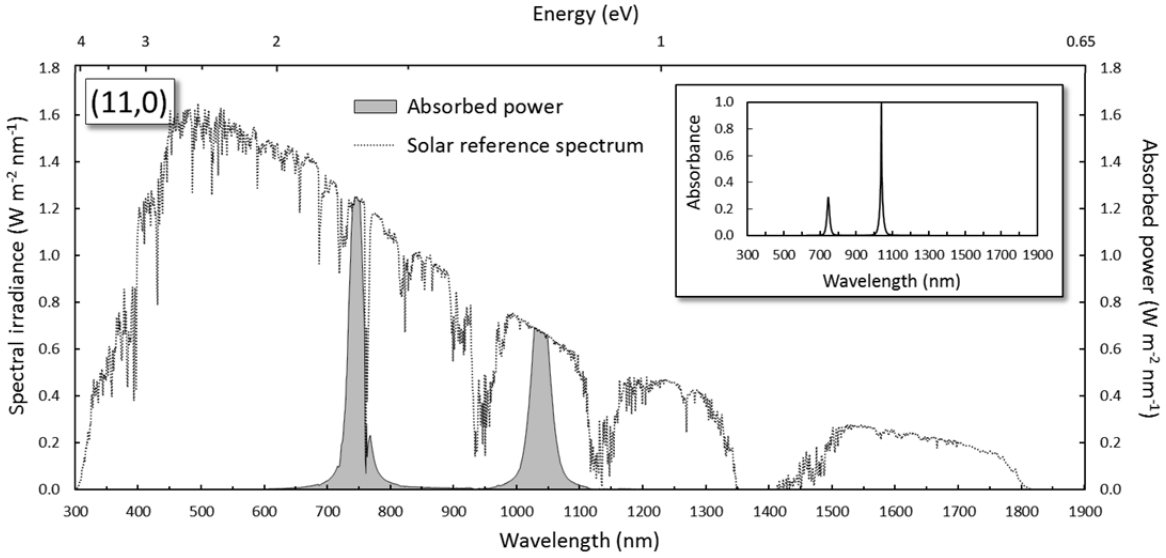
Energy (eV)
(11,0)
Absorbed power
Solar reference spectrum
Absorbance
Wavelength (nm)
Spectral irradiance (W m-2 nm-1)
Absorbed power (W m-2 nm-1)
Wavelength (nm)

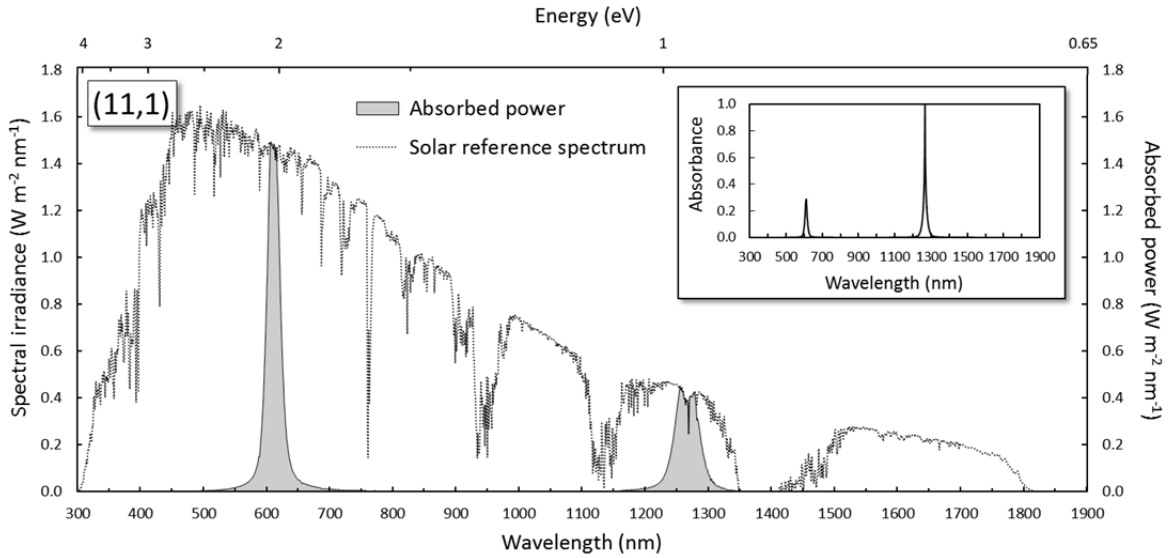
Energy (eV)
(11,1)
Absorbed power
Solar reference spectrum
Absorbance
Wavelength (nm)
Spectral irradiance (W m-2 nm-1)
Absorbed power (W m-2 nm-1)
Wavelength (nm)

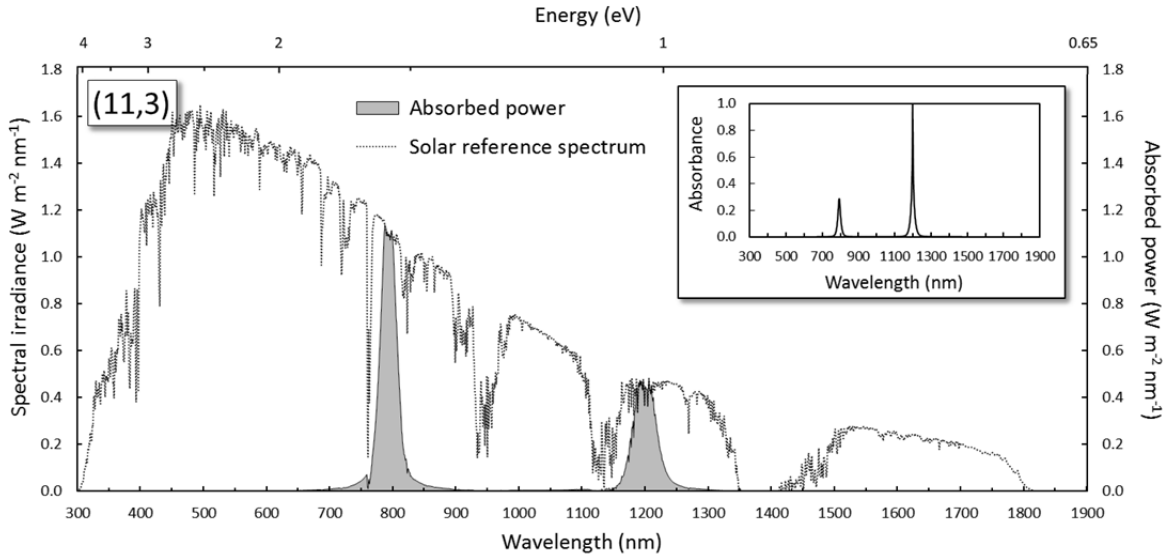
Energy (eV)
(11,3)
Absorbed power
Solar reference spectrum
Absorbance
Wavelength (nm)
Spectral irradiance (W m-2 nm-1)
Absorbed power (W m-2 nm-1)
Wavelength (nm)

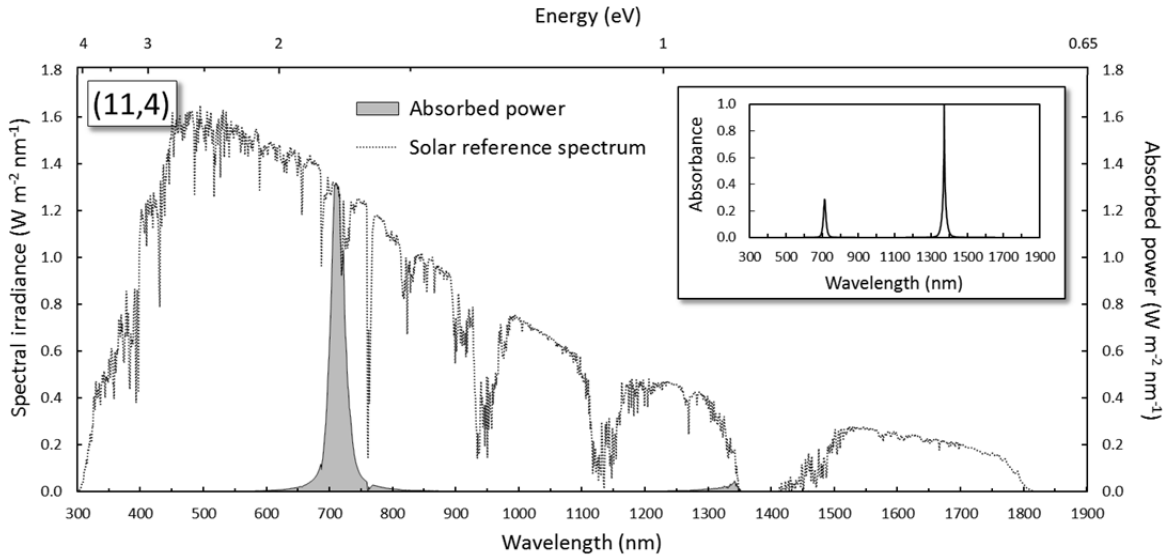
Energy (eV)
(11,4)
Absorbed power
Solar reference spectrum
Absorbance
Wavelength (nm)
Spectral irradiance (W m-2 nm-1)
Absorbed power (W m-2 nm-1)
Wavelength (nm)

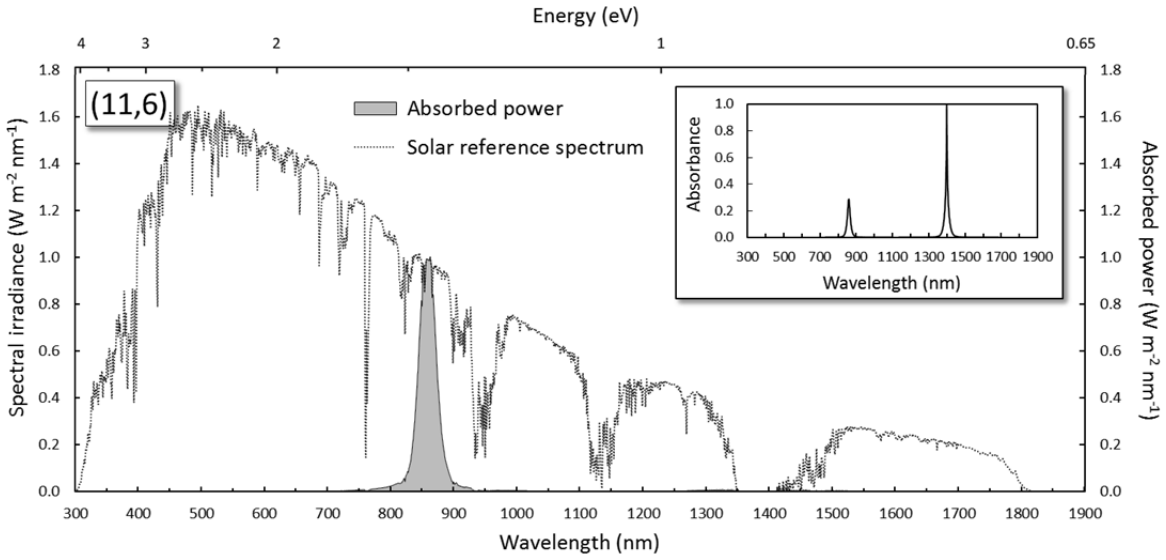
Energy (eV)
(11,6)
Absorbed power
Solar reference spectrum
Absorbance
Wavelength (nm)
Spectral irradiance (W m-2 nm-1)
Absorbed power (W m-2 nm-1)
Wavelength (nm)

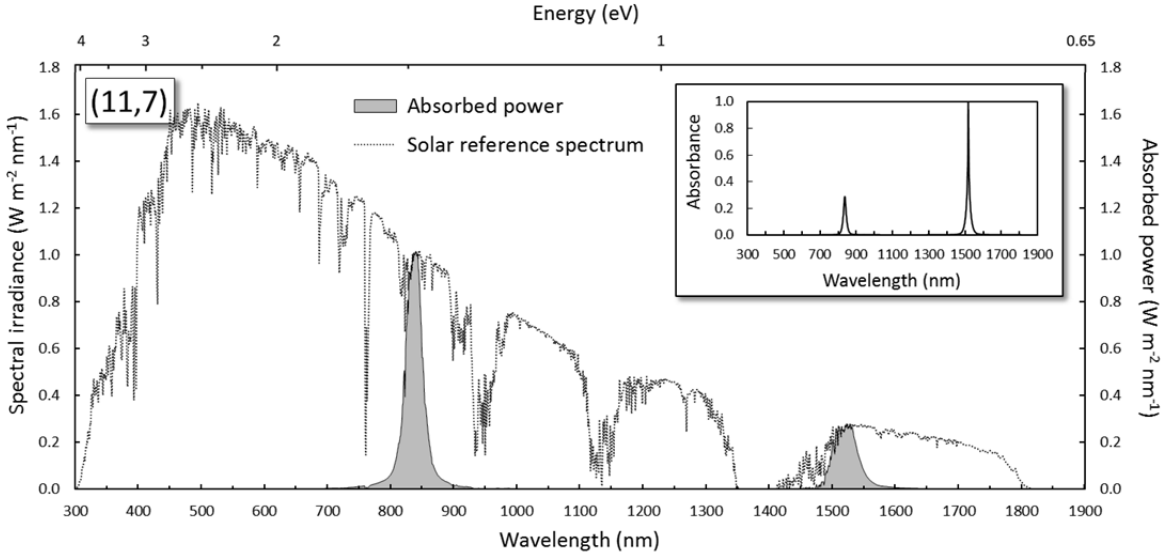
Energy (eV)
(11,7)
Absorbed power
Solar reference spectrum
Absorbance
Wavelength (nm)
Spectral irradiance (W m-2 nm-1)
Absorbed power (W m-2 nm-1)
Wavelength (nm)

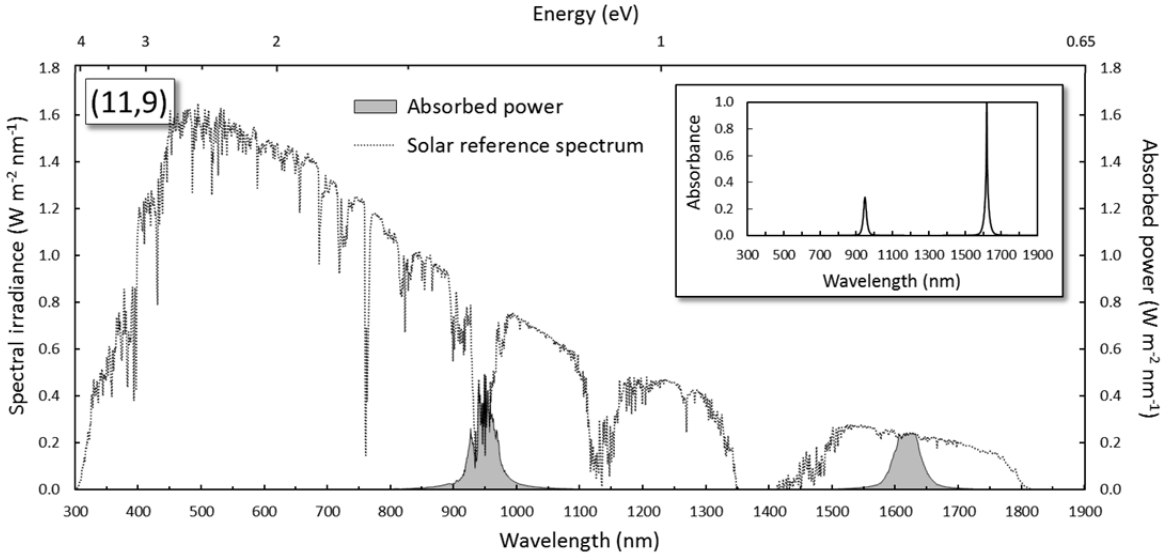
Energy (eV)
(11,9)
Absorbed power
Solar reference spectrum
Absorbance
Wavelength (nm)
Spectral irradiance (W m-2 nm-1)
Absorbed power (W m-2 nm-1)
Wavelength (nm)

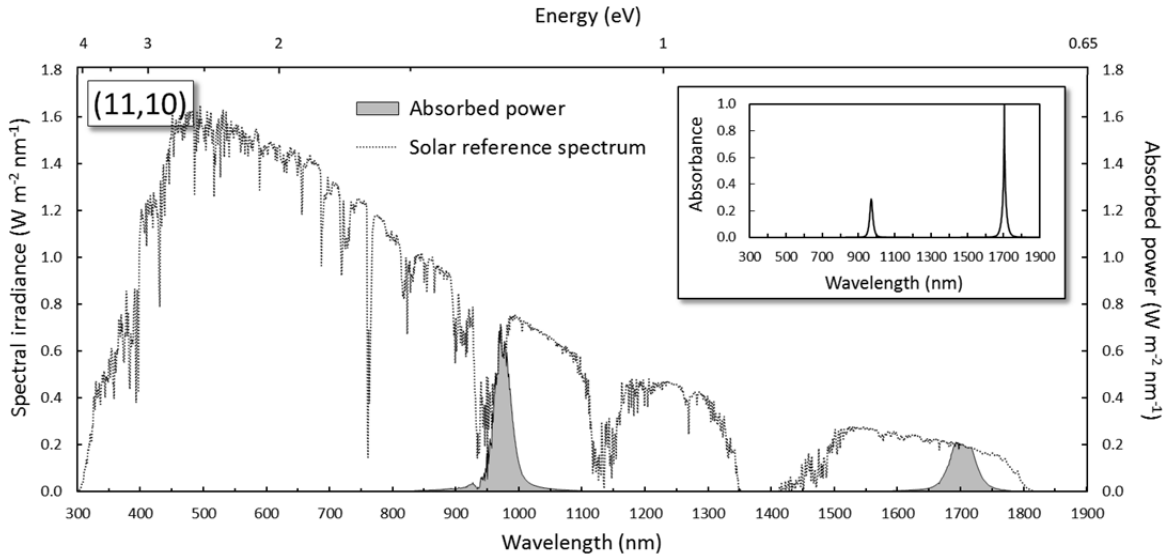
Energy (eV)
(11,10)
Absorbed power
Solar reference spectrum
Absorbance
Wavelength (nm)
Spectral irradiance (W m-2 nm-1)
Absorbed power (W m-2 nm-1)
Wavelength (nm)

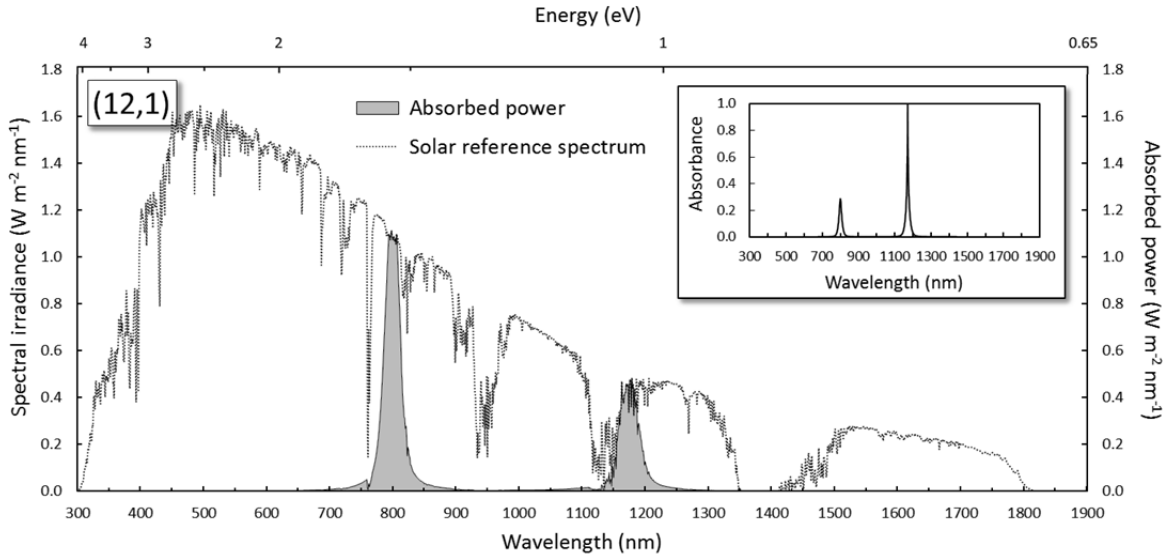
Energy (eV)
(12,1)
Absorbed power
Solar reference spectrum
Absorbance
Wavelength (nm)
Spectral irradiance (W m-2 nm-1)
Absorbed power (W m-2 nm-1)
Wavelength (nm)

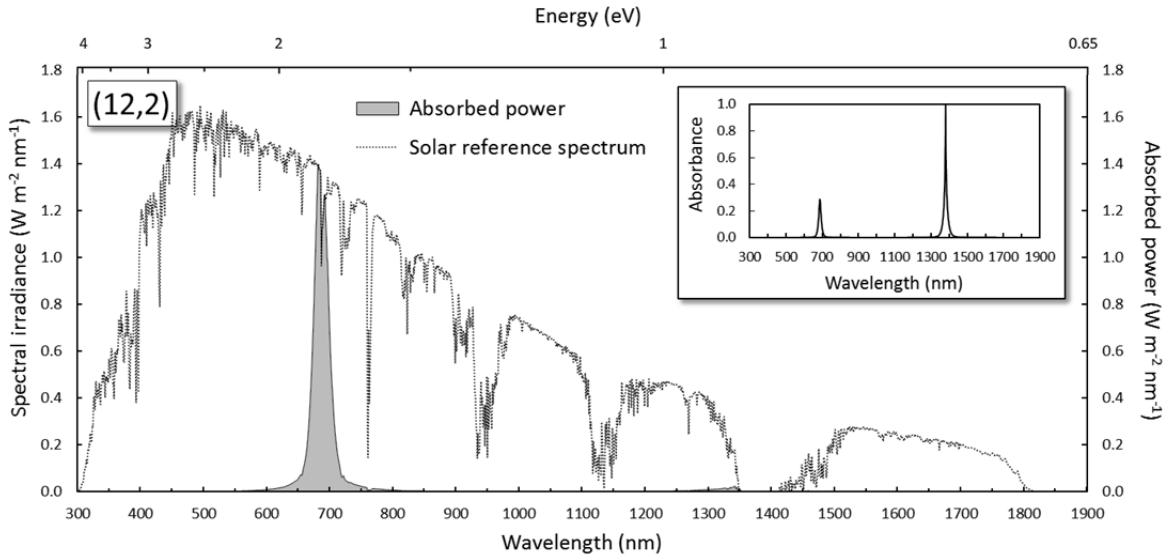
Energy (eV)
(12,2)
Absorbed power
Solar reference spectrum
Absorbance
Wavelength (nm)
Spectral irradiance (W m-2 nm-1)
Absorbed power (W m-2 nm-1)
Wavelength (nm)

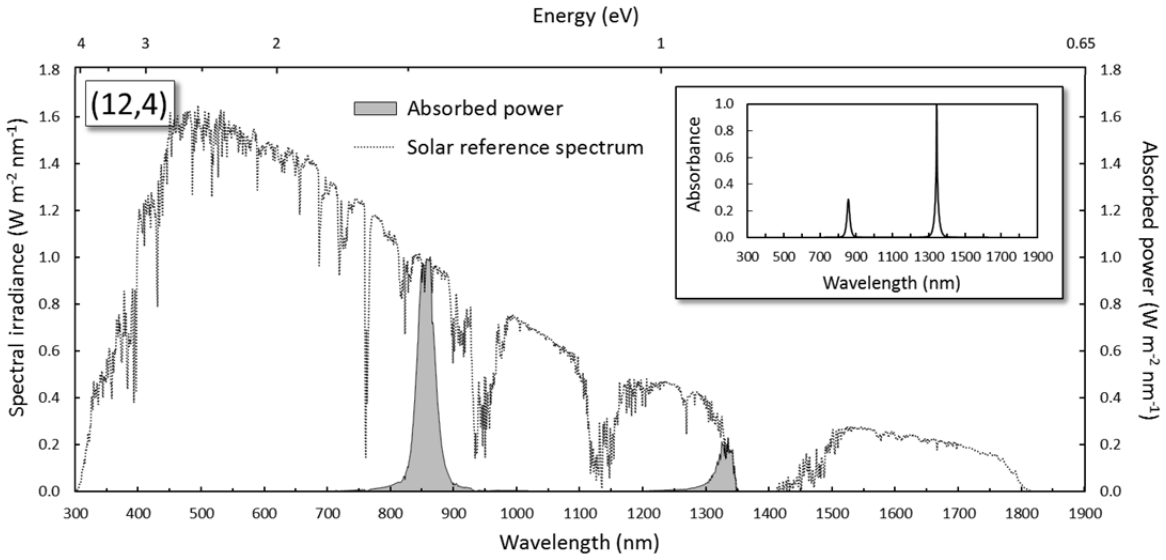
Energy (eV)
(12,4)
Absorbed power
Solar reference spectrum
Absorbance
Wavelength (nm)
Spectral irradiance (W m-2 nm-1)
Absorbed power (W m-2 nm-1)
Wavelength (nm)

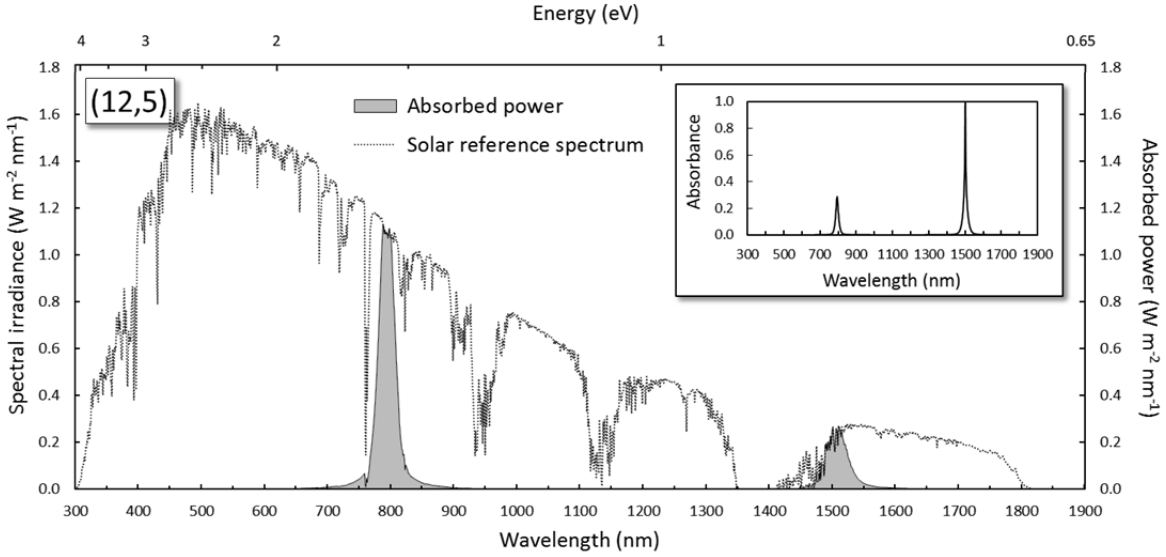
Energy (eV)
(12,5)
Absorbed power
Solar reference spectrum
Absorbance
Wavelength (nm)
Spectral irradiance (W m-2 nm-1)
Absorbed power (W m-2 nm-1)
Wavelength (nm)

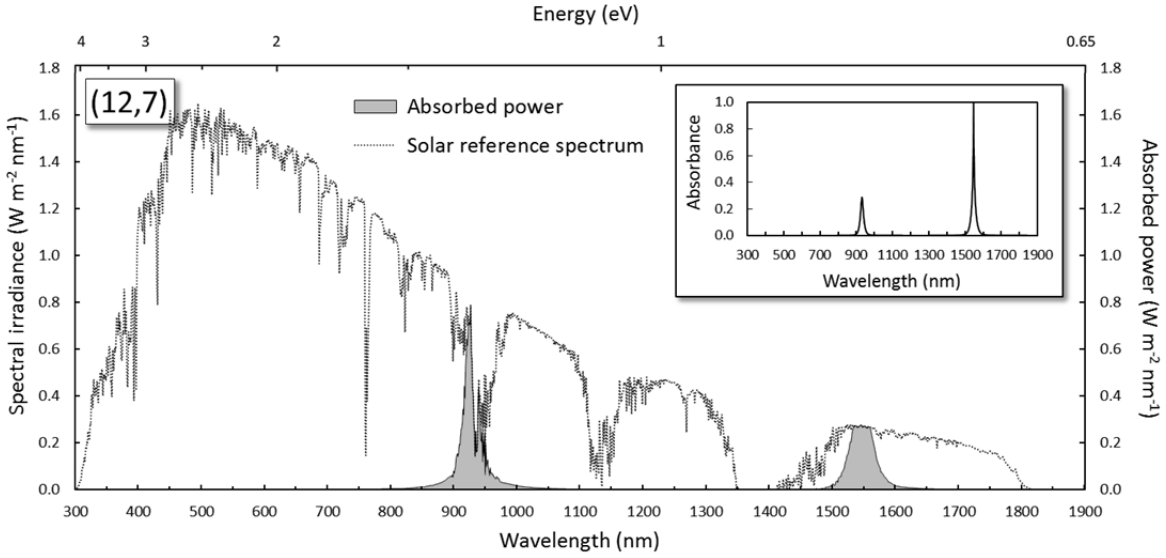
Energy (eV)
(12,7)
Absorbed power
Solar reference spectrum
Absorbance
Wavelength (nm)
Spectral irradiance (W m-2 nm-1)
Absorbed power (W m-2 nm-1)
Wavelength (nm)

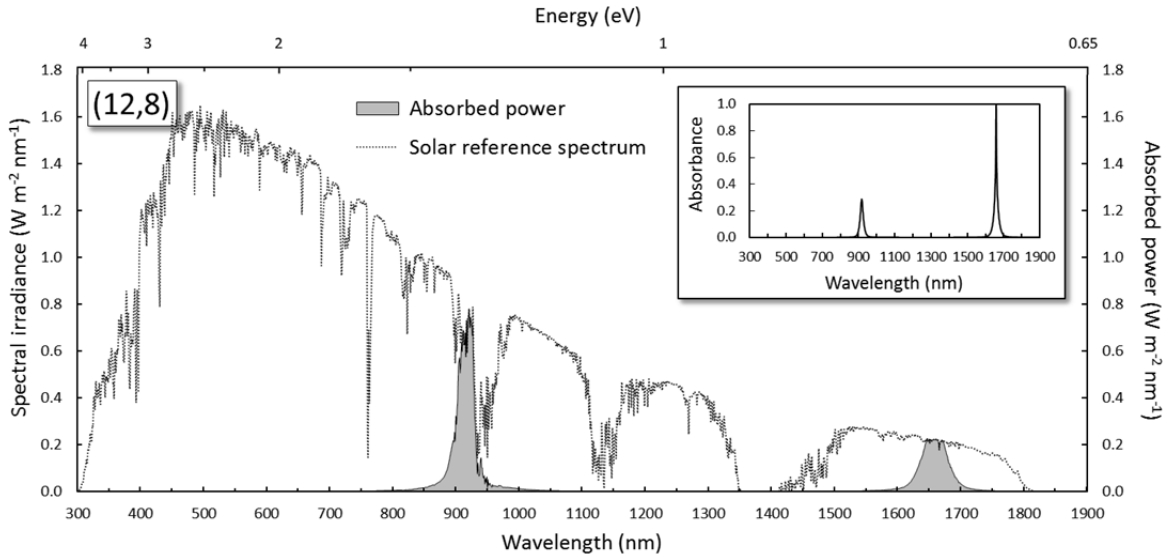
Energy (eV)
(12,8)
Absorbed power
Solar reference spectrum
Absorbance
Wavelength (nm)
Spectral irradiance (W m-2 nm-1)
Absorbed power (W m-2 nm-1)
Wavelength (nm)

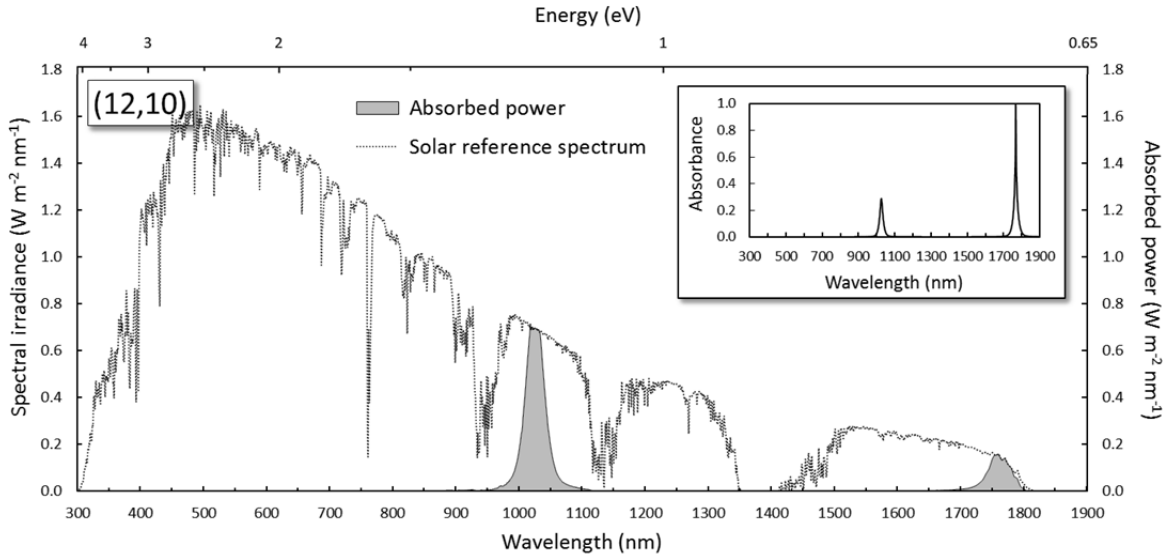
Energy (eV)
(12,10)
Absorbed power
Solar reference spectrum
Absorbance
Wavelength (nm)
Spectral irradiance (W m-2 nm-1)
Absorbed power (W m-2 nm-1)
Wavelength (nm)

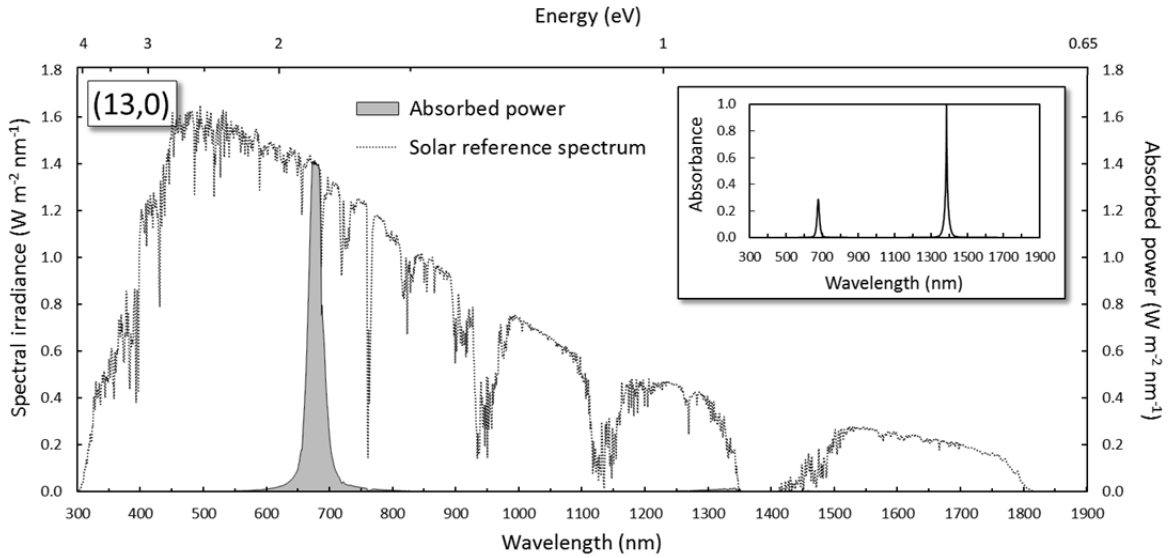
Energy (eV)
(13,0)
Absorbed power
Solar reference spectrum
Absorbance
Wavelength (nm)
Spectral irradiance (W m-2 nm-1)
Absorbed power (W m-2 nm-1)
Wavelength (nm)

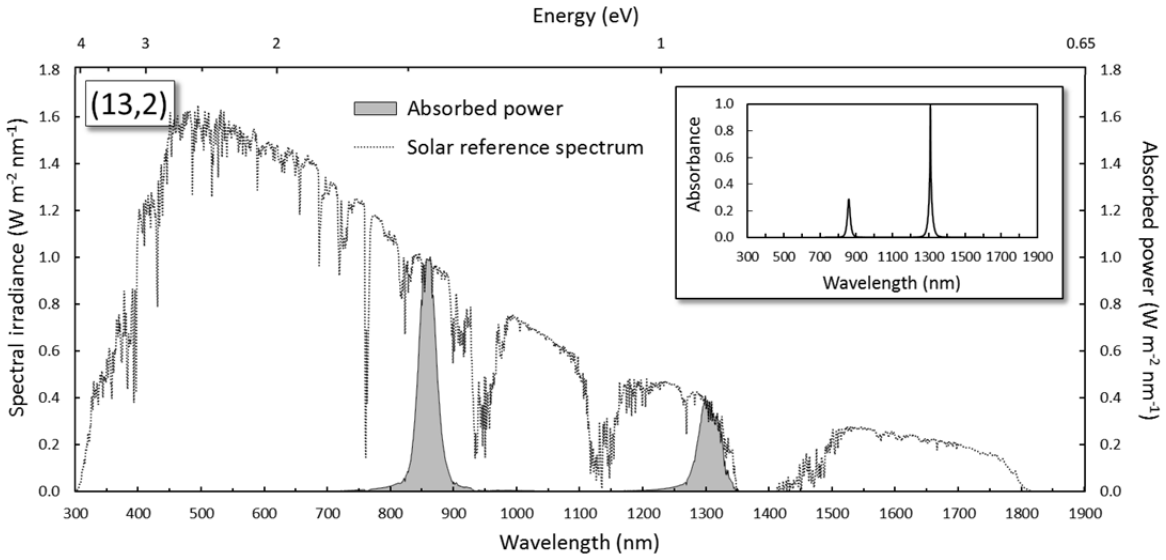
Energy (eV)
(13,2)
Absorbed power
Solar reference spectrum
Absorbance
Wavelength (nm)
Spectral irradiance (W m-2 nm-1)
Absorbed power (W m-2 nm-1)
Wavelength (nm)

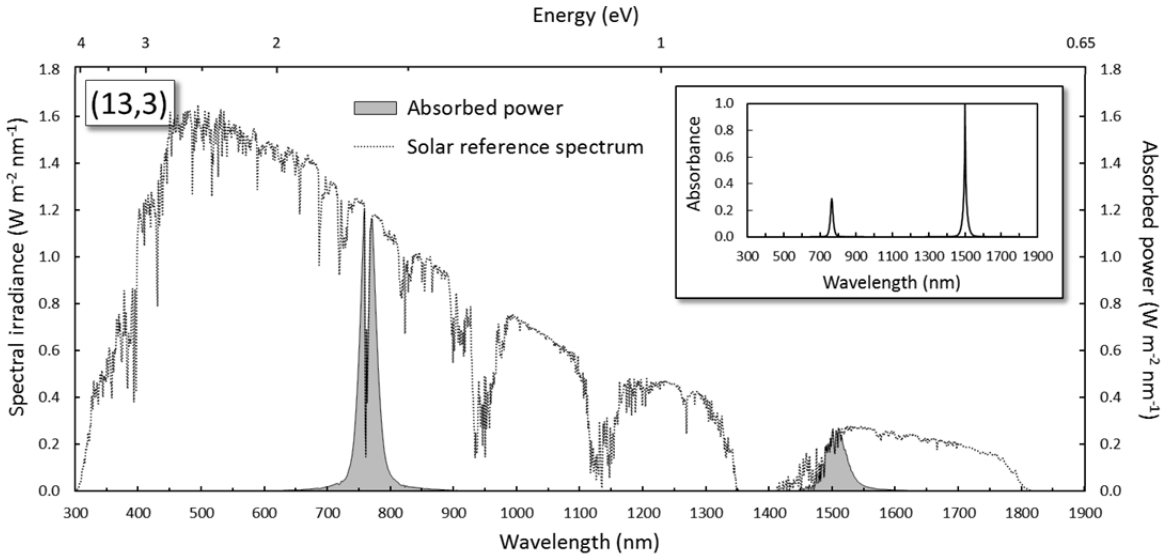
Energy (eV)
(13,3)
Absorbed power
Solar reference spectrum
Absorbance
Wavelength (nm)
Spectral irradiance (W m-2 nm-1)
Absorbed power (W m-2 nm-1)
Wavelength (nm)

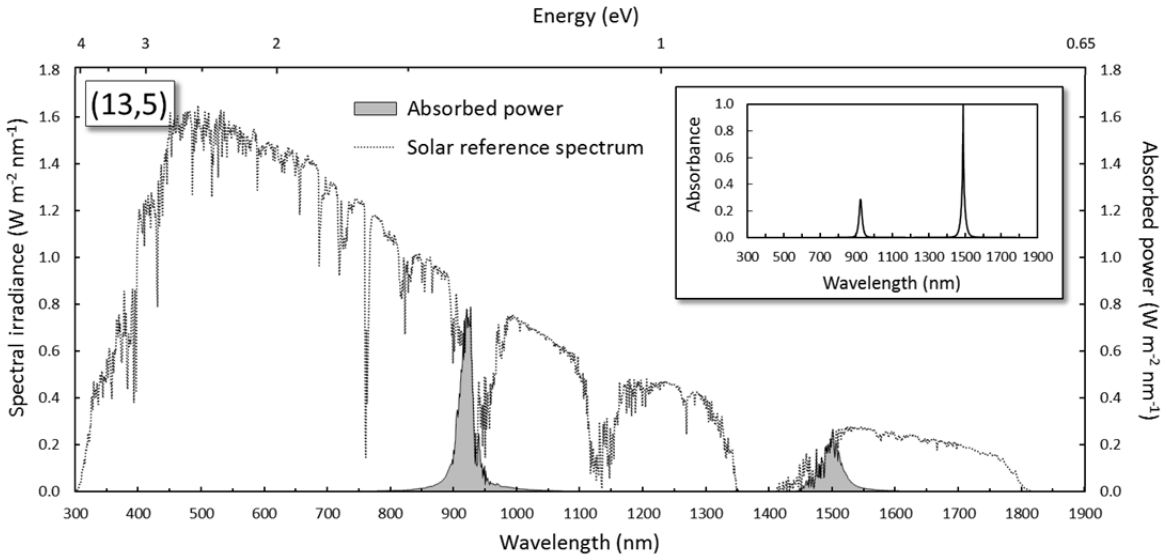
Energy (eV)
(13,5)
Absorbed power
Solar reference spectrum
Absorbance
Wavelength (nm)
Spectral irradiance (W m-2 nm-1)
Absorbed power (W m-2 nm-1)
Wavelength (nm)

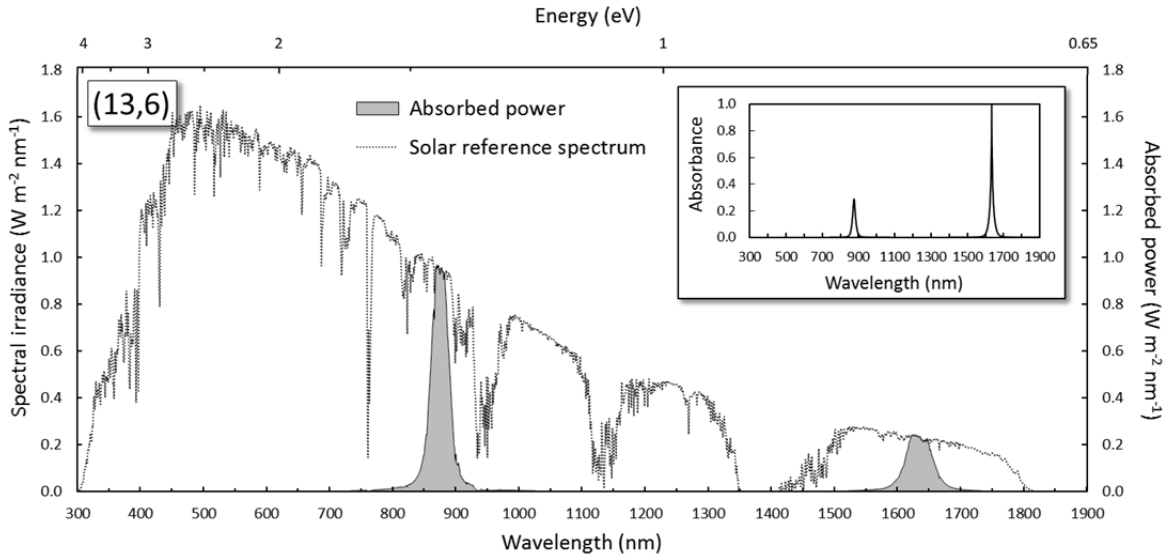
Energy (eV)
(13,6)
Absorbed power
Solar reference spectrum
Absorbance
Wavelength (nm)
Spectral irradiance (W m-2 nm-1)
Absorbed power (W m-2 nm-1)
Wavelength (nm)

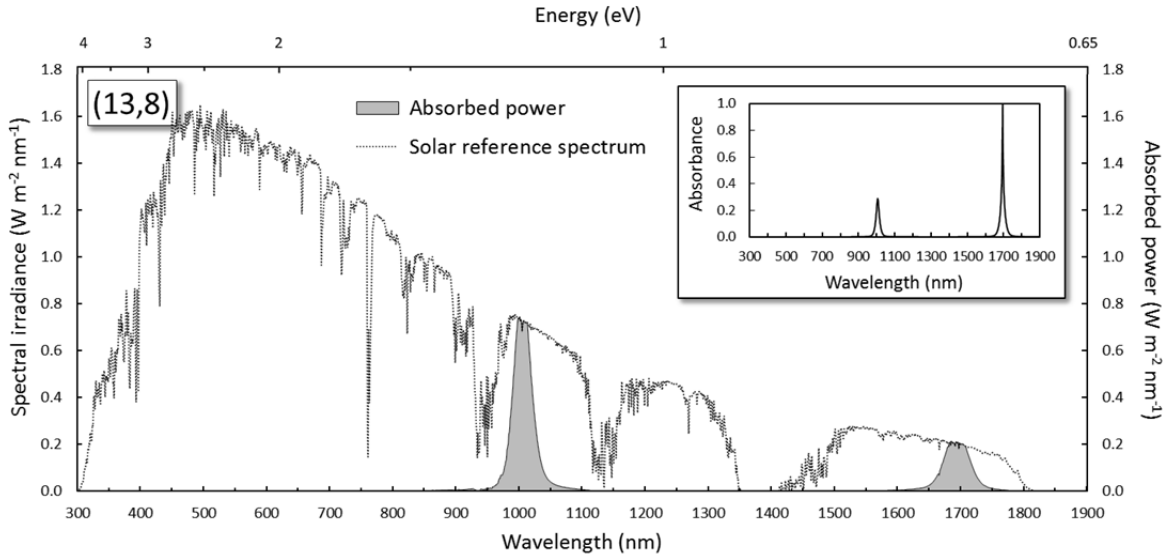
Energy (eV)
(13,8)
Absorbed power
Solar reference spectrum
Absorbance
Wavelength (nm)
Spectral irradiance (W m-2 nm-1)
Absorbed power (W m-2 nm-1)
Wavelength (nm)

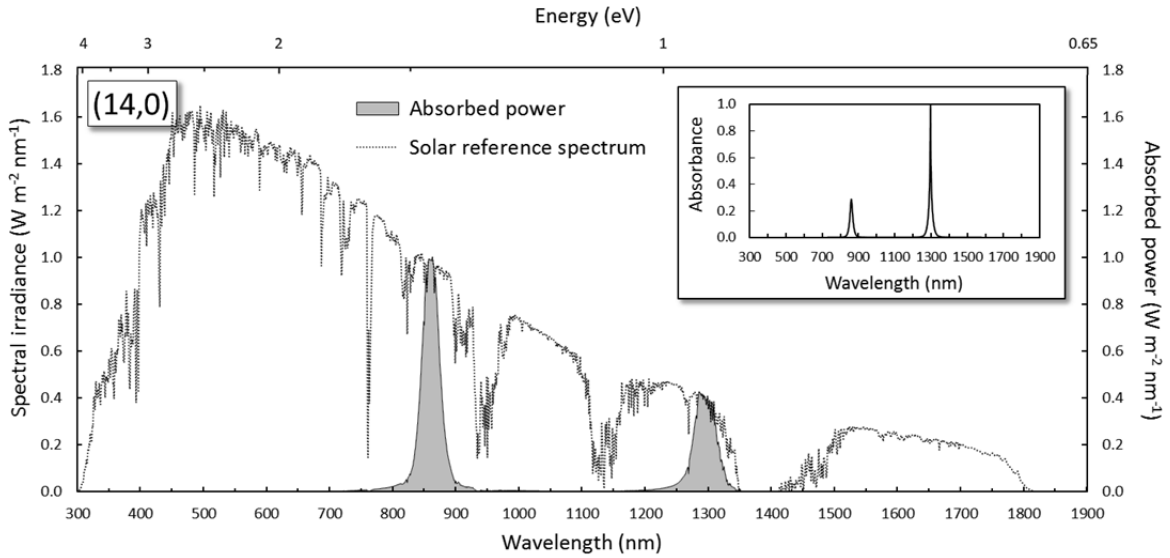
Energy (eV)
(14,0)
Absorbed power
Solar reference spectrum
Absorbance
Wavelength (nm)
Spectral irradiance (W m-2 nm-1)
Absorbed power (W m-2 nm-1)
Wavelength (nm)

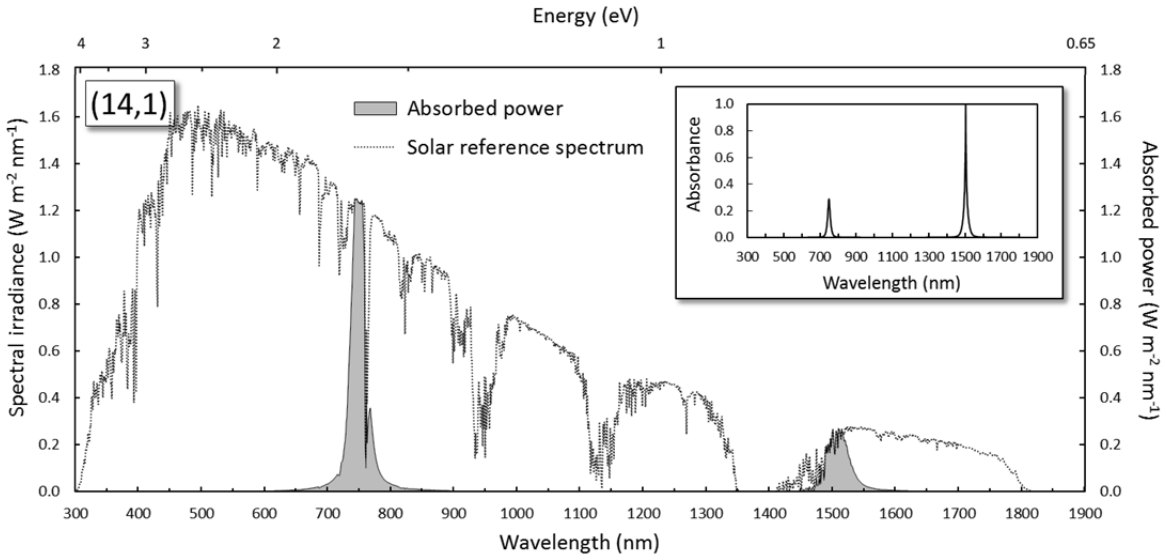
Energy (eV)
(14,1)
Absorbed power
Solar reference spectrum
Absorbance
Wavelength (nm)
Spectral irradiance (W m-2 nm-1)
Absorbed power (W m-2 nm-1)
Wavelength (nm)

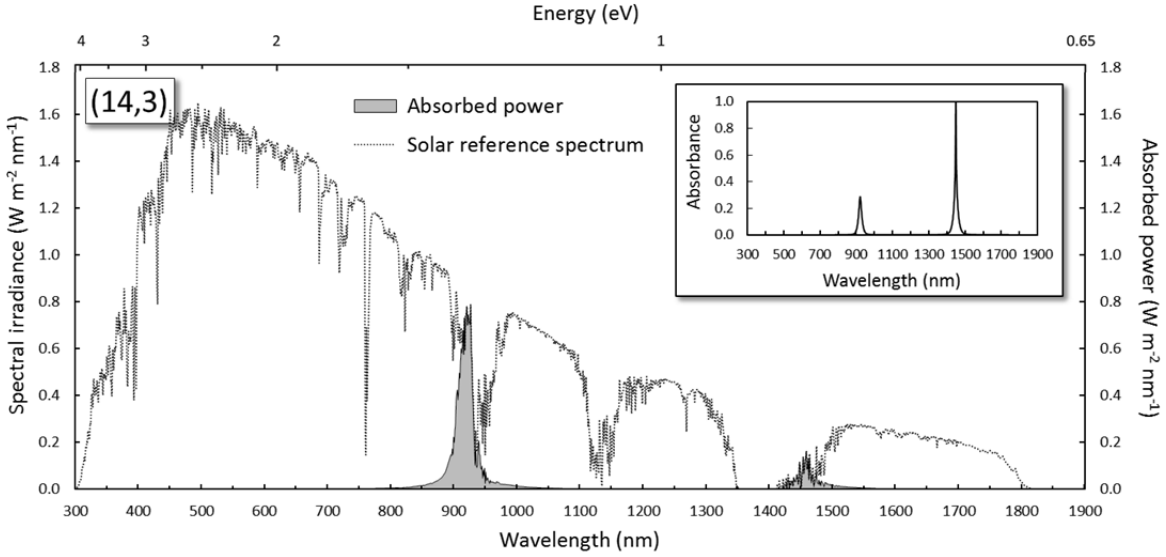
Energy (eV)
(14,3)
Absorbed power
Solar reference spectrum
Absorbance
Wavelength (nm)
Spectral irradiance (W m-2 nm-1)
Absorbed power (W m-2 nm-1)
Wavelength (nm)

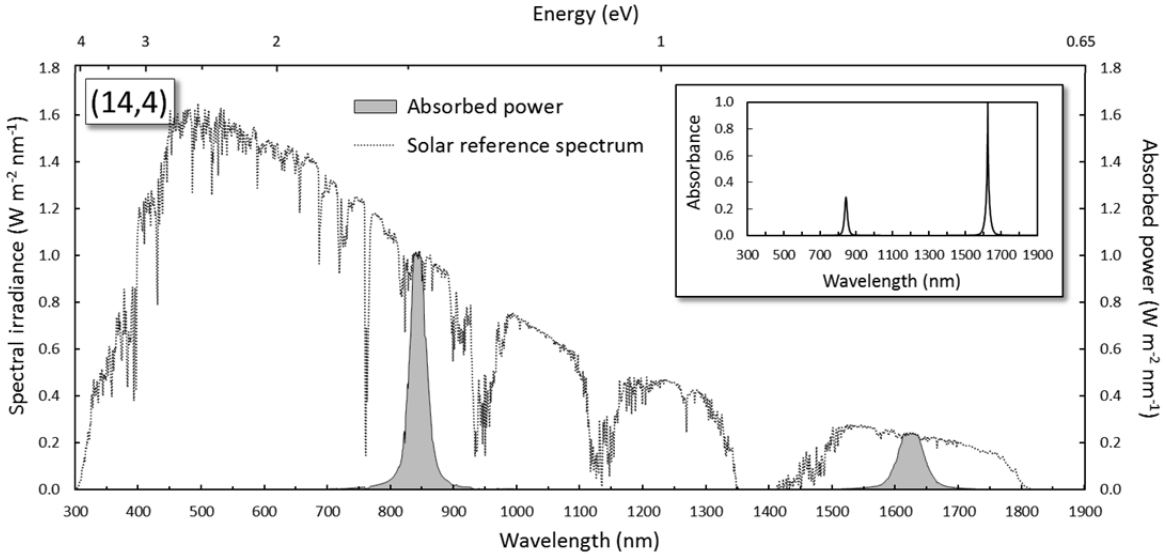
Energy (eV)
(14,4)
Absorbed power
Solar reference spectrum
Absorbance
Wavelength (nm)
Spectral irradiance (W m-2 nm-1)
Absorbed power (W m-2 nm-1)
Wavelength (nm)

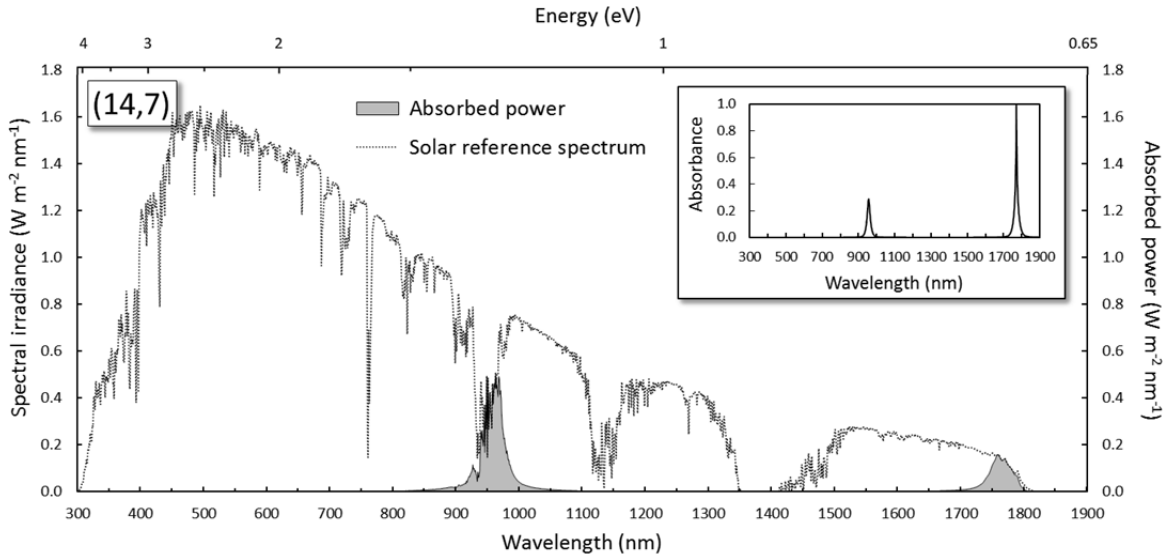
Energy (eV)
(14,7)
Absorbed power
Solar reference spectrum
Absorbance
Wavelength (nm)
Spectral irradiance (W m-2 nm-1)
Absorbed power (W m-2 nm-1)
Wavelength (nm)

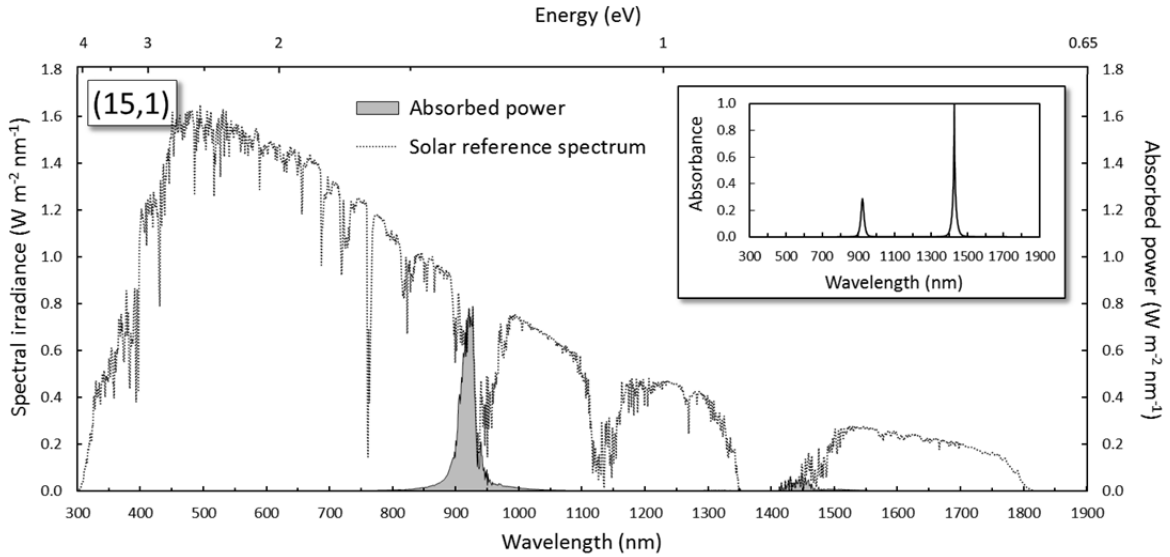
Energy (eV)
(15,1)
Absorbed power
Solar reference spectrum
Absorbance
Wavelength (nm)
Spectral irradiance (W m-2 nm-1)
Absorbed power (W m-2 nm-1)
Wavelength (nm)

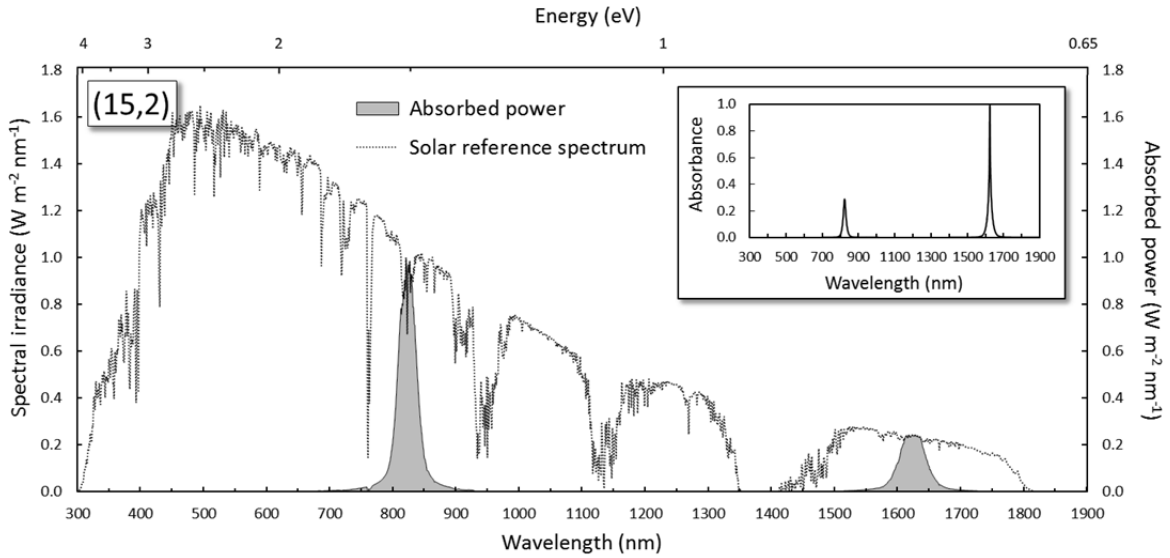
Energy (eV)
(15,2)
Absorbed power
Solar reference spectrum
Absorbance
Wavelength (nm)
Spectral irradiance (W m-2 nm-1)
Absorbed power (W m-2 nm-1)
Wavelength (nm)

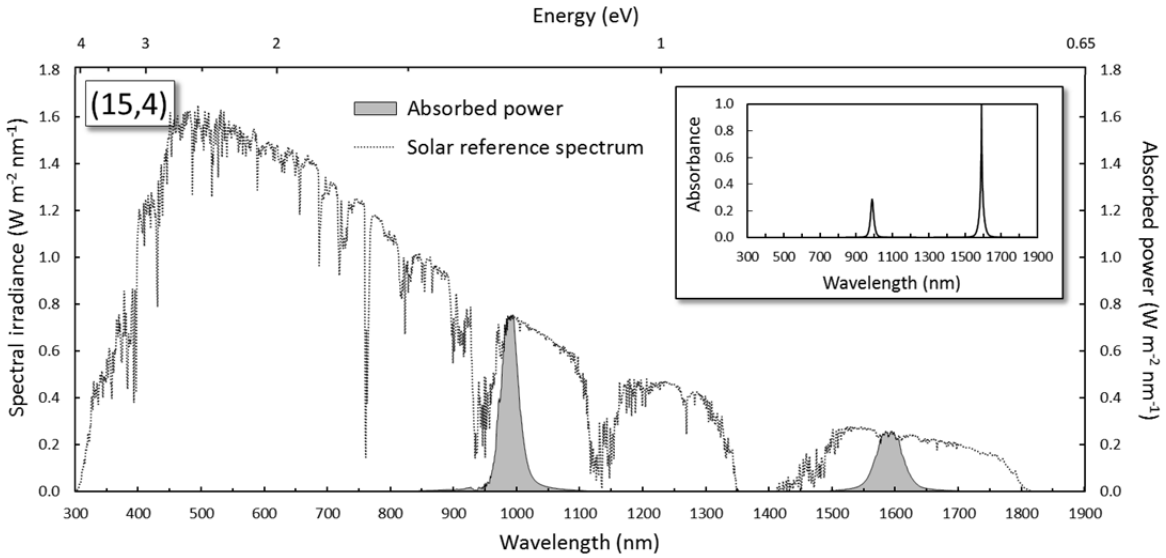
Energy (eV)
(15,4)
Absorbed power
Solar reference spectrum
Absorbance
Wavelength (nm)
Spectral irradiance (W m-2 nm-1)
Absorbed power (W m-2 nm-1)
Wavelength (nm)

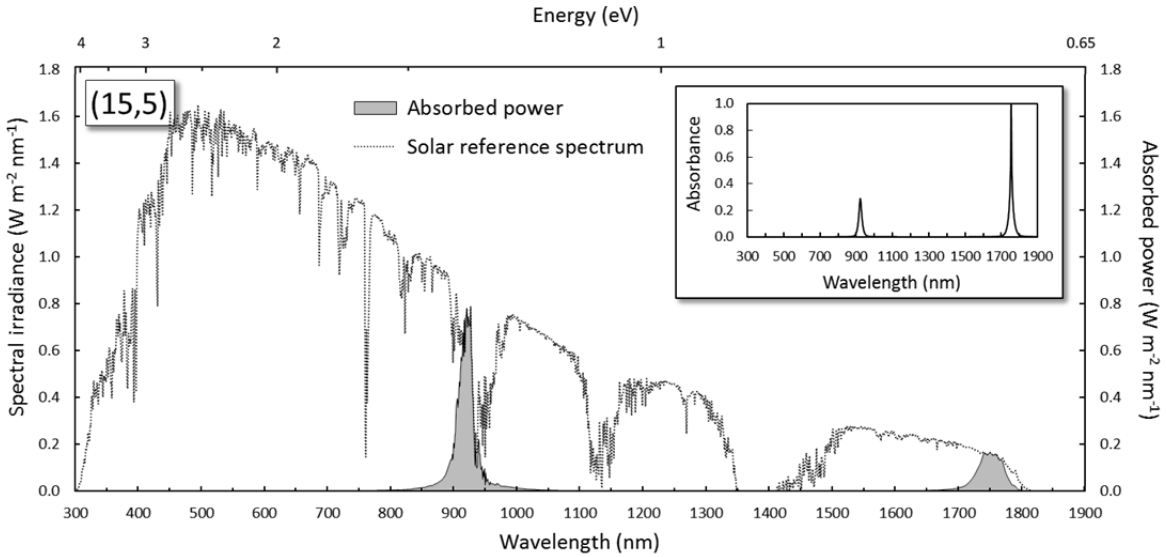
Energy (eV)
(15,5)
Absorbed power
Solar reference spectrum
Absorbance
Wavelength (nm)
Spectral irradiance (W m-2 nm-1)
Absorbed power (W m-2 nm-1)
Wavelength (nm)

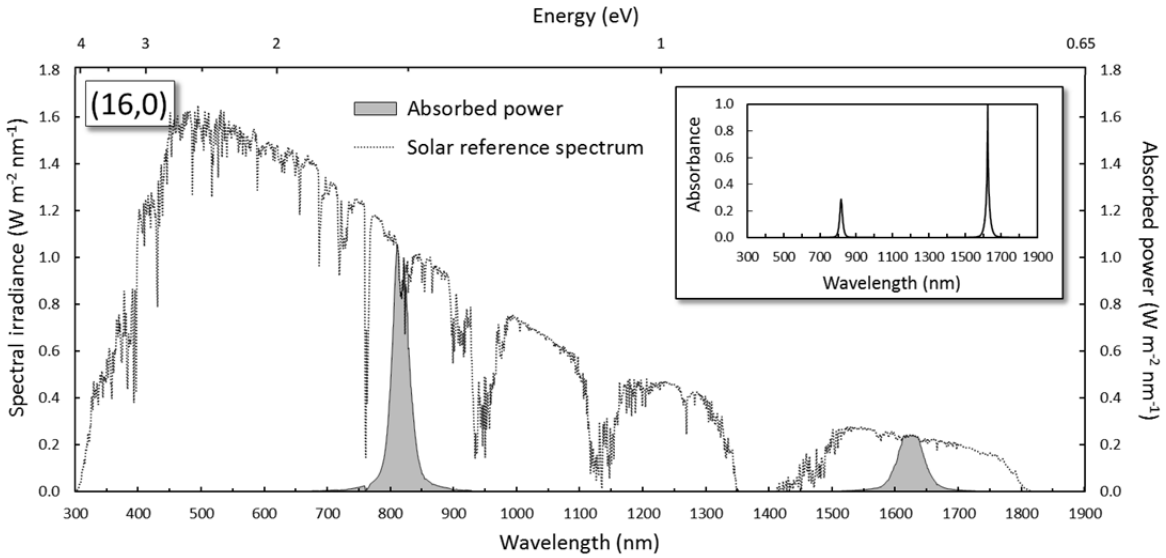
Energy (eV)
(16,0)
Absorbed power
Solar reference spectrum
Absorbance
Wavelength (nm)
Spectral irradiance (W m-2 nm-1)
Absorbed power (W m-2 nm-1)
Wavelength (nm)

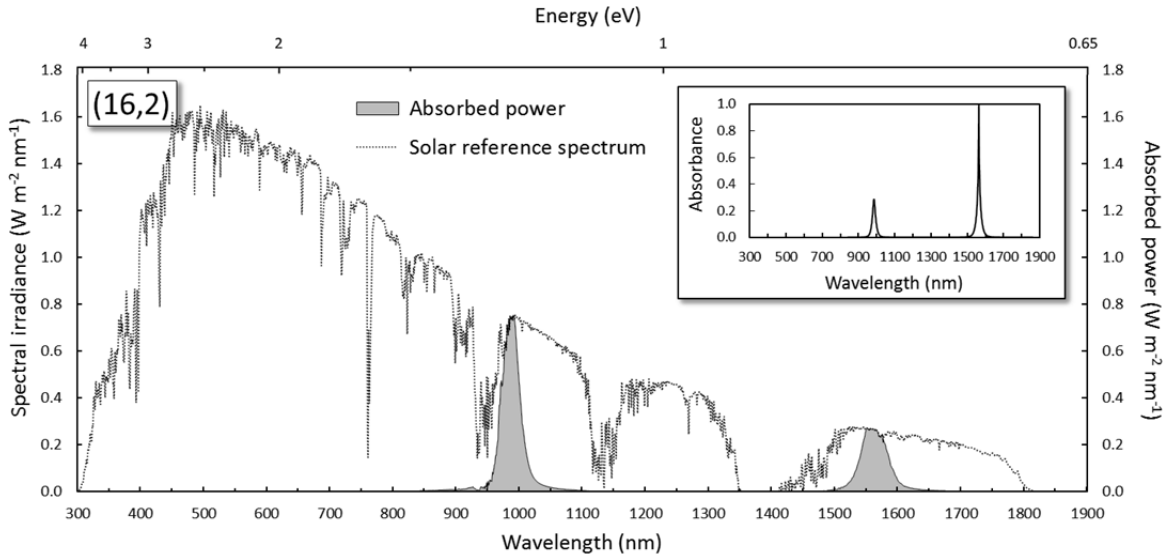
Energy (eV)
4
3
2
1
0.65
(16,2)
Absorbed power
Solar reference spectrum
Absorbance
Wavelength (nm)
Spectral irradiance (W m-2 nm-1)
Absorbed power (W m-2 nm-1)
Wavelength (nm)

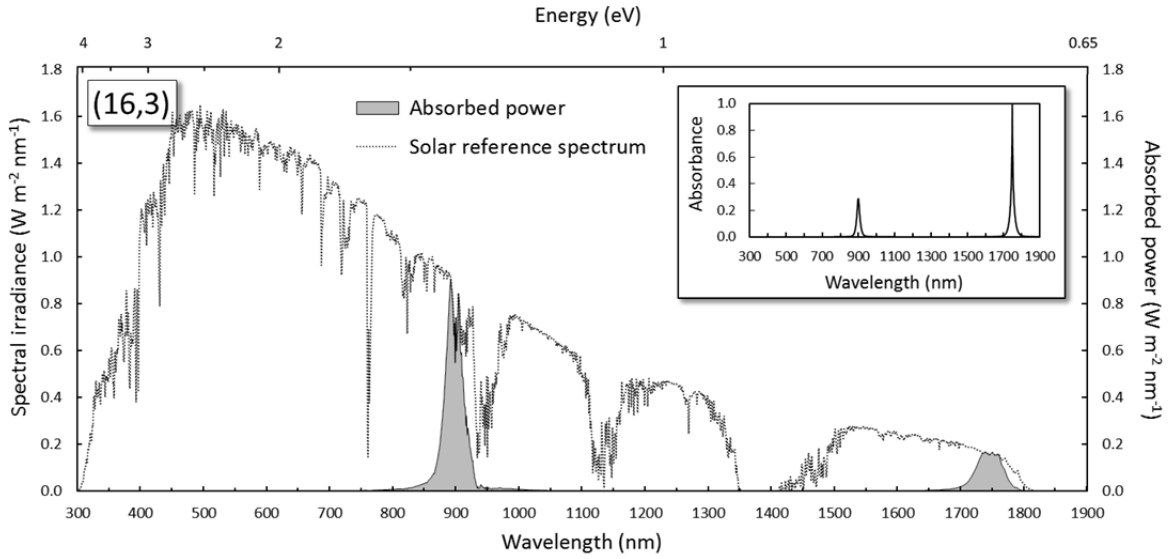
Energy (eV)
4
3
2
1
0.65
(16,3)
Absorbed power
Solar reference spectrum
Absorbance
Wavelength (nm)
Spectral irradiance (W m-2 nm-1)
Absorbed power (W m-2 nm-1)
Wavelength (nm)

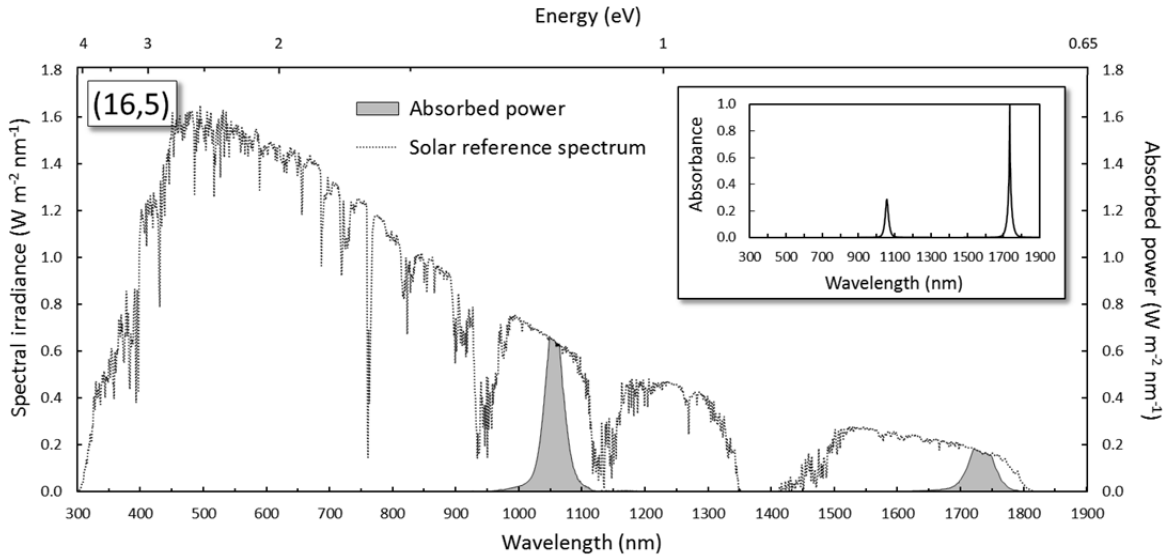
Energy (eV)
4
3
2
1
0.65
(16,5)
Absorbed power
Solar reference spectrum
Absorbance
Wavelength (nm)
Spectral irradiance (W m-2 nm-1)
Absorbed power (W m-2 nm-1)
Wavelength (nm)

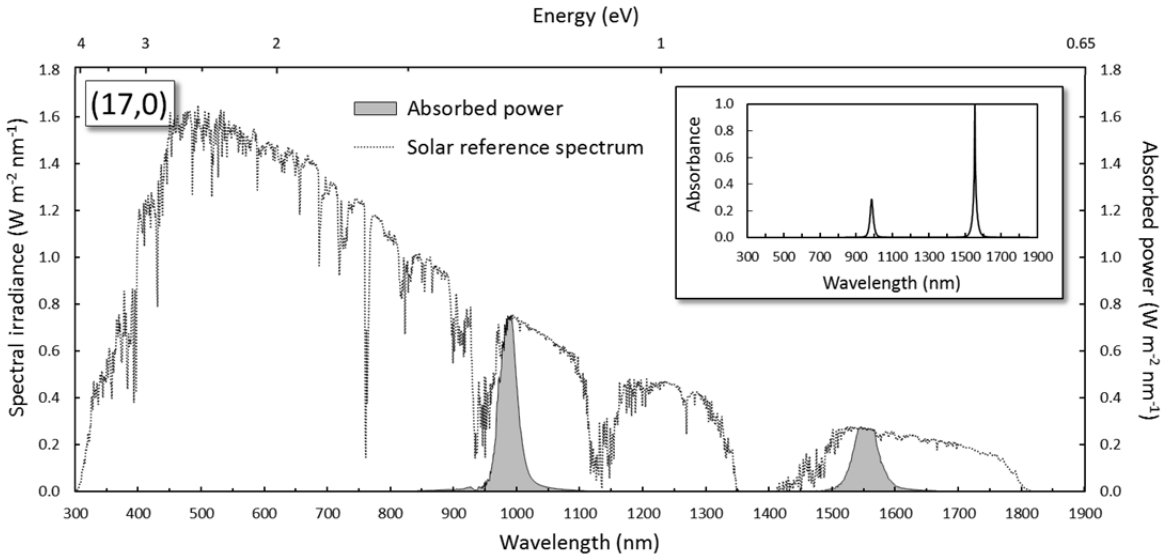
Energy (eV)
(17,0)
Absorbed power
Solar reference spectrum
Absorbance
Wavelength (nm)
Spectral irradiance (W m-2 nm-1)
Absorbed power (W m-2 nm-1)
Wavelength (nm)

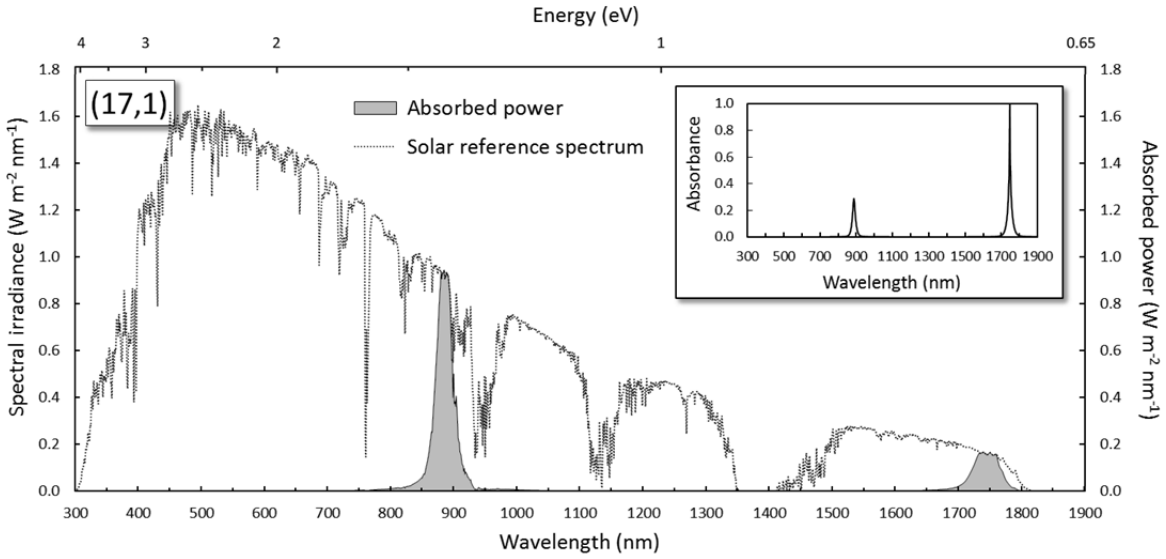
Energy (eV)
(17,1)
Absorbed power
Solar reference spectrum
Absorbance
Wavelength (nm)
Spectral irradiance (W m-2 nm-1)
Absorbed power (W m-2 nm-1)
Wavelength (nm)

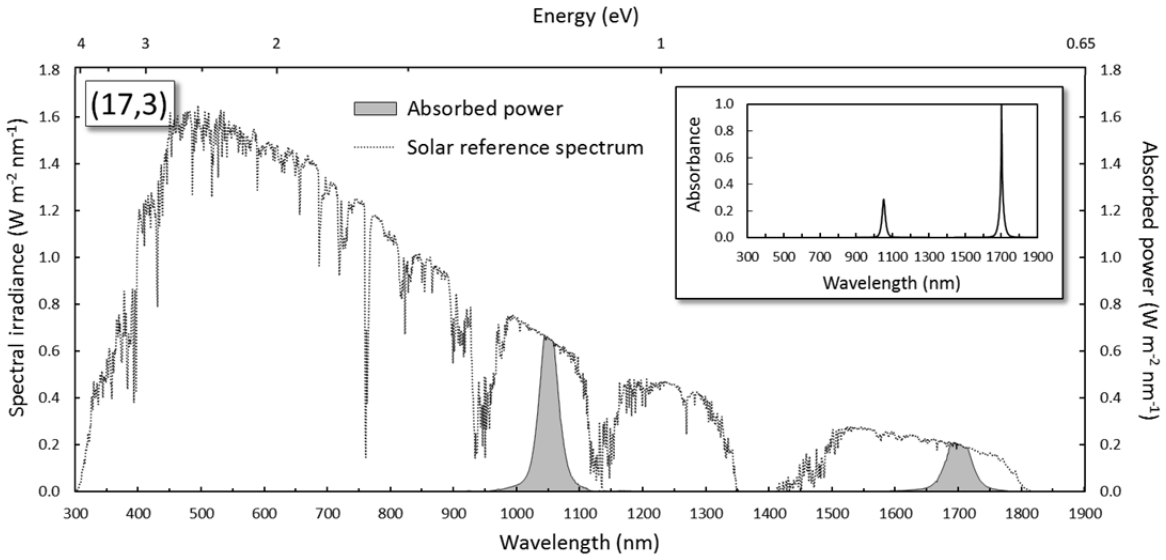
Energy (eV)
(17,3)
Absorbed power
Solar reference spectrum
Absorbance
Wavelength (nm)
Spectral irradiance (W m-2 nm-1)
Absorbed power (W m-2 nm-1)
Wavelength (nm)

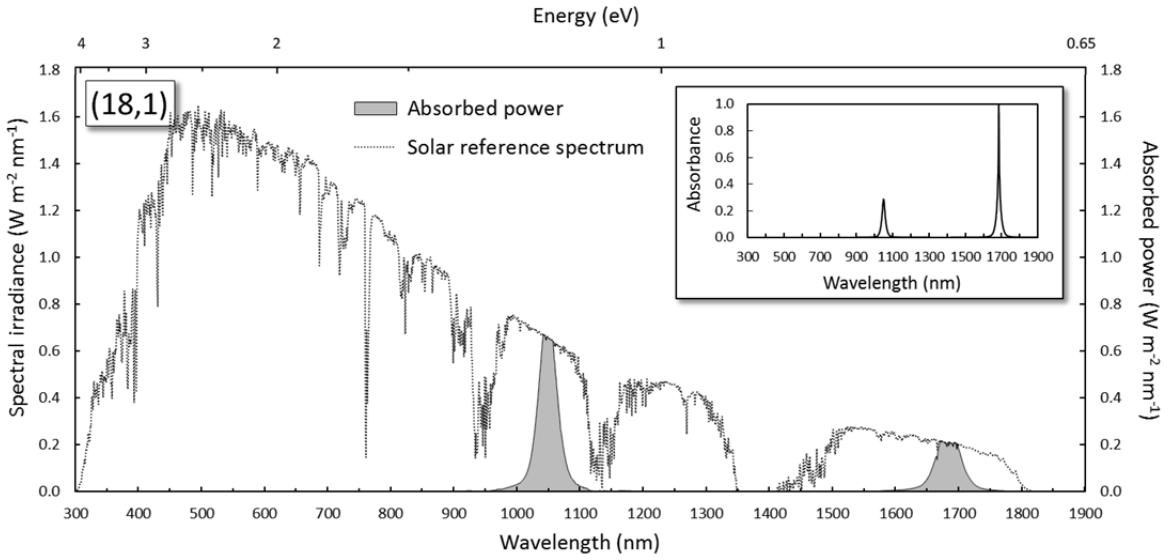
Energy (eV)
4
3
2
1
0.65
(18,1)
Absorbed power
Solar reference spectrum
Absorbance
Wavelength (nm)
Spectral irradiance (W m-2 nm-1)
Absorbed power (W m-2 nm-1)
Wavelength (nm)

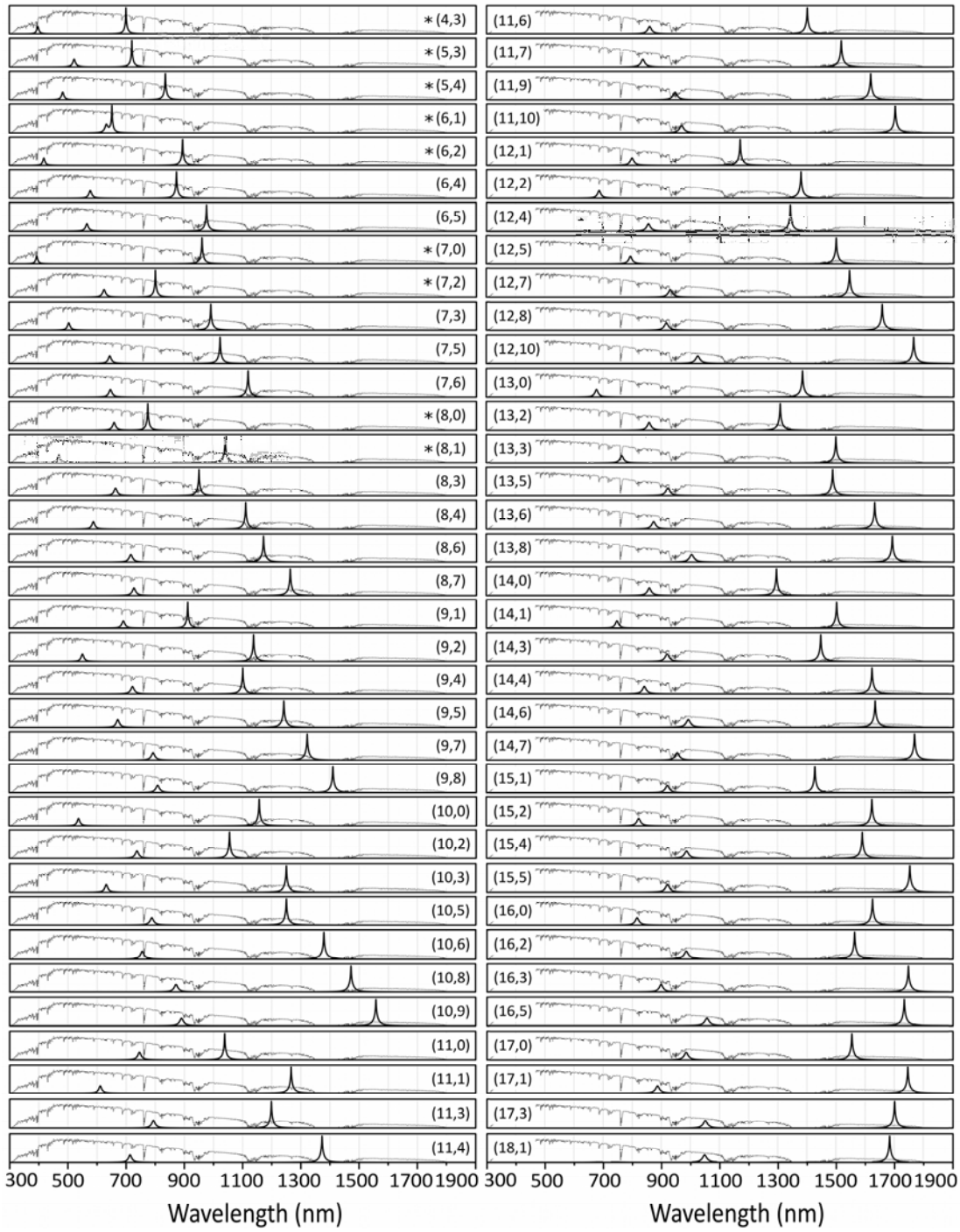

Figure A4.70 The simulated absorption spectra of all of the s-SWNTs considered in Chapter 7, listed in order of (n,m) species and overlaid with the AM1.5G solar reference spectrum. Species marked with an asterisk (*) have not been demonstrated to be stable in the isolated state (diameter less than ~0.7 nm) but are known to exist as the inner walls of double- or multi-walled nanotubes.